Advanced Characterisation of Catalytic Materials Using Synchrotron Radiation Techniques

Thomas Daley

University College London

Thesis presented in partial fulfilment of the requirements for the degree of Engineering Doctorate

2015

Declaration

I, Thomas Daley, confirm that the work presented in this thesis is my own. Where information has ben derived from other sources I confirm it has been indicated in the thesis.

Abstract

Heterogeneous catalysis is a large and important field of research, and is especially of interest to the project sponsors Johnson Matthey (JM). This EngD project focused on studying catalytic materials of interest to JM in order to investigate the metal support interaction and determine the effects of various reaction conditions. The key techniques used in this work are synchrotron radiation based, such as X-ray absorption spectroscopy (XAS), X-ray diffraction (XRD) as well as combinations of techniques. A variety of catalytic materials have been investigated using synchrotron X-ray techniques and conventional laboratory analytical techniques. Understanding these processes will allow for the tailoring of catalyst design and modification of support materials that will lead to improved and more efficient catalytic materials in the future.

Supported platinum group metals were studied during reduction using in situ XAS. The materials were prepared through sequential deposition on an alumina support of first the platinum group metal then a ceria layer; this additional layer of ceria was deposited to cover the metal particles, limiting movement and gas transfer processes. The effect of the MSI on the reduction of Pd nanoparticles supported on a variety of inorganic materials in order to determine the structure of metal particles was also explored using in situ XAS. A combination of the L_{III}- and K-edge analysis was utilised to provide a better understanding of metal support interaction and the changes in the electronic structure for supported Pd nanoparticles.

Other materials investigated include zinc oxide nanoparticles, which are important for a variety of applications due to their semi-conductor properties. Additionally AuCu bimetallic clusters were investigated in situ during reduction, calcination and during the catalytic oxidation of propene. The use of XAS allowed for the probing of the extent of the metal alloying and the effect on the propene catalysis.

Table of Contents

List of Figures

List of Tables

List of Equations

Acknowledgements

First I would like to thank my supervisor Professor Gopinathan Sankar for all his help and support through out my EngD. I would also like to thank my industrial sponsors Johnson Matthey and the staff with whom I've worked, namely my industrial supervisor Dr Tim Hyde, Dr Peter Ellis, Peter Ash Paul, Collier and all the other staff members with whom I have had the privilege to meet. I would like to thank the staff at B18, Prof Andy Dent, Dr Giannantonio Cibin, Dr Silvia Ramos, Dr Steven Parry and the staff at DUBBLE, in particular Dr Wim Bras, Dr Alessandro Longo, Dr Dipanjan Banerjee for all their help and support with my research.

I would like to thank the staff at UCL, from the teaching staff , Prof Andrea Sella, Dr Rowley, Dr David Scalon, Prof Ewing, and technical staff Dr Steve Firth, Martin Vickers and Charles Willoughby and everyone else who has provide me with advice and support through out my time at UCL. I would also like to thank the staff at UCL, the staff in the office, Mary Lou Jabore, Ninik, and Jadranka to the stores manager, Mr Tony Field, and the security staff, this work could not have been completed without you and I am truly grateful for all you do for me and the other students at UCL.

I would like to say a big thank you to the wonderful people in my research group, Dr Rozie Sarip, Dr Nazarudin, Dr Chao Shang (Jeff) Yang, Dr Vladimir Martis, Dr Martin Martis, Dr Jon Keating, Dr Andy Smith, Dr Kerry Simmance-Patrick, and Dr Gregory Gregori and the current members of the Sankar research group, Anastasia Mantalidi, Zarrin Ansari, Huw Marchbank, Ian Godfrey and Glen Smales. My friends from the KLB Dr Alistair Smith, Daniel Deacon-Smith, David Mora-Fonz, Hsin-yi Tiffany Chen, Mohammed, Panagiota Pelekanaki and from the CIB Alex Smith, Iman Hassan, Ogaga Uzoh, Meetal Hirani, Carlos Vazquez, Francesco Di Maggio, Marion Brooks-Bartlett, Marianne Monteforte, Mohammed Haque and everyone else who I've had the pleasure to know and work with the past four years. Special mention must go to Husna, without your encouragement and support I would never have finished this project, and to Saeed, thank you so much for all you've done for me, the words simply are not enough to express my gratitude to you.

Thank you all so much for your contributions to my work, through helpful discussions assistance on beam time, on my career, my life and everything else in-between. You have been the difference that has enabled me to complete this work and I am touched and moved by you support.

I would also like to thank and acknowledge my family, my mother and my brother Daniel, for all their support during my EngD. From the little things to the big things you've been there with me, picked me up when I was down, kicked my behind when I was lazy and laughed when I needed to unwind. I would not have done this without your love and support. I would also like to acknowledge my father, for all the support growing up. You are a constant presence in my life and I hope I've made you proud. Too all the people I love and care for who are not around today, I carry you with me in my heart and everything I do I share with you.

And finally I would like to take this moment to thank all the amazing people I have met during my time at UCL, there are so many of you I simply cannot name you all without writing another thesis! I want you to know you have all had such a profound impact on my life. It's not the destination that counts but the journey, and the people who share that journey with you, I want you to know that although your names may not be on this page, you are in my thoughts and in my heart. Thank you for making me the person that I am and for being such amazing people. It is a privilege to call you my friends.

I love you all.

Chapter 1 - Introduction

1.1 Introduction

The body of work in this thesis is focused on studying catalytic materials *in-situ* under a variety of conditions using synchrotron radiation techniques; the main technique utilised was X-ray absorption spectroscopy (XAS). Presented here is an overview of the field of the catalysis, describing the nature and importance of these materials, before focusing on the area of heterogeneous catalysis, which were the main materials studied. The area of heterogeneous catalysis is of great importance to chemical industry and the wider scientific community.[1] Having the catalyst and reactants in different phases allows for more straightforward catalyst recovery and clean up of the product. The functions of these reactions can be studied using a variety of methods such as IR, UV-Vis and X-ray diffraction. However for fine-tuning of synthesis techniques and determination of key structural features such as active sites, the use of *in situ* techniques, in particular synchrotron radiation techniques, is essential.

Early *in situ* work focused on either UV-Vis or Raman spectroscopy techniques in order to obtain time-resolved data. Temperature Programmed Desorption (TPD) and Reduction (TPR) studies have also been used to obtain an understanding of the catalytic efficency.[1, 2] Conventional laboratory techniques such as Raman and x-ray diffraction can be used to provide information about the structure of the final material. However details of the formation of the structure, and the changes that can occur during operational lifetime, are more difficult to explore. This is mainly due to the reaction conditions, such as high temperatures, hydrothermal conditions, or the use of reaction cells which are impermeable to laboratory techniques or otherwise prevent analysis of the interior. The advent of synchrotron radiation techniques provided scientists with the ability to follow reactions *in situ* with good time resolution.[1]

Presented here is an overview of catalysis, some of the key heterogeneous catalytic materials and the use of synchrotron radiation in the characterisation of materials either on their own or in combination with other techniques.

1.2 Catalysis

The dictionary definition of a catalyst is a chemical that causes or accelerates a reaction without being consumed in the reaction.[2] Essentially the catalyst provides an alternative reaction pathway of lower energy than that normally accessible (Figure 1-1). This is made possible as the catalyst increases the stability in favour of a transition state, rather than the reactant, thus lowering the energy barrier for the reaction. This can be done through a variety of ways, such as the catalyst binding to one of the reactants, or all the reactants binding to the catalyst surface and reacting. In both cases the catalyst takes an active part in the reaction before being reformed at the end (Equation 1). This highlights the slight error in the dictionary definition; the catalyst is an active component in the reaction but is reformed at the end. As with any chemical process the reformation is slightly less than 100% meaning that overtime the catalyst will be consumed; this leads to an interesting field of research into catalyst lifetimes. As such the official IUPAC definition of a catalyst is "a substance that increases the rate of a chemical reaction without modifying the overall standard Gibbs energy change in the reaction".[3]

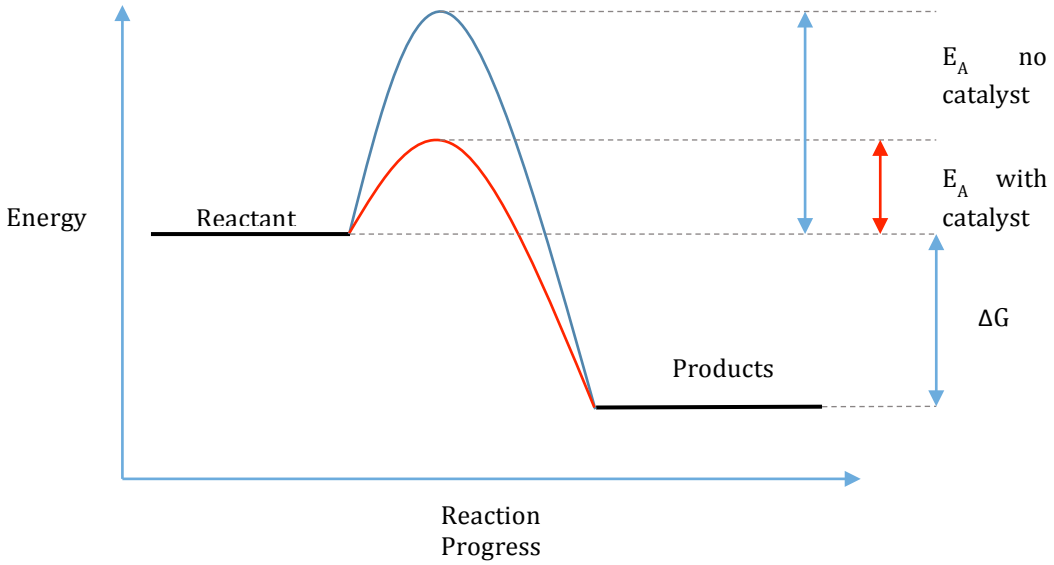

Figure 1-1 - Energy level diagram showing the required activation energy to move from reactants to products in the presence of a catalyst and without a catalyst.

There are several widely known methods for catalyst deactivation; some of the key processes are coking, surface reconstruction and particle aggregation. Each of these deactivation mechanisms are caused by a structural change in the material, limiting access to or otherwise altering the nature of the active site. Hence it is necessary to understand the changes and

transformations that occur to these materials *in situ* under operating conditions and where possible in operando.

The active site is part of a catalytic material responsible for the catalysis; it can be, for example, an exposed metal centre or an acid site. The basic steps for a catalytic reaction are given in Equation 1.

$$X + C \rightarrow XC$$
$$Y + XC \rightarrow XYC$$
$$XYC \rightarrow CZ$$
$$CZ \rightarrow C + Z$$

Equation 1 - Equations showing the consumption and reformation of a catalyst in a reaction process.

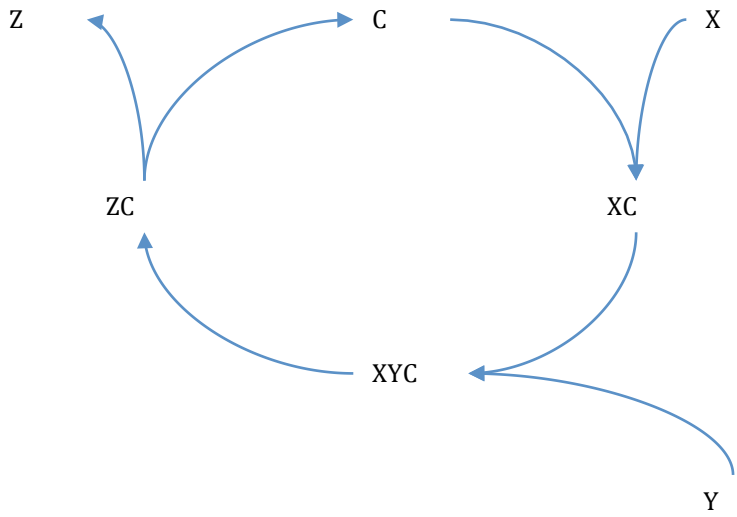

Figure 1-2 - Catalytic cycle for a hypothetical catalyst C showing the consumption and reformation of the catalyst.

The catalytic process can also be expressed in the form of a catalytic cycle (Figure 1-2). This can more easily portray the use and reformation of the catalyst through the reaction process. There are a couple of steps left out of the catalytic cycle for simplicities sake. One omission is the activation step for the catalyst. This can be a relatively simple, or in some cases more complex, procedure depending on the nature of the catalyst. For example it can simply require the reduction a metal nanoparticle to create an active site for catalysis.[4] The other step left out for convenience sake was the regeneration of the catalyst. One of the most common mechanisms for the deactivation of the catalyst is the blocking of the active site. This is

essentially caused by by-products or side products becoming attached to the surface of the catalyst, or binding to the active site thus blocking access to it for further catalysis.[5]

1.3 History

The term catalysis was first coined in the 1830's by Berzilius, who proposed the existence of a new force called the "catalytic force", with catalysis being the decomposition of materials by this force.[6] The first metallic catalysts had in fact already been used in laboratories by some of the famous pioneers of early chemistry such as Joseph Priestly, Marinus Van Marum, and Louis Jacques Thénard, however most of them seemed to regard the metals as merely sources of heat and did not investigate further.[6]

The first clear reported example of a metal being present but undergoing no changes in a chemical reaction is in the famous paper by Humphrey Davy in 1817 on platinum wires exposed to coal gas and air. Davy reported a "new and curious phenomena" whereby the platinum wire became incandescent when introduced into a mixture of coal gas and air.[6] Further work by Davy, in what is one of the earliest recorded patterns of catalytic activity, revealed that only Pt and Pd wires were effective, Cu, Ag, Au and Fe wires being ineffective for the catalysis.[6]

Following on from this important revelation, the application of catalysis for large scale industrial use was appreciated as early as 1831 by Peregrine Phillips, Junior who took out a patent on for the catalytic synthesis of sulphuric acid.[6] Others soon followed suit leading to the vast industrial plants and companies who use catalysis on a daily basis in the modern world today.

1.4 Homogeneous catalysis

Most catalysts fall into two main categories, homogeneous and heterogeneous. Homogenous catalysts are materials that exist in the same phase as the reactants, for example all in the liquid phase. It is a useful process for some fine chemical processing such as drug production, however it has limitations. Homogenous catalysts often find uses in the field of organic reactions for processes such as the Heck reaction.[7,8] One of the drawbacks from utilising a homogenous catalyst is the catalyst recovery, often requiring elaborate separation techniques.[9] Often it easier to make the catalyst inert and leave it in the final product

rather than to attempting to separate it out. Due to the expensive nature of some catalysts this is clearly not the best way to use the materials, although it is necessary in certain cases.

An important review was published in 2003 detailing the difficulties in establishing whether or not a reaction is truly homogenous or if, for example for transition-metal particles in solution, it is heterogeneous but the difference in phases is normally unoticed.[10]

1.5 Heterogeneous Catalysis

Heterogeneous catalysis has the catalyst in a different phase to the reactants, usually a solid catalyst with either liquid or gaseous reactants; this makes it easier to recover and regenerate the catalyst at the end of the reaction. There are other benefits to using heterogeneous catalysts, a key one being the maximisation of surface area. The surface sites of a material, eg ZnO or NiO are the catalytically active sites.[10]

As the materials studied in the thesis work are all heterogeneous catalysts, they will be discussed in more detail. Some of the most important groups of heterogeneous catalysts will be discussed, showing the uses of these materials and their development in the literature.

1.5.1 Zeolite Based Catalysts

Zeolites are crystalline materials formed from corner-linked SiO_4 and AlO_4 tetrahedra, with the separation between Al and Si is governed by Löwenstein's rule; essentially this means that Al-O-Al linkages are forbidden.[13] Ground-breaking work by Barrer and Milton in 1962 led to the creation and use of synthetic Faujasites (zeolites X and Y) for the cracking of petrochemicals.[14] One of the unique features of zeolites is their uniform pore diameters and molecular dimensions, these contribute to their suitability for catalytic applications.[14] The International Zeolite Association (IZA), composed of sixteen experienced crystallographers is responsible for approving new zeolite structures and assigning three letter codes, for example FAU for Faujasite.[14]

The main use for zeolite catalysts has been in the petrochemical industry, though zeolites have also been used as catalysts for organic reactions since the 1960's.[14,15] There have also been increasing investigations in using zeolite catalysts for the production of fine chemicals.[15] In the late 1990's there was a shift in trend for zeolite catalysis with the main emphasis being

on, low temperature, liquid-phase reactions, utilising smaller scale processes for reactants and products containing heteroatoms with a view to increase in the variety of chemical reactions that could be catalysed.[15] A number of chemical species have been successfully encapsulated in zeolite structures, such as metal particles,[16,17] metal oxide clusters (for base and oxidation catalysis)[18,19] and organometallic complexes (for asymmetric catalysis).[20]

Catalysis can proceed from the acid sites, which can be modified by substituting metal ions into framework sites.[15,17,21] This requires the replacement of any tetravalent framework Si^{4+} site with a non-tetravalent ion, e.g. Ga^{3+}, Fe^{3+}, CO^{2+}, Zn^{2+} thus creating lattice charge.[14] The change in charge balance results in a change in strength of the acid site, with the strength of the acid being related to the nature of the substituting element.[15]

One substituting metal of note is titanium, which replaces Si^{4+} with Ti^{4+} ions. Whilst there is no change in charge caused by the substitution the Ti^{4+} centre can be utilised as an active site for oxidation catalysis.[15,16] The key material in this area is TS-1, with an example of it's use as an oxidation catalyst being the ammoxdation of 4-hydroxyacetophenone to the oxime which has a yield of near 100%.[15] The oxime formed is an important component of Tylenol and paracetamol, which can be formed through a Beckman rearrangement. Other substituting elements such as Sn^{4+} and Zn^{4+} have been reported, providing zeolite based catalysts for oxidation and Lewis acid-mediated catalysis reactions.[15] For substituting elements other that Ti^{4+}, there is evidence of leaching suggesting that the ions may not in fact be incorporated into the framework, but residing in extra framework locations.[15]

Another important feature of zeolite catalysis is their ability to control access for solvents and reactants to the active sites through steric hindrance caused by the size of the zeolite pores.[15] Larger molecules and branched systems can be excluded from entering the structure, improving the selectivity for the final product. The main limitation to the use of zeolites is the size of the pores, many fine chemicals and intermediates are too large to enter the structure.[15] By the mid 1980's there were a number of solutions for large pore systems such as phosphate-based molecular sieves, e.g. cacoxenite with a pore diameter of 15 Å. The first extra-large pore material VPI-5 was synthesized and it is aluminophosphate based. Following on from this discovery there were a number of other zeo-type structures reported, such as $GaPO_4$, $FePO_4$ and $AlPO_4$.[15,22] There are also mesoporous materials such as MCM-41, which is an aluminophosphate with a pore size that can vary from 15-100 Å.[23]

There are three main categories of shape selectivity that can be applied to zeolite catayst;[14]

I. **Reactant shape selectivity** – reactants with different molecular dimensions, for example branched hydrocarbons or straight chain hydrocarbons, the bulkier molecules are hindered and the smaller molecules pass through and react preferentially.[24]

II. **Product shape selectivity** – for at least two products with different molecular dimensions, if the diffusion of the larger product is hindered by the pores then the less bulky molecule will be formed preferentially.[25]

III. **Restricted transition state shape selectivity** – in this instance it is the intermediate transition state that is hindered by the pores; with the reactant and product molecules free to move through the structure. Out of two or more possible reaction path ways, the one with the less bulky and hindered transition state will be favoured. This can result in completely suppressing the other reaction pathway.[26]

These are some of the main features for zeolite-based catalysts. They can be used for a variety of different of applications thanks to their structures, solid-acid catalyst nature and their ability to contain other species, such as metal particles, for catalysis.

1.5.2 Metal-Oxide Based Catalysts

One of the most commonly used metal oxide based catalysts is titanium dioxide, TiO_2. Titanium dioxide has found increasing use in environmental photocatalysis, including areas such as self-cleaning surfaces, and photo-induced hydrophilicity which includes self-cleaning and anti-fogging applications.[27] TiO_2 has been widely studied for it's potential as a photocatalyst for the water splitting reaction.[28] In the original investigation, the authors (Akira Fujishima), showed that water could be decomposed using UV-light and platinum and TiO_2 electrodes.[29] the properties of titanium dioxide, such as high chemical stability, low cost and highly oxidising photogenerated holes make it an ideal photocatalyst.[28] One of the main limitations of the materials however is the dependency on UV light. There have been several attempts to achieve photocatalysis with visible light through doping with other metal ions, such as Cr^{3+} and Fe^{3+},[30,31] or rare earth metals,[32] in order to shift the band gap of the material so that absorption bands are accessible in the visible spectral range.

TiO_2 has also shown potential for antibacterial applications under weak UV illumination. . TiO_2 based antibacterial products have been commercialized in Japan, with products such as tiles, fibres and sprays and have been used in hospital operating rooms to maintain sterile

conditions.[28] Commercialisation of titanium dioxide photocatalytic products commenced in the 1990s in Japan, and has grown rapidly.[28]

ZnO has a variety of different applications, including catalysis, this will be discussed in more detail in chapter six.[33] Nickel oxides are well known catalysts for industrial processes such as the reforming of methane,[34] and as hydrogenation catalysts.[12]

Another important metal oxide is vanadium oxide, it is used as an additive in steel and for forming alloys for aerospace applications; here we are interested in it's use as a catalyst.[35] The use of vanadium oxides in catalysis is linked to its chemical properties such as variable oxidation states and geometries.[35] There are also important variations between supported vanadium oxides and unsupported species, as supported species can end up in a variety of forms such as isolated clusters or long chains.[35]

1.5.3 Supported Catalysts

As mentioned previously loading a catalyst on a support can lead to changes in its structure, which can be of major benefit.[35] By utilising a support material there is less expensive catalytic material required, and the number of catalytic active sites can be maximised. Support materials for catalysts are usually chosen for their large surface areas (pore volumes and uniform pore-size distributions), chemical stability and in some cases the interaction between the support and the catalyst.[36–39] This interaction, known as the metal support interaction (MSI), can have some benefits for the material and is widely studied in the literature.[39,40] There are two main distinctions that can be applied to support materials, inert or reactive.

1.5.3.1 Inert Supports

Inert supports are materials that are chemically stable and undergo very few changes over the course of the catalysis. A good example of an inert support material is silica SiO_2, which can be used to support a host of catalytically active species such as metal nanoparticles[41]; although Pt/SiO_2 materials have also been shown to exhibit metal support interactions indicating that the SiO_2 was reduced in the reaction.[42] Another material that can be considered as an unreactive or inert support is alumina, which is also used to support a variety of metal nanoparticles.[38,43] It was found that for supported palladium nanoparticles the sintering mechanisms were dependant as much on the location of the Pd on the surface as the Pd particle size.[38]

1.5.3.2 Reactive Supports

The second class of support materials are reactive supports, also known as reducible supports.[42,44] These are support materials which whilst chemically stable can take an active part in the reaction as well, through having the surface partially reduced.[21] A good example of a group of reactive supports is zeolites and other related porous frameworks. As mentioned previously zeolites can be used to contain metal nanoparticles for catalysis inside the pores, maximising the surface area of the metallic component and taking advantage of the zeolite structure.[21,45]

Transition-metal oxides also make very good catalyst supports, Cu/ZnO_2 catalysts are widely known for there use in methanol synthesis, methanol oxidation, and methanol steam reforming.[46] Titania has also been widely reported for its use a catalyst support, and was one of the first materials for which a metal support interaction (MSI) was reported.[47] The term strong metal-support interactions (SMSI) was coined for group VIII noble metals supported on titania and the vast change in chemisorption properties observed.[47] Titania itself can also be supported for photochemical applications.[48]

Another important reactive support is CeO_2, which is most widely known for its use as a support for three-way catalysts (TWCs).[40,49] Ceria plays an important role in TWCs thanks to it's oxygen storage capacity (OSC), which means it can supply oxygen under fuel rich conditions to convert CO and store it under fuel lean conditions.[49]

The use of a support for catalytically active materials has greatly increased both the potential and complexity of catalyst design. The type of support used and its impact on the catalysis should always be taken into account, in addition to any potential benefits and synergistic effects that can arise from material combinations.

1.6 Catalyst Characterisation

There are several known methods for catalyst deactivation; some of the key methods include coking, surface reconstruction and particle aggregation.[50,51] Each of these processes is caused by a structural change in the material. Hence any technique that can provide information on the structure of a material will be useful for catalyst characterisation. A key technique in this regard would be X-ray diffraction.[52]

X-ray diffraction (XRD) is a long-range structural technique, mainly used for studying crystalline materials, which have an ordered long-range structure. It can also be applied to supported catalysts, through use of peak indexing, to identity the presence of the catalyst on the support in the case where the Bragg peaks do not overlap.[18,43] One of the main advantages of XRD is that it is a non destructive tool for characterisation of inorganic materials.[53] The drawbacks with laboratory XRD is the time-resolution and the tunability of the x-rays. In order to get a decent quality diffraction pattern from a standard laboratory x-ray instrument requires between 10 minutes to 1 hour, with even longer times necessary in order to get a high enough resolution for detailed characterisations such as Rietveld refinements.[52,54] However the tunability of the x-rays is arguably important in order to obtain high angular resolution for structure solutions. this requires high intensity X-rays and a larger range of energy to reduce the instrument effects on peak broadening.

Another commonly employed technique is Infrared (IR) spectroscopy. This technique has applications for catalysis through the ability to detect the molecular vibrations of absorbed species such as reactants and the framework vibrations of the catalysts. IR spectroscopy is also employed in relation to zeolite and mesoporous catalyst frameworks, where the IR spectra can be used to monitor the change in the acid sites of the material through *in-situ* studies.[55] An advantage of using IR techniques *in-situ* is the fast nature of the data collection allows for the use of time-resolved studies to investigate the catalysis and nature of the active sites.[55,56] Another vibrational spectroscopic technique that finds a use for *in situ* characterisation is Raman spectroscopy. Raman spectroscopy takes advantage of the inelastic change in energy caused by exciting a bond, and as such is a much less intense process than infrared.[57] Some catalytic systems that have been investigated with Raman spectroscopy include metal nanoparticles,[58] mesoporous materials such as zeolites, and metal oxides.[59] Raman spectroscopy is a local structural tool, and both Raman and infrared function by measuring the change in energy in molecular bonds as they are excited by radiation. The limiting factor for both infrared and Raman spectroscopy is the bonds must be vibrationally active, for Raman spectroscopy the bond excitations must also be inelastically scattered.

However for the materials, which are vibrationally active, these techniques are powerful tools for characterisation. Probe molecules, and reactions with vibrationally active species, can also be used to reveal information about a catalyst, by binding to the active site thus providing information regarding features of the catalytic active sites such as the quantity and site density.

UV-Vis spectroscopy is another powerful structural characterisation tool utilised for catalysis experiments. The technique has been applied to a diverse array of catalytic systems such as zeolites and gold nanoparticles.[60,61] UV-Vis spectroscopy works based on the principle that chemical systems with non-bonding or π-electrons, which are easily excitable, can absorb UV-Vis radiation. The difference between the incident energy and the energy after passing through the sample is governed by the Beer-Lambert law and can be used to determine information about the absorbing species, based on the wavelength of the energy absorbed. This is another really useful technique for characterising catalytic materials, and can also be used to monitor the change in the reactants for organic catalysis reactions.[62]

Another very powerful technique for characterisation is Transmission Electron Microscopy (TEM). The technique involves the use of an electron beam focused through a series of apertures and lenses onto the sample to produce an image. As the wavelength of the electrons is close in size to the spacing of the atoms, it is possible to get atomic scale resolution of materials. This can be very useful in imaging the surface of catalytic materials and in determining features such as the positions of metal ions on supports[34] or determining particle and pore sizes.[63]

Closely related to TEM is Scanning Electron Microscopy (SEM). This characterisation technique again uses an electron beam, scanned over the surface to interact and produce topographic images of materials with a magnification of up to 1nm on modern instruments. Images can reveal important information on the catalyst such as morphology, particle shapes and sizes, and their distribution throughout the material.[64,65] Samples must be conductive, and as such are usually coated with either carbon black or gold, depending on the sample. SEM is commonly employed to image the surface of porous materials and other bulk catalysts such as zeolites.[66]

This is just a brief overview of some of the techniques utilised in characterising catalytic materials. As can be seen the information provided, and the preparation and sample environments differ greatly so the information desired and the nature of the sample must be carefully considered before selecting which characterisation techniques to use.

1.7 Synchrotron Radiation Techniques

Two of the largest limiting factors for laboratory X-ray techniques are the tunability and the time resolution. It can take so long to collect quality data that truly time-resolved experiments are not feasible. Thankfully there are alternative X-ray sources available in the form of synchrotron radiation facilities.[67] The key advantages of synchrotron radiation are the tunability of the X-rays, along with the flux of the beam and brilliance of the source. synchrotron radiation will be talked about in more detail in chapter two, presented here is an overview of some of the benefits of using these facilities as well as an introduction of the main techniques utilised in this thesis with some literature examples.

1.7.1 X-ray Diffraction

Synchrotron X-ray diffraction combines the long-range structural analysis of traditional XRD with the benefits of synchrotron radiation; this provides a tool to study changes in the long-range structure in-situ with good time resolution and with high quality data.[68] The use of time-resolved experiments allows for changes in the structure under real conditions, such as calcination, reduction, activation and catalysis, providing insights into the material that would otherwise go unobserved.[50,69,70] Additionally thanks to the increased penetrating power of the X-rays, processes such as hydrothermal synthesis which require experimental setups usually unsuitable for X-ray analysis, can also be studied (with suitably designed reaction cells).[70,71]

1.7.2 X-ray Absorption Spectroscopy

One of the main goals of characterising catalytic materials is the determination of the active site and the local structure of the material. This is possible using X-ray absorption spectroscopy, an element specific characterisation technique which can revel information about the local coordination environment around a given element.[67,72] Analysis of XAS data can reveal information about the local geometry, such as bond distances and coordination numbers and also the oxidation states of the elements; this is information that is not available from other experimental techniques.

XAS can utilise the benefits of synchrotron radiation, such as high intensity tunability and collimation, to perform time resolved *in-situ* measurements. These studies can reveal far more information about the structural changes that occur around the active sites, as experiments can be performed under real reaction conditions. Another advantage of XAS is as a local structural tool, there is no need for crystalline materials or materials with long range order.

This means that XAS can be applied to amorphous materials, liquids and in some cases even gases.[73–75]

1.7.3 Combined XAS/XRD

One of the other major benefits of utilising synchrotron radiation facilities is the potential to perform combined experiments. A very useful combination is combined XAS and XRD; whilst X-ray diffraction can provide information on the long-range structure, XAS can be used to describe the local coordination, thus providing an overview of the entire structure of a catalyst. This is of special importance for supported particles, which have low amounts of metal particles on a crystalline or other structured support material.[76,77]

The first reported combined *in-situ* XRD/XAS measurements on a catalytic system was performed in 1991 at the Daresbury Synchrotron facility.[78] Since then combined XRD/XAS experiments have been applied to a variety of catalytic systems under working conditions.[77] Some of the systems that have been investigated include metal oxides, such as Cu/ZnO[78] and TiO_2,[79] iron phosphates and bismuth molybdates,[80,81] and substituted zeo-type materials.[82] The key message from these investigations is not only can combined XAS/XRD measurements provide information on the local and long-range structures but the techniques can be applied *in situ* under a variety of conditions using various reaction cells.[83] This means that real working information can be gathered and related directly to the catalytic systems.

Furthermore other techniques can be combined into the set-up to reveal yet more information on the catalysis and the structural changes occurring in the catalyst. Some examples of other techniques that can be used in conjunction with combined XRD/XAS include, Raman spectroscopy,[84] mass spectrometry[85] and DRIFTS (Diffuse Reflectance Infrared Fourier Transform Spectroscopy).[45] There are other combinations of techniques available focusing on combined XAS with other characterisation methods, all of which can be applied *in-situ* to study catalytic systems. The techniques that can be combined are limited only by the nature of the chemical reaction and the available equipment in the form of reaction cells and instruments, not to mention available space in the experimental hutch.

1.8 Scope of the Thesis

The main aim of this project is to develop methods of collecting and analysing data on catalytic materials investigated *in situ* under a range of conditions. Through these investigations the structural changes of a material under real or operating conditions can be determined providing a lot of information on the local structure around the catalytic active sites, and the structural changes occurring. Understanding these processes will allow for the tailoring of catalyst design and modification of support materials that will lead to improved and more efficient catalytic materials in the future. Whilst this project deals a number of different catalysts, the synthesis of these materials is not the key goal. The main aim is determination of the changes in structure. The development of analytical measurements can then be used to study a range of similar systems.

The systems investigated will be either under activation processes such as calcination and reduction, or during the catalysis. These *in situ* investigations will be combined with other *ex situ* techniques to provide a detailed understanding of the catalytic materials and the structural changes that they undergo.

1.9 References

(1) Beale, A. M.; Jacques, S. D. M.; Weckhuysen, B. M. *Chem. Soc. Rev.* **2010**, *39*, 4656–4672.

(2) Catalyst definition http://dictionary.reference.com/browse/catalyst.

(3) Fechete, I.; Wang, Y.; Védrine, J. C. *Catal. Today* **2012**, *189*, 2–27.

(4) Bracey, C. L.; Ellis, P. R.; Hutchings, G. J. *Chem. Soc. Rev.* **2009**, *38*, 2231–2243.

(5) Beale, A. M.; Gibson, E. K.; O'Brien, M. G.; Jacques, S. D. M.; Cernik, R. J.; Michiel, M. Di; Cobden, P. D.; Pirgon-Galin, Ö.; Water, L. Van De; Watson, M. J.; Weckhuysen, B. M. *J. Catal.* **2014**, *314*, 94–100.

(6) Robertson, B. A. J. B.; Thnard, L. J. *Platin. Met. Rev.* **1975**, *19*, 64–69.

(7) Ronchin, L.; Vavasori, a.; Amadio, E.; Cavinato, G.; Toniolo, L. *J. Mol. Catal. A Chem.* **2009**, *298*, 23–30.

(8) Djakovitch, L.; Wagner, M.; Hartung, C. G.; Beller, M.; Koehler, K. *J. Mol. Catal. A Chem.* **2004**, *219*, 121–130.

(9) Dunnewijk, J.; Bosch, H.; de Haan, a. B. *Sep. Purif. Technol.* **2004**, *40*, 317–320.

(10) Widegren, J. a.; Finke, R. G. *J. Mol. Catal. A Chem.* **2003**, *198*, 317–341.

(11) Xie, Y.; He, Y.; Irwin, P. L.; Jin, T.; Shi, X. *Appl. Environ. Microbiol.* **2011**, *77*, 2325–2331.

(12) K-edge, N. 2–3.

(13) Catlow, C. R. A.; Freemanb, C. M. *Chem. Commun. (Camb).* **1996**, 1311–1312.

(14) Weitkamp, J. *Solid State Ionics* **2000**, *131*, 175–188.

(15) Davis, M. E. *Microporous Mesoporous Mater.* **1998**, *21*, 173–182.

(16) Kitano, M.; Matsuoka, M.; Ueshima, M.; Anpo, M. *Appl. Catal. A Gen.* **2007**, *325*, 1–14.

(17) Ahmed, S. *J. Porous Mater.* **2011**, *19*, 111–117.

(18) Ali, I. O.; El-Molla, S. a.; Ibraheem, I. a.; Salama, T. M. *Microporous Mesoporous Mater.* **2014**, *197*, 48–57.

(19) Ma, Y.; Tong, W.; Zhou, H.; Suib, S. L. *Microporous Mesoporous Mater.* **2000**, *37*, 243–252.

(20) McMorn, P.; Hutchings, G. J. *Chem. Soc. Rev.* **2004**, *33*, 108–122.

(21) Kulkarni, A.; Lobo-Lapidus, R. J.; Gates, B. C. *Chem. Commun. (Camb).* **2010**, *46*, 5997–6015.

(22) Davis, M. E. *Ind. Eng. Chem. Res.* **1991**, *30*, 1675–1683.

(23) Beck, J. S.; Schmitt, K. D.; Higgins, J. B.; Schlenkert, J. L. *J. Am. Chem. Soc.* **1992**, *1*, 10834–10843.

(24) Vandegehuchte, B. D.; Thybaut, J. W.; Marin, G. B. *Am. Chem. Soc. Journals* **2014**, *35*.

(25) Moors, S. L. C.; De Wispelaere, K.; Van der Mynsbrugge, J.; Waroquier, M.; Van Speybroeck, V. *ACS Catal.* **2013**, *3*, 2556–2567.

(26) Sugi, Y. *J. Japan Pet. Inst.* **2010**, *53*, 263–275.

(27) Fujishima, A.; Rao, T. N.; Tryk, D. A. *J. Photochem. Photobiol. C Photochem. Rev.* **2000**, *1*, 1–21.

(28) Fujishima, A.; Zhang, X. *Comptes Rendus Chim.* **2006**, *9*, 750–760.

(29) Fujishima, a; Zhang, X.; Tryk, D. *Surf. Sci. Rep.* **2008**, *63*, 515–582.

(30) Nishikawa, M.; Takanami, R.; Nakagoshi, F.; Suizu, H.; Nagai, H.; Nosaka, Y. *Appl. Catal. B Environ.* **2014**, *160-161*, 722–729.

(31) Li, X.; Guo, Z.; He, T. *Phys. Chem. Chem. Phys.* **2013**, *15*, 20037–20045.

(32) Reszczyńska, J.; Grzyb, T.; Sobczak, J. W.; Lisowski, W.; Gazda, M.; Ohtani, B.; Zaleska, A. *Appl. Catal. B Environ.* **2015**, *163*, 40–49.

(33) Nokkosma, M. I.; Kuoppala, E. T.; Leppa, E. A. *J. Anal. Appl. Pyrolysis* **2000**, *55*, 119–131.

(34) Bradford, M. C. J.; Vannice, M. A. *Appl. Catal. A Gen.* **1996**, *142*, 73–96.

(35) Weckhuysen, B. M.; Keller, D. E. *Catal. Today* **2003**, *78*, 25–46.

(36) Hussain, M.; Fino, D.; Russo, N. *J. Hazard. Mater.* **2012**, *211-212*, 255–265.

(37) Vuurmant, M. A.; Wachs, I. E. *J. Phys. Chem.* **1992**, *96*, 5008–5016.

(38) Chen, J. J.; Ruckenstein, E. *J. Catal.* **1981**, *69*, 254–273.

(39) Van de Loosdrecht, J.; van der Kraan, a. M.; van Dillen, a. J.; Geus, J. W. *J. Catal.* **1997**, *170*, 217–226.

(40) Badri, A.; Binet, C.; Lavalley, J. *J. Chem. Soc. Faraday Trans.* **1996**, *92*, 1603–1608.

(41) Li, W.; Wang, A.; Liu, X.; Zhang, T. *Appl. Catal. A Gen.* **2012**, *433-434*, 146–151.

(42) Bernal, S.; Calvino, J. J.; Cauqui, M. A.; Gatica, J. M.; Cartes, C. L.; Omil, J. A. P.; Pintado, J. M. *Catal. Today* **2003**, *77*, 385–406.

(43) Banerjee, a. M.; Pai, M. R.; Tewari, R.; Raje, N.; Tripathi, a. K.; Bharadwaj, S. R.; Das, D. *Appl. Catal. B Environ.* **2015**, *162*, 327–337.

(44) Arai, M.; Panpranot, J.; Praserthdam, P.; Weerachawanasak, P. *J. Mol. Catal. A Chem.* **2008**, *279*, 133–139.

(45) Kwak, J. H.; Varga, T.; Peden, C. H. F.; Gao, F.; Hanson, J. C.; Szanyi, J. *J. Catal.* **2014**, *314*, 83–93.

(46) Ressler, T.; Kniep, B. L.; Kasatkin, I.; Schlögl, R. *Angew. Chem. Int. Ed. Engl.* **2005**, *44*, 4704–4707.

(47) Tauster, S. J. *Acc. Chem. Res.* **1987**, *20*, 389–394.

(48) Crippa, M.; Callone, E.; D'Arienzo, M.; Müller, K.; Polizzi, S.; Wahba, L.; Morazzoni, F.; Scotti, R. *Appl. Catal. B Environ.* **2011**, *104*, 282–290.

(49) Jen, H.-W.; Graham, G. .; Chun, W.; McCabe, R. .; Cuif, J.-P.; Deutsch, S. .; Touret, O. *Catal. Today* **1999**, *50*, 309–328.

(50) Wragg, D. S.; Grønvold, A.; Voronov, A.; Norby, P.; Fjellvåg, H. *Microporous Mesoporous Mater.* **2013**, *173*, 166–174.

(51) Tanaka, K. *Surf. Sci.* **1996**, *357-358*, 721–728.

(52) Perego, G. *Catal. Today* **1998**, *41*, 251–259.

(53) Sinha, a K.; Sagdeo, A.; Gupta, P.; Upadhyay, A.; Kumar, A.; Singh, M. N.; Gupta, R. K.; Kane, S. R.; Verma, a; Deb, S. K. *J. Phys. Conf. Ser.* **2013**, *425*, 072017.

(54) THOMPSON. *J. Appl. Crystallogr.* **1987**, *20*, 79–83.

(55) Luan, Z.; Fournier, J. a. *Microporous Mesoporous Mater.* **2005**, *79*, 235–240.

(56) Palomares, A. E.; Lercher, J. A. *J. Catal.* **1997**, *449*, 442–449.

(57) Norman B. Colthup, Lawrence H. Daly, S. E. W. *Introduction to Infrared and Raman Spectroscopy*; 1990.

(58) Daniel, M.-C.; Astruc, D. *Chem. Rev.* **2004**, *104*, 293–346.

(59) Catalysis, I. *J. Catal.* **1998**, *13*, 1–13.

(60) Frache, a; Gianotti, E.; Marchese, L. *Catal. Today* **2003**, *77*, 371–384.

(61) Ivanova, S.; Pitchon, V.; Petit, C.; Herschbach, H.; Dorsselaer, a; Leize, E. *Appl. Catal. A Gen.* **2006**, *298*, 203–210.

(62) Tinnemans, S. J.; Mesu, J. G.; Kervinen, K.; Visser, T.; Nijhuis, T. A.; Beale, A. M.; Keller, D. E.; van der Eerden, A. M. J.; Weckhuysen, B. M. *Catal. Today* **2006**, *113*, 3–15.

(63) Jiang, Y.; Ding, X.; Zhao, J.; Zhao, X.; Tian, Y.; Yu, K.; Sheng, Y.; Guo, Y.; Wang, Z. *Mater. Lett.* **2005**, *59*, 2893–2897.

(64) Li, Z.; Gao, L.; Zheng, S. *Mater. Lett.* **2003**, *57*, 4605–4610.

(65) Liu, Y.-M.; Cao, Y.; Yi, N.; Feng, W.-L.; Dai, W.-L.; Yan, S.-R.; He, H.-Y.; Fan, K.-N. *J. Catal.* **2004**, *224*, 417–428.

(66) Narayanan, S.; Sultana, A.; Thinh Le, Q.; Auroux, A. *Appl. Catal. A Gen.* **1998**, *168*, 373–384.

(67) Bunker, G. *Introduction to XAFS A Practical Guide to X-ray Absorption Fine Structure Spectroscopy*; Illinois, 2010.

(68) Wragg, D. S.; Johnsen, R. E.; Balasundaram, M.; Norby, P.; Fjellvåg, H.; Grønvold, A.; Fuglerud, T.; Hafizovic, J.; Vistad, Ø. B.; Akporiaye, D. *J. Catal.* **2009**, *268*, 290–296.

(69) Chang, H.-Y.; Wang, S.-P.; Chang, J.-R.; Sheu, H.-S.; Shyu, S.-G. *Appl. Catal. B Environ.* **2012**, *111-112*, 476–484.

(70) Mi, J.; Clausen, C.; Bremholm, M.; Lock, N.; Jensen, K. M. Ø.; Christensen, M.; Iversen, B. B. **2012**.

(71) Mamakhel, A.; Bøjesen, E. D.; Hald, P.; Iversen, B. B. *Cryst. Growth Des.* **2013**, *13*, 4730–4734.

(72) Bus, E.; Ramaker, D. E.; Bokhoven, J. A. Van; Washington, G.; Uni, V. **2007**, 8094–8102.

(73) Ash, P. W.; Boyd, D. a; Hyde, T. I.; Keating, J. L.; Randlshofer, G.; Rothenbacher, K.; Sankar, G.; Schauer, J. J.; Shafer, M. M.; Toner, B. M. *Environ. Sci. Technol.* **2014**, *48*, 3658–3665.

(74) Sarma, L. S.; Chen, C.-H.; Kumar, S. M. S.; Wang, G.-R.; Yen, S.-C.; Liu, D.-G.; Sheu, H.-S.; Yu, K.-L.; Tang, M.-T.; Lee, J.-F.; Bock, C.; Chen, K.-H.; Hwang, B.-J. *Langmuir* **2007**, *23*, 5802–5809.

(75) Bergmann, U.; Glatzel, P.; Cramer, S. P. *Microchem. J.* **2002**, *71*, 221–230.

(76) Sankar, G.; Thomas, J. M. *Top. Catal.* **1999**, *8*, 1–21.

(77) Sankar, G.; Wright, P. A.; Natarajan, S.; Thomas, J. M.; Greave, G. N.; Dent, A. J.; Dobson, B. R.; Ramsdale, C. A.; Jones, R. H. *J. Phys. Chem.* **1993**, *97*, 9550–9554.

(78) John W. Couves, John Meurig Thomas, David Waller, Richard H. Jones, Andrew J. Dent, G. E. D. & G. N. G. *Nature* **1991**, *354*, 465–468.

(79) Sankar, G.; Thomas, J. M.; Catlow, C. R. A. *Top. Catal.* **2000**, *10*, 255–264.

(80) Beale, A. M.; Sankar, G. *Nucl. Instruments Methods Phys. Res. Sect. B Beam Interact. with Mater. Atoms* **2003**, *199*, 504–508.

(81) Beale, A. M.; Reilly, L. M.; Sankar, G. *Appl. Catal. A Gen.* **2007**, *325*, 290–295.

(82) Sankar, G.; Muncaster, G.; Catlow, C. R. A.; Meurig, J.; Mosselmans, J. F. W.; Harvey, I.; Dent, A. J. *J. Synchrotron Radiat.* **2001**, *8*, 622–624.

(83) Aquilanti, G.; Crichton, W. a.; Pascarelli, S. *High Press. Res.* **2003**, *23*, 301–305.

(84) Grunwaldt, J.-D.; Vegten, N. Van; Baiker, A.; Beek, W. Van. *J. Phys. Conf. Ser.* **2009**, *190*, 012160.

(85) Tsakoumis, N. E.; Dehghan, R.; Johnsen, R. E.; Voronov, A.; van Beek, W.; Walmsley, J. C.; Borg, Ø.; Rytter, E.; Chen, D.; Rønning, M.; Holmen, A. *Catal. Today* **2013**, *205*, 86–93.

Chapter 2 - Methodology

Abstract

Throughout the course of this EngD project a variety of catalytic materials of various compositions and phases will be investigated using synchrotron x-ray techniques and conventional laboratory analytical techniques. The main emphasis of this thesis work is on understanding and characterising these materials both *ex situ* and *in situ* under working conditions. This section provides an overview of the theory behind the techniques that have been utilised throughout the thesis work in addition to explanations of data collection and where applicable how to perform these investigations *in situ.*

Also included is an outline of the synchrotron radiation techniques used during the thesis work, mainly x-ray absorption and x-ray diffraction. Explanations for the data processing using Artemis and Excurve software packages are provided to give the reader a sense of the work behind each analysis in the experimental chapters. Finally an overview and explanation of other characterisation techniques utilised is provided.

2.1 Introduction

The main objective of this EngD project is to characterise catalytic materials using advanced characterisation techniques. Heterogeneous catalysis is a large and important field of research, and is especially of interest to the project sponsors Johnson Matthey.[1,2] This EngD project focuses on studying catalytic materials of interest to JM in order to investigate the metal support interaction and determine the effects of various reaction conditions.

The key techniques used in this work are synchrotron radiation based, such as X-ray absorption spectroscopy (XAS), X-ray diffraction (XRD) as well as combinations of techniques. This chapter begins with an introduction to synchrotron radiation, explaining briefly the history, key components and some of the theory, followed by explanations of XAS and XRD. The methodology behind data collection and analysis will be discussed to give an idea of the benefits of these techniques and the methodology of the data analysis. Other characterisation methods such as TEM and Raman spectroscopy, which can provide additional complimentary information, are also mentioned.

2.2 X-rays

X-ray radiation is referred to in some languages as Röntgen radiation, after the man credited with the discovery, Wilhelm Röntgen. He was a German physicist who was experimenting with cathode ray tubes in 1895. A cathode ray tube is essentially a low-pressure glass tube with two metal plates inside, when a potential difference is applied this can cause radiation to be emitted (Figure 2-1). [3]

Figure 2-1 – Image of a double focus X-ray tube of the type used by Röntgen. [4]

These devices were also known as Crookes tubes after the British scientist Sir William Crookes, his work on radiant matter (cathode rays) inspired many other scientists of the time.[5] Whilst several researchers, such as Nikola Tesla, had noticed that this radiation caused photographic paper to appear cloudy, Röntgen went a stage further when he realised that a plate of barium platino-cyanide crystals six feet away from his tube was glowing. He suspected that a previously undescribed type of radiation caused the effect. He dubbed the radiation X, for unknown; this name stuck leading to the term X-rays still used today. [3]

Subsequently he used the radiation to take one of the first X-ray images of a human being, using his wife as his subject. Upon viewing her own skeletal hand in the image she is quoted as saying "I have seen death". His findings were published in the paper "On a new Kind of Rays" (Uber eine neue Art con Strahlen) on December 28 1895, subsequently scientists all around the world repeated the experiments with their own cathode ray tubes.[3] Röntgen should also be recognized for being one of the few early experimenters with X-rays to make regular use of lead shielding as a precaution; this was before the discovery that over exposure was hazardous to health. His discovery lead to a knew field of medical and scientific research, from medical X-ray imaging that was first used in the Boer war to the pioneering work by the Bragg family, and as such he was awarded the first Nobel prize in physics in 1901. His dedication and passion meant that Röntgen did not keep the prize money but instead donated it to his university, and refused to take out patents on his discoveries so that the world could benefit their practical applications.

One of the substantial advantages of X-rays is the ability to penetrate matter. The extent of the penetration is related to the density and absorption coefficient of the material, which is the reason why bones can be seen in X-ray images but the flesh and muscle is not visible. X-rays are normally split into two classes, soft X-rays, which have an energy of 0-5 keV and hard X-rays with an energy above 5 keV. Whilst soft X-rays can be stopped by air after a short distance hard X-rays can penetrate through most materials, making them ideal for studying a variety of materials and reaction vessels.

2.3 X-ray Sources

Traditional X-ray sources generated electrons through bremsstrahlung or "braking radiation". This effect is caused by the rapid deceleration of electrons striking a target material, with the excess energy being released as X-rays. [6]

The original laboratory machines used for X-ray experiments are X-ray tubes. These instruments consisted of an evacuated tube, with an electron source such as a heated tungsten filament and an anode. The anode is typically made from metals such as copper, molybdenum, silver or tungsten, which have fluorescence energies of 8.0, 17.5, 22.2 and 59.3 KeV respectively.[6] A large potential difference is applied between the electron source (cathode) and the target material (anode). When the electrons strike the target material they have enough kinetic energy to excite electrons out of the core energy levels in the atoms of the target material; when electrons from higher shells fill these holes the fluorescence produces X-rays of a characteristic energy, which is dependant upon the target material.

Whilst this process does produce X-rays it is far from efficient; only a fraction of the energy used is converted to X-rays, the vast majority of the energy is dissipated as heat. This needs to be removed through a cooling system to prevent over heating. Early X-ray tube designs had a fixed anode, whilst later instruments rotated the anode to minimise the localised heating and reduce the cooling requirements (Figure 2-2).[7] These Rotating Anode instruments are more complex and require specialist care to maintain them in good working order.[7]

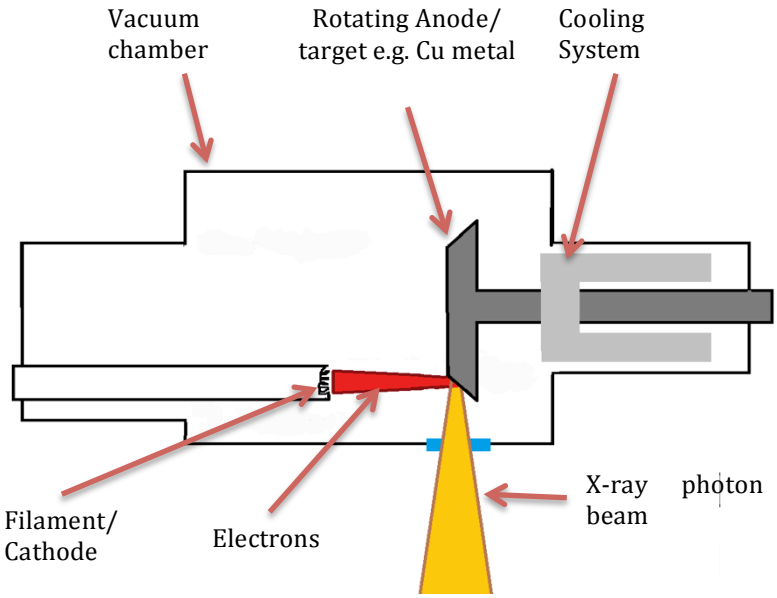

Figure 2-2 - Diagram of a rotating anode X-ray instrument, with key features labelled.

Whilst it is possible to generate X-rays using stand alone instruments there are limitations. The radiation produced has a fixed wavelength and the total flux is relatively low requiring long scan times in order to produce quality data.[6] This makes laboratory-based instruments unsuitable for both X-ray absorption, which requires a tuneable wavelength and *in-situ* measurements, which require time-resolved scans. Fortunately there is an alternative source of X-rays, synchrotron radiation facilities.

2.3.1 Synchrotron X-ray Sources

Synchrotron radiation is the electromagnetic radiation emitted when the velocity of a charged particle ν (such as an electron) approaches the speed of light in a curved path. Each time the particle changes direction it emits a fan of radiation ranging from x-rays to microwaves.[6] It was first reported by Frank Elder, Anatole Gurewitsch, Robert Langmuir, and Herb Pollock in a letter entitled "Radiation from Electrons in a Synchrotron", after they discovered the emission of X-rays from a particle accelerator built by General Electric.[6]

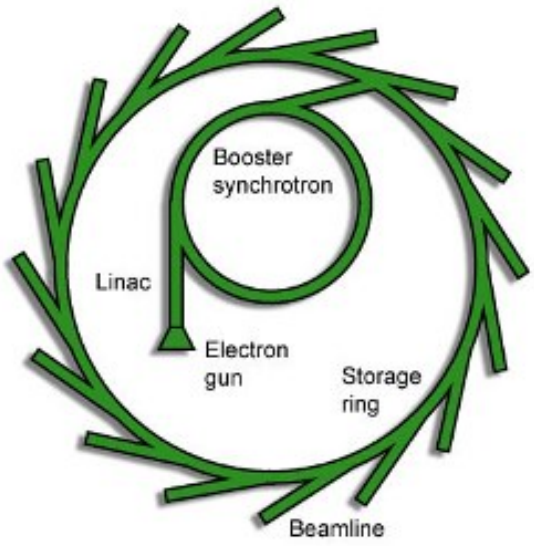

Figure 2-3 - Diagram of diamond light source showing the major components of synchrotron radiation facilities.[8]

Following this discovery the first purpose built synchrotron radiation facilities such as Daresbury light source were constructed to harness this radiation for X-ray experiments, by bending beams of electrons with magnets. Advances in technology leading to the development of insertion devices such as wigglers and undulators improved upon these initial synchrotron facilities, culminating with the development of 3rd generation sources such as the ESRF in Grenoble and Diamond Light Source in Oxford and forth generation X-ray Free Electron Laser (XFEL) sources. These facilities have been used to harness synchrotron radiation for use in a variety of different analytical techniques.[9] Modern synchrotron radiation sources facilities share the same basic components for generating and storing electrons; these are the injection system, booster ring and the storage ring (Figure 2-3).

The injection system is comprised of an electron generator and a linear accelerator, which accelerates the injected electrons as they enter the booster ring. This ring is essentially a small synchrotron with the purpose of boosting the speed of the electrons to relativistic velocity. The booster ring is comprised of an injector magnet, bending magnets and an extraction magnet. It also includes an RF cavity for recovering energy lost as the electrons are bent.[6,10] Electrons travelling in groups, known as bunches, are passed through the cavity where a radio frequency standing wave is maintained. The timing of the bunches is carefully controlled so that the electrons "surf" through the oscillating wave giving the particles a boost in energy along the direction of travel.[6,10,11] Electrons are injected into the booster ring when the magnetic field (B-field) is low and accelerated by increasing the B-field. At the peak of the magnetic field the electrons are extracted by pulsing the magnets and are then transferred to the storage ring.[6]

The storage ring is essentially a larger version of the booster ring, designed to keep the electrons circulating at relativistic velocities for long periods of time; this can be anywhere between a few hours to 2 days.[12] The electron beam is contained in evacuated pipes under ultra high vacuum (approximately 10^{-10} – 10^{-11} mbar) with the orbits contained by powerful magnets.[6] The electrons travel in straight lines until they encounter a strong magnetic field from the bending magnets altering their path. As such the storage ring is not a perfect circle but is instead a polygon, made up of many straight sections with bending magnets along at the corners.[6] Relativistic effects cause the radiation to strongly tilt in the same direction as the electrons instantaneous velocity.[6,12] As the electrons sweep around their path the radiation is emitted in a fan of the order of $1/\gamma$ radians perpendicular to the orbital plane, where;

$$\gamma = \frac{E}{mc^2}$$

Where E is the electron energy and mc^2 is the electrons rest energy (0.511 MeV). Quadrapole and sixtupole magnets are used to focus the beam in the transverse and longitudinal directions along the beam path, helping to maintain the beam.[6] RF cavities are also present in the storage ring to make up for energy lost due to synchrotron radiation emission.

The other major components are the bending magnets used to alter the path of the electron beam and insertion devices, such as undulators and wigglers designed to emit synchrotron radiation. [13]

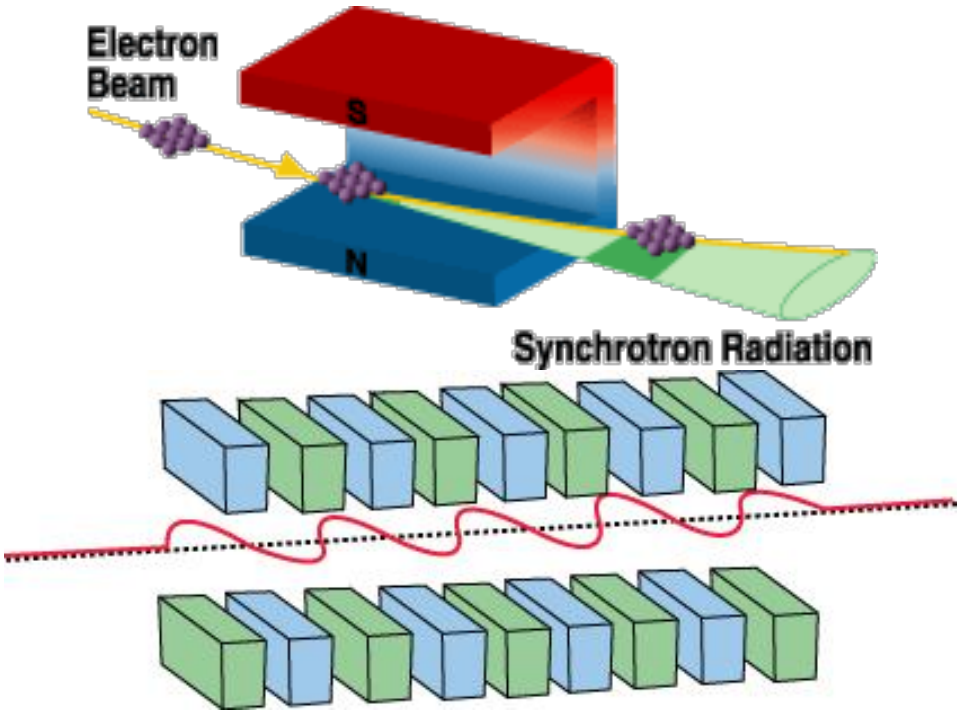

Figure 2-4 - Diagrams depicting; top bending magnets[14] and; bottom insertion devices for generating synchrotron radiation.[15]

Bending magnets generate a broad fan of synchrotron radiation, typically producing hard x-rays, which can be utilised by a variety of different experimental set-ups (Figure 2-4).[6,16] Wigglers and undulators are made up of arrays of magnetic pairs of alternating orientation which subject the electrons passing through to a magnetic field of alternating polarity which produces an almost sinusoidal variation of the B-field Equation 2-1; where, B_0 is the initial magnetic field $\boldsymbol{\lambda_u}$ is the undulating wavelength. This results in the electron beam being wiggled or undulated as it passes through the magnetic field (Figure 2-4). [6]

$$B(s) = -B_0 \sin\frac{2\pi s}{\lambda_u}$$

Equation 2-1

The configuration of magnets in wigglers and undulators is very similar but the devices are operated under different conditions. This difference is essentially due to the extent of the angular deflection produced by the magnetic field in comparison with the intrinsic radiation width 1/γ. Wigglers produce a larger deflection and as a result the radiation produced on each oscillation does create interference patterns. Undulators are made up of an array of small magnets that oscillate (or undulate) the electron beam by more than $\sim\frac{1}{\lambda}$ and create a smaller deflection than wigglers. The arrangement of the magnets generates well-confined forward-directed cones of radiation, which can overlap leading to interference effects, which can as a

result generate a more intense beam than bending magnets. The major advantage of wigglers and undulators is that they can be optimised to produce radiation tailored to experimental needs.[6]

2.3.1.1 Benefits of Synchrotron Radiation

There are a number of benefits to utilising synchrotron radiation over laboratory X-ray sources. One of the major advantages of synchrotron radiation is the intensity of the X-rays generated. This allows for experiments to be conducted on relatively dilute samples. Also due to the high flux, detailed data sets can be collected in a very short amount of time, allowing for fast data collection and time-resolved *in situ* experiments. Another advantage is the vast spectrum of energy available from hard X-rays to microwaves and in some cases infra-red radiation.[17] Additionally the energy is tuneable to a high degree of accuracy, which is essential for techniques such as X-ray absorption spectroscopy.[18]

Another key advantage of synchrotron radiation is the brilliance of the source which is defined as the number of photons per second per source area (photons/seconds/source area mm^2).[6] This is related to Liouville's theorem from classical mechanics where by any optical source can reduce its spatial size at the cost of increasing angular divergence or vice versa unless photons are discarded.[6] Synchrotron radiation sources are several orders of magnitude more brilliant than laboratory X-ray sources and allow for the beam to be tuned to almost any required setting, provided the optics are available.[6] As such synchrotrons have point like highly collimated photon beams with a small source size and a small angular divergence; this makes the tuning of the beam via optics such as mirrors possible.[6]

However by far the most important benefit of synchrotron radiation is the tunability of the X-ray beam. Thanks to the broad energy range generated by synchrotron sources the X-ray beam can be tailored to almost any desired energy from 10 – 120 keV (hard x-rays) and below 10 keV (soft X-rays), with an accuracy of up to 1eV.[6] This has many applications from being able to obtain high angular momentum in X-ray diffraction, to being able to excite specific absorption edges in XAS.

2.4 X-ray Absorption Spectroscopy

X-ray absorption spectroscopy (XAS) is a powerful characterisation technique for studying the local structure of a material. One of the main advantages of XAS is that it is not limited to investigating crystalline materials. As the method is dependent upon the absorption capabilities of the material, XAS can be applied to amorphous materials, liquids and in some cases even gases. Additionally due to the benefits of synchrotron radiation, data can be collected *in situ* allowing for investigations into material formation, decomposition, catalyst activation etc.[1]

2.4.1 XAS theory

X-ray absorption spectroscopy is a quantum mechanical phenomenon, which utilises the X-ray photoelectron effect where an atom absorbs an X-ray photon with enough energy to eject a core electron.[6] The photoelectron liberated behaves as a wave and interacts with the electron shells of neighbouring atoms creating an interference pattern between the outgoing photoelectron and the electron shells of neighbouring atoms (Figure 2-11).

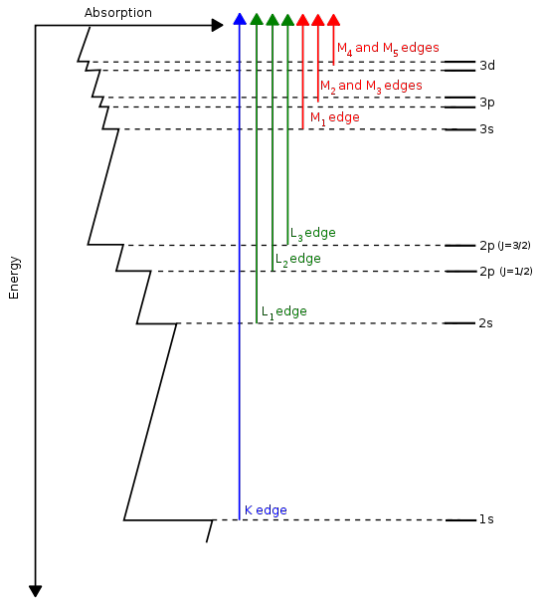

Figure 2-5 - Diagram showing XAS edge transitions and the energy levels responsible for them.[19]

XAS is an atom specific technique, as the energy required to remove an electron from an inner atomic orbital is dependent upon the binding energy between the electron and the nucleus being irradiated. Due to the tunability of synchrotron radiation, the energy of the incident X-rays can be set to trigger excitations from a specific orbital, known as the threshold energy, e.g. 11919 eV for Au L_3 edge (Figure 2-5).[8] This creates the characteristic

absorption edge associated with XAS, and corresponds to the energy required to excite an electron from an inner orbital to a vacant excited state, or to a continuum (Figure 2-6).[19] At the absorption edge the kinetic energy (E_k) of the electron is defined as being equal to the minimum energy required to release an electron E_0 or the zero-point energy. Above the edge the photoelectron kinetic energy is given by Equation 2-2; h is Planck's constant and ν is frequency.

$$E_k = h\nu - E_{edge}$$

Equation 2-2

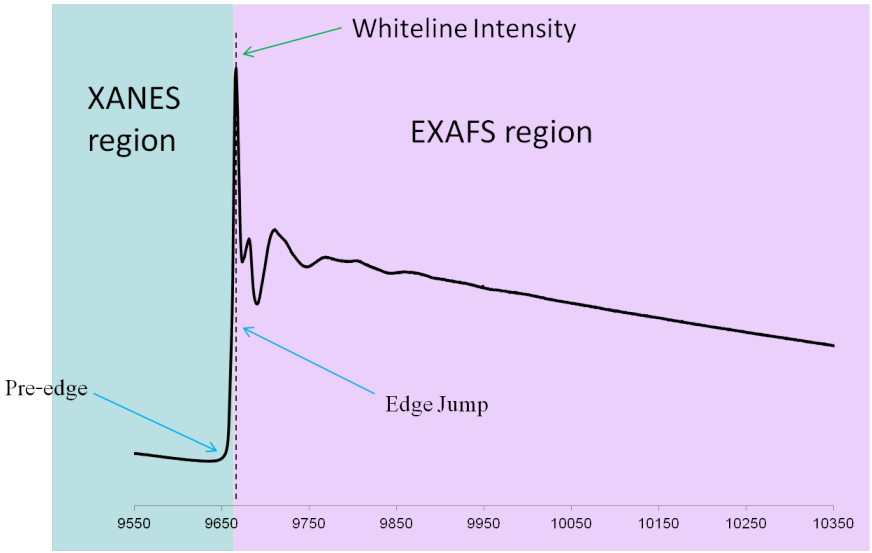

Figure 2-6 - Diagram of a XAS spectra highlighting key features.

The outgoing electron can also be represented quantum mechanically as a spherical wave as defined in Equation 2-3; where k is the wave vector m is the electron mass E_{edge} is the edge energy and E_0 is a correction for the zero energy.

$$\lambda = \frac{2\pi}{k}$$

$$\text{Where; } k = \sqrt{\left(\frac{8\pi^2 m}{h^2}\right)\left(h\nu + E_0 - E_{edge}\right)}$$

Equation 2-3

The principles of XAS can be best explained by considering the transmission of X-rays through a thin sample (Figure 2-7). When radiation, such as X-rays, is passed through a sample part of the radiation is scattered and some of it is absorbed. The result is that the intensity of the radiation after the sample is less than the incident radiation. With

monochromatic X-ray radiation in XAS experiments, part of the photons are absorbed leading to a decrease of the transmitted intensity I_t compared to the initial intensity I_0. This can be related, through Beer Lambert's Law, to state that the absorption of X-rays is dependent upon the properties of the material through which the X-rays are travelling (Equation 2-4); where $\mu(E)$ is the linear absorption coefficient, I_0 and I_t are the initial and transmitted X-ray intensities and x is the sample thickness:

$$I_t = I_0 \, e^{-\mu(E)x}$$

Equation 2-4

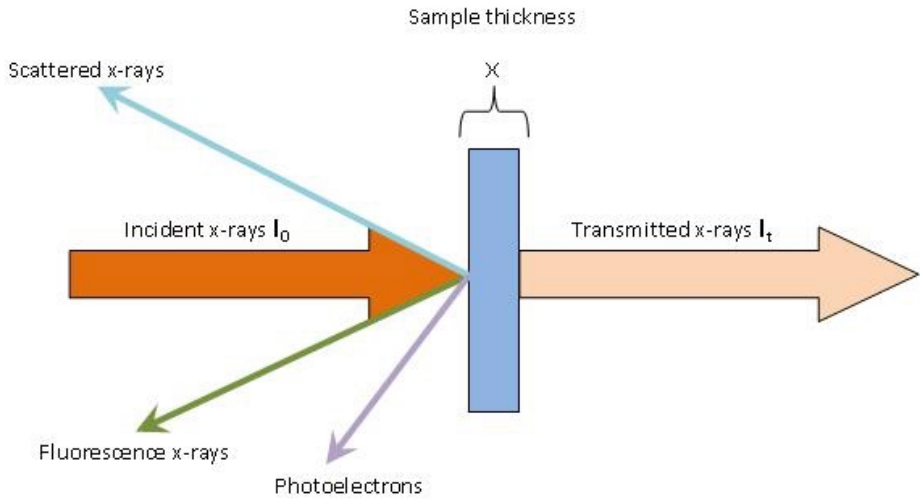

Figure 2-7 - Diagram showing the transmission of an x-ray beam through a sample and the various effects this produces.

When an electron is ejected from a core orbital it leaves a hole in the core shell. A higher level electron can drop into this core hole emitting a photon with energy equal to the difference in binding energy between the shells. The radiation emitted for the K shell is dominated by K_α radiation. These emissions occur at discrete energies that are characteristic of the absorbing atom due to quantum mechanical effects. As such this radiation can be detected and used to characterise the material in a similar way to X-ray transmission.[6]

2.4.2 X-ray Absorption Near Edge Structure (XANES)

The X-ray absorption near edge spectroscopy (XANES) technique focuses on the area of the XAS spectra before and immediately after the edge (Figure 2-6). XANES is a useful tool for studying the oxidation state and local structural geometry[9] of a material as the XANES region is sensitive to the chemistry of the absorbing atom.[10] The pre-edge feature in the XANES region is caused by forbidden electronic transitions, transitions that do not follow the dipole selection rule $\Delta l = \pm 1$, eg a 1s to 3d transition in a k-edge XAS spectra. The intensity of the pre-edge feature is proportional to the transition probability and the density of the unoccupied state. By fitting standards with various coordination geometry the coordination of an unknown system can be determined (Figure 2-8).[9]

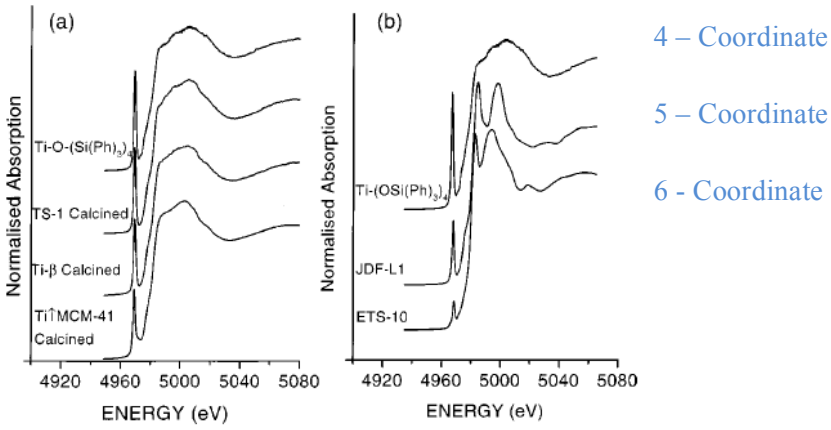

Figure 2-8 - Ti XANES of; left calcined catalyst of varying coordination geometry; right XANES of relevant model compounds representing 4, 5, 6 coordination environments.[9]

Another key feature of the XANES region is the whiteline intensity (Figure 2-6), which gains its name from the original photographic films that were used to capture XAS data; on the films it would appear as a whiteline at the top of the absorption edge. The whiteline intensity is formed by transitions to unoccupied excited states in the material; the more of these excited energy levels that are available the larger the whiteline intensity. This can be used to characterise the coordination of materials, as generally higher coordination numbered structures will have larger whiteline intensity (Figure 2-9).[6,9,11]

The position of the Edge jump also varies depending upon the chemistry of the sample; in general the edge shifts to higher energy with increasing oxidation state (Figure 2-10).[11] One method of data analysis utilises this effect by taking a series of standards with varying oxidation state and plotting the change in edge position against the charge on the absorbing

atom. Following this an unknown material can be analysed with XAS and the edge position compared with the graph to determine the oxidation state.

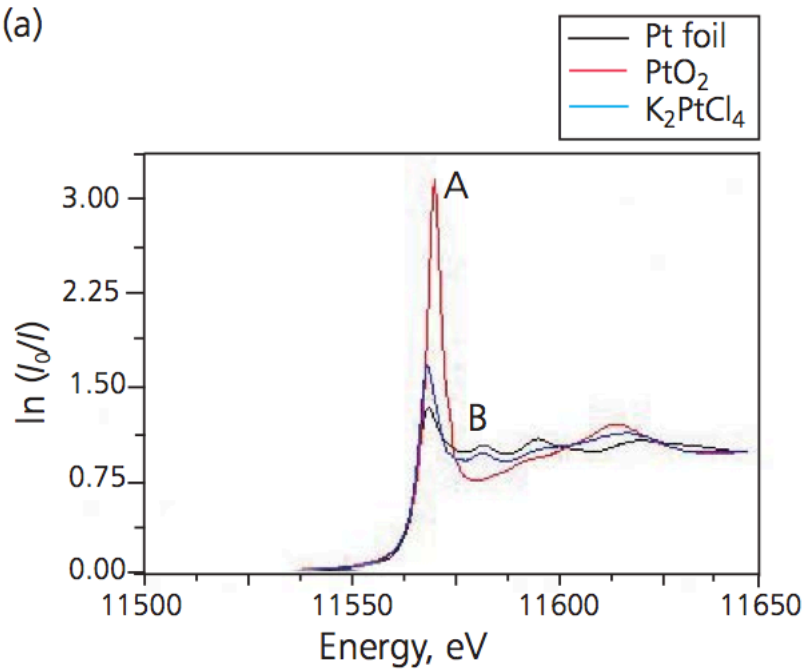

Figure 2-9 - plot of Pt L_{III}-edge XANES for Pt materials with various oxidation states showing the differences in the whiteline intensities of the materials.

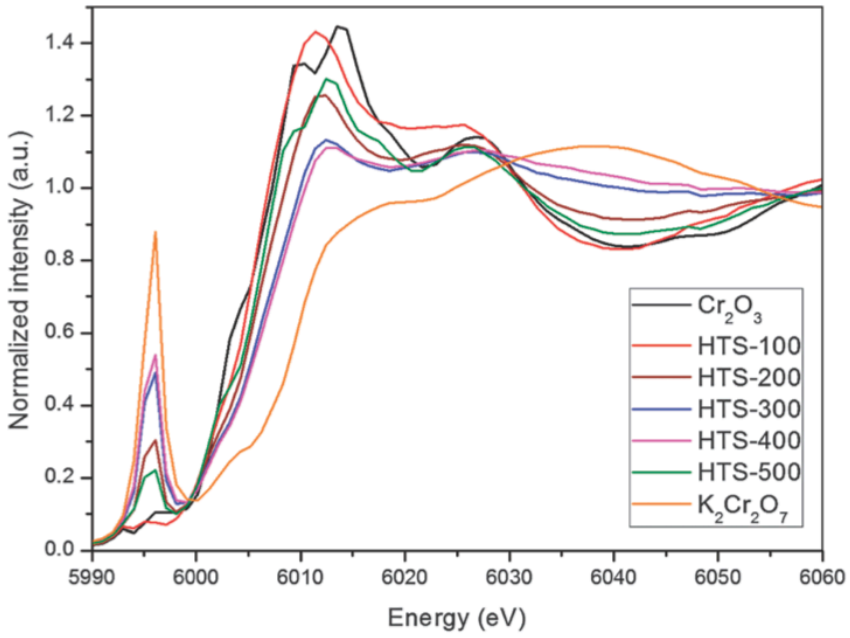

Figure 2-10 - Cr XANES showing the variation in XANES region for different oxidation states of Cr ranging from Cr^{3+} to Cr^{6+}.[20]

2.4.3 Extended X-ray Absorption Fine Structure (EXAFS)

The extended X-ray absorption fine structure (EXAFS) is the name given to the oscillatory structure above the X-ray absorption edge and extending up to about 1000 eV from the absorption edge. The region was first noticed by Kronig in 1932 and was initially considered to be due to the periodic arrangement of atoms.[8] However this theory proved to be unsupportable when similar oscillatory structures were observed for amorphous materials. It wasn't until the ground breaking theory from Stern, Sayers and Lytle that these oscillations were found to arises from interference effects.[13]

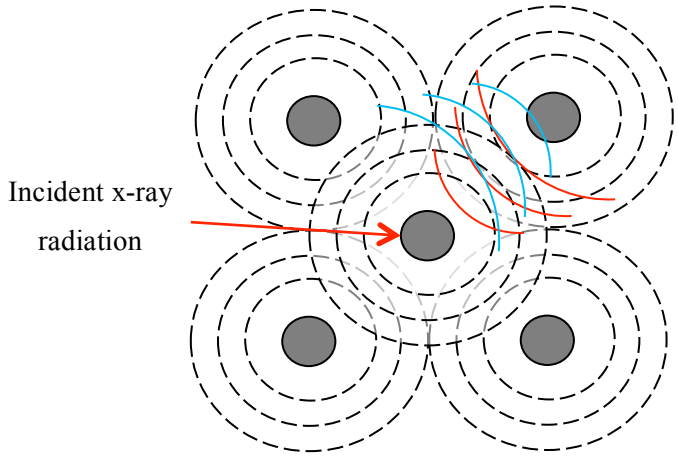

Figure 2-11 - Scattering of ejected electron by surrounding orbitals giving rise to oscillations observed in EXAFS.

When the sample being investigated absorbs X-rays, it may promote an electron to higher energy state, releasing a photon or ejecting an electron – this is similar to the photoelectric effect. If the absorber is a single atom once the electron is released it can be considered as a wave, and the resulting graph would be a straight line after the absorption edge. However as the absorber is surrounded by other atoms, this is not the case. Instead the electron orbitals of the surrounding atoms repel the expelled photoelectric wave, giving rise to constructive and destructive interference (Figure 2-11).[6,13]

A Fourier Transform (FT) of the isolated EXAFS function with respect to the photoelectron number generates a partial radial distribution function for the region surrounding the absorbing species.[13] This can be used to extract information about the nearest neighbour coordination shell of atoms and the structure and the short range order around the X-ray absorber.[14] Hence a common definition of the EXAFS function $\chi(E)$ is extracted from the X-

ray absorption coefficient μ(E) by subtracting the atomic background μ_0(E) and normalising the edge jump (Equation 2-5).

$$\chi(k) = \frac{\Delta\gamma}{\mu_0} = \sum_j \left(\frac{N_j}{kR_j^2}\right) f_j(k) \exp\left(-2\sigma_j^2 k^2\right) \sin\left(2kR_j + \varphi_j(k)\right)$$

Equation 2-5 – the EXAFS equation

Where N_j is the coordination number of the j^{th} shell, R_j is the mean distance between the absorbing atom and the j^{th} shell, σ_j is the Debye-Waller factor for the shell, k is the photoelectron wave vector, $f_j(k)$ is the magnitude of the backscattering amplitude of the j^{th} neighbouring atom and φ_j(k) is the electronic phase shift due to the atomic potentials.[6,13]

Analysis of the EXAFS region can yield detailed information on the local environment about the absorbing atom.[15] This includes bond distances and coordination numbers of the atoms surrounding the absorber. This information can be obtained with good accuracy and compared with chemical standards or computational results.[21]

2.4.4 Data Collection

XAS data is usually collected in one of two main experimental set-ups, transmission or fluorescence mode. On some beamlines it is possible to collect data in both transmission and fluorescence mode simultaneously. This can be advantageous, but is not available at all facilities; as such the techniques are all presented seperately here. Which set-up is used is dependant upon the concentration and nature of the material being studied.[6] Presented here is a summary of the XAS techniques and the experimental set-ups.

2.4.4.1 Transmission XAFS Experiments

Transmission mode is the most prevalent method for collecting XAS data. The transmission set up involves two detectors, one before and one after the sample with the change in the intensity being related to the sample (Figure 2-12).

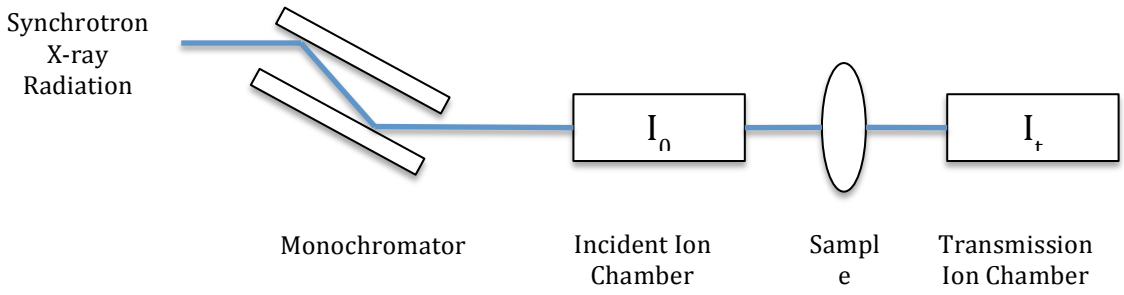

Figure 2-12 - Diagram of typical XAS set-up for transmission.

For succesful transmission measurements there must be a significant change in the edge step, which is essentially the height of the edge jump (Equation 2-6); where μ is the absorption coefficient, t is the sample thickness, I_0 and I_t are the initial intensity and the intensity of the X-ray beam and the intensity after passing through the sample respectively. The edge jump should ideally be a change of between 0.5-1.5 in μ(E).[6] This is to minimise the signal to noise (S/N) ratio ensuring better quality data is collected. The S/N ratio can be improved by ensuring the sample is homogenous as a non-uniform sample can introduce noise into the spectra.

$$\mu t = ln\frac{I_0}{I_t}$$

Equation 2-6

2.4.4.2 Fluorescence XAFS Experiments

In cases where it is not possible to collect transmission data, XAS spectra may also be collected from the fluorescence photons and electrons. The absorption coefficient for fluorescence is different to transmission (Equation 2-7);

$$\mu(E) = \frac{I_f}{I_0}$$

Equation 2-7

In this mode the fluorescence detector is positioned at 90° to the incident beam to minimise scatter and the sample is placed at a 45° angle to the incident beam to ensure maximum amount of fluorescence electrons are detected. Fluorescence signals are much lower than transmission chamber readings, and as a result there is proportionally more noise. However in cases where there is a dilute/low concentration sample or a sample that is too highly absorbing it can be more beneficial to record the XAS data in fluorescence mode, due to it having a better signal to noise ratio than the corresponding transmission data.

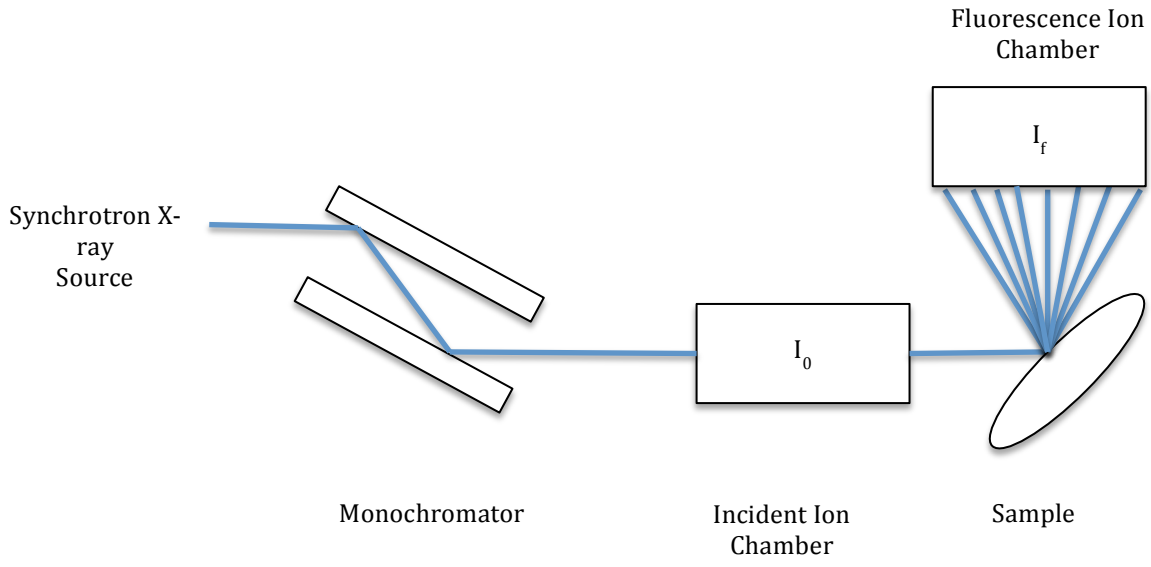

Figure 2-13 – Diagram of a typical XAS set-up for Fluorescence experiments.

2.4.4.3 Dispersive XAFS Experiments

In order to study time-dependant phenomena, short timescales are required. Despite the advances in data acquisition for transition mode EXAFS or QuXAFS, the speed of data collection is limited by the speed of the monochromator and the data acquisition process; as such the fast QuXAFS measurements take place over time-scales of seconds to minutes. However some phenomena occur over much shorter timescales, and as such are undetectable by standard XAS techniques. One technique that can be used to probe such effects is Dispersive XAFS or DXAFS.

DXAFS is usually performed in transition mode using polychromatic radiation. The sample is irradiated by a number of beams, which are then detected using a position sensitive detector. This allows for the collection of a XAS pattern without any mechanical movement from the monochromator, which means that provided the flux is high enough and the data acquisition is fast, the study of time-dependant phenomena is possible.

No DXAFS experiments were performed over the course of the thesis work, however it is important to understand the techniques available and the benefits in order to be certain that the right analytical technique is chosen to answer the experimental question.

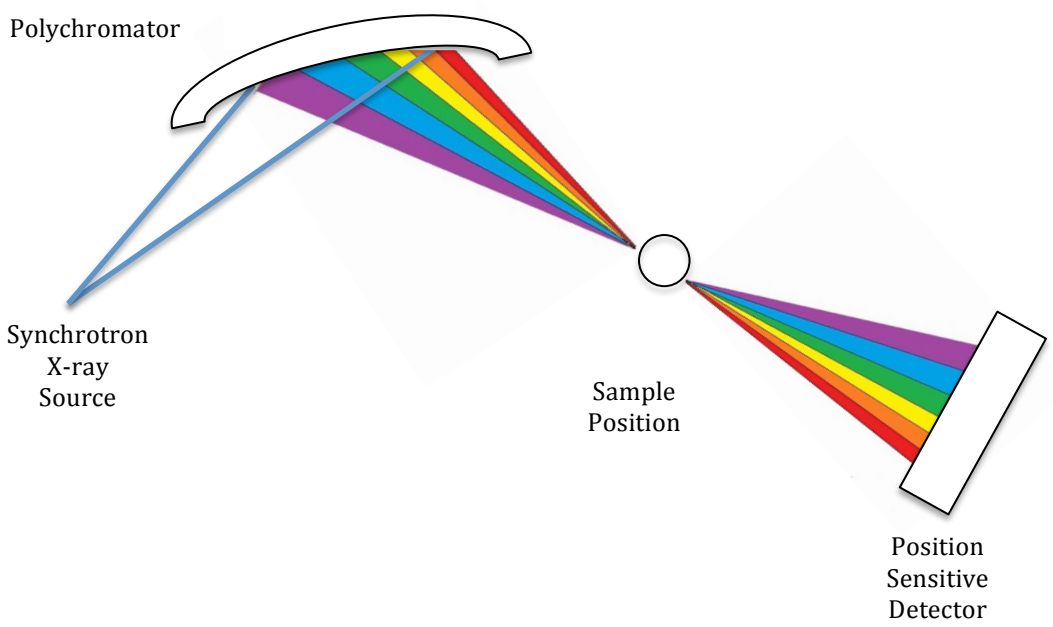

Figure 2-14 - Diagram of Dispersive XAFS experimental setup.

2.4.4.4 Electron Yield XAFS Experiments

Electron Yield (EY) - XAFS measurements can be used to study the surfaces of materials. Again no EY-XAFS measurements were taken during this thesis work; this section is added in order to show the various techniques available. The detection method is similar to fluorescence measurements, in that it indirectly measures the absorption by detecting the decay products as the core-hole is refilled. The electrons detected are mainly the auger electrons ejected from near the surface of the material. The surface sensitive nature of the technique makes this method suitable for studying near surface phenomenon; it can also be useful for avoiding self-absorption effects that can occur when measuring in fluorescence.

The set-up for electron yield measurements is different compared to fluorescence and transmission as the sample is essentially inside the detector (Figure 2-15). For total electron-yield measurements the sample is kept under ultra-high vacuum, and the sample is irradiated by soft X-rays. For higher-energy measurements, known as conversion electron detection, the electrons that are emitted by the sample collide with a gas within the detector such as helium gas. This produces secondary electrons that can be collected as in standard detector ion chambers.

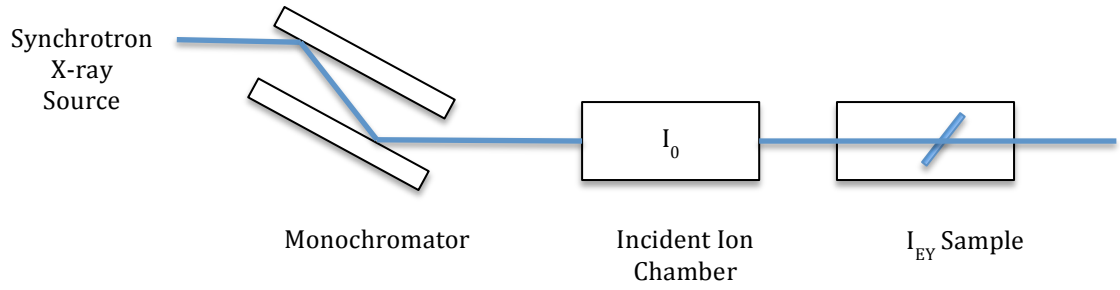

Figure 2-15 - Diagram of a typical XAS set-up for Electron Yield XAS experiments

2.4.4.5 In-situ cells

The work undertaken in this thesis project involves a lot of *in situ* characterisation under a variety of conditions such as heating at high temperatures, under reducing atmosphere, steaming etc. Additionally whilst most experiments will involve solid samples, a variety of different phases may also be considered such as solids, solutions and gels. These cannot be mounted in simple sample holders but require specially designed cells.

A variety of different cells have been designed and used by the Sankar research group over the course of many years and these can all be utilised for a wide number of *in situ* experiments under different conditions (Figure 2-16).

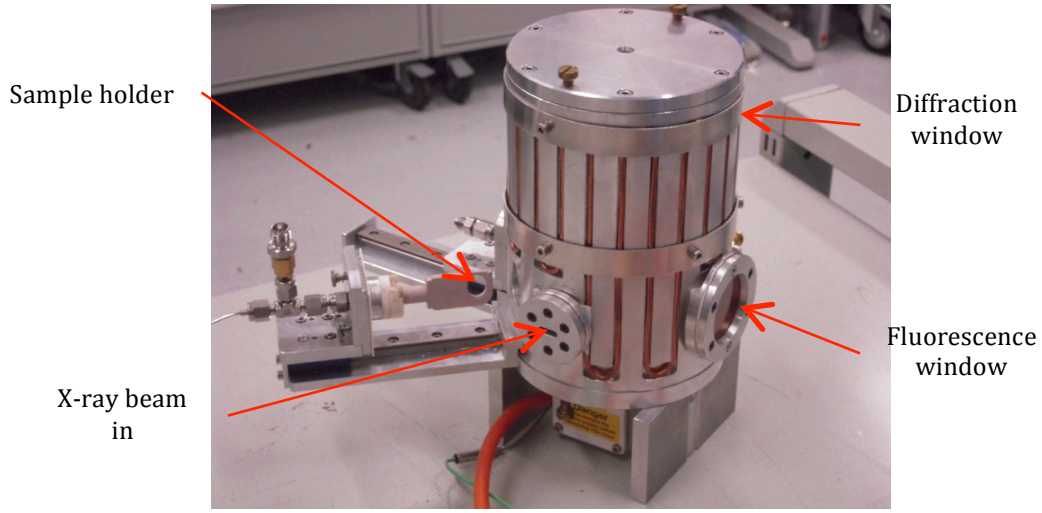

Figure 2-16 - Example of one of the in situ cells designed and used by the Sankar research group. This is a furnace cell designed to mount 13mm pellets and heat them to temperatures of near 1000°C. This cell was used for the experiments in chapter 6.

2.4.5 Data Analysis

The typical procedure for data collection is, to first set up the beamline for the desired absorption edge. This involves tuning the monochromator to the required energy, and filling the ion chambers I_0 and I_t with the correct mixture of gases to ensure sufficient absorption. This is typically around 20% absorption for the first ion chamber (I_0) and between 50-80% absorption for the second ion chamber (I_t). Once the monochromator has been set-up and ion chambers filled it is ideal to run either a standard material or a foil, e.g. for Cu edge running either CuO powder or Cu metal foil.[22] This allows users to determine whether the data is of a reasonable quality and to check the edge position to ensure the monochromator is calibrated properly.

Once standards have been run, everything is ready to start experiments. If in situ measurements are being performed the cell would need to be aligned at this point to ensure that all data taken is of a good quality. Care needs to be taken to ensure that when the cell is mounted on the beamline the beam does indeed pass through the sample and does not clip the cell. This would result in vast abnormalities in the data, in addition to an unnatural loss in intensity of the x-rays.

2.4.5.1 Multiphase and Multi-Cluster Analysis

For data collected on more than one absorption edge, it can be beneficial to fit the data sets simultaneously. This allows for terms and interactions present in both files to be fitted together increasing the integrity of the fitting model. The same principle can also be applied to setting up a multi-cluster model, where by the same edge but two or more different structures are fitted simultaneously.

It is a relatively simple task to achieve in Artemis, in the top window simply select add data set to add another data window to the calculation. This can then be set up as outlined in the previous section with the data from another absorption edge and using a separate .cif file. The real power of using multiple absorption edges becomes visible in the parameterisation step. There will be paths, for example Au-Cu in copper gold bimetallic clusters that are present in both the Au L_{III}-edge and Cu k-edge data. By setting up these paths with the same parameters it provides a link between the results of the two models. This can be used to verify the presence of a species in the system and also to improve the accuracy of the filling model.

Aside from the ability to fit multiple datasets the other most powerful aspect of using Artemis for data analysis is the throughput rate. Once a model has been set up it is possible to simply read in data sets and analyse using the same model. User discretion is required to monitor the quality of the results and the integrity of the fitting model, however this provides a powerful method to process large datasets in a short amount of time. This is one of the main reasons for the significant use of Artemis analysis in the thesis work.

2.4.5.2 EXAFS Analysis: Excurve Software

Excurve is another software package used for analysing EXAFS. The program is able to read any input file as long as the column layout is known. As such it is possible to convert Athena, Viper and potentially other software outputs into a form readable by Excurve. As Excurve is a much older program and does not have the same community support and updates that the Athena and Artemis packages have, however the versatility of the software means that it is updated periodically by experienced users to the benefit of the EXAFS community. In contrast to Artemis, Excurve is an Ab-initio based software package, which has its own advantages and disadvantages.

The program is command driven, and it can generate graphical outputs to assess the quality of the fitting model. When starting an analysis, the first set is to input the types of atoms. Taking Au metal as the example again, the first step would be to input two types of Au atoms, one for

the first and second shells respectively. Following this the potentials between the atoms are calculated, followed by the phase shifts. Also the symmetry of the system can be set as this will aid in generating the theoretical model. The most important feature of Excurve lies here; a model can be created without symmetry using atomic coordinates to manually enter a model. This is a distinct difference to Artemis and it's reliance on crystallographic information or model building, and allows for a much more interactive analysis of amorphous materials.

Once the model has been constructed and the number of shells selected the experimental data can be read in. it is essential to start with a standard such as a foil or material of precisely known composition as this will be used to obtain the AFAC term. This value is constant through out all experiments on the same edge during a beamtime and is analogous to the amplitude (amp) term in Artemis, it typically has a value of between 0.6 and 1. When running fits it Excurve it is possible to set a limit for the number of iterations; this is a maximum value, though the software will ask for permission to continue if a stable answer isn't obtained within the iteration limit. It is possible to save all of the calculations, such as the phase shifts, in addition to the fit data so that simply reloading the files in the future can perform a perfect reconstruction.

Another powerful feature of Excurve is the ability to utilise multiple scattering in the calculations. Whilst Artemis takes into account multiple scattering from the FEFF calculation, Excurve calculates them all separately. Activating the function in the software converts every degenerate path into separate on atom paths and calculates the positions and interactions independently. Whilst this is very beneficial in terms of the integrity of the fit, it does increase the calculation time. Another drawback to this feature is the number of independent parameters required. This usually requires some creative fitting strategies in order to produce good results.

This is a short overview in the Excurve EXAFS analytical software; whilst there are many more features this is sufficient information to communicate the benefit of the software as an alternative to Artemis and also to outline the limitations. Like any technique or data processing method it is not flawless, but by selecting the right software, based on the nature of the material, the best possible interpretations for the experimental data can be obtained.

2.5 X-Ray Diffraction

X-ray diffraction is widely used to characterise materials ex-situ in order to determine the structure and crystallinity.[23] Most laboratories have access to some form of X-ray diffractometer. These operate at fixed wavelength depending on the core used to generate the X-rays. XRD can also be performed at synchrotron radiation sources; this has the added benefit of allowing for higher resolution data and shorter scan times which allows for *in situ* experiments.[24]

2.5.1 X-ray theory

The diffraction of x-rays by crystals was first reported being observed by Von Laue, Fredrich and Knipping in 1912. The following year W.L.Bragg showed that the angular distribution of the scattered X-rays could be understood by interpreting them as waves reflected from planes passing through points in the crystal lattice (Figure 2-17).[25]

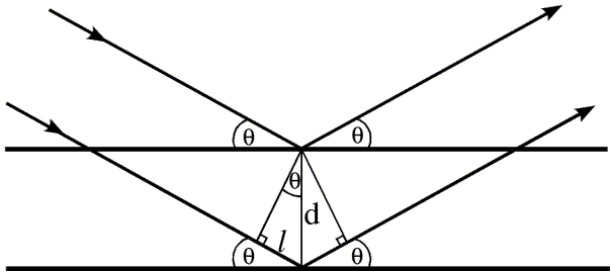

Figure 2-17 - Diagram illustrating the scattering of x-rays as they pass through a crystal lattice.[26]

The equation states that the interaction of X-rays can be explained in terms of their reflection from crystal planes. This means that the wavelength of the scattered X-rays does not change upon scattering allowing the scattered X-rays to interfere with each other in such a way that the intensity distribution is determined by the wavelength, the incident angle of the X-rays and the long-range arrangement of atoms in the structure (Equation 2-8). When operating at fixed wavelength the angles at which the X-rays will be deflected depend solely upon the d-spacing.

$$n\lambda = 2d \sin\theta$$

Equation 2-8 - Bragg's Law

The structure of a material can be determined by indexing the peak positions of a diffraction pattern to that of a known pattern in a database such as the Inorganic Crystal Structure Database (ICSD).[27] Detailed analysis of the diffraction data can yield information on

crystallinity, lattice parameters and particle sizes. This can be done through refinement methods such as Rietveld analysis[28] and software such as fityk[29] and Topas.[30]

2.6 Data collection

X-ray diffraction data can be collected using two different methods, angle dispersive diffraction (ADD) and energy dispersive diffraction (EDD). Whilst both methods are explained here, only ADD was utilised for the thesis work. The EDD description is included merely for additional knowledge.

2.6.1.1 Angle dispersive X-ray diffraction

In angle dispersive mode the wavelength of the X-rays is kept constant (monochromatic) and the detector moved through increments in 2θ (Figure 2-18). The scan time is determined by the size of the steps and the mechanical properties of the detector. This technique is used to obtain data with high resolution for characterisation. Due to the stepwise data collection method it is not as suitable for *in situ* work, but is commonly found in laboratories for its usefulness as a structural characterisation tool.

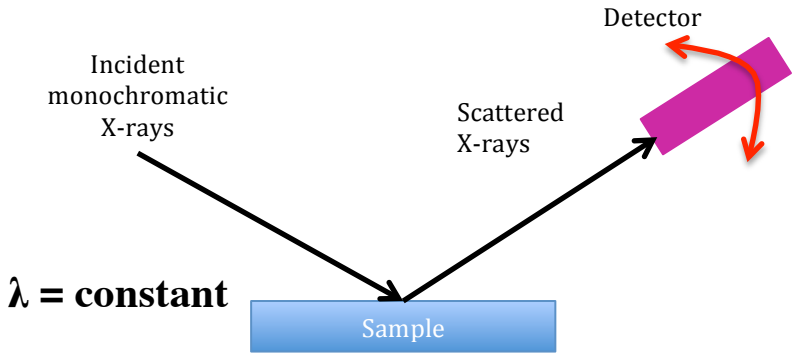

Figure 2-18 - Basic diagram of an angle dispersive X-ray diffraction set-up.

2.6.1.2 Energy dispersive X-ray diffraction

In energy dispersive mode the detector is keep at a fixed angle in 2θ and white (polychromatic) radiation is used with the energy recorded by an energy dispersive diffractometer (Figure 2-19). This technique has some advantages such as much shorter scan times; as a full diffraction pattern can be recorded in one go. Another significant advantage is the larger range in penetration depth of the X-rays allowing for non-destructive measurements

on thicker sample cells, for example monitoring the formation of nanoparticles in a stainless steel reactor vessel. Additionally due to the fixed optics of the beam smaller X-ray windows can be utilised on sample holders/cells. This in conjunction with the hard X-rays used allows for transmission through dense materials such as steel, helping to simplify cell design allowing for a wider range of *in situ* investigations such as surface crystallisation studies and porosity studies for oil wells.[31,32]

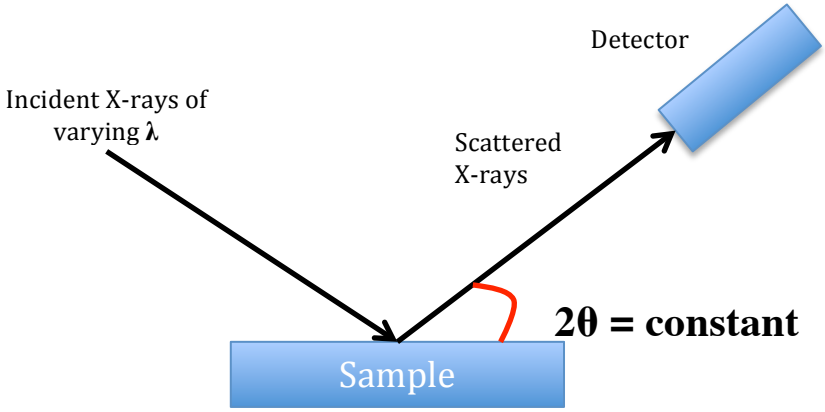

Figure 2-19 - Basic diagram of an energy dispersive diffraction set-up.

The disadvantage is the quality of the data can be lower than that obtained for angle dispersive techniques. However this is offset by the ability for energy dispersive diffraction to be used with extreme conditions and to the ability to follow reactions *in situ* due to the greater time-resolution of the technique.[32,33] Additionally the equipment used for energy dispersive diffraction may also be applied to X-ray spectroscopy allowing for information on both the structure and chemical composition to be recorded simultaneously.[34]

2.7 Raman Spectroscopy

Infrared and Raman spectroscopy are both techniques, which take advantage of the vibrational effects of molecules and bonds. The energy of a molecule is composed of translational, rotational, vibrational and electronic energy.[35] As a first approximation these contributions can be considered separately. Electronic energy transitions usually lead to absorption in the ultraviolet and visible regions of the electromagnetic spectrum whilst rotation and vibrational absorption tend to occur in the microwave and infrared regions.

2.7.1 Vibrational theory

Infra-red spectroscopy is based on the molecular vibrations of bonds in a molecule. By passing infra-red radiation through a sample and determining the fraction of incident radiation absorbed at particular energy allows for determination of the structure and interactions of the sample material.[36] Whenever a molecule interacts with radiation a photon is either absorbed or emitted. The energy of the photon generated or absorbed by this interaction must match the energy gap E_1-E_0, E_2-E_1 as shown in Equation 2-9.[36]

$$\Delta E = hv$$

Equation 2-9 - Equation for change in energy of a photon where h is Planck's constant and v is the wavenumber

This leads to the frequency of absorption or emission for a transition between the initial and first excited states (E_0 and E_1 respectively) is given by Equation 2-10,

$$v = \frac{E_1 - E_0}{h}$$

Equation 2-10

There are a number of vibrational modes associated with the interactions of infrared radiation with molecules. The interaction of radiation with molecules causes a change in the dipole moment of the molecule leading to a number of modes of vibration depending upon the symmetry of the molecule (Table 2-1).[36]

Table 2-1 - Table showing degrees of freedom for polyatomic molecules

Degrees of Freedom	linear	non-linear
Translational	3	3
Rotational	2	3
Vibrational	3N-5	3N-6
Total	3N	3N

The other concept used in order to explain the frequency of vibrational modes involves the stiffness of the bond and the mass of the atoms on either end. By utilising Hooke's law and the reduced mass, μ as a means of simplifying the calculation an equation relating the force constant reduced mass and frequency can be derived (Equation 2-11).

$$v = \frac{1}{2\pi c}\sqrt{\frac{k}{\mu}}$$

Equation 2-11 - Equation relating force constant (k), reduced mass (μ) to the wavenumber value of bond vibrational frequencies (v), where c is the speed of light

By this equation incident radiation can only be absorbed when it is of the same frequency as one of the fundamental vibrational modes (E_1-E_0 transitions) of the molecule. The intensity of this transition will vary depending on the size of the dipole moment of the molecule. The larger the dipole moment the more intense the vibrational mode will appear in the IR spectra. This can be used to determine acid sites in zeolite materials through CO sorption or to distinguish between organic molecules such as alcohols and ketones.

2.7.2 Raman theory

Raman spectroscopy differs from infra-red spectroscopy in that a single frequency of radiation is used and the radiation scattered from the sample, one vibrational unit of energy different from the incident beam which is detected.[35] As such Raman scattering is not dependant on matching the energy of the incident radiation to the energy difference from the ground and excited states in the sample. Instead the incident radiation interacts with the sample distorting the electron cloud around the nuclei to form short lived virtual states which quickly destabilise re-radiating the photon.[32]

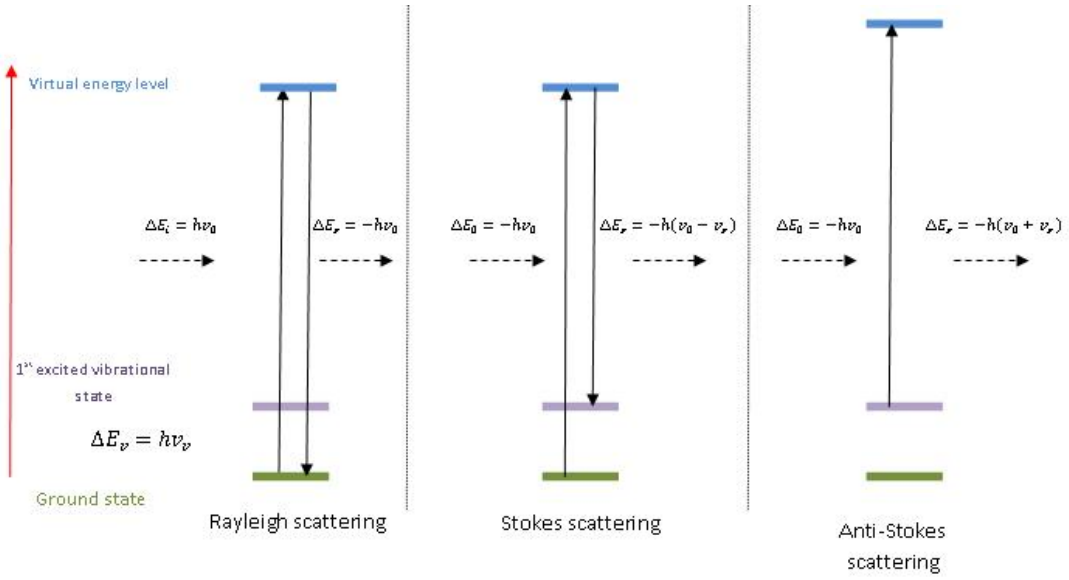

Figure 2-20 - Diagram of stokes and anti-stokes scattering

In vibrational spectroscopy, the energy changes detected are those that cause nuclei motion. If the electron cloud is the only thing involved in scattering then the photons will be scattered with relatively small frequency changes, as the electrons are exceptionally light. This is called elastic scattering, and is also known as Rayleigh scattering after the British physicist Lord Rayleigh, and is the dominant process (Figure 2-20).[35]

If the scattering process induces nuclear motion, energy will be transferred either from incident photon to molecule or from molecule to the scattered photon. This change is inelastic, and is also known as Raman scattering.[37] The energy of the scattered photon is different from the energy of the incident photon by one vibrational unit. In essence the Raman effect is an inelastic collision between the incident photon and the molecule where the result of the collision is a change in the vibrational or rotational energy of the molecule ΔE_m.

$$h\nu_i - h\nu_s = \Delta E_m$$

Equation 2-12 - Equation for change in energy as a result of an inelastic collision

If the molecule gains energy going from ground state to an excited state, then ΔE_m is positive and ν_s is smaller than ν_i giving rise to Stokes lines in the Raman spectrum (Equation 2-12). If the reverse happens and the molecule loses energy, going from an excited state to a ground state then ΔE_m is negative giving rise to anti-Stokes lines in the Raman spectrum (Figure 2-20). Anti-Stokes scattering is an inherently weaker effect as it requires molecules to be in the excited state, and at ambient conditions this is less likely, however as temperature increases the amount of anti-Stokes scattering increases as well.[35,37]

Raman scattering is a relatively weak process as only one photon per every 10^6-10^8 photons is scattered inelastically.[37] This means that care must be taken to minimise other effects such as fluorescence and sample degradation, the latter which can occur when using high power density lasers. Typically Raman instruments have integrated microscopes, which allow for focusing on specific features of a sample.[38] This also has the benefit of ensuring that the focus of the beam is on the desired feature and not elsewhere such as clipping a sample holder. Additionally use of a microscope helps to discriminate against fluorescence from the sample as only a small region is irradiated at high power.[37]

Like infrared spectroscopy materials can be investigated in a variety of different phases through Raman spectroscopy such as solids, liquids and gases provided there are suitable sample holders/cells for them.[39] The majority of the materials produced and analysed during the course of this work will be solids or supported nanoparticles for heterogeneous catalysis.

These require minimal preparation as they can be examined at room temperature under ambient conditions.

2.7.2.1 In-situ studies

Raman spectroscopy can be used to follow a reaction *in situ*. Utilising an *in situ* cell samples can be heated under various different atmospheres to study reactions under different conditions. This provides an opportunity to study local structural changes without the use of XAS, which can be beneficial when preparing for beamtime. By performing preliminary tests using *in situ* Raman spectroscopy, the regions of interest such as structural rearrangement can be highlighted for more in-depth analysis. Additionally this information can then be used to support later findings.

2.8 References

(1) Corma, A.; Garcia, H. *Top. Catal.* **2008**, *48*, 8–31.

(2) Fechete, I.; Wang, Y.; Védrine, J. C. *Catal. Today* **2012**, *189*, 2–27.

(3) C, R. W. *Science* . **1896**, *3*, 227–231.

(4) BIRCHALL, D. OBJECT OF THE MONTH: THE UNKNOWN X http://blog.wellcomecollection.org/tag/wilhelm-rontgen/ (accessed Nov 9, 2014).

(5) Parsons, K. *Am. J. Phys.* **1967**, *35*, 890.

(6) Bunker, G. *Introduction to XAFS A Practical Guide to X-ray Absorption Fine Structure Spectroscopy*; Illinois, 2010.

(7) Taylor, A. *Rev. Sci. Instrum.* **1956**, *27*, 757–759.

(8) Guo, N.; Fingland, B. R.; Williams, W. D.; Kispersky, V. F.; Jelic, J.; Delgass, W. N.; Ribeiro, F. H.; Meyer, R. J.; Miller, J. T. *Phys. Chem. Chem. Phys.* **2010**, *12*, 5678–5693.

(9) Thomas, J. M.; Sankar, G. *Acc. Chem. Res.* **2001**, *34*, 571–581.

(10) Ankudinov, A. L.; Ravel, B.; Rehr, J. J.; Conradson, S. D. **1998**, *58*, 7565–7576.

(11) Sinclair, P. E.; Sankar, G.; Catlow, C. R. A.; Thomas, J. M. **1997**, *5647*, 4232–4237.

(12) Stern, E. A. **1921**, 328–330.

(13) Sayers, D. E.; Stern; Lytle, F. *Phys. Rev. Lett.* **1971**, *2*, 1204.

(14) Rehr, J. J.; Kas, J. J.; Vila, F. D.; Prange, M. P.; Jorissen, K. *Phys. Chem. Chem. Phys.* **2010**, *12*, 5503–5513.

(15) Rehr, J. J. *Rev. Mod. Phys.* **2000**, *72*, 621–654.

(16) Woo, S. I.; Carol, R. J.; Toshima, N.; Harada, M.; Yamazaki, Y.; Asakurat, K. **1992**, *9933*, 9927–9933.

(17) Binsted, N.; Strange, R. W.; Hasnain, S. S. *Biochemistry* **1992**, *31*, 12117–12125.

(18) Ravel, B.; Newville, M. *J. Synchrotron Radiat.* **2005**, *12*, 537–541.

(19) Atenderholt. XASEdges.svg http://en.wikipedia.org/wiki/File:XASEdges.svg (accessed Mar 10, 2013).

(20) Martis, V.; Oldman, R.; Anderson, R.; Fowles, M.; Hyde, T.; Smith, R.; Nikitenko, S.; Bras, W.; Sankar, G. *Phys. Chem. Chem. Phys.* **2013**, *15*, 168–175.

(21) Rehr, J. J.; Mustre de Leon, J.; Zabinsky, S. I.; Albers, R. C. *J. Am. Chem. Soc.* **1991**, *113*, 5135–5140.

(22) Silversmit, G.; Poelman, H.; Balcaen, V.; Heynderickx, P. M.; Olea, M.; Nikitenko, S.; Bras, W.; Smet, P. F.; Poelman, D.; De Gryse, R.; Reniers, M.-F.; Marin, G. B. *J. Phys. Chem. Solids* **2009**, *70*, 1274–1284.

(23) Kei Inumarua, Makoto Misonoa, Toshio Okuhara, B. *Catal. Appl. Chem. Appl. Sci. Enmronmental Earth* **1997**, *149*, 133–149.

(24) Yang, X.; Mcbreen, J.; Yoon, W.; Grey, C. P. *Electrochem. commun.* **2002**, *4*, 649–654.

(25) Bragg, S. L. *Sci. Am.* **1968**, *219*, 58–70.

(26) Read, R. J. Basic diffraction: Waves, interference and reciprocal space. http://www-structmed.cimr.cam.ac.uk/Course/Basic_diffraction/Diffraction.html (accessed Oct 17, 2014).

(27) Inorganic Crystal Structure Database http://cds.dl.ac.uk/cds/datasets/crys/icsd/llicsd.html.

(28) THOMPSON. *J. Appl. Crystallogr.* **1987**, *20*, 79–83.

(29) Wojdyr, M. *J. Appl. Crystallogr.* **2010**, *43*, 1126–1128.

(30) Software, C. TOPAS-Academic V5 http://www.topas-academic.net (accessed Aug 6, 2014).

(31) Middelkoop, V.; Boldrin, P.; Peel, M.; Buslaps, T.; Barnes, P.; Darr, J. a.; Jacques, S. D. M. *Chem. Mater.* **2009**, *21*, 2430–2435.

(32) Fuess, H. *Le J. Phys. IV* **1993**, *03*, C7–C2129 – C7–C2136.

(33) Francis, R. J.; Brien, S. O.; Fogg, A. M.; Halasyamani, P. S.; Hare, D. O.; Loiseau, T.; Fe, G. *J. Am. Chem. Soc.* **1999**, *121*, 1002–1015.

(34) Sankar, G.; Thomas, J. M. *Top. Catal.* **1999**, *8*, 1–21.

(35) Norman B. Colthup, Lawrence H. Daly, S. E. W. *Introduction to Infrared and Raman Spectroscopy*; 1990.

(36) Barbara Stuart, Bill George, P. M. *MODERN INFRARED SPECTROSCOPY*; Wiley India Pvt. Limited, 2008.

(37) Ewen Smith, G. D. *Modern Raman Spectroscopy: A Practical Approach*; John Wiley & Sons, 2013.

(38) Delhaye. *J. Raman Spectrosc.* **1975**, *3*, 33–43.

(39) Vuurmant, M. A.; Wachs, I. E. *J. Phys. Chem.* **1992**, *96*, 5008–5016.

Chapter 3 - Investigation of the Metal Support Interaction of Supported Pd Nanoparticles Through the Use of K- and L_{III}-Edges

Abstract

In this chapter the reduction of supported Palladium catalysts is explored through the use of L_{III}- and K- edge XAS, to reveal important information with regards to the electronic structure and orbital overlap which can be used to improve the understanding of metal nanoparticle bonding to the support. Materials were also studied *in situ* at the Pd k-edge and these measurements combined with L_{III} – edge XANES was used to characterise the changes in the local structure occurring during the reduction. Materials investigated included Pd supported on silica, alumina, ceria and a 0.85% Pd/ 15% ceria/alumina catalyst designed to investigate the SMSI. These catalysts were investigated whilst being reduced and heated to 460 K in a stepwise process. This work would lead to the development of a methodology for studying second row transition metals, and can be applied to a variety of other materials such as Ruthenium and Rhodium catalysts, in addition to expanding the characterisation of bimetallic systems.

3.1 Introduction

Reducing the amount of precious metal used in catalyst formation is a large and important area of research.[1] One well-known and utilised method is the use of an inert/unreactive support for supporting precious metal nanoparticles; this reduces the amount of catalyst required whilst maintaining a high number of active sites.[2,3] The downside to these materials is that they can be deactivated due to processes such as aggregation, surface reconstruction and deposition such as coking blocking the active site. Understanding the how the metal interacts with the support, can help with the design of materials that take advantage of the metal support interaction to improve catalytic properties and lifetime.[4,5]

In situ studies focusing on the reduction of supported Pd nanoparticles in hydrogen (5% H_2/N_2) were conducted in order to determine the structure of metal particles and the effect of different supports for the metal support interaction (MSI). Materials were studied *in situ* using a custom set-up and monitored using XAS on the Pd K- and L_{III} edges. The Pd L_{III} -edge provides information from the binding orbitals which can be used to monitor the formation and removal of the Pd hydride phase in addition to following the reduction.[6] The combination of the two edges allows for a better understanding of metal support interaction for supported Pd nanoparticles, which can hopefully be used to aid in catalyst development.[6,7]

3.2 Metal-support interaction

The metal support interaction was coined in 1978 as a way to describe the dramatic changes in chemisorption properties of group 8-10 noble metals when supported on TiO_2.[8] The chemisorption of hydrogen and CO was observed to be suppressed or removed completely when group 8-10 metals were supported on titania.[4,8] The adsorption of H_2 and CO was previously used to determine the particle size of precious metal particles on support surfaces for catalysis.[8] With the effect too large to describe by sintering, it was concluded that there must be another interaction responsible; the metal support interaction.[8] Initially this was believed to be a negative effect however subsequent studies have found that the effect can have advantages. By choosing materials with synergistic properties between the metal and the support, various improvements to catalyst lifetime and properties can be made.[5]

3.3 Importance of the L_{III}-edge

The utilisation of the Pd L_{III}-edge is a key element in this investigation as the Pd L-edges allow for the direct investigation of the bonding d-orbitals; this is essential for understanding

the electronic structure of transition metal compounds.[6] Due to core-hole lifetime lengthening, there are extra features present in L-edge XANES, such as peaks near the whiteline intensity, which can be directly related to the density of states of the element being investigated.[6,7] Additionally the whiteline intensity (p→d transition) can be used to give an indication of the d-orbital, for example the absence of a whiteline would indicate a filled d-band.[6] Variations in the whiteline intensity of the L_{III}-edge can be related to changes in the d-orbital. For example, a filled d-orbital with coordinating ligands shares some electrons with ligands resulting in hybridisation and this is reflected by a visible change in the whiteline intensity.[7]

The absorption edge from the Pd L_{III}-edge arises from transitions from the $2p_{3/2}$ to the $4d_{3/2}$ and $4d_{5/2}$ orbitals as outlined by the selection rules and spin-orbit coupling (Figure 3-1).[9,10] As this is an electronic transition it is also governed by Laporte's rule, which is a spectroscopic selection rule, that states an electronic transition must involve a change of ±1.[11] This coupled with the spin rule, that allowed transitions must not involve a change in the spin of the electron, governs the electronic transitions of metals, such as Pd and it's compounds.

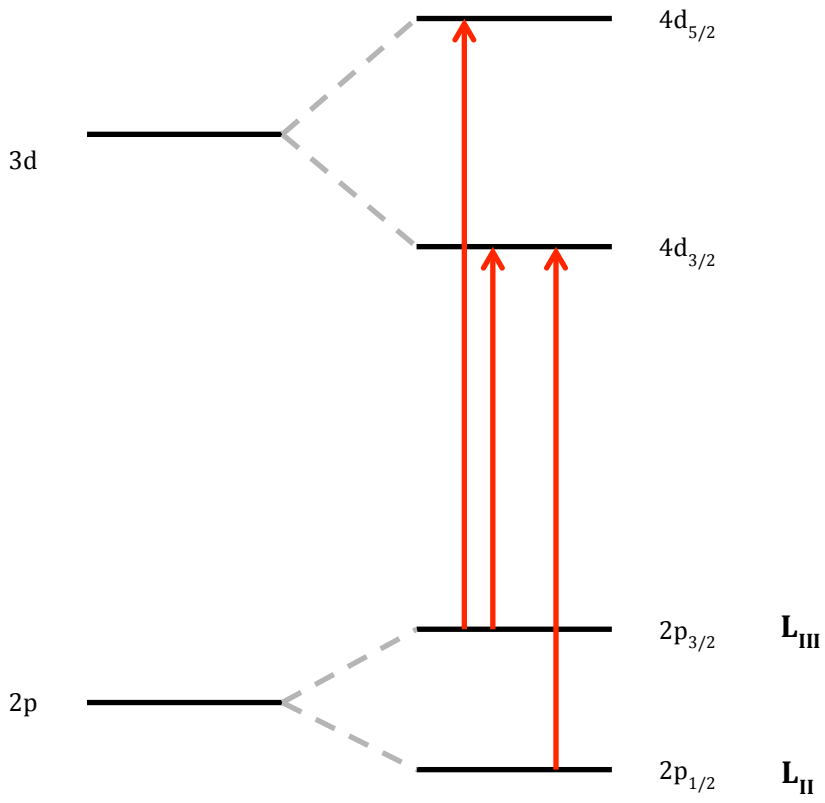

Figure 3-1 - Diagram showing the energy levels for the p and d orbitals and allowed transitions for the L_{III}-edge.

Disallowed transitions are also possible due to orbital mixing of the p and d orbitals which can be caused by ligand interaction, this is explored using ligand field theory.[12] Furthermore the features of the post edge region are sensitive to perturbations in the electronic state of the bonding orbitals, such as those caused by the insertion of H 1s orbitals into the electronic structure during Pd hydride formation.[10] As such the utilisation of the L-edge for catalysts can provide information on how the catalyst is affected by reactants, gas adsorption, and support interaction effects in addition to providing evidence of compound or alloy formation through charge redistribution.[6,7,13] An example of the use of the Pd L_{III}-edge is the investigation of Pd carbide formation, where it was used to probe the changes in the bonding orbitals during reduction of the catalysts.[14] Another advantage of XANES measurements is the weaker temperature dependence compared to EXAFS (Debye-Waller has less effect). This means it is easier to collect and interpret data at reaction temperatures *in situ.*

3.4 Palladium Catalysts

Palladium catalysts are widely used for a variety of reactions and in particular in the auto-exhaust catalysis area where palladium, along with other platinum group metals (PGMs), have been used and studied extensively.[15–17] As Palladium, and other platinum group metals are expensive elements, it is important to maximise the surface area, for catalysis whilst also improving the metal support interaction to increase catalyst reusability.

Supported palladium catalysts are widely used for hydrogenation reactions and palladium along with other PGMs are used as diesel oxidation catalysts.[18] While many characterisation methods are commonly used (examples include XRD, FTIR and electron microscopy), X-ray absorption spectroscopy is advantageous due to the low levels of metal loading and the ability to be employed *in situ* under operating conditions.[19] A variety of different synthesis techniques can also be used to produce the catalysts such as sol-gel,[20] electrochemical reduction,[21] and pulsed laser ablation.[22] Here some of the more common synthesis methods for Pd on different inorganic supports will be outlined, along with the characterisation and analysis of the catalytic materials.

3.4.1 Pd/Alumina

Pd/Alumina catalysts have been used for a variety of different catalysis reactions such as hydrogenation[23], oxidation[24] and enantio-selective catalysis.[25] Many hydrogenation catalysts incorporate palladium on alumina, making the understanding of the local structure important. As such the drying and calcination of supported Pd catalysts was followed using EXAFS, by

Lesange-Rosenberg in 1985.[26] This study looked at two loadings 0.3 and 0.7%, which are close to industrial loadings. The materials were prepared using two different precursors palladium acetylacetonate [$Pd(acac)_2$] and palladium nitrate [$Pd(NO_3)_2$].[26]

EXAFS analysis of the initial [$Pd(NO_3)_2$] solutions reveals that the material exists predominately as palladium oxide though at a lower intensity than the standard.[27] This is comparable to a previous study, which used palladium nitrate precursors, that revealed they form an initial PdO species also shown in electron microscopy.[28] The clusters appear larger for the material prepared from [Pd (acac) $_2$] rather than for the nitrate.

Palladium nanoparticles supported on alumina have been used to catalyse the oxidation of methane.[29] This is an important environmental reaction, which can help to reduce the pollutant emission from fossil fuel combustion.[30] This was explained by the way oxygen could bind to the surface of the catalyst and activate it towards the methane reaction, with the stability of the metal phase in reaction conditions dependent on the support utilised.[29] The supported palladium nanoparticles were shown to have a favourable interaction with γ-alumina, which is partially due to its high surface area.[29] The catalytic oxidation of methane occurs in excess of air, and results in the palladium particles being broken into smaller pieces and coated in a layer of oxide, with the extent of oxidation increases with decreasing crystallite size and increasing lattice dislocations.[29]

The sintering behaviour of Pd crystallites, produced through vacuum evaporation, supported on γ-alumina has been investigated in reducing atmosphere (1 atm of H_2).[28] Electron microscopy revealed that during the initial stages of calcination, the majority of changes in the Pd dispersion are local and limited to small effects such as limited particle migration and coalescence of crystallites.[27,28,31] After 30 minutes there is evidence of large-scale crystallite migration and coalescence. The surface area was shown to drop 66% of the original value during the first 10 minutes and reduced further to 30% after 20 hours. Additionally nearly all large crystallites changed shape from spherical to faceted after 4 hours with further sintering resulting in irregular shaped particles.[28]

On drying the impregnation of palladium is best described by first understanding the structure of the alumina support.[28] The surface was found to be predominately [1 0 0] with a low amount of [1 1 0] also present; this means there are a number of tetrahedral and octahedral vacancies, which can accept palladium atoms. The octahedral vacancies allow for the possibility of six cation-oxygen distances up to 2Å; this was supported by electron microscopy revealing that the steps and kinks of the surface provide space for the higher

palladium oxygen bonding.[1, 11] During the calcination step the coordination number of the Pd-O shell drops to 4 indicating a removal of some of the oxygen species presumed to be the acetylacetonate group. In addition the Pd-Pd coordination number grows to 12.[1] The choice of calcination temperature was found to be critical in obtaining the maximum decomposition of the precursor and minimal sintering of the palladium species. This impregnation model is similar to that for Ni on Co/Al_2O_3 where the metal ion binds by building up links with the oxygen network on the surface. [28]

Pd/Al_2O_3 catalysts can also be produced through co-precipitation, with some of the advantages of this method including a narrower particle size distribution in addition to increased homogeneity of the particles, which in turn leads to increased reactivity.[1] It was found that calcining the material in inert atmosphere leads to the formation of pure nano Pd^0 whilst calcination in air results in the formation of PdO in addition to the Pd metal phase.[1] The support exists in the γ-Al_2O_3 phase as determined by x-ray diffraction.

3.4.2 Pd/Ceria

Ceria supported platinum group metals have a variety of uses in catalysis, the most well-known being as part of the three way catalyst (TWC) in catalytic converters for converting harmful exhaust gases from combustion engines.[32] The metal-support interactions between the palladium particles and the ceria support are not necessarily the same as for other metal oxide supports.[33] Due to the fluorite structure of CeO_2 it is more difficult for the Pd to penetrate into the material.

The effects of the ceria support were investigated by Badri et al, who focused on using Fourier Transform Infrared Spectroscopy (FTIR) on Pd supported on high surface (HS) area and low surface (LS) area ceria.[34] Previous IR spectroscopy work identified the presence of two ν(CO) bands at 1730 and 1630 $cm^{-1,}$ which are characteristic of the metal support interaction. Whilst it could not be confirmed it is believed these bands are caused by the adsorption of CO at the metal-support interface.[35] The two main factors investigated were the ceria surface area and the dispersion of the Pd. It was found that HS ceria had favoured higher Pd dispersion, with the unfortunate side-effect of increased encapsulation of the Pd in the ceria at reducing temperatures higher than 623K, whilst LS ceria had lower dispersion (ca 30%) and no encapsulation was observed.[34] Decoration of palladium on reduced ceria was shown to be reversible for the (111) faces but only partially reversible for the (100) faces and edges upon reoxidation at 873 K.[34] the Pd/Ceria catalysts were prepared via microemulsion technique.[36] The metal ions were reduced with hydrazine hydrate at room temperature

following which the ceria was added with THF. A variety of Pd loadings were employed 0.5, 2.5 and 5 wt. %, however the behaviour of the catalysts appeared independent of the morphology.[37]

Pd/ceria catalysts are also used for the water-gas-shift (WGS) reaction, as their activity can exceed some of the more common low-temperature catalysts such as Cu/ZnO_2; in addition the reactions produce low levels of CO.[38] One of the major limitations of Pd/ceria however is the high rate of deactivation.[39] By performing accelerated aging studies on Pd/ceria it was shown that over reduction of the support was not the cause of catalyst deactivation as previously believed. Instead the deactivation is due to the growth of the metal particles in CO environment. This was discovered by heating fresh catalyst in the presence of an individual reactant or product gas.[39] Catalysts were prepared by the decomposition of $Ce(NO_3)$ in air followed by wet impregnation of $Pd(NH_3)_4$, with the surface area varied by careful control of the calcination temperature.[39]

Pd/ceria materials are also subject to a lot of computational studies, due to the materials importance in TWCs and solid oxide fuel cells (SOFCs).[40,41] One such study investigated the oxygen vacancy at the Pd/CeO_2 (111) interface.[41] the calculations utilised the Vienna Ab Initio Simulation Package (VASP) using a first principles projector-augmented-wave (PAW) method based DFT with a generalised gradient approximation (GGA) and the inclusion of onsite columbic interactions (GGA+U).[41] The calculations showed that there existed a stronger adsorption for the Pd on reduced surfaces compared to *stoichiometric* surfaces. It was also shown that the formation of an oxygen vacancy is easier at the $Pd/CeO_2(111)$ interface than on the clean $CeO_2(111)$ surface. The main result of this is that the adsorption of a Pd atom enhances the oxygen storage capacity (OSC) of the ceria which is in agreement with previously seen experimental results.[40,41]

The growth of Pd particles on ceria during the methanol synthesis reaction was reported by Shen et al.[42] Pd/CeO_2 works in a synergistic way with the palladium producing atomic hydrogen that spills over to the $Pd\text{-}CeO_2$ interface, where adsorbed CO (or other potential methanol intermediates) can be hydrolysed.[42,43] The Pd/CeO_2 catalysts were prepared by deposition precipitation, and characterised using a combination of techniques including EXAFS.[42,43] The catalysts were then reduced at high (HTR) and low temperatures (LTR).[42] The Pd-Pd peak in the Fourier transform is present in both the LTR and HTR catalysts and appears similar to Pd foil. The roughly calculated coordination number is significantly higher for the HTR catalyst at 8.0 compared with 4.0 for the LTR catalyst. However after methanol synthesis SEM imaging reveals that the particle size increases substantially, with the

morphological forms related to the previous reduction temperature.[42] As such The particle growth can be directly correlated to the time-on-stream (TOS) and the methanol yield.[42]The deactivation of the catalyst during methanol synthesis was found to be due to the structural changes in the Pd-CeO_2 interface whilst under reaction conditions.

3.4.3 Pd/Silica

Pd/Silica materials are important in catalysis due to the importance of the silica-meta interface in heterogeneous catalysis.[44] Silica, being irreducible, is generally a more inert support than titania or ceria, and is not widely known for exhibiting the strong metal-support interaction (SMSI).[4,44,45] It is useful however as silica can take a wide variety of different structures with different pore-sizes and internal structures.[46] This is useful in organic synthesis and catalysis as the support can help to promote certain reactions through steric hindrance.[47]

One use for silica supported Pd catalysts is in the liquid phase hydrogenation of phenyl alkyl acetylene mixtures.[48] In one such investigation authors investigated two supports, a commercial silica support (BASF D11-11) and a MCM-41 support.[48] It was found that there was a hydrogen transfer mechanism on the surface which increased the selectivity for alkene formation driven by competing reactions.[48]

Palladium has been known to form palladium silicide under certain conditions such as high temperature and reducing atmosphere.[49] The formation of Pd silicide is considered negative, as the transformation lowers the catalytic activity, decreasing the activation energy and increasing the selectivity towards isomerisation.[17,49] However for certain reactions Pd/silicide materials are more favourable than their Pd/silica equivalents such as the semi hydrogenation of a propargylic alcohol.[49] Palladium silicide can be formed on silica nano-crystals through ion exchange method, with XPS measurements of the material revealing that Pd binding energy shifted toward larger binding energy when in the supported on silicide indicating that the Pd exists in an electron deficient state.[49] This resulted in an increase in styrene selectivity through an inhibition of styrene on the catalyst surface. However use of Pd/silicide catalysts can lead to lower turnover frequencies (TOFs) and reduced catalyst lifetime due to the larger particle sizes and reduced dispersion.[49]

It is also possible to synthesis Pd/silica catalysts with the Pd particles embedded in the mesoporous framework.[6b] This is achieved by introducing the palladium source, in this case H_2PdCl_4 to the silica gel; this gel is the same as the one mentioned previously for the sol-gel

synthesis.[17,49] Alternatively the palladium can be added after the formation of the silica network, however this results in lower Pd content and a decrease in the silica surface area.[20]

The combination of Pd nanoparticles with different solid supports is important for organic synthesis as different combinations can be used to promote specific reactions. However as stated previously the relative inertness of the silica support to Pd nanoparticles can make deposition more difficult. It is possible to functionalise the silica surface to improve the interaction; one such method is to functionalise the surface using amines, creating amine-functionalised supports.[50] It was shown that by varying the amine used and selecting diamine or triamine functionalities different catalysts for the Suzuki coupling reaction can be prepared with high activity. Catalyst lifetime is still relatively low, with deactivation occurring after four runs.[50]

3.4.4 Summary

This is just a brief overview of the literature available on supported Pd catalysts, which hopefully highlights the importance of these materials, and the various uses of the different metal oxide supports. The metal support interaction is a useful and usable effect that can support and stabilise a catalyst in certain reaction conditions. Understanding the MSI can help with the future design of supported Pd catalysts in order to improve lifetime and reusability.

3.5 Palladium Hydride

The interactions of palladium with hydrogen are a key area of research due to the use of Pd catalysts in reactions involving hydrogen, with the formation of Pd hydrides during catalytic reactions also being observed.[51,52] Palladium hydrides are also investigated in the scientific literature due to their ability to easily absorb large amounts of hydrogen through electrolysis or gas loading.[53] As such PdH has the potential to be developed into a hydrogen storage material and for fuel cell applications, with chemical hydrogen storage becoming an increasingly important field of research.[54–56] Palladium has been shown to adsorb large amounts of hydrogen into its structure,[57] and Pd is known to adsorb hydrogen readily at even low temperatures and pressures.[58] Whilst the adsorption and desorption of hydrogen in bulk Pd is completely reversible, it has been shown that some residual hydrogen remains in nanoparticles smaller than 4nm.[56]

In Pd hydride, the hydrogen is typically found to occupy the octahedral sites of the FCC Pd structure (Figure 3-2).[53] This was demonstrated computationally with a first principles electronic structure investigation using three different types of Pd hydride. For the face-

centred cubic Pd it was shown that the insertion of hydrogen led to the formation of bonding and anti-bonding 4d-1s states, which lie above and below the Pd 4d bands respectively.[57]

There are two main hydride phases, α-hydride which has a hydrogen concentration of below 0.3 occupancy and β-hydride which has a concentration of 0.58-1.[53] A high resolution X-ray study on Pd nanoparticles supported on carbon showed that the transition from α- to β-hydride, or vice versa, had no effect on the size or state of the defects in the Pd lattice.[59] As such the Pd lattice is said to "breathe" hydrogen, as it can pass through the structure without causing major alterations. The lattice however does expand uniformly to accommodate the hydrogen into the structure.[56,60] Monte Carlo simulations were used to demonstrate that the transformation from α- to β-hydride is evidenced by a widening of the Pd lattice.[61] It was found that for small Pd nanoparticles (2-4 nm) that the distribution of the hydrogen within the lattice was suniform as only a single FCC phase was observed in the X-ray diffraction (XRD) patterns.[56] Bulk Pd however undergoes a process termed "hydrogen embrittlement" where the uptake of hydrogen leads to a change in the ductile/fragile behaviour of the Pd matrix.[59]

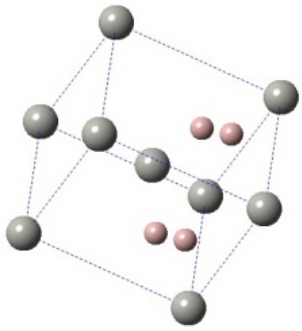

Figure 3-2 - Diagram showing the FCC structure of Pd metal (grey) with interstitial hydrogen (pink) forming Pd hydride.

The formation of Pd hydride in Pd/SiO_2 materials was investigated using transmission electron microscopy (TEM) and selected area electron diffraction (SAED). It was found that the hydride had a relatively high stability of up to 673K.[58] After this temperature the material formed a Pd silicide that was resistant to hydride formation.[58]

There is limited literature published about the Pd hydride investigated using the L_{III}-edge. One early report form 1993 describes the successful determination of a spectral feature 6 eV above the edge ascribed to hydrogen, as proven with experimental and calculated spectra.[10]

By comparison the existence of Pd hydride is inferred from K-edge EXAFS measurements by an expansion of the lattice, attributed to the inclusion of H.[62]

3.6 Aim of the Work

Whilst there is a large amount of literature regarding the Pd K-edge XAS measurements, there has been little work with the L_{III} - edge. Due to the nature of the orbital interactions, the L_{III} - edge is linked directly to the bonding orbitals; investigation of this edge would provide direct information on the nature and changes of the bonding orbitals.[6,7]

In this study we investigate reduction of Pd nanoparticles on a variety of inorganic supports, using both L_{III}-and K-edge XAS. This was done to provide additional information on the bonding orbitals and to help in determining the formation and removal of a potential Pd hydride intermediate. The focus of the work is not on the synthesis of the materials, which will all be prepared via standard methods, but on the differences between the supports with regards to reduction of palladium and hydride formation. The reduction step is chosen as this stage is crucial for catalyst activation, and changes that occur during the reduction stage can have a large impact on the catalytic performance.[4,17,37] The materials investigated are Pd on alumina, ceria and silica providing a mixture of metal oxide supports with both reactive and inert surfaces.

3.7 Experimental

3.7.1 Sample Preparation

Materials were then pressed into pellets using fumed silica to make up to 200mg and loaded into the cell, which was borrowed from Dr Andrew Smith at Daresbury Laboratory. The cell has a sealed chamber containing the pellet holder with heating elements and gas inlets and outlets for flowing gases over the sample (Figure 3-3). The sample holder was then mounted in a sealed vessel, which was pumped full of helium to limit the absorption of X-rays due to air (Figure 3-4). This included extending the beampipe and keeping it under He atmosphere to ensure the data quality was not impinged. A similar set-up was used for both K- and L_{III}-edge measurements, however the extended beampipe was removed for the K-edge studies (Figure 3-4).

Table 3-1 - ICP Pd Assay results for materials utilised during this work. Percentage of supported material given by weight percent.[63]

Sample	Pd (%)
2%Pd/HSA20 CeO_2	2.05
4%Pd/HSA20 CeO_2	3.88
0.5%Pd/SiO_2	0.52

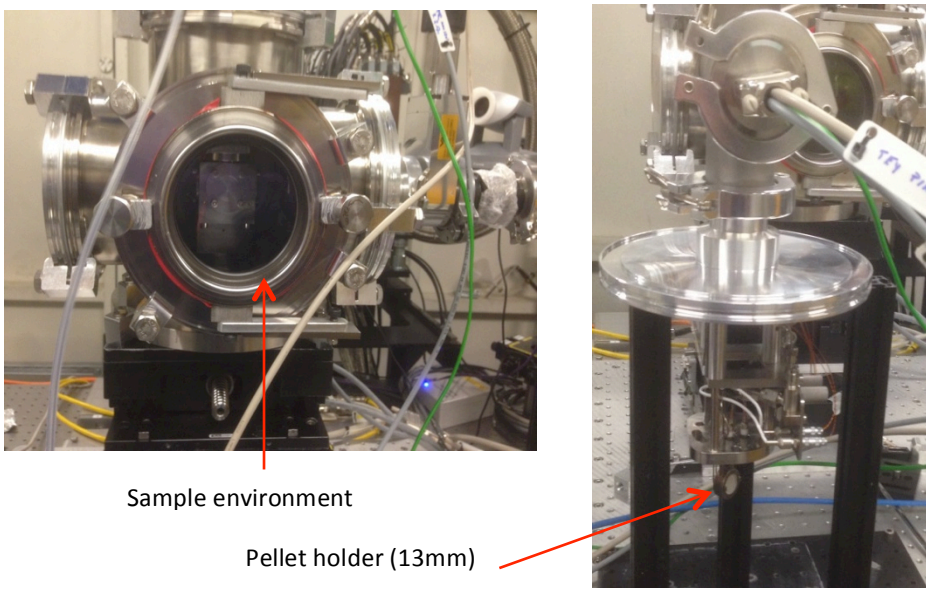

Figure 3-3 - Close up image of the sample holder.

Materials were then pressed into pellets using fumed silica to make up to 200mg and loaded into the cell, which was borrowed from Dr Andrew Smith at Daresbury Laboratory. The cell has a sealed chamber containing the pellet holder with heating elements and gas inlets and outlets for flowing gases over the sample (Figure 3-3). The sample holder was then mounted in a sealed vessel, which was pumped full of helium to limit the absorption of X-rays due to air (Figure 3-4). This included extending the beampipe and keeping it under He atmosphere to ensure the data quality was not impinged. A similar set-up was used for both K- and L_{III}-edge measurements, however the extended beampipe was removed for the K-edge studies (Figure 3-4).

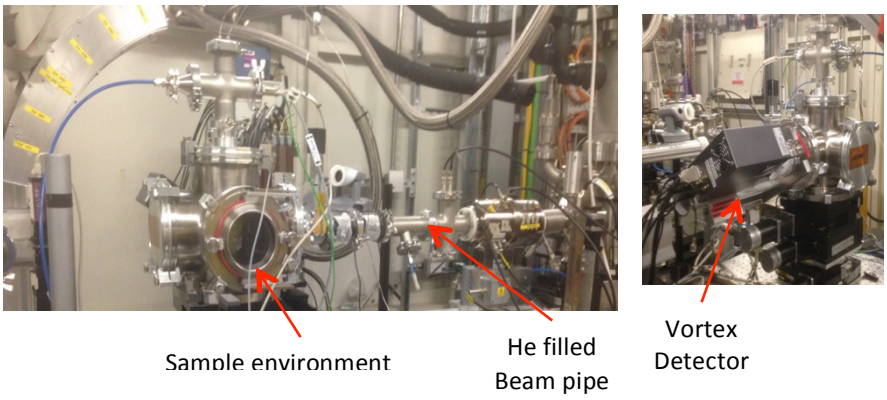

Figure 3-4 - Image of beamline set up for low-energy experiments highlighting key features, such as the extended beam pipe, sample environment and detector position.

3.7.2 *In situ* data collection

Data was collected at beamline B18 at diamond light source, operating with ring energy of 3.0 GeV. The energies were obtained using a Si (111) monochromator calibrated to either the K- or L_{III}-edge energy of a palladium foil. Due to the low energy nature of the Pd L_{III} – edge work, it was not possible to record those datasets in transition mode, instead all L_{III} – edge data was recorded in fluorescence mode. This was done using a 4 element Si Drift detector (vortex detector), which is designed for use at low energy. K-edge measurements were performed in transition mode; with complementary fluorescence data recorded using a 9 element Ge detector more suited for high energy use. The scan parameters were kept the same across the experiments, with a k-range of 0-15 $Å^{-1}$. The samples were measured at room temperature in He, then at room temperature in H_2/He both with a flow rate of 10 cc/min. The sample was heated in a stepwise process to 460 K with step sizes of 20K in H_2/He with a flow rate of 10cc/min. Measurements were also taken once the sample cooled to room temperature, in H_2/He before switching to He for the final set of scans.

3.8 L_{III}-edge XANES Analysis

Materials were then pressed into pellets using fumed silica to make up to 200mg and loaded into the cell, which was borrowed from Dr Andrew Smith at Daresbury Laboratory. The cell has a sealed chamber containing the pellet holder with heating elements and gas inlets and outlets for flowing gases over the sample (Figure 3-3). The sample holder was then mounted in a sealed vessel, which was pumped full of helium to limit the absorption of X-rays due to air (Figure 3-4). This included extending the beampipe and keeping it under He atmosphere to ensure the data quality was not impinged. A similar set-up was used for both K- and L_{III}-edge measurements, however the extended beampipe was removed for the K-edge studies (Figure 3-4).

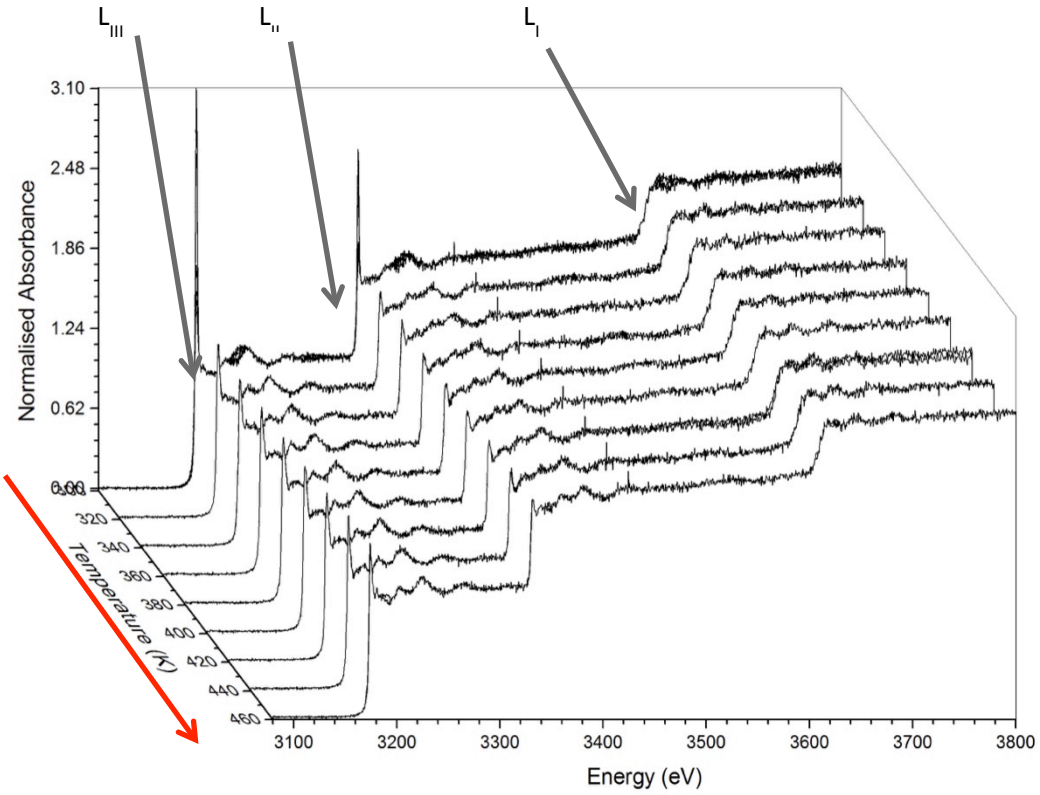

Figure 3-5 - XANES plot for 2% Pd/Silica sample during reduction showing the L_I, L_{II} and L_{III} edges.

The L_I-edge, which is caused by transitions from s – p orbitals, was used as a check to follow the reduction of the materials, as it is comparable to known and previously observed K-edge data.[43]

3.8.1 Pd/Silica Comparison of Mixed and Chemically loaded Samples

The physical mixture of PdO and fumed silica was investigated to allow for the behaviour of unsupported PdO to be determined. This is to provide a suitable comparison to the supported materials and as the interactions between the PdO and the fumed silica will be minimal. The amount of Pd was calculated to match the 2% Pd loading for the supported catalysts. It is expected that there will be a difference in the reduction behaviour of the supported PdO and the physically mixed sample, however as the interactions between Pd and Si are relatively small this difference is not expected to be large.

3.8.1.1 PdO + Fumed Silica Physical Mixture

The first set of data is of pure PdO mixed physically with fumed silica (Figure 3-6). The initial scan at room temperature on the L_{III}-edge in helium atmosphere shows what is expected from previous literature sources for a PdO spectrum. There is a large and sharp whiteline intensity followed by a small shoulder then a broad peak between ca 3185-3246 (Figure 3-7).

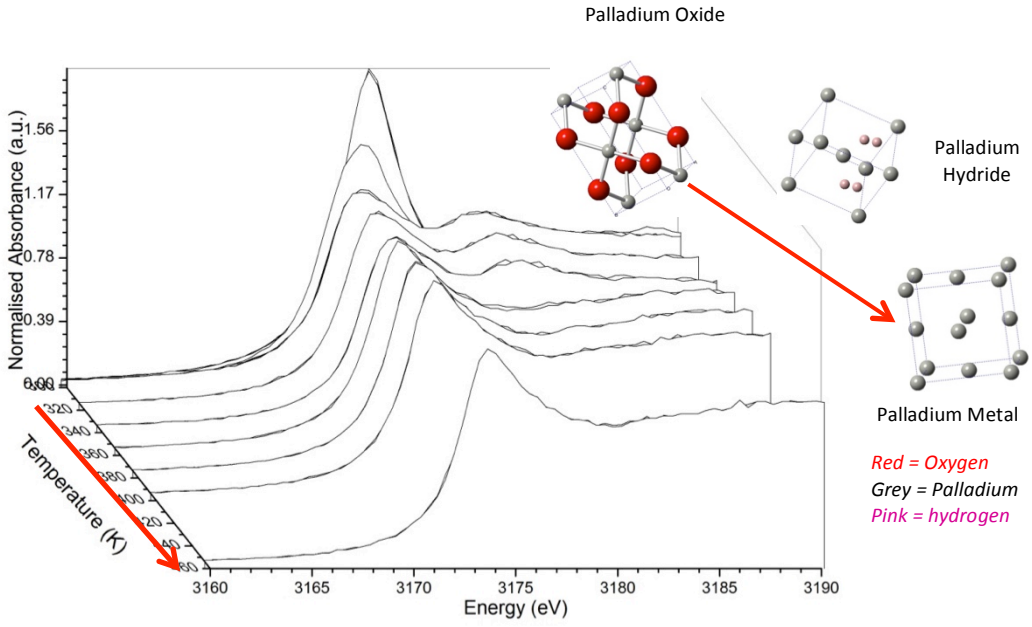

Figure 3-6 - Plot of fumed silica Pd L_{III}-edge data against temperature during reduction in hydrogen. Diagram shows the local structures for palladium oxide to palladium metal.

The material at the end of the reduction process, after once again being in a helium environment, is more representative of Pd metal. There is a large decrease in the size of the whiteline intensity of the material. There are also distinct changes in the post-edge region

when compared with the PdO spectrum. The shoulder feature after the whiteline intensity disappears and small peaks appear between 3180-3193eV and 3197-3207eV (Figure 3-7).

Upon introduction of hydrogen to the reaction chamber the PdO reduces almost instantly, as can be seen from the clear reduction of the whiteline intensity (Figure 3-8 and Table 3-2). The decrease of the whiteline intensity signifies a redistribution of the d-band charge.[6,7] Initially in He atmosphere the value of the whiteline intensity is 1.93, upon the introduction of H_2 this drops to 1.48. At the end of the room temperature reduction this value has decreased further to 1.21. Due to the link between the whiteline intensity (p→d transition intensity) and the d-band charge, these results can be interpreted as the Pd species gaining charge. This is in agreement with the known reduction from PdO to Pd metal and the accompanying change in oxidation state from +2 to 0.[5] During the temperature ramp the value of the whiteline intensity remains below 1.35 and at the end of the process at room temperature in the presence of He the value remains around ca 1.3.

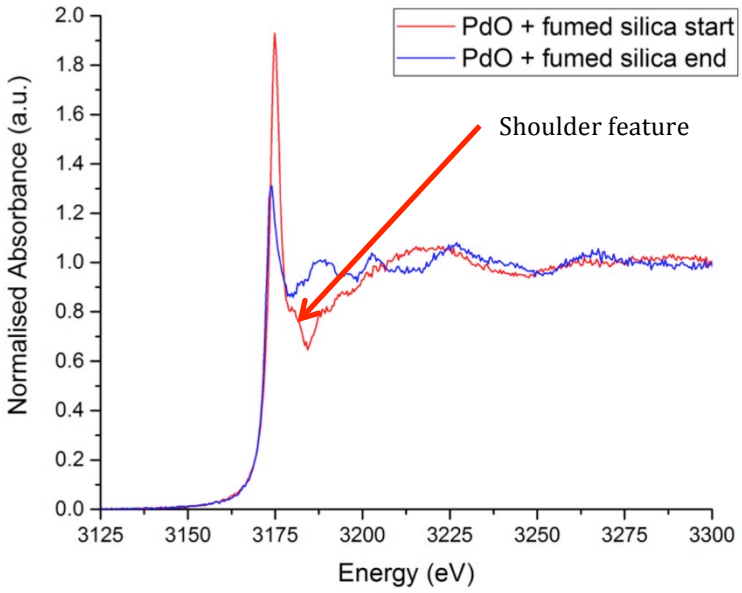

Figure 3-7 - L III-edge XANES for PdO + Fumed silica at the beginning and end of the reduction. Post reduction material appears as Pd metal.

Along with the change in whiteline intensity there is also the emergence of peaks between 3180-3193eV and 3197-3207eV upon addition of hydrogen to the reaction chamber (Figure 3-10). The second scan after the introduction of hydrogen shows additional features that can be interpreted as being from the hydride phase.[10] This can be inferred from the appearance of a peak between 3178-3185eV; Pd metal does not cause this peak, as the final scan in helium does not show this peak. It has been shown in a previously published paper that this peak is caused by hydrogen absorbed in the Pd lattice perturbing the electronic state.[10]

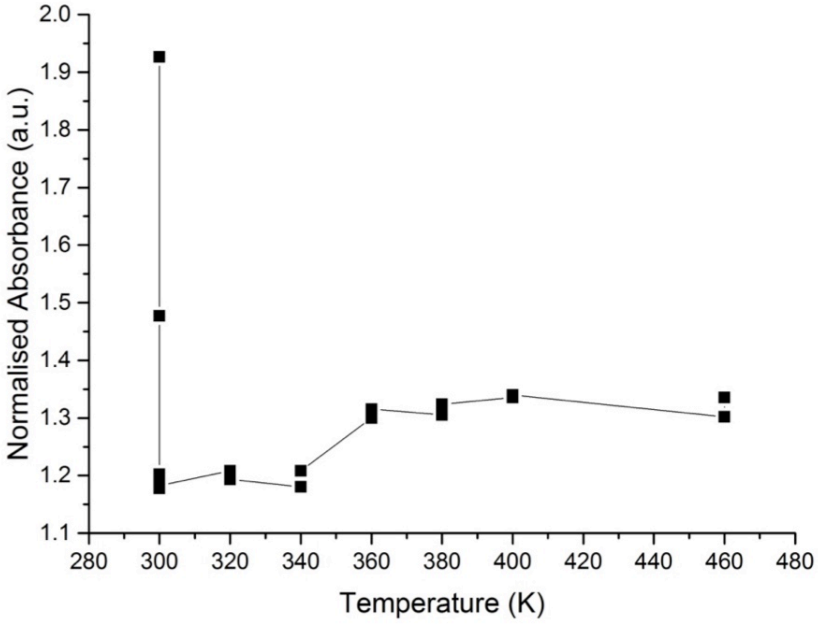

Figure 3-8 - Change in whiteline intensity with temperature for fumed silica + PdO mixture.

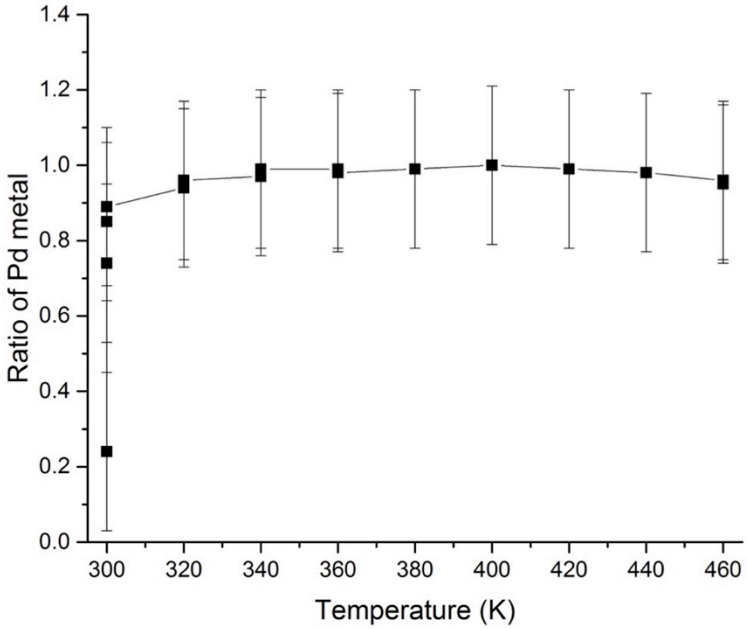

Figure 3-9 - Ratio of Pd metal formed during the reduction for PdO + fumed silica.

The palladium appears fully reduced at the end of the reaction; this is confirmed from XANES observations. As the PdO reduction is a model system, the change in the whiteline intensity can be used as a guide to the reduction to Pd metal (Figure 3-9). As can be seen in the plot the material reduces almost completely at room temperature, with only slight variations occurring at higher temperatures. The error in the measurement was calculated by

taking the variance between the ratios from the room temperature results at the end of the reduction. This was done as the material should be the same composition for all these scans.

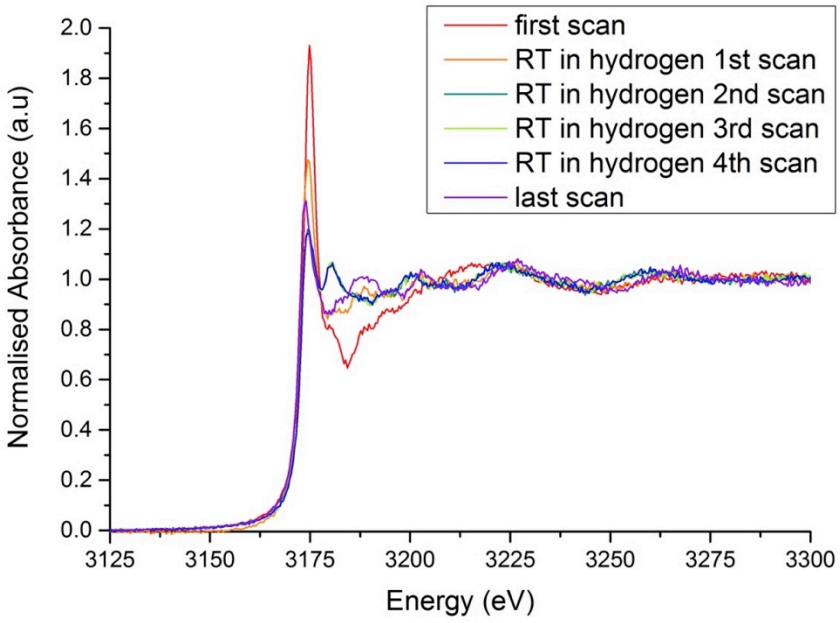

Figure 3-10 - Comparison of the Pd L_{III}-edge XANES scans immediately after hydrogen introduction and the initial and final scans of the reduction experiment, highlighting the difference in the features.

This extra hydride peak continues to be visible until 360 K after this point it disappears and the data more closely resembles that for the final material. Upon cooling the sample the extra hydride peak reappears at room temperature in hydrogen; this peak disappears again in subsequent room temperature scans in He.

What we therefore propose is that the PdO reduces to Pd metal upon coming into contact with hydrogen. Further exposure to hydrogen leads to the incorporation of hydrogen in the Pd framework and the formation of the hydride phase as seen from the appearance of the extra peak after the edge. Heating above temperatures of 360K leads to the removal of hydrogen from the structure and results in the disappearance of the extra peak after the whiteline. Cooling to room temperature allows the hydrogen to once again enter the Pd structure reforming the hydride phase (Figure 3-6). Subsequent dwelling in helium atmosphere reveals this through the disappearance of the extra peak at ca 3178-3185 eV once again. This shows the metastable nature of the Pd hydride formed, as the phase is removed shortly after switching to He atmosphere. A previous computational study linked the stability of Pd hydride to the location of the hydrogen in the metal whether located near defect sites and whether in octahedral or tetrahedral sites; all of these factors affect the stability of the final material.[64]

Table 3-2 - Values for the change in the whiteline intensity and edge position at 0.6 (normalised absorbance) for PdO + fumed silica mixture.

Temperature (K)	Gas	Whiteline Intensity (a.u)	Edge Position (at 0.6 na)
300	He	1.93	3172.13
300	He	1.94	3172.13
300	He	1.91	3172.12
300	He	1.93	3172.1
300	H_2/He	1.48	3171.85
300	H_2/He	1.20	3172.34
300	H_2/He	1.18	3172.41
300	H_2/He	1.18	3172.35
320	H_2/He	1.21	3172.34
320	H_2/He	1.19	3172.28
340	H_2/He	1.18	3172.28
340	H_2/He	1.21	3171.8
360	H_2/He	1.30	3171.77
360	H_2/He	1.32	3171.72
380	H_2/He	1.31	3171.73
380	H_2/He	1.32	3171.73
400	H_2/He	1.34	3171.72
400	H_2/He	1.34	3171.72
460	H_2/He	1.30	3171.69
460	H_2/He	1.34	3171.74
300	H_2/He	1.19	3172.37
300	H_2/He	1.21	3172.32
300	H_2/He	1.19	3172.4
300	He	1.20	3172.4
300	He	1.26	3172.01
300	He	1.31	3171.75

The edge position used in the table was taken at a fixed value (0.6) from the normalised absorbance and reading of the corresponding energy for that value. This method was used for all samples.

3.8.1.2 2% Pd/Silica

The 2% Pd/silica sample was formed from chemical deposition; therefore it is expected to have a reasonable stabilising interaction with the support. However as the interaction between the Pd nanoparticles and the support are weak, the material reduces at room temperature just like the physically mixed PdO fumed silica sample.[44] Almost as soon as the hydrogen is

allowed into the reaction chamber the Pd reduces, this can be confirmed through the sharp decrease in the whiteline intensity from ca 3.1 to 1.4 (Table 3-3). Additionally there is a peak in the region 3179-3184 which is the characteristic Pd-hydride peak (Figure 3-12).[10]

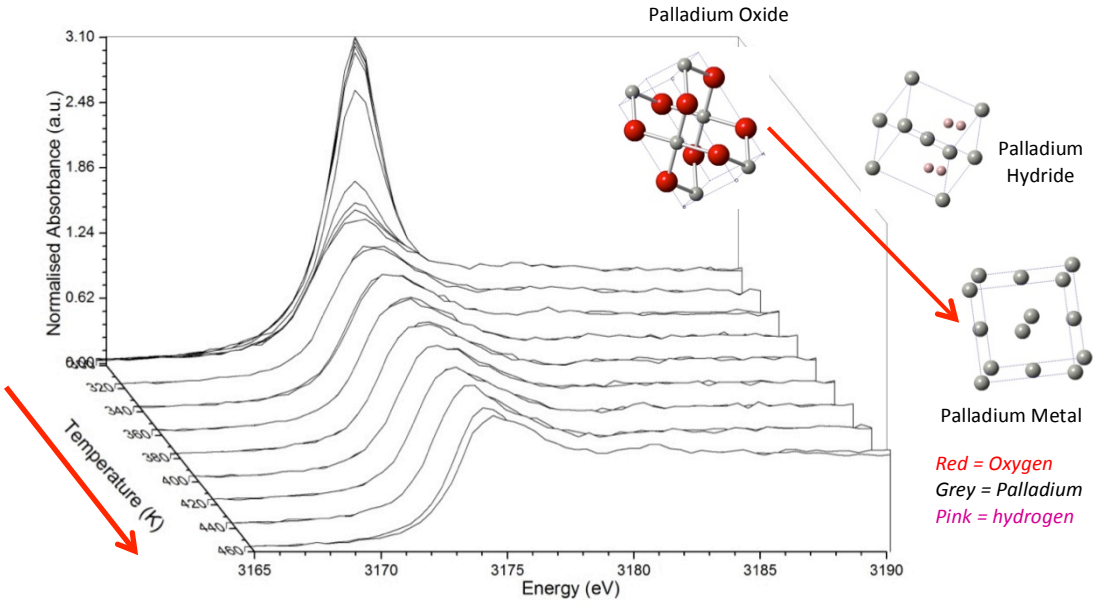

Figure 3-11 - 2% Pd/silica XANES against temperature during reduction in hydrogen. Diagram shows the local structures for palladium oxide to palladium metal.

During the temperature ramp the hydride phase is completely removed by 400K, as evidenced by the disappearance of the hydride peak and the emergence of a peak between 3183-3194 eV, which belongs to the metallic phase of Pd. Upon cooling to room temperature the hydride reforms in hydrogen environment and is removed when the gas flow is switched to helium (Figure 3-13). Again this shows that the Pd is accessible to the H_2 throughout the reaction and the reduction process does not cause structural changes on the support that hinders access. This highlights the weakness of the interaction between silicon and palladium as the chemical deposited and physically mixed samples have no difference in the reduction.

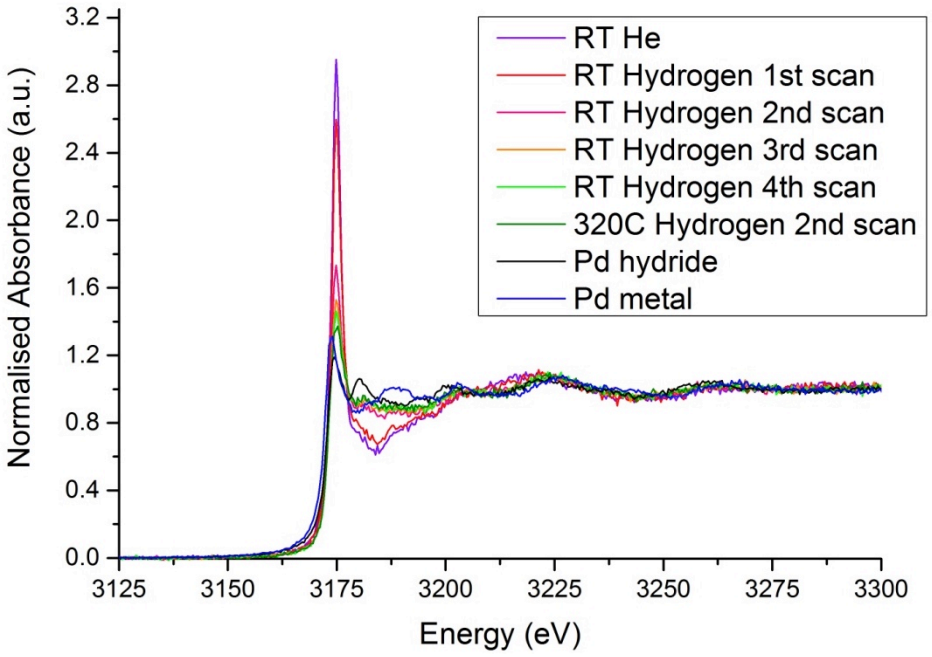

Figure 3-12 - Comparison of the XANES for 2% Pd silica sample at room temperature in both helium and hydrogen.

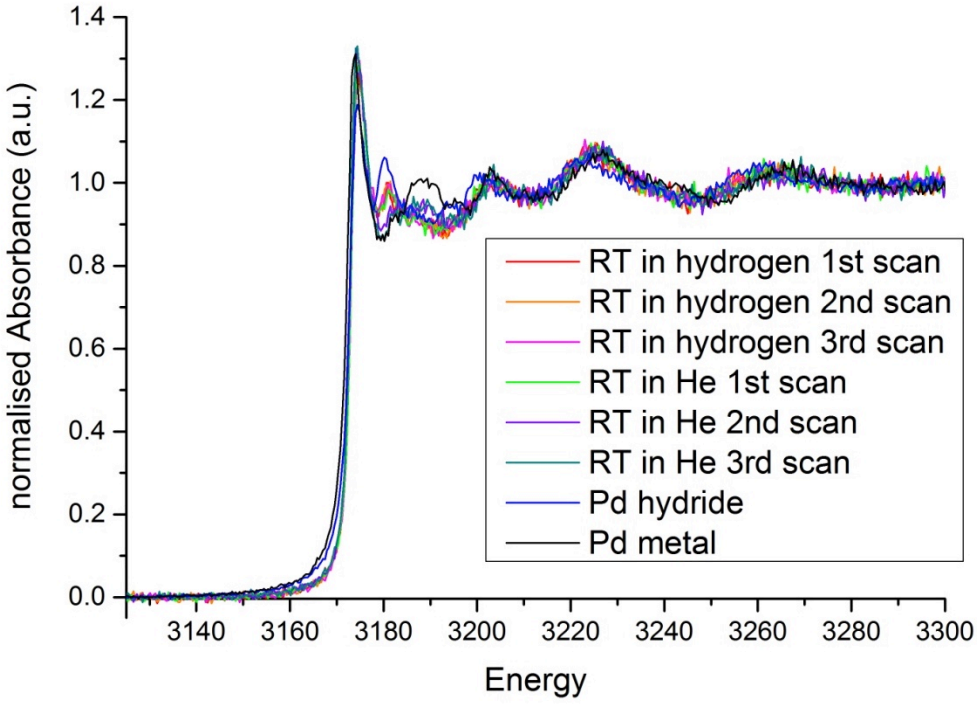

Figure 3-13 - Comparison of the XANES for Pd/Silica sample at the end of reduction in both helium and hydrogen.

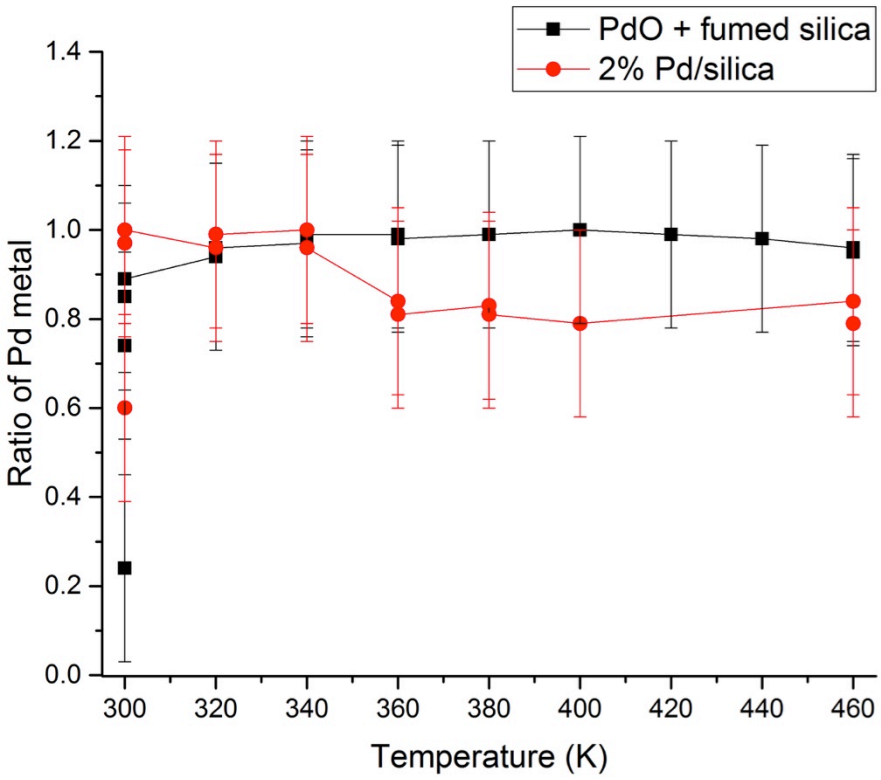

Figure 3-14 - Ratio of Pd metal formed during the reduction for 2%Pd/silica, compared with the reduction of PdO + fumed silica.

The variation in the whiteline intensity can be related back to the ratio of PdO and Pd, using the PdO + fumed silica result as a standard (Figure 3-14). From the plot it can be seen that the 2% Pd/silica material also reduces at room temperature with a complete conversion from the oxide observed. This is matches the reduction observed in the physically mixed sample and suggests that there is little to no interaction between the Pd and the silica support to limit the reduction. Interestingly the amount of Pd metal formed at room temperature appears to higher for the supported Pd/silica than for the physical mixture, 605 compared with 20%. This could be related to the particle size, as it is assumed that the deposited Pd has smaller PdO particles on the surface than the standard PdO.

Table 3-3 - Values for the change in the whiteline intensity and edge position at 0.6 (normalised absorbance) for 2% Pd/silica.

Temperature (K)	Gas	Whiteline Intensity	Edge Position (at 0.6 na)
300	He	3.11	3172.43
300	He	3.09	3172.43
300	He	3.05	3172.39
300	He	3.02	3172.43
300	He	2.95	3172.59
300	H_2/He	2.60	3172.56
300	H_2/He	1.73	3172.81
300	H_2/He	1.53	3172.78
300	H_2/He	1.46	3172.74
320	H_2/He	1.37	3172.74
320	H_2/He	1.34	3172.82
340	H_2/He	1.32	3172.71
340	H_2/He	1.29	3172.67
360	H_2/He	1.28	3172.76
360	H_2/He	1.30	3172.65
380	H_2/He	1.28	3172.55
380	H_2/He	1.28	3172.55
400	H_2/He	1.26	3172.53
400	H_2/He	1.27	3172.53
420	H_2/He	1.28	3172.52
420	H_2/He	1.28	3172.47
440	H_2/He	1.30	3172.43
440	H_2/He	1.31	3172.45
460	H_2/He	1.34	3172.41
460	H_2/He	1.35	3172.41
300	H_2/He	1.28	3172.71
300	H_2/He	1.30	3172.71
300	H_2/He	1.29	3172.71
300	He	1.28	3172.7
He	He	1.32	3172.53
He	He	1.33	3172.51

3.8.2 Pd/Alumina Investigation of Percentage Loading

Alumina supported Pd is known to have reasonable interactions between the Pd and the support.[28] In order to investigate this further the loading of the Pd on alumina was varied in this set of experiments to monitor the effect if any with regards to reduction. It is expected that Pd will have a stronger interaction with the alumina due to it being a reactive support, and this should translate to higher reduction temperature for the catalysts.[28]

3.8.2.1 0.5% Pd/alumina

The *in situ* L_{III}-edge XANES data for the reduction of 0.5% Pd/alumina is shown in Figure 3-15, with the structures of the initial PdO and final Pd metal shown. Also shown is the structure of Pd hydride that is suggested to be formed during the reduction process.

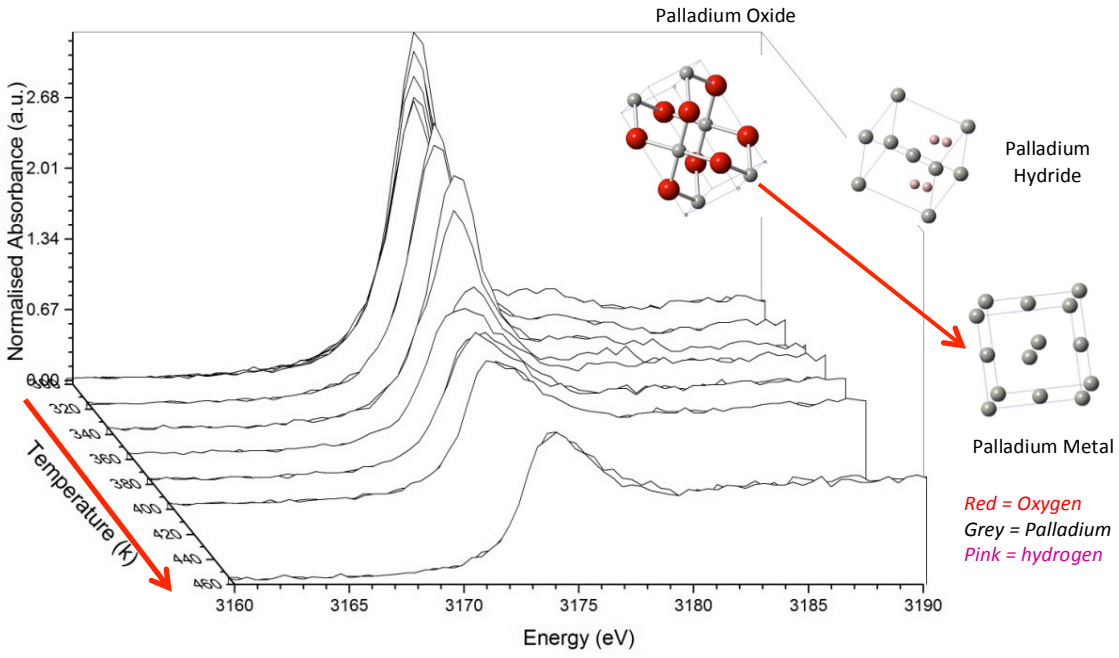

Figure 3-15 - Plot of XANES for 0.5% Pd alumina against temperature during reduction in hydrogen. Diagram shows the local structures for palladium oxide to palladium metal.

The 0.5% Pd/alumina sample looks very similar to PdO at room temperature with subtle additional features after the edge (Figure 3-16). There are two very broad peaks in the region from 3183-3200 eV that may be due to palladium metal but due to the data resolution it is not possible to confirm this accurately. If the peaks were genuine it would be evidence to suggest that the Pd is in a mixed metal and metal oxide phase at room temperature. Upon the introduction of hydrogen to the sample there is no change in the phase of the material, as evidenced from the similarities in the post edge features, however the intensity of the

whiteline decreases from 3.15 to 1.9 indicating some chemical change has occurred within the material (Table 3-4). This shows that there is a change in the density of available free states.

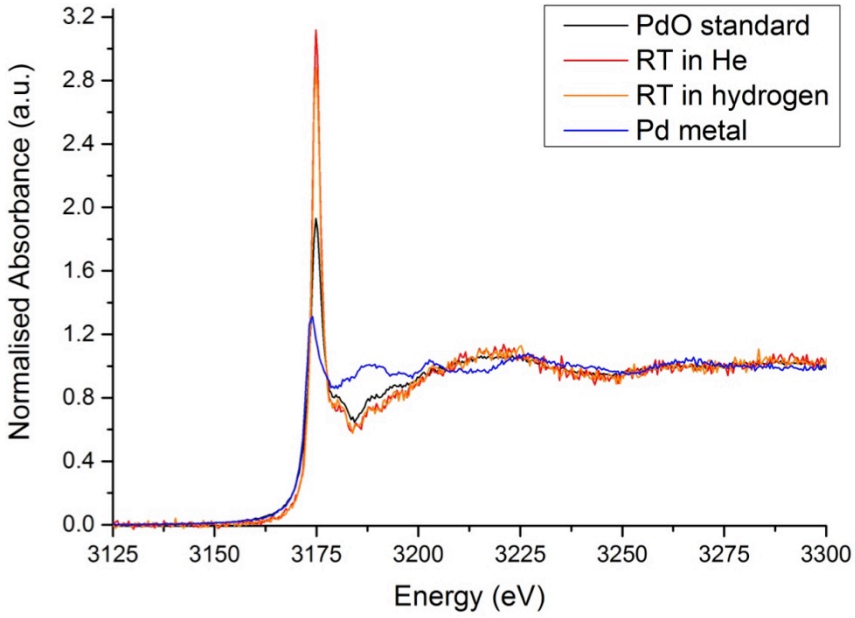

Figure 3-16 - XANES data 0.5% Pd/alumina sample at room temperature in helium and after introduction of hydrogen compared with PdO sample and Pd metal standards.

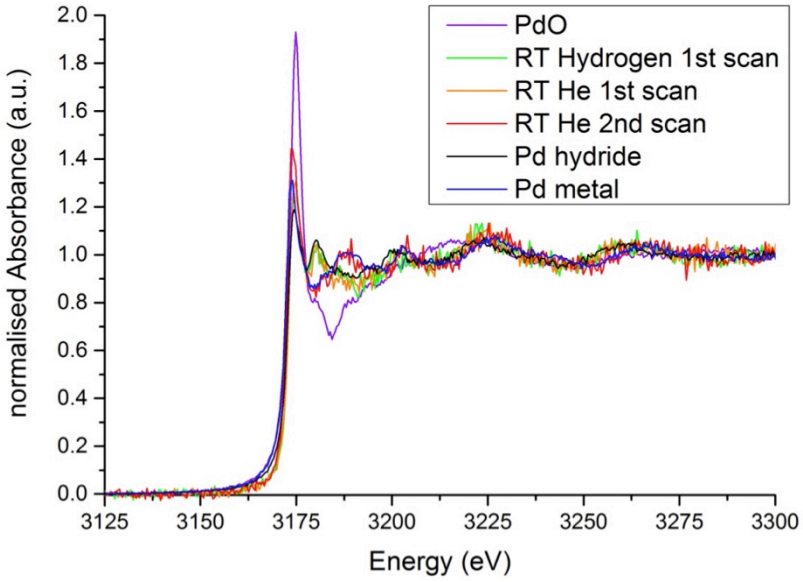

Figure 3-17 - Plot of 0.5% Pd/alumina XANES data at room temperature in hydrogen and helium with standard models.

At the end of the room temperature reduction there is a slight increase in the region 3178-3183 eV, which might be indicative of hydride formation. Upon heating to 360 K the palladium reduces fully to the metal with no hydride phase visible. Prior to full reduction there is a peak visible in the region 3178-3183eV, which is indicative of hydride formation.

Further heating to 360 K results in no further decrease of the whiteline intensity, which remains at 1.4 (a.u.).

Upon cooling to room temperature in hydrogen the hydride phase is reformed as clearly indicated by the re-emergence of the peak at 3178-3183eV (Figure 3-17). Replacing the gas in the reaction chamber with helium results in the loss of this peak, confirming it to be hydride based, with the scan looking resembling the data collected at the end of the fumed silica experiment.

Table 3-4 - Change in whiteline intensity and edge position for the reduction of 0.5% Pd/Alumina.

Temperature (K)	Gas	Whiteline Intensity	Edge Position (at 0.6 na)
300	He	3.03	3172.52
300	He	3.09	3172.47
300	He	3.05	3172.46
300	He	3.12	3172.35
300	H_2/He	2.88	3172.49
300	H_2/He	2.68	3172.54
300	H_2/He	2.64	3172.53
300	H_2/He	2.67	3172.55
320	H_2/He	2.47	3172.51
320	H_2/He	2.42	3172.56
340	H_2/He	2.08	3172.59
340	H_2/He	1.60	3172.51
360	H_2/He	1.39	3172.22
360	H_2/He	1.40	3172.22
380	H_2/He	1.41	3172.17
380	H_2/He	1.36	3172.25
400	H_2/He	1.37	3172.2
400	H_2/He	1.41	3172.18
460	H_2/He	1.40	3172.13
460	H_2/He	1.41	3172.17
300	H_2/He	1.27	3172.68
300	H_2/He	1.26	3172.64
300	H_2/He	1.30	3172.68
300	He	1.31	3172.64
300	He	1.43	3172.22
300	He	1.44	3172.14

3.8.2.2 2% Pd/alumina

2% Pd was deposited on γ-alumina and tested for the same reduction experiment. The initial scans at room temperature in helium show some differences to the initial scans for PdO. There is a significant post-edge feature at 3178-3184 eV, which remains upon initial introduction of hydrogen (Figure 3-18). Additionally there are two small peaks between ca 3185-3190 and 3191-3197 eV which is very close to the values for the Pd metal phase. This could mean that the material is not purely PdO but is already partially reduced prior to the experiments being performed. Upon introduction of hydrogen to the system there is no formation of the Pd hydride phase (Figure 3-19). This can be seen by the lack of an extra peak between 3178-3185eV.

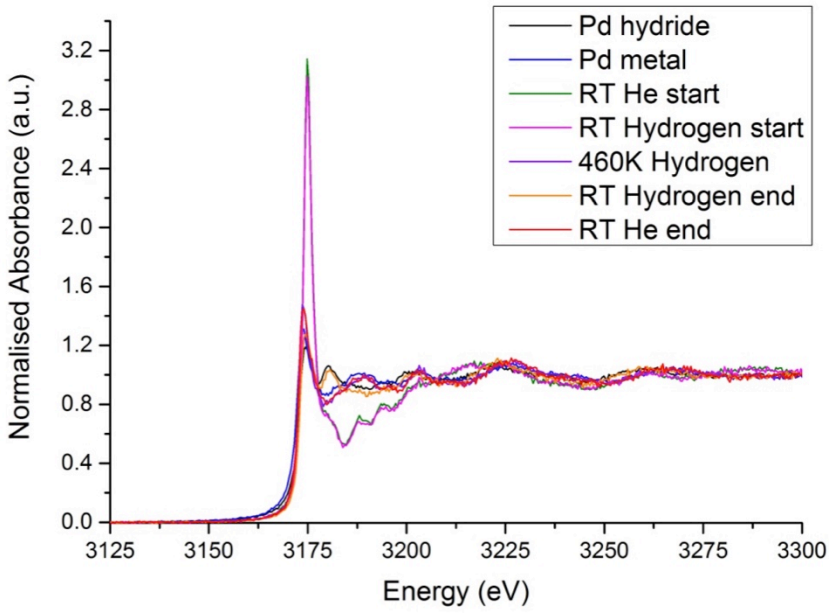

Figure 3-18 - Scans during the reduction process showing the initial scan, after switch to hydrogen, at 460K after cooling to RT in hydrogen and at room temperature in helium.

However this may also be due to the lack of hydrogen in the system; at this point due to user error the hydrogen cylinder was not open meaning the hydrogen reaching the sample was merely the gas already in the lines. Once it was exhausted the air in the experimental hutch was able to enter the cell resulting in the appearance of an extra Ar edge. The significance of this on the results is unknown; however we do have a confirmed hydride phase formation at 340K, which is swiftly removed upon further heating. The hydride phase appears to be removed at a lower temperature in Pd/alumina when compared to the free material in fumed silica. The pre-existence of metallic phase Pd may have some contribution to that. However the material reduces at 340 K, which is slightly higher than the 300 K for reduction in PdO fumed silica.

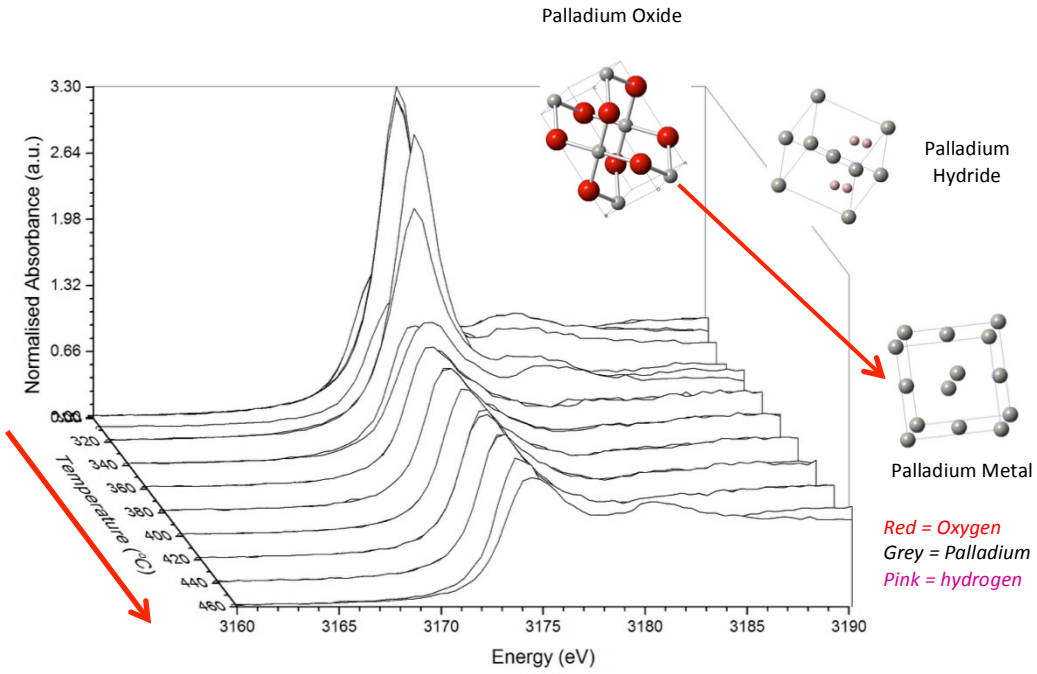

Figure 3-19 - 2% Pd alumina plot of XANEs against temperature during reduction in hydrogen. Diagram shows the local structures for palladium oxide to palladium metal.

The reduction of the Pd can also be followed through the change in the whiteline intensity, which drops from 3-2.3 at 300 K in hydrogen to ca, 1.4 at 340 K when the material is reduced (Table 3-5). The variation in the whiteline intensity between the scans at 300K can be related to the lack of hydrogen flow to the system, and as such these changes can be ignored.

The hydride peak reappears at the end of the reduction at room temperature whilst in hydrogen atmosphere. The peak disappears upon switching from hydrogen to helium gas. This again supports the theory from the fumed silica sample about the formation and removal of Pd hydride.

Table 3-5 - whiteline intensity and change in edge position for the reduction of 2%Pd/alumina.

Temperature (K)	Gas	Whiteline Intensity	Edge Position (at 0.6 na)
300	He	3.15	3172.56
300	He	3.13	3172.56
300	He	3.18	3172.56
300	He	3.18	3172.56
300	He	3.19	3172.54
300	He	3.17	3172.58
300	He	2.11	3173.11
300	H_2/He	2.35	3172.98
300	H_2/He	2.61	3172.83
300	H_2/He	2.84	3172.75
300	H_2/He	2.94	3172.69
300	H_2/He	3.02	3172.64
300	H_2/He	3.02	3172.61
320	H_2/He	3.07	3172.61
320	H_2/He	2.33	3172.61
340	H_2/He	1.42	3172.6
340	H_2/He	1.39	3172.32
360	H_2/He	1.39	3172.29
360	H_2/He	1.41	3172.23
380	H_2/He	1.43	3172.22
380	H_2/He	1.43	3172.24
400	H_2/He	1.43	3172.22
400	H_2/He	1.46	3172.21
420	H_2/He	1.49	3172.21
420	H_2/He	1.44	3172.21
440	H_2/He	1.49	3172.19
440	H_2/He	1.47	3172.19
460	H_2/He	1.48	3172.19
460	H_2/He	1.29	3172.72
300	H_2/He	1.27	3172.72
300	H_2/He	1.29	3172.71
300	H_2/He	1.28	3172.67
300	He	1.46	3172.2
300	He	1.45	3172.2

3.8.2.3 4% Pd/Alumina

The maximum percentage loading used during these experiments was 4% Pd/alumina and at room temperature the material closely resembles the 2% Pd/alumina catalyst (Figure 3-20). There are small peaks indicative of a metallic phase being present along with the large broad peak expected for PdO.

After initial introduction of hydrogen there is no immediate change in the structure of the material; no reduction and no hydride formation is visible. This suggests that there is a stabilising interaction helping to maintain the Pd in comparison to the unsupported PdO fumed silica sample; we would suggest this is due to the MSI. Further evidence for this to be a support effect, is the 2% Pd/silica sample also reduced at room temperature due to the weak interactions between the support and the Pd particles as noted in the literature.[44,65]

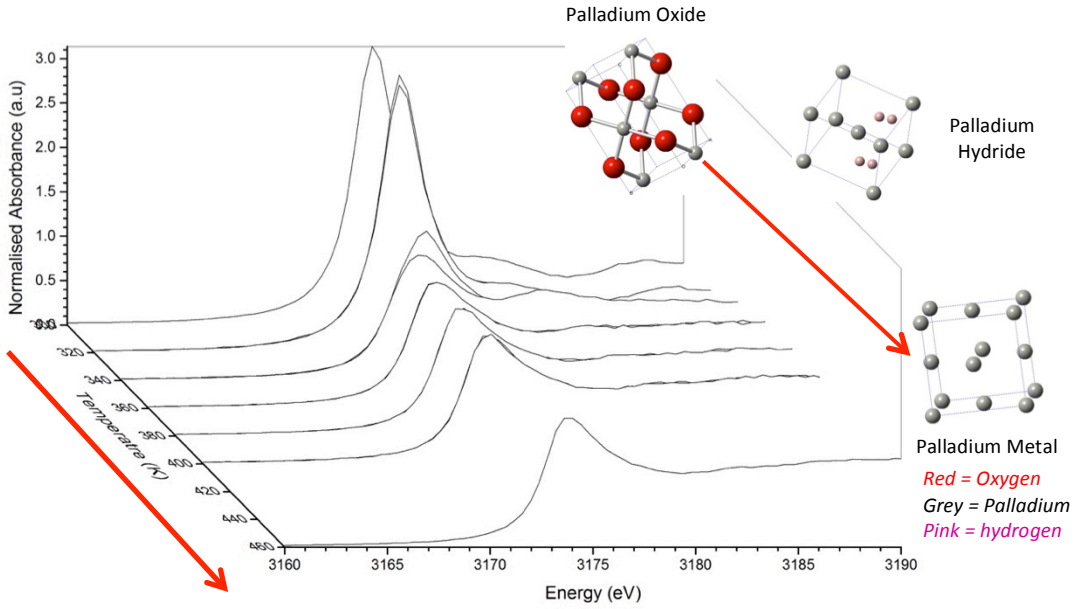

Figure 3-20 - plot of XANES for 4% Pd alumina against temperature during reduction in hydrogen. Diagram shows the local structures for palladium oxide to palladium metal.

The palladium is reduced by 340 K, with no delay between the formation of hydride phase and the reduction to metallic state. This reduction is supported by the change in the whiteline intensity, which decreases from 3.17 at 300 K to 1.68 at 340 K (Figure 3-21). By 360K the hydride phase has been removed leaving the material as metallic palladium, as evidenced by the disappearance of the peak at 3178-3185 eV. Once the material returns to room temperature in hydrogen the Pd hydride phase reforms, with the peak at 3178-3185 eV reappearing, upon switching back to helium the hydride phase is removed.

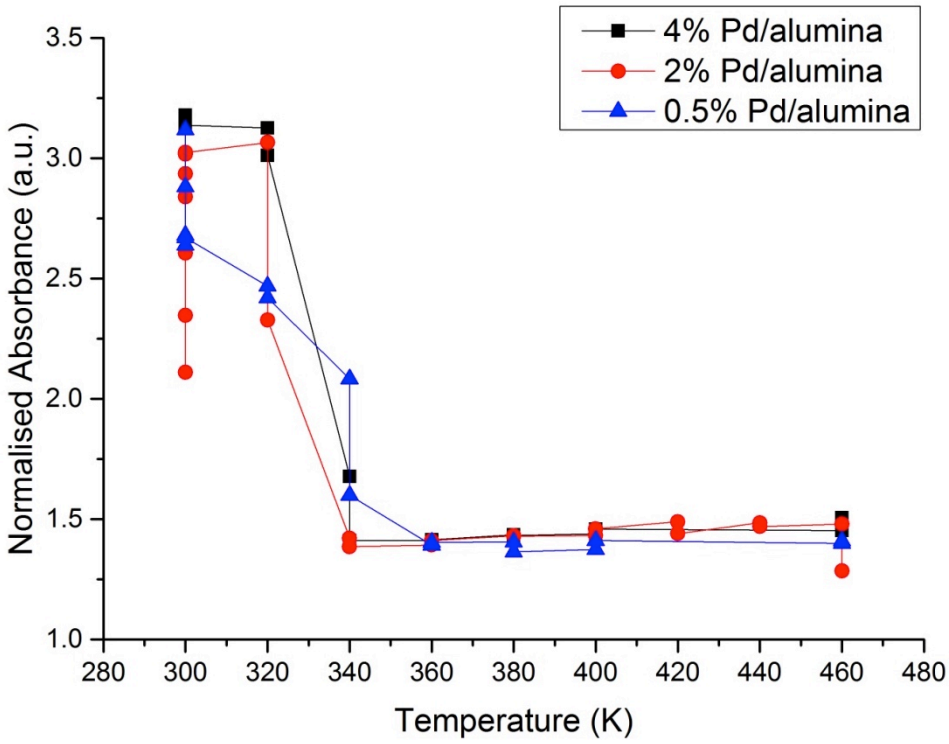

Figure 3-21 - Change in the whiteline intensity for Pd nanoparticles supported on alumina.

Taking the change in the whiteline intensity for the 3 alumina supported materials the general trend in the reduction can be seen much more clearly (Figure 3-21). The alumina supported materials all reduce by at 340 K, with minimal variations in the whiteline intensity observed at higher temperature. This would seem to indicate that the percentage loading of Pd on the alumina support has no influence on the reduction temperature.

Using the whiteline intensities to estimate the amount of Pd metal in the alumina supported catalysts shows a similar trend for the reduction (Figure 3-22). For the 2% and 0.5% Pd loaded samples there is a 20% reduction at room temperature, whilst the 4% Pd loaded sample does not appear to reduce. Reduction for the 4% Pd/alumina sample instead begins at 320 K, reaching complete reduction by 340 K. The 2% Pd/silica is also completely reduced by 340 K, however the 0.5% Pd/alumina sample reduces fully at the slightly higher temperature of 380 K. The reasons for this could be related to the particle size and the strength of the interaction between the Pd and the support. It could be that smaller Pd particles have a stronger interaction and hence reduce at higher temperatures.[28]

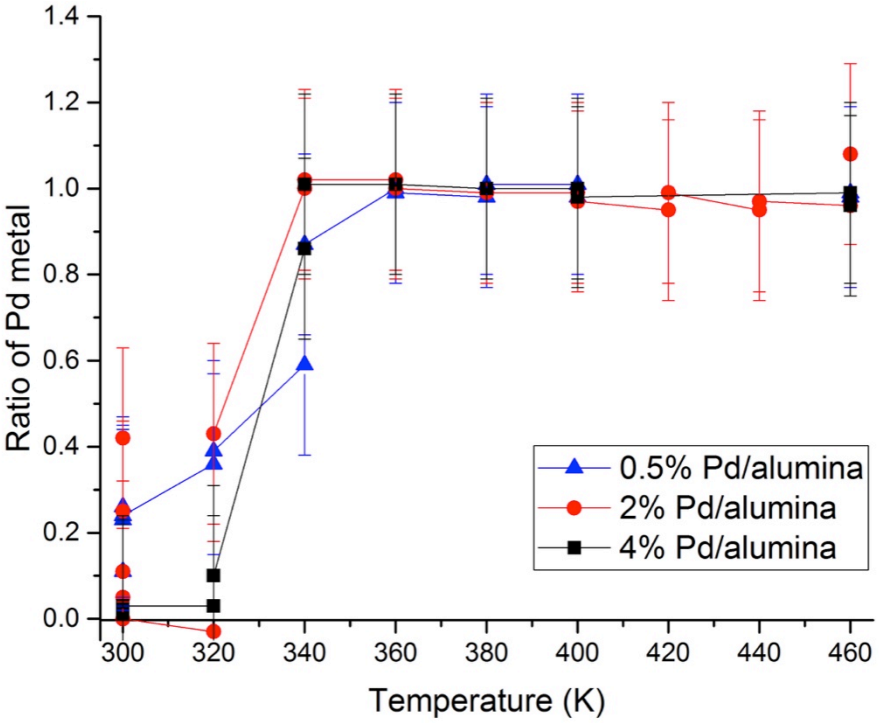

Figure 3-22 - Ratio of Pd metal formed during the reduction for the alumina supported catalysts.

There are many similarities between the 2% and 4% Pd/alumina catalysts in terms of their reduction processes. Despite the lack of evidence for initial hydride phase formation in the case of the 2% Pd/alumina due to the air leak, its presence can be inferred due to the similarities with the 4% Pd/Alumina catalyst. The L_{III}-edge method has also been demonstrated on the relatively low loaded 0.5% Pd/Alumina material and has been successfully used to determine the differences between the oxide, metallic and hydride forms of Pd.

Table 3-6 - Change in whiteline intensity and edge position for the reduction of 4% Pd/alumina, with the edge position taken at normalised absorbance.

Temperature (K)	Gas	Whiteline Intensity	Edge Position (at 0.6 na)
300	He	3.16	3172.5
300	He	3.20	3172.51
300	He	3.20	3172.5
300	He	3.18	3172.49
300	H_2/He	3.17	3172.52
300	H_2/He	3.17	3172.52
300	H_2/He	3.15	3172.51
300	H_2/He	3.14	3172.51
320	H_2/He	3.13	3172.51
320	H_2/He	3.01	3172.54
340	H_2/He	1.68	3172.55
340	H_2/He	1.41	3172.55
360	H_2/He	1.41	3172.21
360	H_2/He	1.42	3172.21
380	H_2/He	1.44	3172.21
380	H_2/He	1.43	3172.19
400	H_2/He	1.44	3172.14
400	H_2/He	1.46	3172.19
460	H_2/He	1.45	3172.19
460	H_2/He	1.51	3172.14
300	H_2/He	1.30	3172.66
300	H_2/He	1.32	3172.66
300	H_2/He	1.31	3172.66
300	He	1.3	3172.66
300	He	1.46	3172.19
300	He	1.47	3172.19

3.8.3 Pd Ceria Investigation of Percentage loading

It has been extensively documented that Pd has a synergistic interaction with ceria.[41,65] Here we explore this interaction the effect if any of Pd loading on ceria with regards to reduction. Increasing the loading of Pd should lead to the formation of larger Pd particles upon reduction, if the Pd particles are free to move across the surface. The difference in the amount of Pd loaded onto a ceria substrate was also examined, with 2% and 0.5% materials reduced and monitored *in situ*. A comparison was also made with a Pd/alumina catalyst, which had a 15% ceria overlayer. Here the difference in the materials, with regards to Pd reduction, is explored.

3.8.3.1 0.5% Pd/Ceria

The 0.5% Pd/ceria sample shows a different behaviour to the alumina-supported material. Whilst at room temperature in helium the spectra look relatively similar between the two supports. Once hydrogen is introduced there is an increase in the whiteline intensity from 4.09 to 4.3 (Figure 3-23). There is also a strong shoulder feature after the edge, not seen on the previous alumina samples 3179-3182 eV. This should be related to the interaction between Pd and the ceria support. The oscillations observed in the post edge region are due to orbital interactions, in this case between the orbitals of Pd and ceria. The fact that this peak appears here and not for alumina could indicate one of two things, either it is unique to the electronic structure of ceria or it is due to the geometry of the Pd ceria altering the electronic interaction.

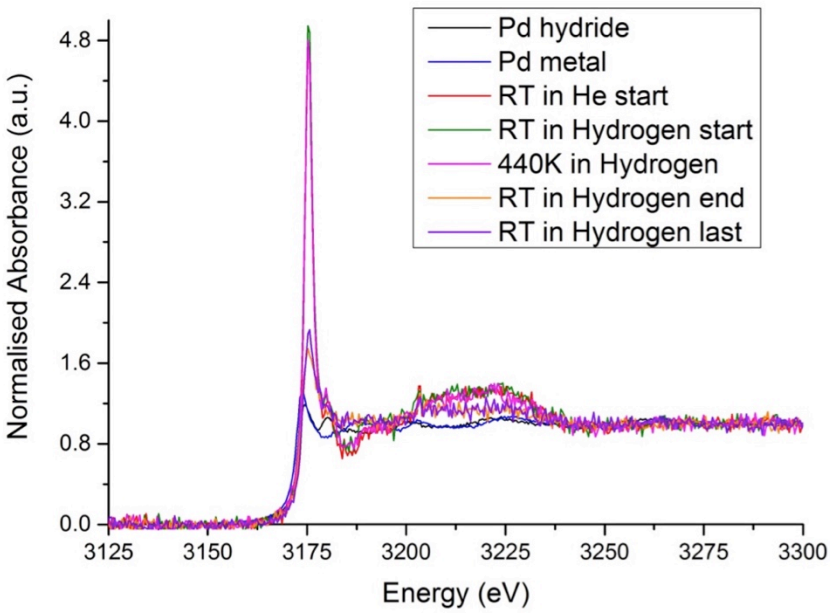

Figure 3-23 - Plot of 0.5% Pd/ceria data with standards showing the key features.

The XANES spectra for the reduction are shown in Figure 3-24. Upon heating to 400K the material reduces as evidenced from the significant decrease in whiteline intensity from 4.38 to 1.89 (Table 3-7). The features previously seen in the alumina and fumed silica samples such as the two peaks between ca 3185-3190 and 3191-3197 eV are not visible. Neither is the hydride peak. After returning to room temperature in hydrogen no hydride phase is observed, furthermore even after switching to helium no changes can be discerned. This leads to conclusions that either there is not enough Pd loaded to observe the changes or that the interactions between Pd and Ceria stabilise the material against hydride formation. This could be due to a surface rearrangement covering the Pd, as reported in the literature.[66,67]

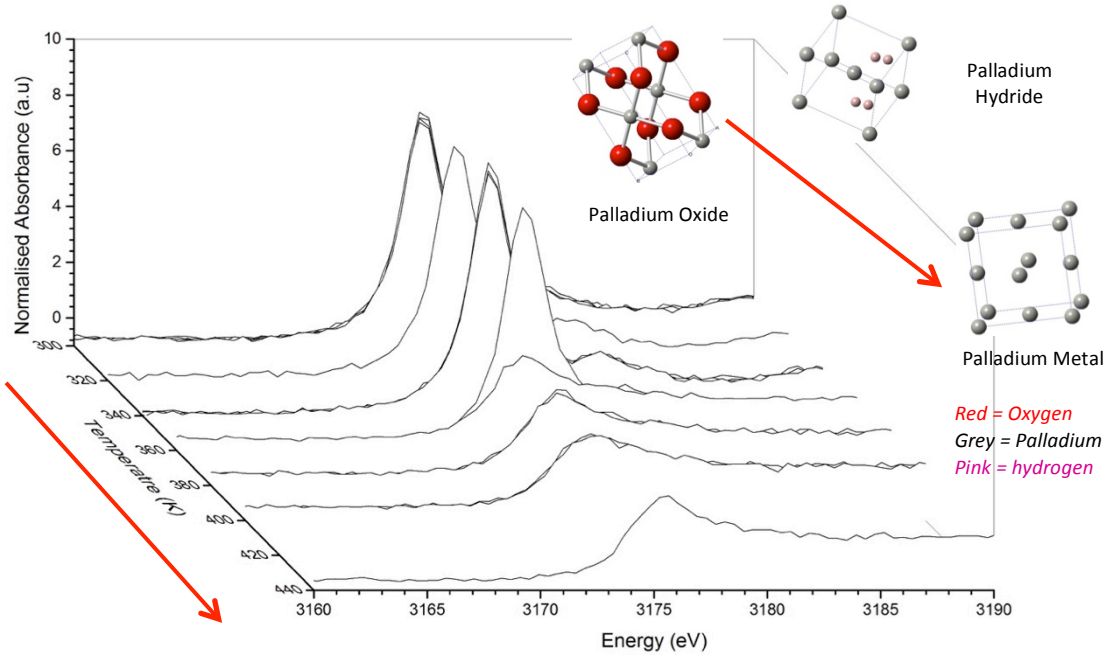

Figure 3-24 - Plot of XANES for 4% Pd alumina against temperature during reduction in hydrogen. Diagram shows the local structures for palladium oxide to palladium metal.

Table 3-7 - Comparison of the change in whiteline intensity and edge position for the reduction of 0.5% Pd/Ceria.

Temperature (K)	Gas	Whiteline Intensity	Edge Position (at 0.6 na)
300	He	4.7	3172.74
300	He	4.99	3172.4
300	H_2/He	4.90	3172.3
300	H_2/He	4.78	3172.3
300	H_2/He	4.64	3172.47
300	H_2/He	4.72	3172.58
320	H_2/He	4.48	3172.51
320	H_2/He	4.73	3172.43
340	H_2/He	4.73	3172.44
340	H_2/He	4.76	3172.51
360	H_2/He	4.73	3172.46
360	H_2/He	4.81	3172.25
380	H_2/He	4.79	3172.79
380	H_2/He	1.98	3173.34
400	H_2/He	1.82	3173.38
400	H_2/He	1.86	3173.36
440	H_2/He	1.75	3172.65
440	H_2/He	1.76	3172.71
300	H_2/He	1.93	3172.03

3.8.3.2 2% Pd Ceria

The reduction of the 2% Pd/Ceria sample looks very similar to the previous 0.5% loaded sample (Figure 3-25). There is a strong shoulder feature in the region from 3179-3182eV. There is also an additional peak in around 3187-3196 eV. This peak may be due to Pd metallic phase but further analysis of the K-edge region is needed in order to confirm this. After the introduction of hydrogen to the system there is no immediate change at room temperature.

The 2% catalyst appears to reduce at much lower temperature than the 0.5%, with reduction visible at 340K as opposed to 400K in the 0.5% case (Figure 3-26). Additionally there are extra peaks visible in the post-edge region from 3198-3210 and 3216-3238 eV, which correspond to the oscillations previously seen in the Pd metallic phase.

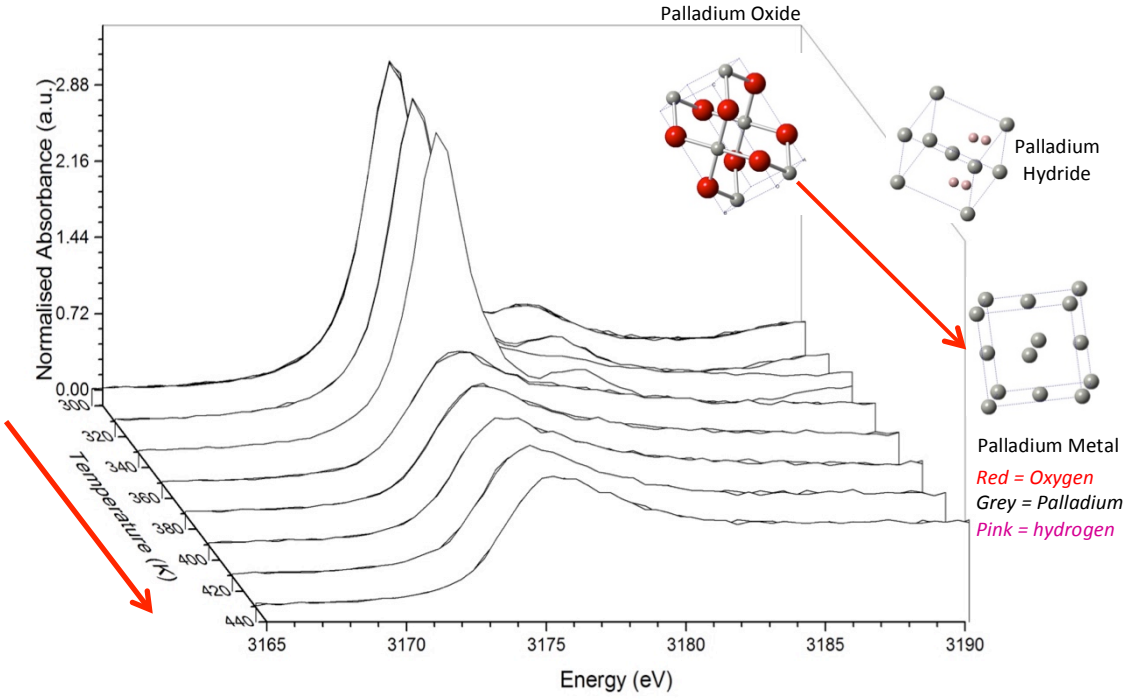

Figure 3-25 - Plot of 2% Pd Ceria XANES with temperature during reduction in hydrogen. Diagram shows the local structures for palladium oxide to palladium metal.

At the end of the reduction the material undergoes very few changes; the extra peaks in the region from 3198-3210 and 3216-3238 eV remain. However the region between 3177-3192 eV, which previously showed peaks for the Pd hydride, and Pd metallic phases now contains no features. The reasons for this are unknown at this time, though it may be due to the interactions between Pd and ceria. The lack of the hydride features could be interpreted as a lack of hydride formation, however there is clearly a reduction in the material as evidenced by

the change in whiteline intensity. The lack of the extra features for the metallic phase could therefore indicate either an incomplete reduction or a different electronic structure caused by overlap between the orbitals of Pd and the oxygens bonded to Ce that does not occur for the other supports.

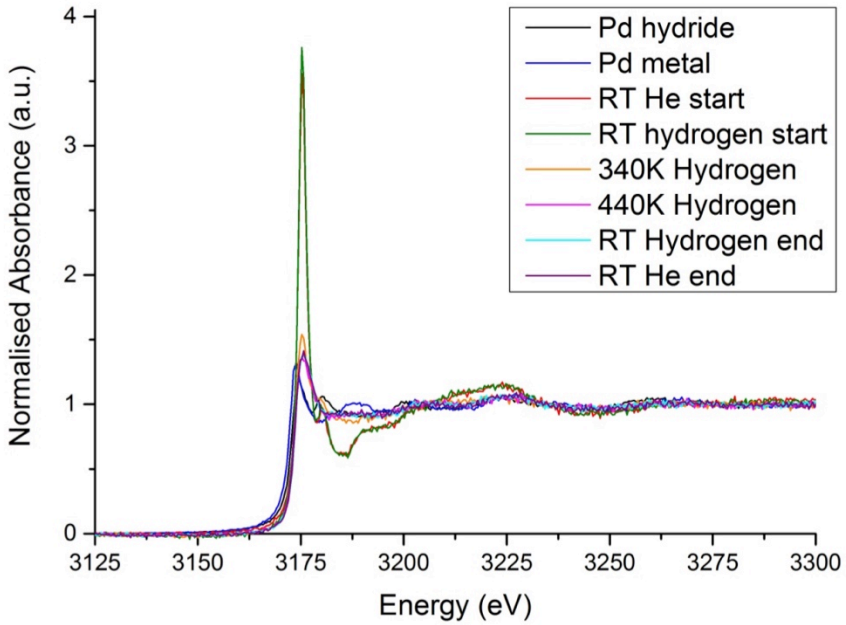

Figure 3-26 - 2% Pd/ceria at various stages through the reduction in helium and hydrogen, compared with Pd hydride and metal standards.

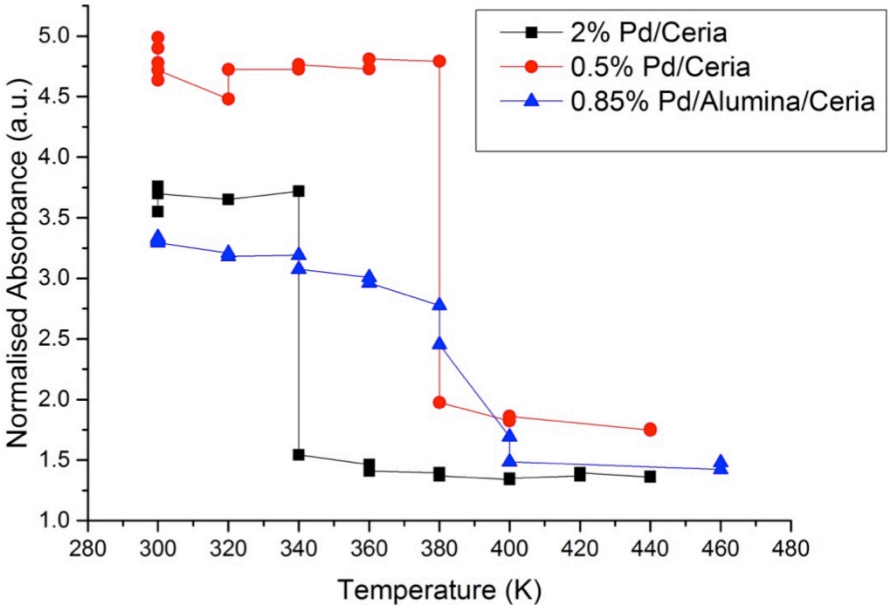

Figure 3-27 - Comparison of the change in whiteline intensity of Pd nanoparticles supported on Ceria.

The ceria supported Pd shows a number of changes compared to the alumina and fumed silica examples. The strong interactions widely reported in the literature will have an effect on the

XANES observed. The stronger interaction could lead to incomplete reduction or to the formation of an intermediate not seen for the other supports. This may prove to be a limitation of using the L_{III}-edge to determine the differences between hydride metallic and oxidic phases for Pd/Ceria samples.

Comparison of the whiteline intensity for the supported ceria materials shows that the reduction occurs at different temperatures with the 0.5 % Pd/ceria catalyst reducing at 380 K and the 2 % Pd/ceria catalyst reducing at the lower temperature of 340 K (Figure 3-27). This may be related to the amount of Pd deposited as the 0.85% Pd/ceria/alumina sample demonstrates a similar reduction temperature to the 0.5 % catalyst.

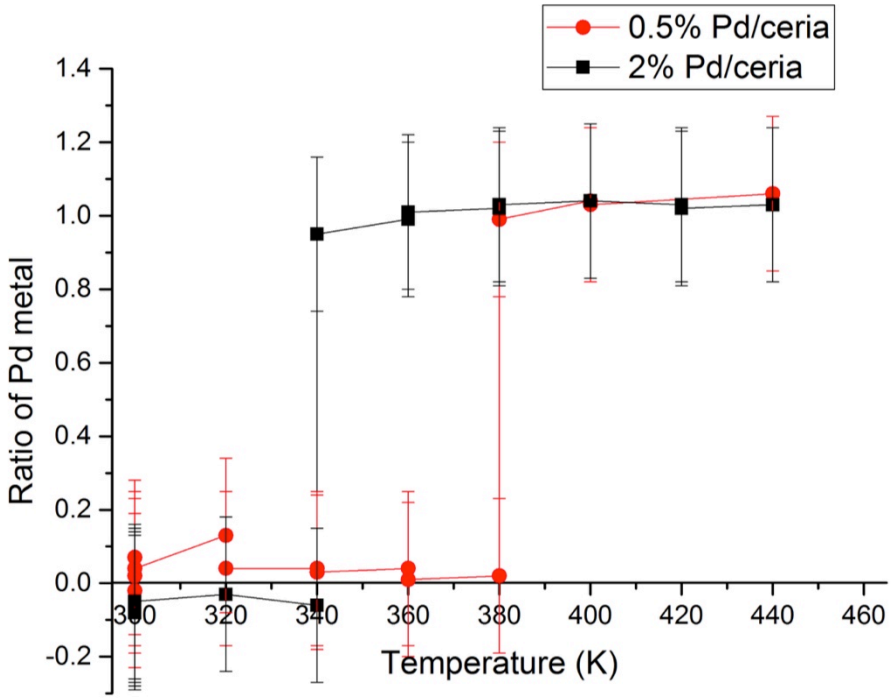

Figure 3-28 - Ratio of Pd metal formed during the reduction for the Ceria supported catalysts.

The change in the amount of Pd metal formed during the reduction can be followed using the whiteline intensity as a guide (Figure 3-28). The figure shows that the 0.5% Pd reduces at higher temperature than the 0.5% loaded catalyst, which reduces at 340 K compared to 380 for the 2% loaded material; this is similar to what is observed for the 0.5% Pd/alumina. This appears to indicate that the percentage loading of the Pd has an effect on the reduction temperature. Whether this is due to particle size, dispersion or increased interaction with the support, is inconclusive at this point.

Table 3-8 - Comparison of the change in whiteline intensity and edge position for the reduction of 2% Pd/Ceria.

Temperature (K)	Gas	Whiteline Intensity	Edge Position (at 0.6 na)
300	He	3.56	3172.85
300	He	3.59	3172.85
300	He	3.63	3172.85
300	He	3.55	3172.85
300	H_2/He	3.76	3172.86
300	H_2/He	3.73	3172.89
300	H_2/He	3.72	3172.86
300	H_2/He	3.70	3172.88
320	H_2/He	3.65	3172.89
320	H_2/He	3.65	3172.87
340	H_2/He	3.72	3172.89
340	H_2/He	1.54	3173.1
360	H_2/He	1.46	3173.01
360	H_2/He	1.41	3172.96
380	H_2/He	1.40	3172.93
380	H_2/He	1.37	3172.98
400	H_2/He	1.34	3172.97
400	H_2/He	1.35	3172.97
420	H_2/He	1.37	3172.97
420	H_2/He	1.40	3172.97
440	H_2/He	1.36	3172.97
440	H_2/He	1.37	3172.97
300	H_2/He	1.36	3172.95
300	H_2/He	1.37	3172.94
300	H_2/He	1.42	3173.14
300	H_2/He	1.37	3173.16
300	H_2/He	1.42	3173.16
300	H_2/He	1.40	3173.21
300	H_2/He	1.41	3173.1
300	H_2/He	1.41	3173.12

3.8.3.3 0.85% Pd/Ceria/Alumina

This sample was prepared via a two step deposition first of Pd on alumina which was followed by a second deposition of 15% Ceria.[68] The idea behind this process was to limit the sintering of Pd on an alumina support by adding a ceria overlayer and in doing so improve the stability and catalyst lifetime of the material.[69]

During the room temperature scans in helium, and at the beginning of the reduction process, the material looks very similar to previous scans for the alumina samples (Figure 3-29). This includes the twin extra peaks in the region between ca 3185-3190 and 3191-3197 eV. As these peaks are also seen for the Pd/silica supported material it is likely that they are caused by the reduction of the Pd.

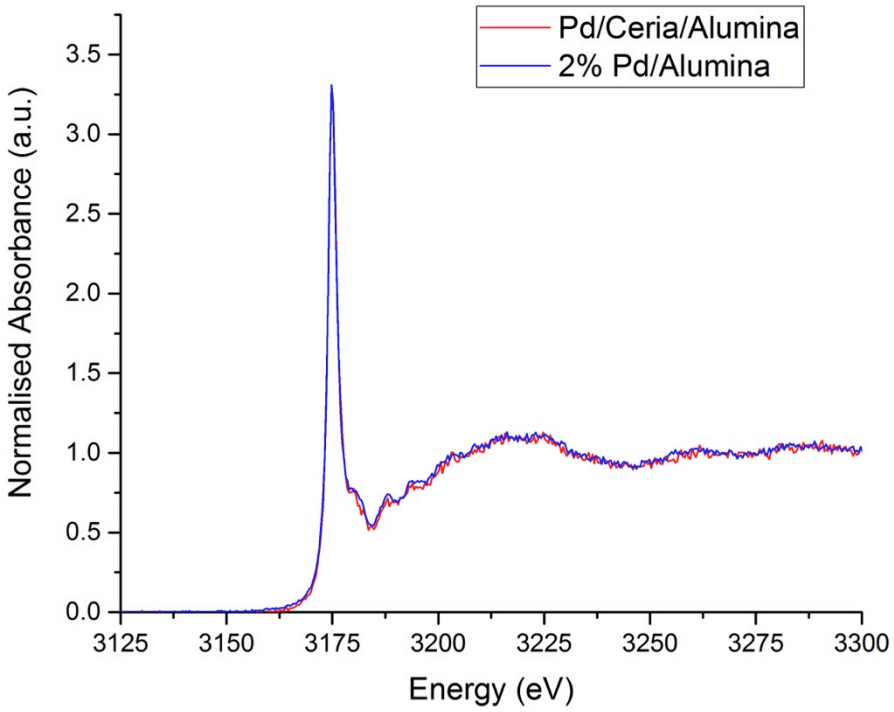

Figure 3-29 - XANES comparison of 2% Pd Alumina with the Pd/Ceria/Alumina sample at room temperature in H_2.

The sharp shoulder feature from the ceria measurements is also present in this dataset, though it is not as well defined as in the pure ceria supported spectra. Upon introduction of hydrogen there is no initial change in the material (Figure 3-30). Indeed at the end of the room temperature reduction the material still looks very similar to the initial starting material.

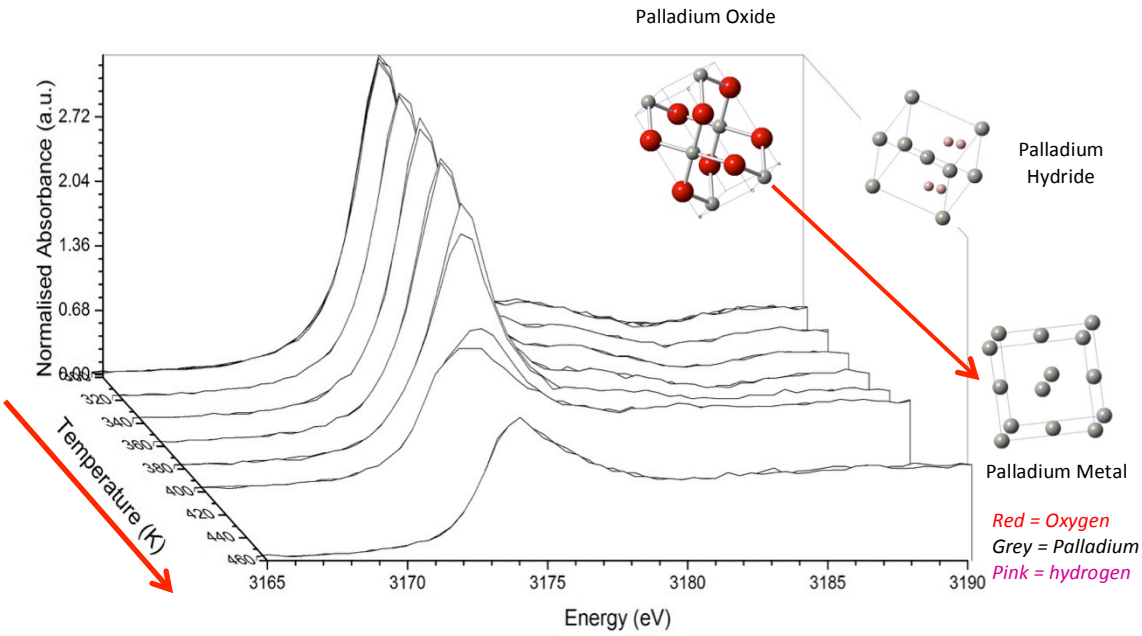

Figure 3-30 - Pd ceria alumina sample XANES plots against temperature during reduction in hydrogen. Diagram shows the local structures for palladium oxide to palladium metal.

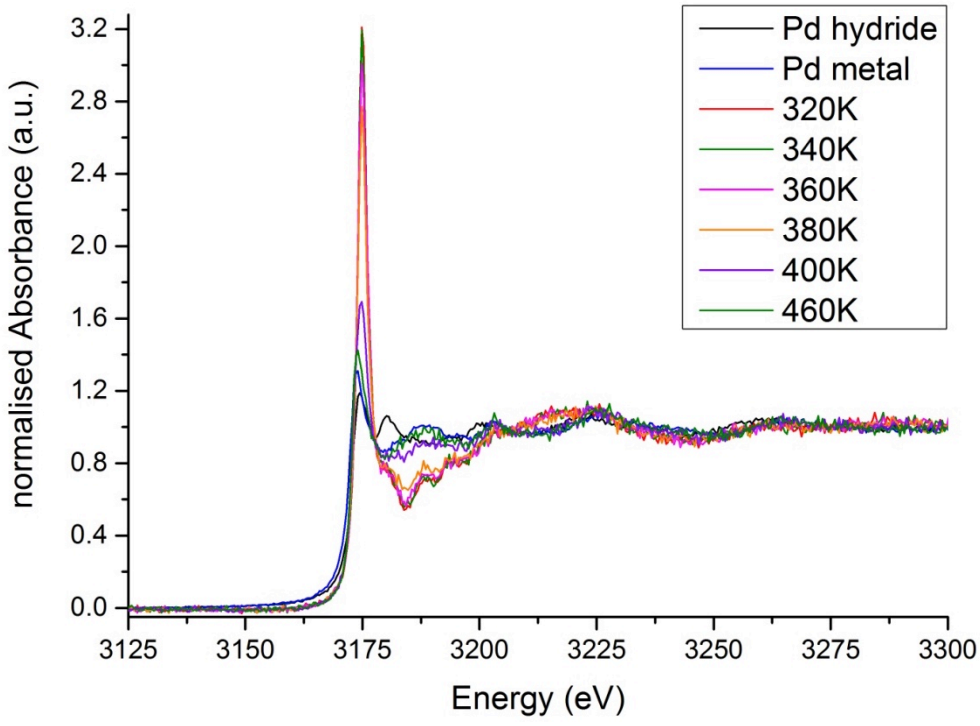

Figure 3-31 – XANES data for the reduction ramp of Pd/ceria/Alumina sample compared to standards.

The reduction begins at around 360K as evidenced by the decrease in the whiteline intensity from ca, 3.22 to 2.77 (Figure 3-27 and Figure 3-31). The whiteline intensity continues to

decrease until reaching a minimum around ca, 1.4 at a temperature of 460K. Values for the change in the whiteline intensity are given in Table 3-9.

During the reduction process and temperature ramp there is no hydride phase visible. However upon cooling to room temperature in hydrogen, the peak between 3178-3185eV, which is characteristic of Pd hydride appears. This peak then disappears after the reaction chamber is flushed with helium. This shows that although initially the hydride phase is not formed upon cooling back to room temperature in hydrogen it is observed. This seems to indicate that the reduction of the material alters the accessibility of the Pd particles on the surface of the material.

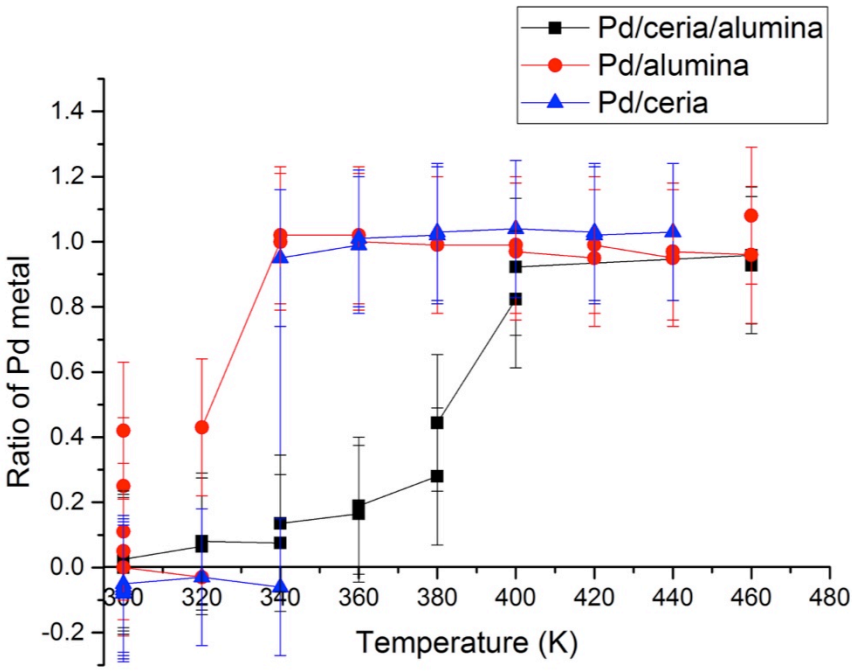

Figure 3-32 Ratio of Pd metal formed during the reduction for the Pd/ceria/alumina catalyst compared with the 2% Pd/alumina and 2% Pd/ceria catalysts

Comparison of the ratio of Pd metal formation during reduction for the Pd/ceria /alumina material and the alumina and ceria supported materials shows it has a different reduction rate (Figure 3-32). Where as the 2% alumina and ceria supported Pd catalysts reach full reduction at the lower temperatures of 340K, the Pd/ceria/alumina catalyst reaches complete reduction at 400 K. Further more the reduction whilst the reduction begins at 340 K it proceeds at a slower rate than the other samples, with the amount of Pd reduced increasing by 20% per step. The reduction of the Pd/ceria/alumina therefore does not match with either the 2% ceria and alumina supported Pd and has a different rate of reduction to the 0.5%, loaded catalysts.

This shows that there is another effect at work, likely the SMSI, arising from the added ceria overlayer.

Table 3-9 - Change in whiteline intensity and edge position for the reduction of 0.85%Pd/15%Ceria/Alumina.

Temperature (K)	Gas	Whiteline Intensity	Edge Position (at 0.6 na)
300	He	3.30	3172.63
300	He	3.37	3172.58
300	He	3.37	3172.52
300	He	3.32	3172.59
300	H_2/He	3.33	3172.53
300	H_2/He	3.31	3172.6
300	H_2/He	3.34	3172.58
300	H_2/He	3.29	3172.62
320	H_2/He	3.21	3172.62
320	H_2/He	3.18	3172.65
340	H_2/He	3.19	3172.63
340	H_2/He	3.07	3172.62
360	H_2/He	3.01	3172.55
360	H_2/He	2.96	3172.51
380	H_2/He	2.78	3172.49
380	H_2/He	2.45	3172.41
400	H_2/He	1.69	3172.35
400	H_2/He	1.49	3172.33
460	H_2/He	1.42	3172.29
460	H_2/He	1.48	3172.26
300	H_2/He	1.30	3172.69
300	H_2/He	1.33	3172.69
300	H_2/He	1.30	3172.76
300	He	1.29	3172.74
300	He	1.36	3172.33
300	He	1.43	3172.28

3.9 K-edge Analysis

Materials were then pressed into pellets using fumed silica to make up to 200mg and loaded into the cell, which was borrowed from Dr Andrew Smith at Daresbury Laboratory. The cell has a sealed chamber containing the pellet holder with heating elements and gas inlets and outlets for flowing gases over the sample (Figure 3-3). The sample holder was then mounted in a sealed vessel, which was pumped full of helium to limit the absorption of X-rays due to air (Figure 3-4). This included extending the beampipe and keeping it under He atmosphere to ensure the data quality was not impinged. A similar set-up was used for both K- and L_{III}-edge measurements, however the extended beampipe was removed for the K-edge studies (Figure 3-4).

3.9.1 K-edge XANES

3.9.1.1 PdO + Fumed Silica

The PdO fumed silica sample reduction is clearly viewed from the change in the edge feature from a single to a double peak (Figure 3-33). There is little indication on the K-edge of hydride formation and no difference can be seen between the material at the end of the reduction at room temperature in hydrogen or in helium; where we know from the L_{III}-edge analysis that a Pd hydride phase was observed.

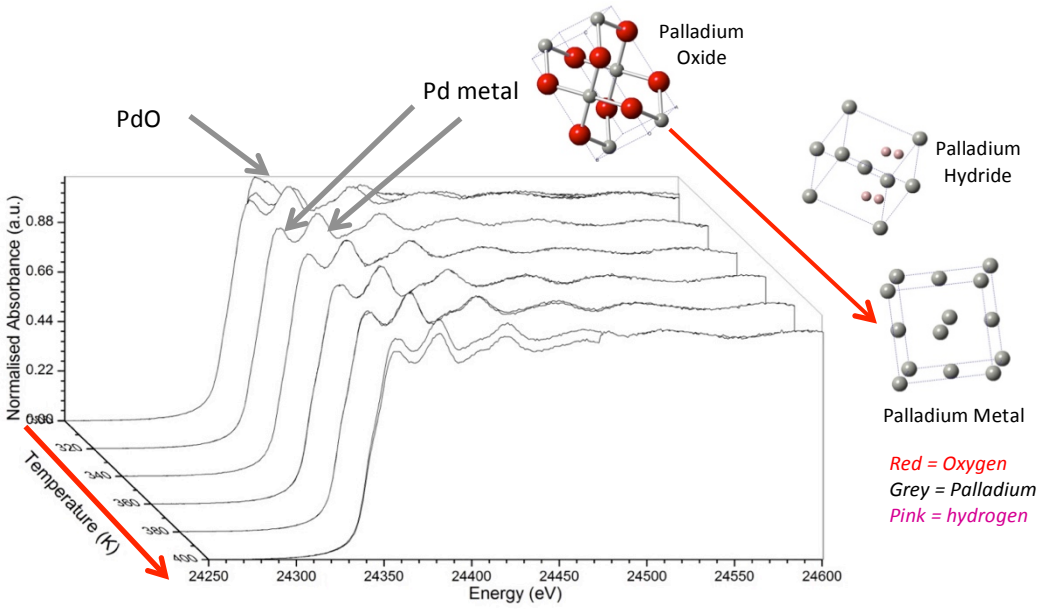

Figure 3-33 - Pd fumed silica K-edge XANES against temperature during reduction in hydrogen. Diagram shows the local structures for palladium oxide to palladium metal.

This is due to the K-edge measurements being generated by transitions from the core s-orbital, whereas the data on the L_{III} –edge is from transitions from the p-orbital. This means that excitations on from L_{III}-edge measurements can interact directly with the bonding orbitals and detect the presence of the hydrogen due to perturbations in the electronic structure of these orbitals.[6]

3.9.1.2 2% Pd/Silica

The reduction of the 2% Pd/silica sample occurs virtually as soon as the hydrogen enters the reaction chamber at room temperature (Figure 3-34). There is a difference in the intensity of the post edge features, with the PdO + fumed silica sample having more intense oscillations than the 2% Pd/silica. This is theorised to be due to the nature of the supported Pd particles having an altered electronic structure compared to the unsupported material. It is not a vast change but enough to be visible in the EXAFS region, which is sensitive to changes in the local structure. This is consistent with the previously observed results for Pd + fumed silica and the L_{III}-edge results for both Pd Silica samples. The ease of reduction from PdO to Pd is linked to the relatively weak interaction between Pd and the silica substrate.[50]

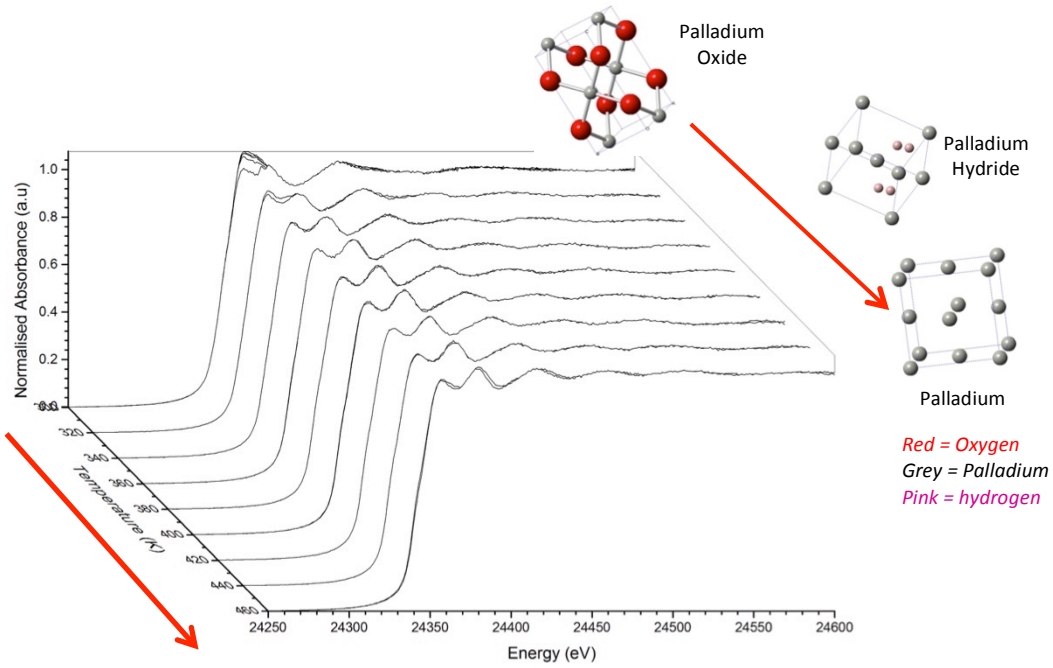

Figure 3-34 - 2% Pd silica K-edge XANES against temperature during reduction in hydrogen. Diagram shows the local structures for palladium oxide to palladium metal.

3.9.1.3 2% Pd/alumina

No reduction at room temperature is observed for the 2% Pd/alumina sample at room temperature (Figure 3-35). The data also shows a partial reduction at 320K as evidenced from the change in edge feature from a singlet to a shallow doublet. This occurs at 20K lower than observed on the Pd L_{III}-edge. Once the sample is at 340K it be said to be fully reduced from the XANES perspective. There is no further large change in the edge features or intensities. Upon cooling back to room temperature a small switching experiment was carried out, switching between hydrogen and helium in an attempt to create and remove the hydride phase. From the XANES all that can be determined is a small shift (about 1-2 eV) to lower energy when the sample was in hydrogen environment. Further analysis of the EXAFS region is needed to determine the significance of this; if there is an increase observed in the Pd-Pd bond distance in hydrogen atmosphere, that vanishes in He; it is a strong indicator of the formation of a Pd hydride phase.

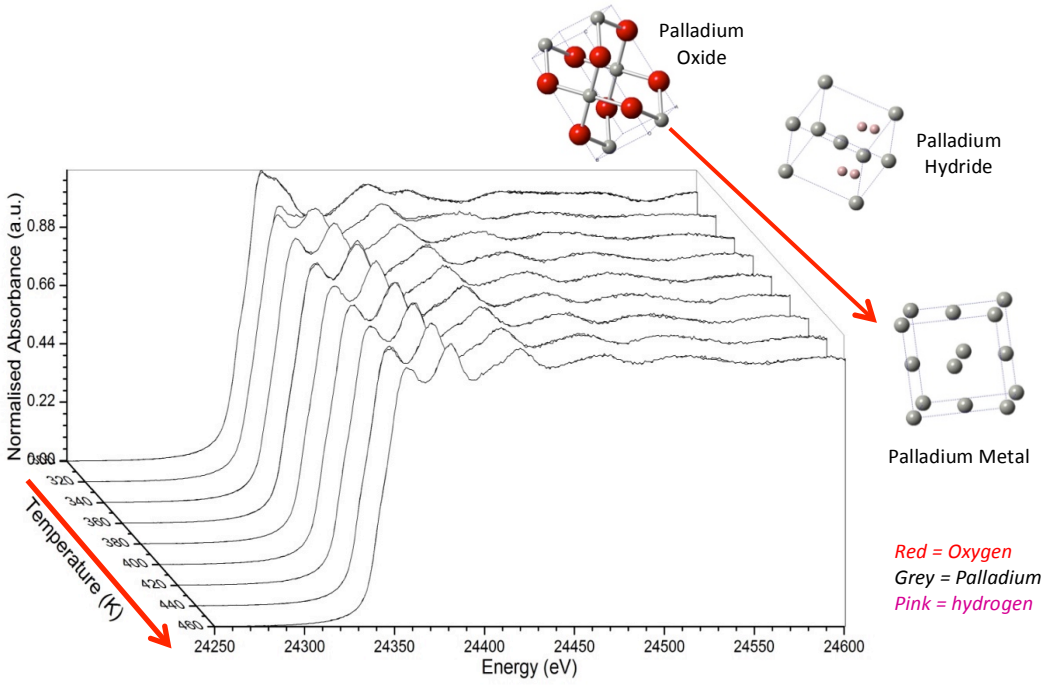

Figure 3-35 - 2% Pd Alumina K-edge XANES against temperature during reduction in hydrogen. Diagram shows the local structures for palladium oxide to palladium metal.

3.9.1.4 2% Pd/Ceria

The 2% Pd/ceria sample showed no reduction at room temperature in hydrogen (Figure 3-36). The material appears completely unchanged in the XANES, with no characteristic metallic Pd doublet formation observed.

Upon heating to 340K the sample begins to reduce, however the material does not appear to reduce completely. This can be inferred by the shape of the edge feature which rather than having a sharp doublet, indicative of Pd metal, has a shallow doublet. This may be due to support interactions between the Pd and the Ceria altering the shape of the peaks observed in the XANES. By 400K the doublet has much sharper and defined features, matching the expected shape for Pd metal. At the end of the reduction the room temperature scans in both He and H_2 show no differences in the XANES. This correlates well with the L_{III}-edge results in which no hydride was observed when reducing Pd/ceria supported catalysts.

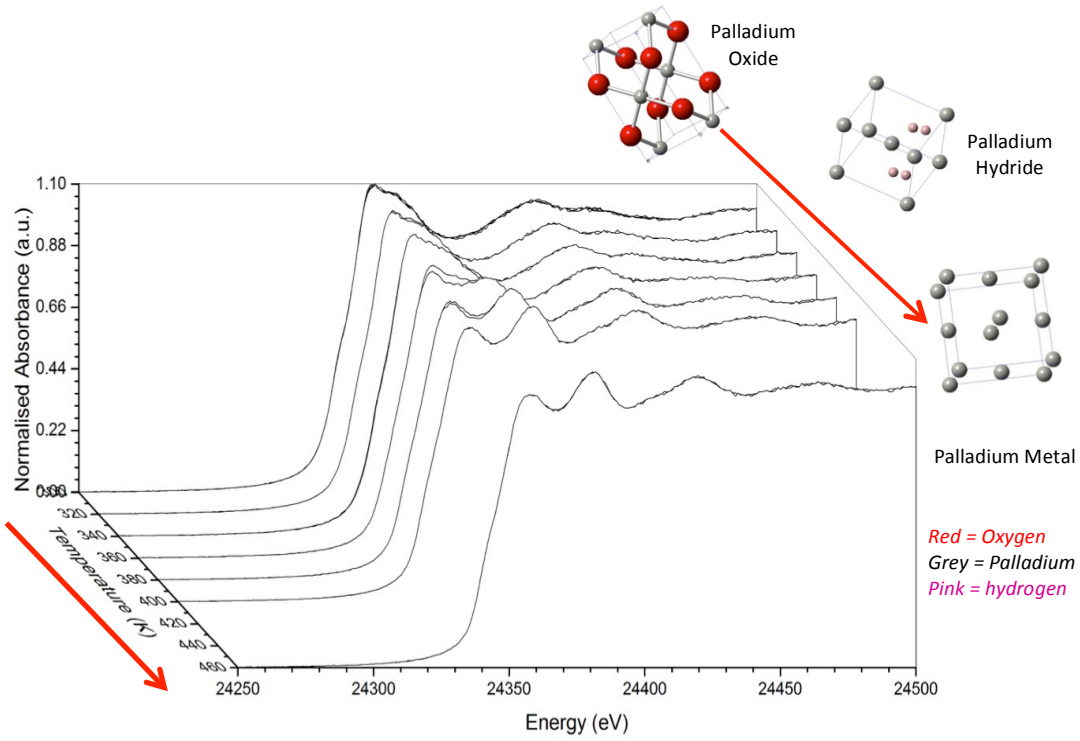

Figure 3-36 - 2% Pd ceria K-edge XANES against temperature during reduction in hydrogen. Diagram shows the local structures for palladium oxide to palladium metal.

3.9.1.5 0.85% Pd/Ceria/Alumina

The Pd/Ceria/Alumina catalyst shows no reduction at room temperature in hydrogen, consistent with the L_{III}-edge results and those previously observed for ceria-supported material (Figure 3-37). The sample begins to reduce at 340K, which is consistent with the results for ceria-supported material; full reduction appears to occur at the higher temp of 360K. The peaks are much sharper than those observed for the Pd/ceria material, which may indicate a difference in the nature of the Pd sites due to the ceria overlayer. For the Pd ceria sample the post edge oscillations were of smaller amplitude than those observed for the PdO and Pd/alumina samples. Here the shape of the oscillations is resembles the Pd/alumina rather than Pd/ceria.

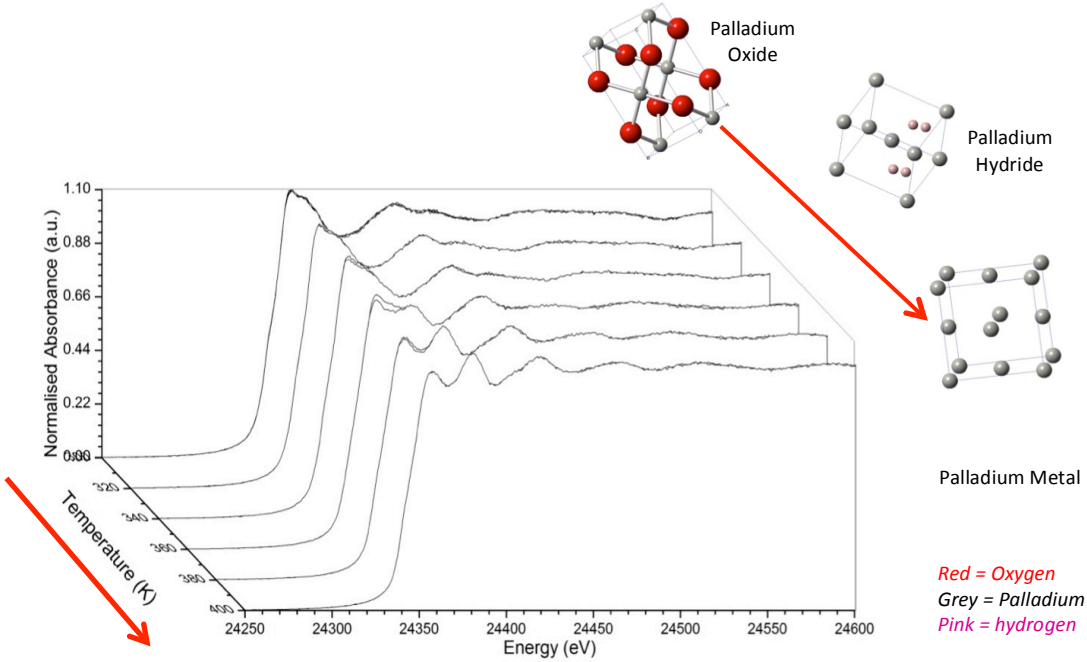

Figure 3-37 - 2% Pd alumina ceria K-edge XANES against temperature during reduction in hydrogen. Diagram shows the local structures for palladium oxide to palladium metal.

In all cases for the supported Pd catalysts there is no clear difference on the Pd k-edge between Pd hydride and Pd metallic phases. This serves to highlight the benefits of utilising the Pd L_{III}-edge for studying the reduction mechanisms of catalytic materials, as it enables the detection of other phases, in this case Pd hydride; additionally low loadings of Pd, down to at least 0.5%, can be observed. This is due to the interactions of the hydrogen atoms with the bonding orbitals of the Pd, an effect that cannot be seen on the K-edge due to the nature of the transitions. The advantage of using the K-edge is the ability to analyse the EXAFS region; combining the two edges promises to reveal more about the electronic and local structures of supported Pd catalysts.

A point of interest is the analysis of the data for the ceria-supported material, which was not as straightforward as the other supports used. This is possibly due to the nature of the material, or the strong interactions between the Pd and the support.

3.9.2 EXAFS Analysis

EXAFS analysis of the samples was performed using the first shells of PdO and Pd metal (Pd-O and Pd-Pd respectively), utilising Artemis software as outlined in chapter 2. A mixing parameter was added to the amp term in order to estimate the amount of each phase, oxide and metallic, present during the reduction. The Pd-Pd bond distance was one of the most important parameters to monitor, as this has been shown to increase depending on whether or not Pd hydride has been formed from 2.75 Å to 2.8 Å.[10,70] In order to help with visualizing the data, the various shells discussed are presented below. Figure 3-38 and Figure 3-39 are representative of the PdO first and second shells respectively, with the first shell consisting of oxygen nearest neighbours at a distance of 2 Å and the second shell composed of Pd atoms at a distance of 3 Å. Figure 3-40 and Figure 3-41 are diagrams of the first and second shells of Pd metal, both comprised of Pd atoms at distances of 2.75 Å for the first and 3.88 Å for the second shells. The Pd hydride structure, which features an expanded bond distance of 2.75 Å due to the presence of the Pd metal FCC caused by hydrogen in the lattice, is provided in Figure 3-42.[14] Details of bond distances, coordination numbers and other details are provided in Table 3-10 for PdO and Figure 3-40 for Pd metal.

The quality of the fits is determined by a number of factors, relying on just one can lead to error. The most important factor to consider id the R-factor, this is a statistical measure of the quality of the fit.[71,72] An overly large R-factor is usually an indicator that he fit is inaccurate. The other aspect is a visual comparison of the fit and the experimental data. Sometimes a fit with a good R-factor has little resemblance to the experimental data. Of course other parameters such as the bond distances and coordination numbers and disorder terms are also taken into account. Large differences in the bond distances (more than ± 0.7) indicate that the involved is either not present or heavily distorted.

Errors in the bond distance are calculated in the fitting model and reported in the tables for each material. The errors for the coordination number can be fitted a number of ways. For example the error for the error in the CN parameter used in the fitting model can be multiplied by the CN for the given shell to give a value, alternatively it can be used directly as the error. In this work the error for the CN was taken to be ± 10% as determined by the developers of the software.[71]

Table 3-10 - Scattering paths and details for PdO.

Shell	Scatterer	Bond distance (Å)	Coordination number
1	O	2.02	4
2	Pd	3.02	4
3	Pd	2.40	8

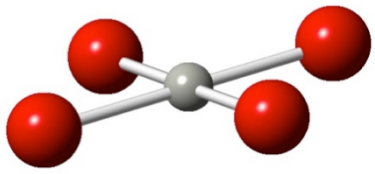

Figure 3-38 - Diagram of the first shell of PdO showing a palladium core, with 4 oxygen nearest neighbours at a distance of 2 Å.

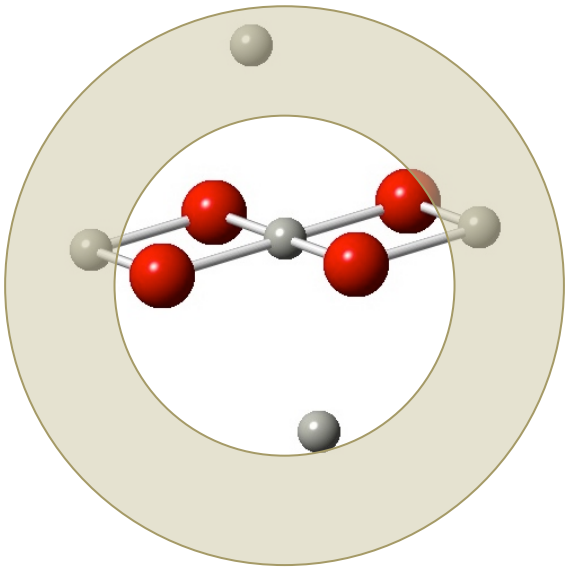

Figure 3-39 - Diagram showing the second shell of PdO, consisting of 4 Pd atoms at a distance of 3 Å.

Table 3-11 - Scattering paths and details for Pd metal.

Shell	Scatterer	Bond distance (Å)	Coordination number
1	Pd	2.75	12
2	Pd	3.88	6

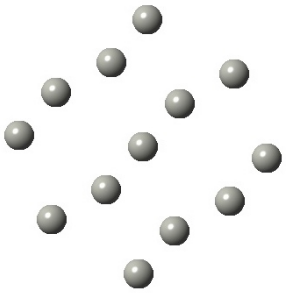

Figure 3-40 - Diagram showing the first shell of Pd metal, which has central Pd atom surrounded by 12 neighbouring Pd atoms at a distance of 2.75 Å.

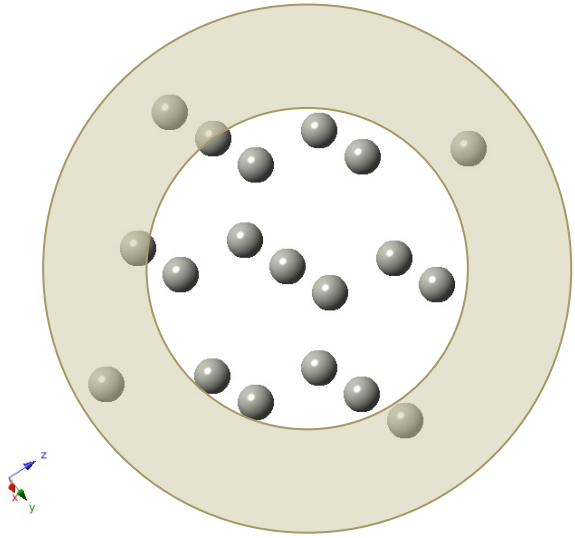

Figure 3-41 - Second shell of Pd metal showing 6 neighbouring Pd atoms at a distance of 3.88 Å.

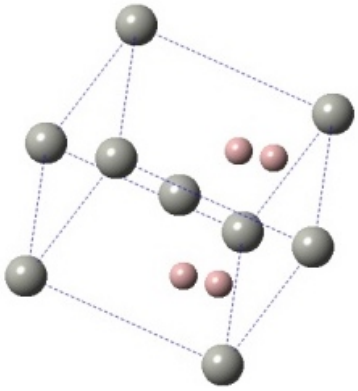

Figure 3-42 - FCC structure of Pd metal showing the hydrogen locations for the Pd hydride phase.

3.9.2.1 PdO + fumed silica (physical mixture)

The full table of values, including the R-factors for the statistical fit quality, are given in Table 3-12. An example of the physical mixture of PdO and fumed silica fits in k-space and the Fourier transforms at room temperature are in Figure 3-43. The plots show the quality of the fitting model for the first shells of PdO and Pd metal with the experimental data in the k-range of 2.5-10 $Å^{-1}$ and R-range 1-4 Å. The data shows that at room temperature the PdO is almost fully reduced at room temperature. The main peak at 2.8-3 Å is due to Pd-Pd from Pd metal. There is a peak at 3.75 Å, which may be due to a higher shell from the oxide, however it may also be caused by background noise, or by a higher shell from Pd metal. The magnitude of this peak decreases steadily during the reduction, from an initial value of 9 at 300 K to 5.5 at the end of the reduction. This is an indication of a decrease in the coordination number (CN) of the Pd-Pd shell.

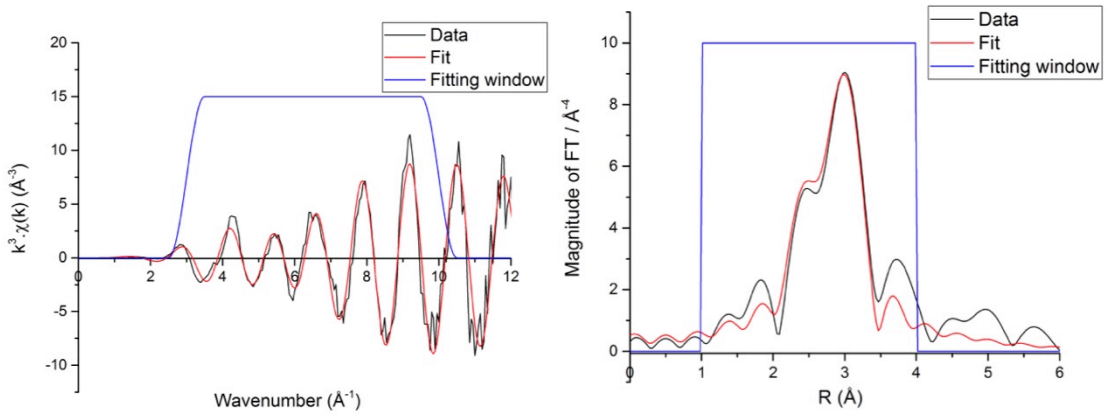

Figure 3-43 - Plot of the k^3 weighted data (left) and the Fourier transform (right) for PdO + fumed Silica sample at 300K in H_2.

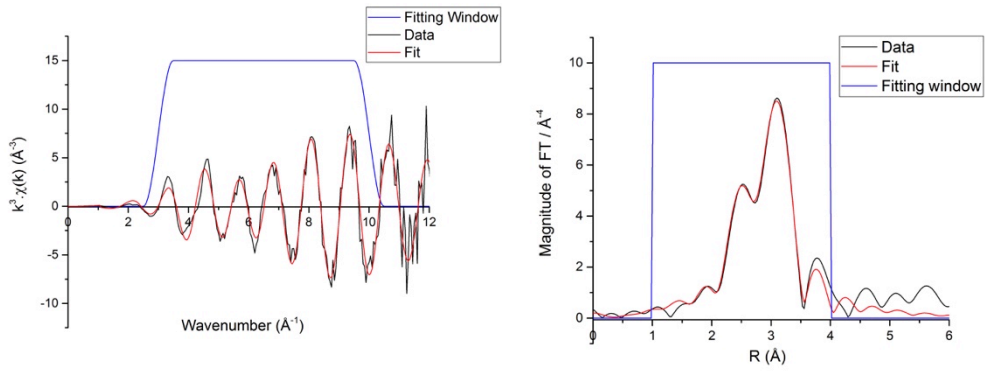

Figure 3-44 - Plot of the k^3 weighted data (left) and the Fourier transform (right) for PdO + fumed Silica sample at 460K in H_2.

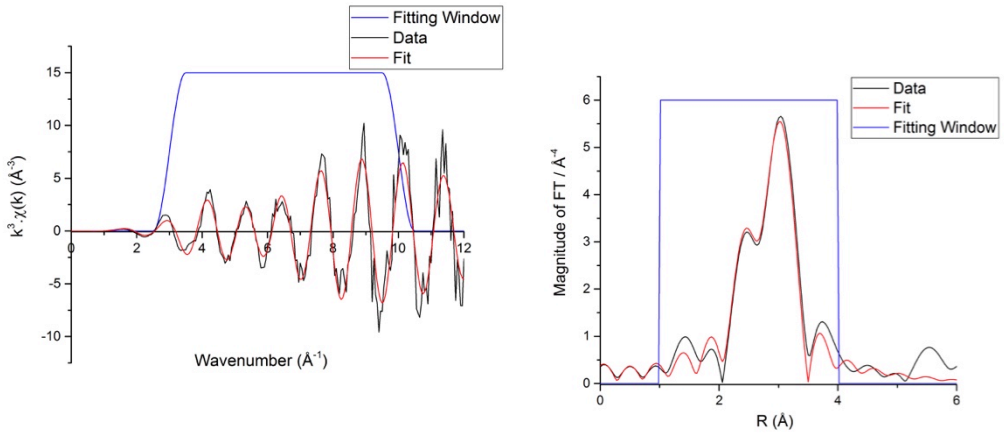

Figure 3-45 - Plot of the k^3 weighted data (left) and the Fourier transform (right) for PdO + fumed Silica sample at 300K after reduction in H_2.

The fit quality has been maintained at higher temperatures up to 460K (Figure 3-44) and upon cooling back to 300K (Figure 3-45). The magnitude of the main peak decreases steadily from the initial value of ca, 9 at 300 K to 7 at the end of the reduction process. As the magnitude of the peaks in the Fourier transform are related to the degeneracy of the shells, it indicates that there is a change occurring; however it may also be affected by the increasing temperature.

EXAFS fitting can provide a more detailed look at the change in the CN for the shells (Figure 3-46). For the fumed silica sample the Pd-O coordination number (CN) drops at room temperature, which is in agreement with the results from the XANES analysis that the material reduces at room temperature. The CN, determined through EXAFS fitting, for the Pd-Pd shell raises rapidly at room temperature from 6 though to 8 and remains this value for the remainder of the reduction; this is lower than the literature value of 12 for the Pd-Pd first shell perhaps indicating the formation of smaller Pd particles (Figure 3-46). The fitting model used in this analysis, assumed the initial scans in He to be pure PdO and subsequent scans in H_2 had the Pd-Pd shell added due to improved fit quality. Scans above room temperature were fitted as pure Pd metal as the contributions from the Pd-O shell were minimal.

The change in the bond distance is the biggest indicator on the K-edge of hydride formation. Incorporation of hydrogen into the Pd structure results in an increase of the bond distance; this has been reported in the literature.[14] The bond distance for the Pd-Pd shell is 2.85 Å at room temperature that is significantly higher than the expected value of 2.75 Å (Figure 3-47). Although the bond distance drops to the expected value, subsequent cooling in H_2 it raises to 2.85 Å again, indicating a reformation of the Pd hydride phase.

Table 3-12 - EXAFS results for the PdO + fumed silica physically mixed sample.

			Pd Oxide PdO								Pd metal PdPd							
Gas	Temperature (K)	R-factor	x	error	CN	Error	S02	σ2	R	Error	x	error	CN	Error	S02	σ2	R	Error
He	300	0.0398	0.65	0.09	2.61	0.26	0.57	0.0011	2.03	0.04	0	-	0.00	0.00	-	-	-	-
He	300	0.0369	0.62	0.08	2.50	0.25	0.54	0.0000	2.01	0.07	0	-	0.00	0.00	-	-	-	-
H2/He	300	0.0434	0.00	-	0.00	0.00	-	-	-	-	0.52	0.08	6.24	0.62	0.449	0.0055	2.74	0.01
H2/He	300	0.0277	0.00	-	0.00	0.00	-	-	-	-	0.65	0.12	7.84	0.78	0.564	0.0081	2.83	0.01
H2/He	300	0.0277	0.00	-	0.00	0.00	-	-	-	-	0.67	0.08	8.01	0.80	0.577	0.0071	2.84	0.09
H2/He	300	0.0100	0.00	-	0.00	0.00	-	-	-	-	0.71	0.04	8.47	0.85	0.61	0.0079	2.84	0.09
H2/He	320	0.0413	0.00	-	0.00	0.00	-	-	-	-	0.69	0.07	8.31	0.83	0.598	0.0079	2.83	0.09
H2/He	340	0.0299	0.00	-	0.00	0.00	-	-	-	-	0.69	0.06	8.27	0.83	0.595	0.0087	2.82	0.09
H2/He	340	0.0311	0.00	-	0.00	0.00	-	-	-	-	0.70	0.06	8.42	0.84	0.606	0.0085	2.83	0.09
H2/He	360	0.0088	0.00	-	0.00	0.00	-	-	-	-	0.69	0.04	8.29	0.83	0.597	0.0070	2.74	0.09
H2/He	360	0.0337	0.00	-	0.00	0.00	-	-	-	-	0.66	0.07	7.87	0.79	0.566	0.0063	2.74	0.09
H2/He	380	0.0179	0.00	-	0.00	0.00	-	-	-	-	0.72	0.05	8.64	0.86	0.622	0.0079	2.75	0.09
H2/He	380	0.0155	0.00	-	0.00	0.00	-	-	-	-	0.74	0.05	8.93	0.89	0.643	0.0078	2.75	0.09
H2/He	400	0.0223	0.00	-	0.00	0.00	-	-	-	-	0.73	0.05	8.76	0.88	0.631	0.0084	2.74	0.09
H2/He	460	0.0069	0.00	-	0.00	0.00	-	-	-	-	0.74	0.03	8.91	0.89	0.641	0.0087	2.74	0.09
H2/He	300	0.0143	0.00	-	0.00	0.00	-	-	-	-	0.76	0.05	9.12	0.91	0.656	0.0091	2.74	0.09
H2/He	300	0.0257	0.00	-	0.00	0.00	-	-	-	-	0.66	0.06	7.88	0.79	0.567	0.0071	2.85	0.09

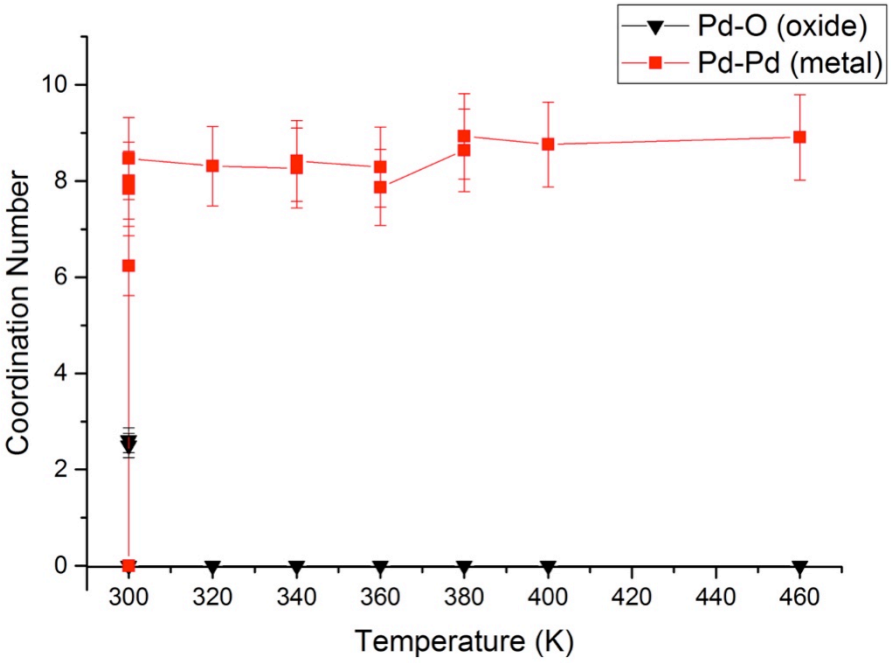

Figure 3-46 - Change in coordination number with temperature for Pd + fumed silica sample during reduction in hydrogen.

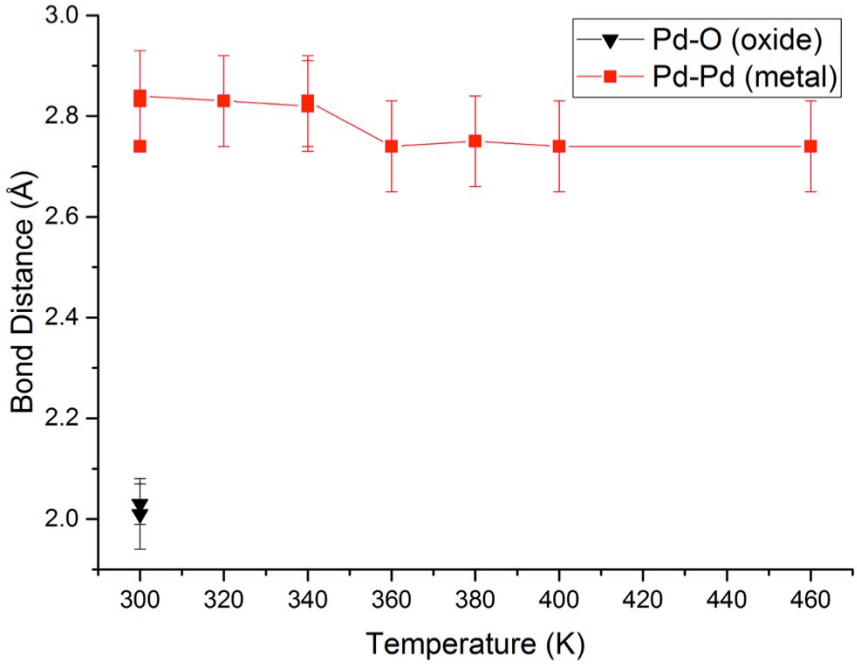

Figure 3-47- Change in bond distance with temperature for Pd + fumed silica sample during reduction in hydrogen.

3.9.2.2 2% Pd/Silica

Examples of the k^3-weighted data and the Fourier transforms of the EXAFS data are given in Figure 3-48, Figure 3-49, and Figure 3-50. The plots show the quality of the fitting model for the first shells of PdO and Pd metal with the experimental data in the k-range of 2.5-10 $Å^{-1}$ and R-range 1-4 Å. The data at 300 K shows a lot of noise at higher k values when compared to the PdO + fumed silica sample (Figure 3-48). At 460 K the magnitude of the main peak at ca, 3 Å (Pd-Pd) decreases to around 4 (Figure 3-49), and on cooling to room temperature the magnitude increases to ca 5.5 (Figure 3-50). These variations indicate that there is a change in coordination number around the Pd metal centres occurring. The full table of results is provided in Table 3-13.

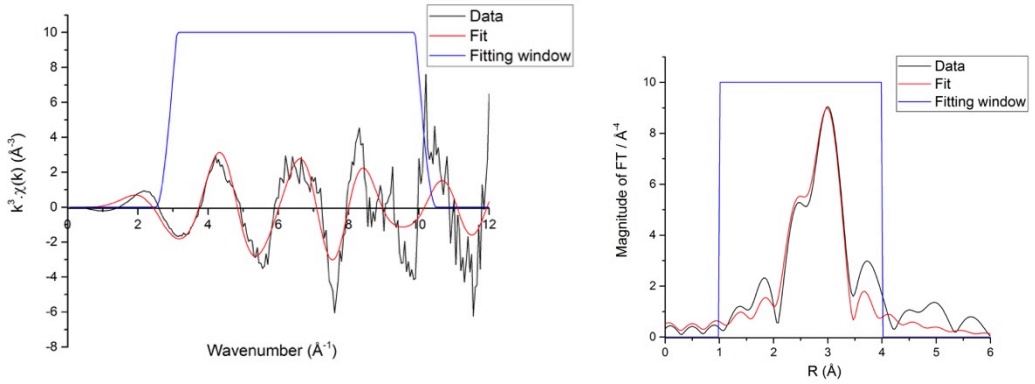

Figure 3-48 - Plot of the k^3 weighted data (left) and the Fourier transform (right) for 2% Pd/Silica sample at 300K in H_2.

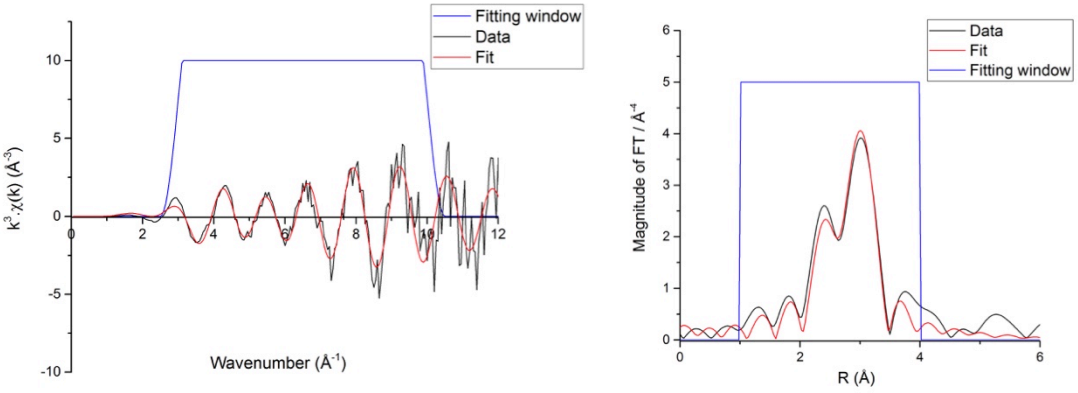

Figure 3-49 - Plot of the k^3 weighted data (left) and the Fourier transform (right) for 2% Pd/Silica sample at 460K in H_2.

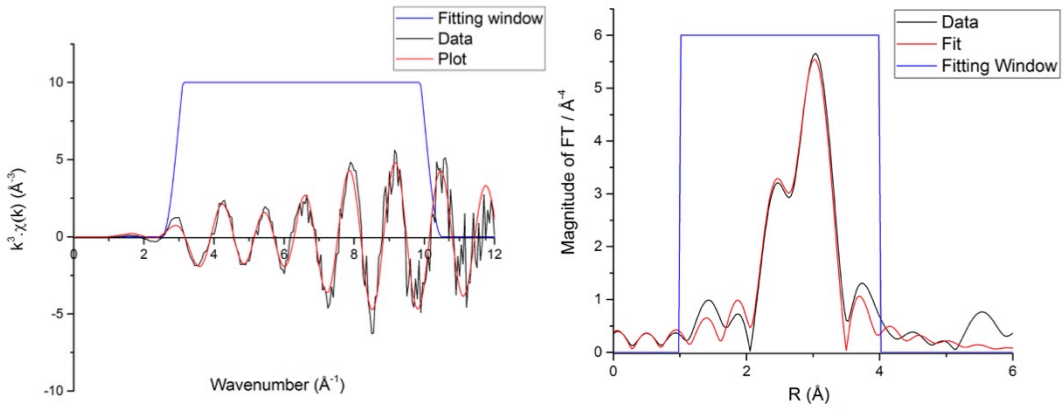

Figure 3-50 - Plot of the k^3 weighted data (left) and the Fourier transform (right) for 2% Pd/Silica sample at 300K at the end of reduction in H_2.

The 2%Pd/silica supported material was shown to match the fumed silica PdO model in terms of the change of bond distance and hydride formation (Figure 3-52). The bond distance increases from 2.75 Å to 2.8 Å in the presence of H_2 at room temperature. However the coordination numbers for the PdO and Pd phases are different, with the PdO coordination not dropping below 2 and the Pd metal coordination number not rising beyond 5.4 (Figure 3-51). This is in contrast to the findings from XANES on both the K- and L_{III}-edge, which seemed to indicate an almost total conversion to the metallic state, and to the physical mixture of PdO and fumed silica in which not only did the material reduce completely but also the CN for the Pd-Pd shell was higher in value. This would seem to suggest that chemical bonding to the silica surface results in a change in the reduction capabilities of the Pd particles. As the physically mixed silica and Pd catalyst was completely reduced it can be assumed that support effects are responsible for this change in reduction behaviour; or the altered behaviour arises through some action of deposition resulting in either smaller more accessible Pd particles or similar effects.

It could also be a problem with the fitting model, as both the Fourier transforms and the XANES show that the material should be almost pure Pd metal. The best way to confirm this would be to refit the data using the same fitting model as for the PdO + fumed silica physical mixture. For this sample it was not possible to fit as a mixture so the PdO path was removed. For the supported 2% Pd/silica sample the increased noise from arising from being supported may helped to include a of Pd-O path for longer than it was actually present.

Table 3-13 - EXAFS results for the 2% Pd/Silica sample for the reduction in H_2.

			Pd Oxide PdO								Pd metal PdPd							
Gas	mperature	R-factor	x	error	CN	Error	S02	σ2	R	Error	x	error	CN	Error	S02	σ2	R	Error
He	300	0.1451	0.97	0.0608	3.90	0.39	0.84	0.0071	2.01	0.04	0.03	0.06	0.31	0.03	0.02	-0.0023	2.68	0.04
He	300	0.1631	0.90	0.1399	3.61	0.36	0.78	0.0048	2.00	0.04	0.10	0.14	1.18	0.12	0.09	0.0104	2.66	0.07
H2/He	300	0.1394	0.94	0.1138	3.75	0.38	0.81	0.00531	1.98	0.03	0.06	0.11	0.74	0.07	0.05	0.0059	2.66	0.06
H2/He	300	0.0918	0.57	0.1444	2.29	0.23	0.50	0.00024	2.00	0.02	0.43	0.14	5.12	0.51	0.37	0.0616	2.89	0.25
H2/He	300	0.1257	1.00	0.0004	4.00	0.40	0.86	0.00967	2.02	0.04	0.00	0.00	0.00	0.00	0.00	-0.0389	2.77	0.04
H2/He	300	0.0530	0.81	0.0977	3.24	0.32	0.70	0.00841	1.98	0.02	0.19	0.10	2.28	0.23	0.16	0.0098	2.80	0.02
H2/He	320	0.0242	0.76	0.0478	3.04	0.30	0.66	0.01663	2.00	0.02	0.24	0.05	2.89	0.29	0.21	0.0074	2.81	0.01
H2/He	320	0.0459	0.65	0.0744	2.60	0.26	0.56	0.01894	2.00	0.02	0.35	0.07	4.21	0.42	0.30	0.0090	2.81	0.01
H2/He	340	0.0330	0.64	0.0622	2.55	0.25	0.55	0.02487	1.99	0.03	0.36	0.06	4.35	0.44	0.31	0.0076	2.79	0.01
H2/He	340	0.0459	0.65	0.0713	2.59	0.26	0.31	0.02698	2.00	0.03	0.35	0.07	4.24	0.42	0.31	0.0083	2.79	0.01
H2/He	360	0.0177	0.59	0.0510	2.37	0.24	0.51	0.03962	1.98	0.05	0.41	0.05	4.89	0.49	0.35	0.0085	2.76	0.01
H2/He	380	0.0451	0.58	0.0787	2.33	0.23	0.50	0.04158	1.95	0.08	0.42	0.08	5.00	0.50	0.36	0.0088	2.77	0.01
H2/He	380	0.0326	0.60	0.0674	2.42	0.24	0.52	0.04342	1.97	0.01	0.40	0.07	4.75	0.47	0.34	0.0080	2.74	0.01
H2/He	400	0.0172	0.57	0.0522	2.28	0.23	0.49	0.04534	1.99	0.06	0.43	0.05	5.17	0.52	0.37	0.0095	2.75	0.01
H2/He	420	0.0414	0.56	0.0789	2.23	0.22	0.48	0.03978	1.88	0.07	0.44	0.08	5.30	0.53	0.38	0.0097	2.75	0.01
H2/He	420	0.0459	0.65	0.0744	2.60	0.26	0.56	0.01894	2.00	0.10	0.35	0.07	4.21	0.42	0.30	0.0090	2.81	0.01
H2/He	440	0.0420	0.57	0.0753	2.27	0.23	0.49	0.04129	1.96	0.07	0.43	0.08	5.19	0.52	0.37	0.0115	2.74	0.01
H2/He	440	0.0344	0.56	0.0705	2.22	0.22	0.48	0.04432	1.88	0.10	0.44	0.07	5.33	0.53	0.38	0.0111	2.73	0.01
H2/He	460	0.0374	0.61	0.0648	2.44	0.24	0.53	0.05346	1.95	0.10	0.39	0.06	4.69	0.47	0.34	0.0095	2.74	0.01
H2/He	300	0.0271	0.56	0.0643	2.24	0.22	0.48	0.04111	1.99	0.10	0.44	0.06	5.29	0.53	0.38	0.0089	2.79	0.01
H2/He	300	0.0450	0.59	0.0774	2.37	0.24	0.51	0.05893	1.92	0.10	0.41	0.08	4.89	0.49	0.35	0.0076	2.79	0.01
He	300	0.0237	0.58	0.0611	2.32	0.23	0.50	0.06282	1.97	0.10	0.42	0.06	5.03	0.50	0.36	0.0069	2.78	0.01
He	300	0.0326	0.55	0.0734	2.21	0.22	0.48	0.05695	1.97	0.10	0.45	0.07	5.37	0.54	0.39	0.0078	2.76	0.01

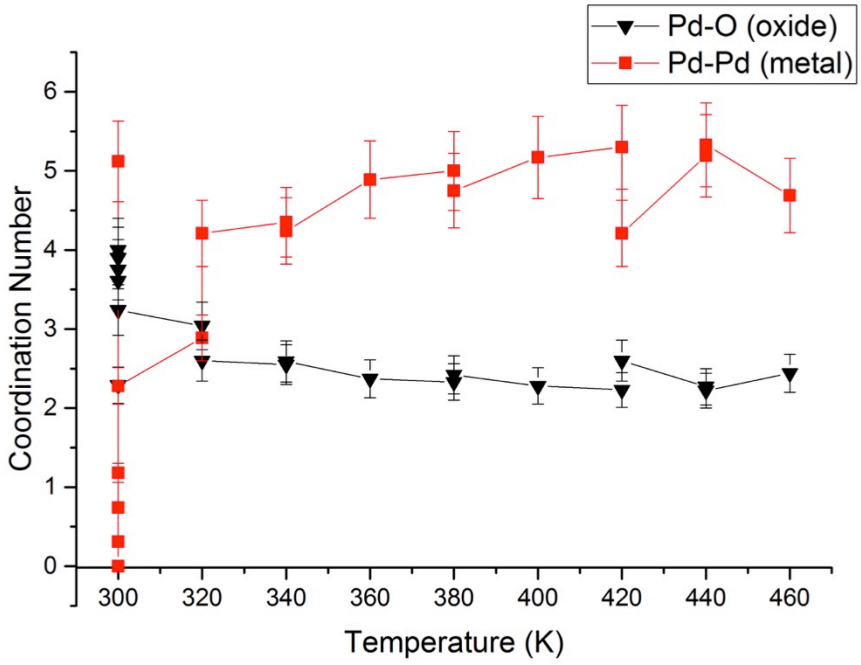

Figure 3-51 - Change in coordination number, from EXAFS fitting, with temperature for 2% Pd silica.

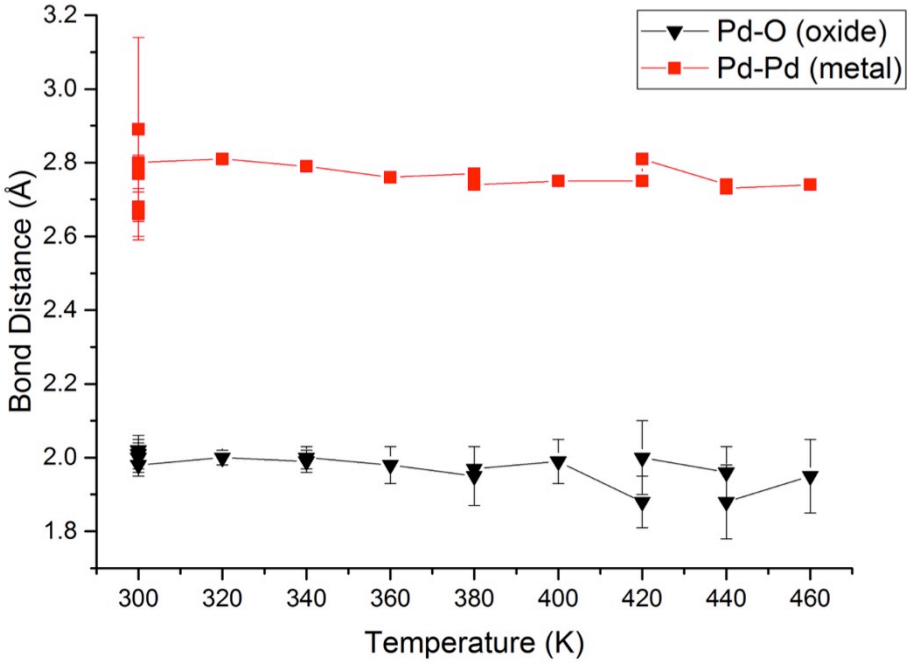

Figure 3-52 - Change in bond distance, from EXAFS fitting, with temperature for 2% Pd silica.

3.9.2.3 2% Pd/alumina

An example of the data at the beginning of the reduction at 300 K is given in Figure 3-53. The plots show the quality of the fitting model for the first shells of PdO and Pd metal with the experimental data in the k-range of 2.5-10 $Å^{-1}$ and R-range 1-4 Å. The two peaks clearly indicate the presence of both Pd-O and Pd-Pd from the oxide at ca 1.98 Å and 3.5 Å respectively in hydrogen. By 460 K the material has been reduced to metallic Pd with the dominant peak at 2.7 Å being due to Pd-Pd in metallic phase (Figure 3-54). The intensity and sharpness of this peak increases on cooling back to room temperature, with the noise in k^3-weighted data shown to decrease (Figure 3-55). The full table of results for the EXAFS analysis is presented in Table 3-14.

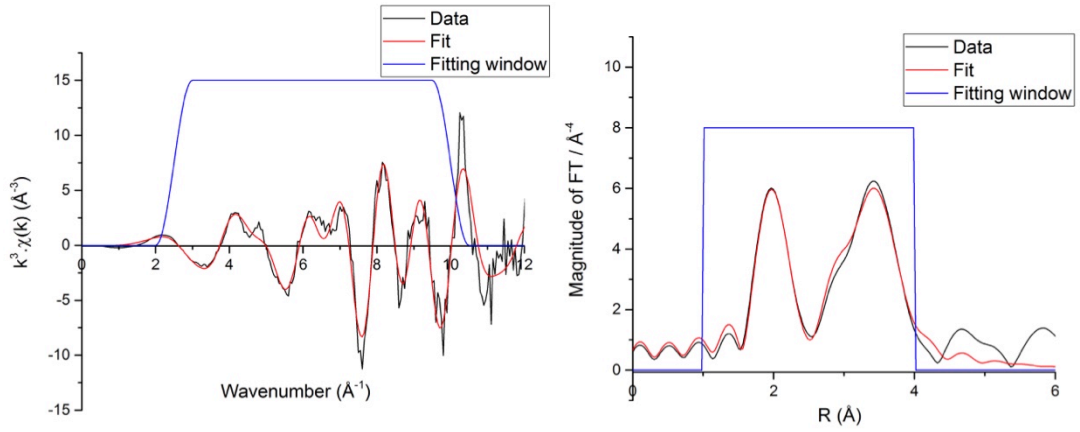

Figure 3-53 - Plot of the k^3 weighted data (left) and the Fourier transform (right) for 2% Pd/alumina sample at 300K in H_2.

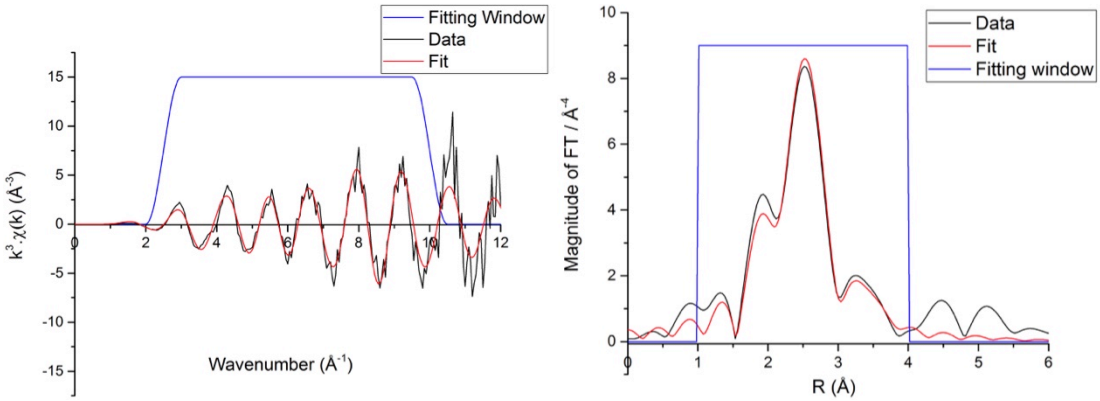

Figure 3-54 - Plot of the k^3 weighted data (left) and the Fourier transform (right) for 2% Pd/alumina sample at 460K in H_2.

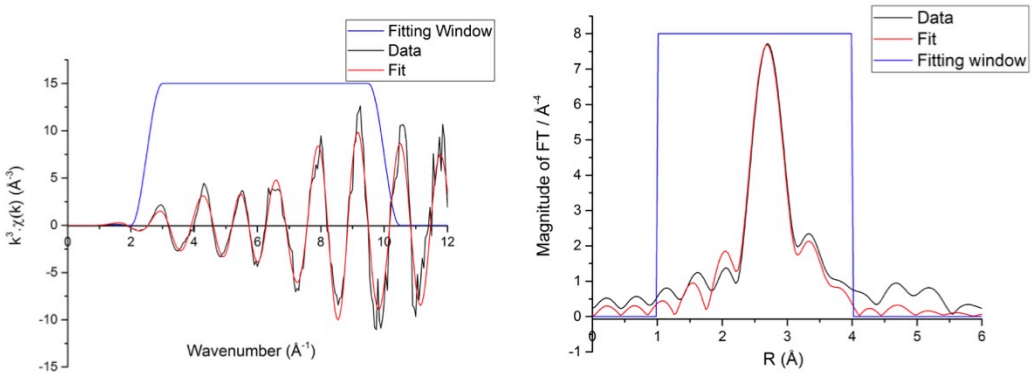

Figure 3-55 - Plot of the k^3 weighted data (left) and the Fourier transform (right) for 2% Pd/alumina sample at 300K at the end of the reduction in H_2.

Analysis of the coordination numbers shows that the Pd-Pd coordination number increases with increasing temperature and is accompanied by a decrease in the PdO from 4 to ca, 1 (Figure 3-56). The coordination number for the Pd-Pd shell rises steadily between 320-360 K. The CN then peaks at ca, 8, which is lower than the literature value of 12 for the Pd-Pd first shell; upon cooling back to room temperature this value remains at 8, indicating an almost complete reduction of the material. This contrasts with the 2% Pd/silica results, in which the palladium was not fully reduced. According to the fitting model complete reduction to the metallic state occurs by 360 K, which matches the results from the L_{III} – edge. It is worth noting that the CN for the Pd-O shell does not fall to zero.

The change in the Pd-Pd bond distance indicates that the Pd hydride phase is formed around 320 K and is removed by 360 K. Hydride formation is shown by an increase in the bond distance to 2.8 Å in the presence of hydrogen, a 0.05 Å increase on the literature value (Figure 3-57).[10] This change is matched by the observed difference in the L_{III}-edge for the whiteline intensity, showing consistency. The errors for the Pd-O shell increase dramatically beyond 360 K, providing an indication as to the reliability of the results due to the low amount of PdO in the sample. Subsequent dwelling in hydrogen at room temperature at the end of the reduction process leads to a reformation of the Pd hydride, indicated again by an increase in the Pd-Pd bond distance. The Pd hydride can be created and removed simply by altering the gas environment. Dwelling in He leads to a removal of the hydride phase, whilst switching back to H_2 allows for the incorporation of hydrogen into the support once more. This result is used to support the findings of this investigation that dwelling in hydrogen rich environment leads to Pd hydride formation and this can be directly observed with L_{III}-edge XANES and Pd K-edge EXAFS.

Table 3-14 - EXAFS results for the 2% Pd/alumina material during reduction in H_2.

			Pd Oxide PdO								Pd metal PdPd							
Gas	Temperature (K)	R-factor	x	error	CN	Error	S02	σ2	R	Error	x	error	CN	Error	S02	σ2	R	Error
He	300	0.3223	0.99	0.0466	3.96	0.40	0.86	0.0033	2.02	0.06	0.01	0.05	0.13	0.01	0.01	-0.0137	2.72	0.05
He	300	0.3610	0.99	0.0651	3.94	0.39	0.54	0.0000	2.01	0.06	0.01	0.07	0.17	0.02	0.01	-0.0114	2.72	0.05
H2/He	300	0.3577	0.99	0.0611	3.94	0.39	0.85	0.00291	2.02	0.06	0.01	0.06	0.17	0.02	0.01	-0.0120	2.71	0.05
H2/He	300	0.3665	0.98	0.0786	3.92	0.39	0.85	0.00278	2.02	0.06	0.02	0.08	0.24	0.02	0.02	-0.0099	2.71	0.05
H2/He	300	0.3884	0.98	0.0898	3.92	0.39	0.85	0.00272	2.02	0.07	0.02	0.09	0.25	0.02	0.02	-0.0092	2.72	0.06
H2/He	300	0.3645	0.99	0.0485	3.96	0.40	0.86	0.00393	2.03	0.07	0.01	0.05	0.12	0.01	0.01	-0.0141	2.73	0.05
H2/He	320	0.1610	0.62	0.2022	2.49	0.25	0.54	0.00739	1.98	0.03	0.38	0.20	4.52	0.45	0.54	0.0079	2.81	0.03
H2/He	320	0.0466	0.46	0.4000	1.85	0.19	0.40	0.0174	2.00	0.04	0.54	0.40	6.44	0.64	0.60	0.0087	2.82	0.01
H2/He	340	0.0410	0.51	0.0956	2.04	0.20	0.44	0.01951	2.00	0.04	0.49	0.10	5.87	0.59	0.42	0.0070	2.81	0.01
H2/He	340	0.0152	0.37	0.0712	1.50	0.15	0.32	0.02376	2.03	0.05	0.63	0.07	7.51	0.75	0.54	0.0086	2.82	0.01
H2/He	360	0.0181	0.40	0.0787	1.61	0.16	0.35	0.03765	1.98	0.11	0.60	0.08	7.16	0.72	0.52	0.0070	2.75	0.01
H2/He	360	0.0249	0.39	0.0937	1.56	0.16	0.34	0.03725	2.02	0.13	0.61	0.09	7.31	0.73	0.62	0.0069	2.75	0.01
H2/He	380	0.0193	0.37	0.0853	1.48	0.15	0.32	0.04062	2.00	0.14	0.63	0.09	7.55	0.75	0.54	0.0074	2.74	0.01
H2/He	380	0.0293	0.37	0.1032	1.47	0.15	0.32	0.03695	2.04	0.16	0.63	0.10	7.60	0.76	0.55	0.0068	2.74	0.01
H2/He	400	0.0313	0.34	0.1091	1.36	0.14	0.29	0.02908	2.02	0.11	0.66	0.11	7.91	0.79	0.57	0.0080	2.75	0.01
H2/He	400	0.0173	0.34	0.0861	1.37	0.14	0.30	0.02917	2.03	0.09	0.66	0.09	7.90	0.79	0.57	0.0077	2.75	0.01
H2/He	420	0.0414	0.38	0.1172	1.53	0.15	0.33	0.02223	2.03	0.08	0.62	0.12	7.41	0.74	0.53	0.0075	2.75	0.01
H2/He	420	0.0288	0.37	0.1040	1.46	0.15	0.32	0.04013	1.98	0.18	0.63	0.10	7.61	0.76	0.55	0.0073	2.75	0.01
H2/He	440	0.0171	0.35	0.0811	1.40	0.14	0.30	0.05299	1.92	0.24	0.65	0.08	7.80	0.78	0.56	0.0076	2.74	0.01
H2/He	440	0.0181	0.39	0.0805	1.58	0.16	0.34	0.02732	2.03	0.07	0.61	0.08	7.27	0.73	0.52	0.0074	2.75	0.01
H2/He	460	0.0321	0.30	0.1135	1.19	0.12	0.26	0.04165	2.04	0.22	0.70	0.11	8.43	0.84	0.61	0.0097	2.74	0.01
H2/He	460	0.0316	0.39	0.1027	1.58	0.16	0.34	0.02851	2.06	0.09	0.61	0.10	7.27	0.73	0.52	0.0073	2.75	0.01
H2/He	300	0.0256	0.35	0.0972	1.40	0.14	0.30	0.03118	2.13	0.11	0.65	0.10	7.80	0.78	0.56	0.0067	2.82	0.01
He	300	0.0162	0.30	0.0829	1.18	0.12	0.26	0.02531	2.16	0.09	0.70	0.08	8.45	0.84	0.61	0.0079	2.82	0.01
He	300	0.0291	0.37	0.1074	1.49	0.15	0.32	0.03528	1.99	0.15	0.63	0.11	7.53	0.75	0.54	0.0056	2.75	0.01
H2/He	305	0.0311	0.31	0.1079	1.25	0.13	0.27	0.02691	2.07	0.10	0.69	0.11	8.25	0.82	0.59	0.0078	2.82	0.01
H2/He	305	0.0206	0.33	0.0892	1.34	0.13	0.29	0.04462	2.05	0.19	0.67	0.09	7.99	0.80	0.58	0.0067	2.82	0.01
H2/He	300	0.0111	0.36	0.0655	1.44	0.14	0.31	0.04312	2.05	0.12	0.64	0.07	7.68	0.77	0.55	0.0064	2.83	0.01
H2/He	300	0.0200	0.31	0.0878	1.26	0.13	0.27	0.03273	2.07	0.11	0.69	0.09	8.23	0.82	0.59	0.0072	2.82	0.01
He	300	0.0138	0.34	0.0741	1.35	0.14	0.29	0.04141	2.07	0.13	0.66	0.07	7.95	0.79	0.57	0.0073	2.82	0.01
He	300	0.0221	0.38	0.0950	1.52	0.15	0.33	0.0337	2.08	0.13	0.62	0.09	7.43	0.74	0.54	0.0053	2.75	0.01
He	300	0.0190	0.33	0.0951	1.33	0.13	0.29	0.02953	2.03	0.12	0.67	0.10	8.00	0.80	0.58	0.0056	2.74	0.01

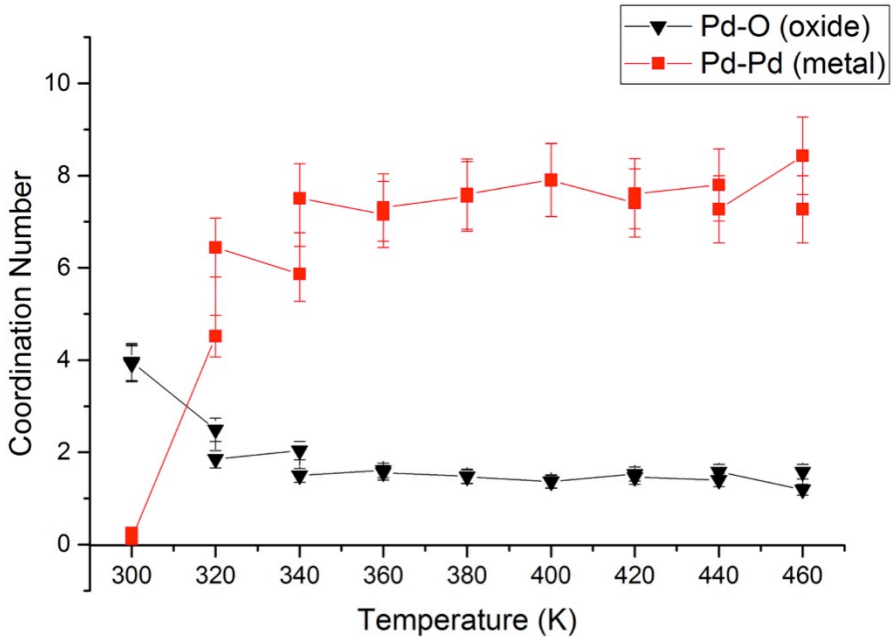

Figure 3-56 - Change in coordination number, from EXAFS fitting, with temperature for 2% Pd Alumina.

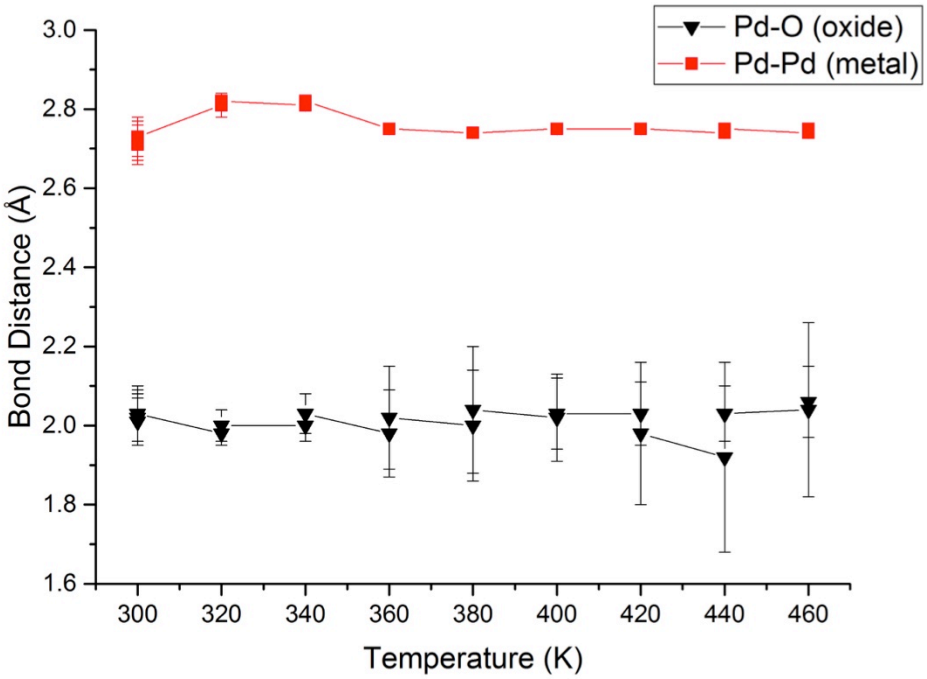

Figure 3-57- Change in bond distance, from EXAFS fitting, with temperature for 2% Pd alumina.

3.9.2.4 2% Pd/Ceria

The 2% Pd/Ceria sample showed a lot of interesting results in both L_{III}- and K-edge XANES. An example of the data at 300 K at the beginning of the reduction is given in Figure 3-58. The plots show the quality of the fitting model for the first shells of PdO and Pd metal with the experimental data in the k-range of 2.5-10 $Å^{-1}$ and R-range 1-4 Å. The full table of results from EXAFS fitting is given in Table 3-15.

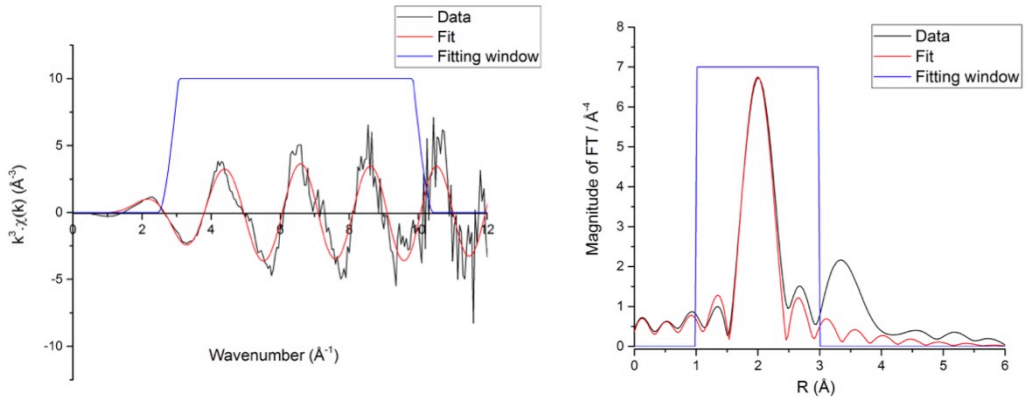

Figure 3-58 - Plot of the k^3 weighted data (left) and the Fourier transform (right) for 2% Pd/ceria sample at 300K in H_2.

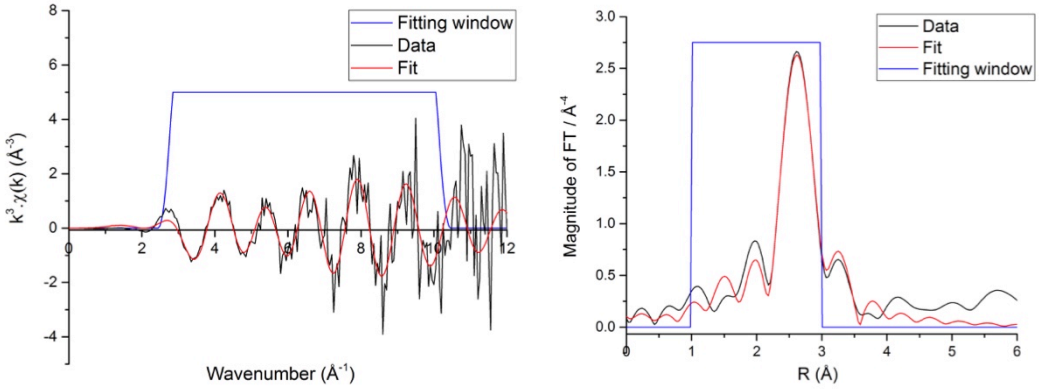

Figure 3-59 - Plot of the k^3 weighted data (left) and the Fourier transform (right) for 2% Pd/ceria sample at 460K in H_2.

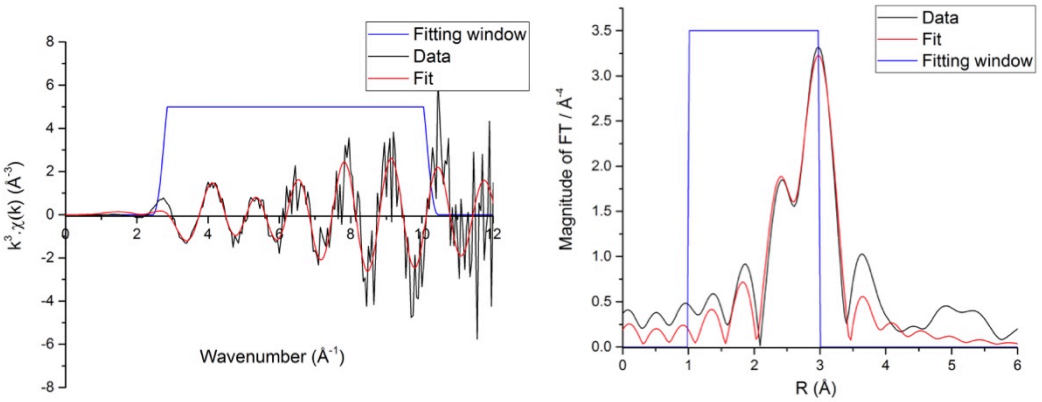

Figure 3-60 - Plot of the k^3 weighted data (left) and the Fourier transform (right) for 2% Pd/ceria sample at 300K after reduction in H_2.

The two peaks clearly indicate the presence of both Pd-O and Pd-Pd at ca 2.00 Å and 3.5 Å respectively in hydrogen. It can be seen from the k^3 – weighted plots that the data is quite noisy at higher k-values with the amount of noise increasing during the reduction (Figure 3-59 and Figure 3-60). As such the fits were focussed on the first shell of both Pd metal and Pd oxide, the fitting window was kept between 1-3 Å. By 460 K the material has been reduced to metallic Pd with the dominant peak at 2.7 Å being due to Pd-Pd (Figure 3-59). There is also a peak at 2 Å, indicating the presence of Pd-O; this confirms the findings from XANES that the material is not completely reduced. The intensity and sharpness of the Pd – Pd peak increases on cooling back to room temperature, with Pd-O peak still present at the end of the reduction (Figure 3-60).

The change in the coordination number for the 2% Pd/Ceria catalyst shows limited conversion from the PdO to Pd metal (Figure 3-61). At the end of the reduction process the coordination number for the Pd – Pd shell is 3.54 whilst the value for the Pd – O shell is 2.82; this does not match with the visual comparison of the amplitudes of the two shells, however it does appear to fit with the XANES measurements and the results from the L_{III}-edge analysis, which indicated that a complete reduction of Pd may not have taken place.[73] The extent of the difference between the visual amplitude and the coordination numbers leads to the possibility that there are other effects occurring such as self-absorption.[73] Ceria is known to be strongly absorbing and due to the strong affinity for Pd it could perhaps have distorted the results.[43] The large outlier at 420 K is due to the poor quality of the fit, and should be disregarded.

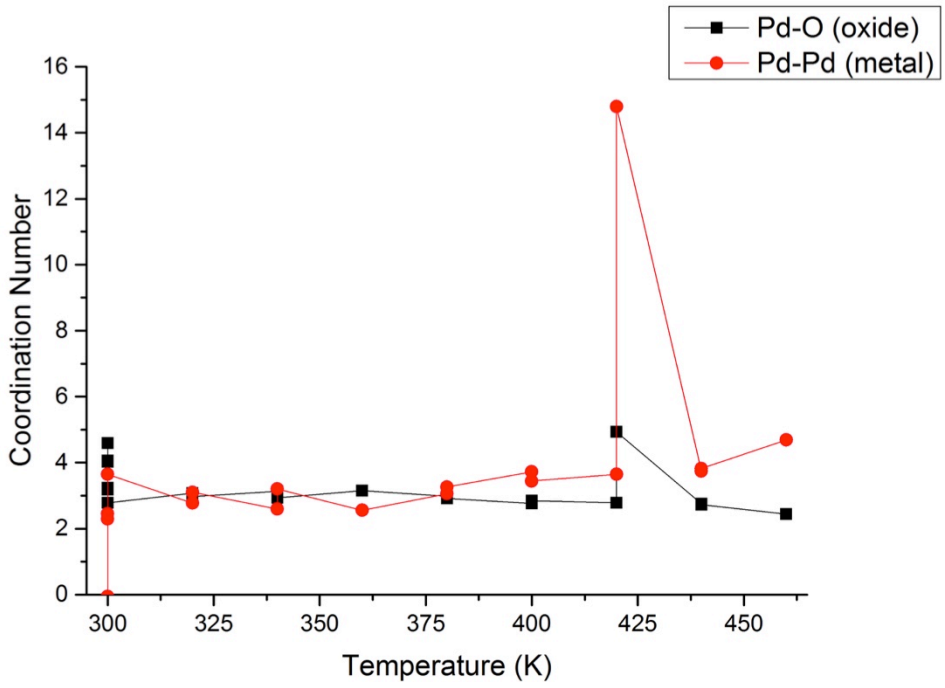

Figure 3-61 - Change in coordination number, from EXAFS fitting, with temperature for 2% Pd ceria.

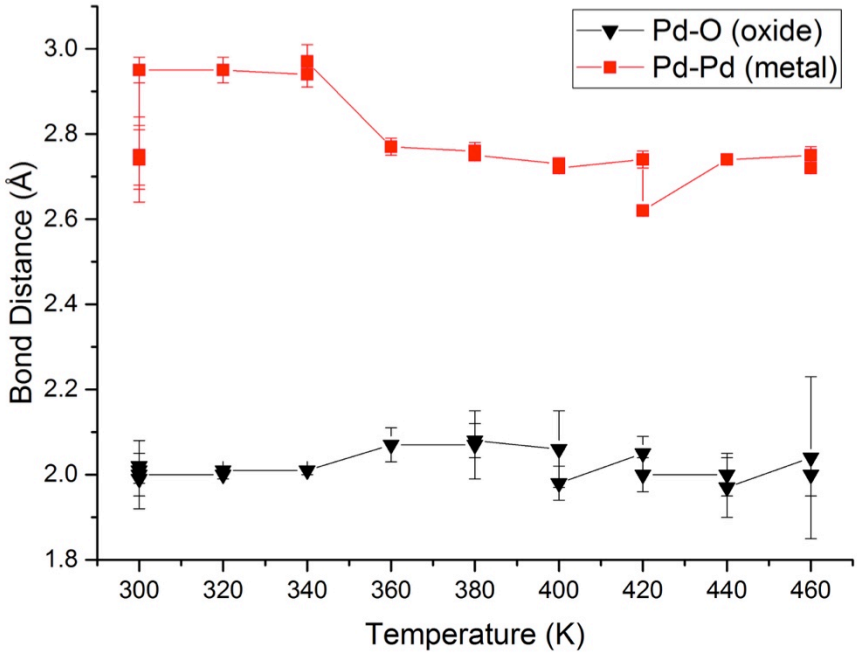

Figure 3-62 - Change in bond distance, from EXAFS fitting, with temperature for 2% Pd ceria.

The bond distance for Pd/ceria rises higher than the value for other supports when the hydride phase is formed, giving a bond distance of 2.95 Å compared with 2.85 Å for other materials (Figure 3-62). Similarly to the alumina support, by 360 K the hydride phase is removed as evidenced by the decrease in the bond distance. Interestingly upon cooling to room temperature the Pd hydride does not reform according to the EXAFS measurements. This would indicate a change in the access to the Pd sites, possibly resulting from encapsulation or another surface rearrangement.

The usefulness of the combined L_{III}- and K-edge measurements is perhaps best shown from this sample. Due to the strong absorption of the ceria, the K-edge EXAFS fittings are unreliable, however the information from the L_{III}- edge remains relatively unaffected. As such the L_{III}- edge results can be used as a guide when analysing the K-edge measurements, and for determining the changes in the electronic structure.

Table 3-15 results from EXAFS fitting for 2%Pd/Ceria.

			Pd Oxide PdO								Pd metal PdPd							
Gas	Temperature (K)	R-factor	x	error	CN	Error	S02	σ2	R	Error	x	error	CN	Error	S02	σ2	R	Error
He	300	0.0584	1.02	0.08	4.06	0.41	0.88	0.0042	2.00	0.08	-0.02	0.08	0.00	0.00	-0.01	-0.0050	2.75	0.07
He	300	0.0733	0.81	0.21	3.24	0.32	0.70	0.0009	2.00	0.02	0.19	0.21	2.29	0.23	-	-	-	-
H2/He	300	0.0542	1.00	0.03	4.02	0.40	0.87	0.00322	1.99	0.04	0.00	0.03	0.00	0.00	-0.01	-0.0120	2.74	0.07
H2/He	300	0.0608	1.15	0.08	4.59	0.46	0.99	0.00367	2.02	0.03	-0.15	0.08	0.00	0.00	-0.13	0.0118	2.74	0.10
H2/He	300	0.0383	0.80	0.11	3.18	0.32	0.69	0.00096	2.01	0.01	0.20	0.11	2.45	0.25	0.18	0.0082	2.95	0.03
H2/He	300	0.0453	0.70	0.12	2.78	0.28	0.60	-0.00066	2.00	0.01	0.30	0.12	3.65	0.36	0.26	0.0131	2.95	0.03
H2/He	320	0.0482	0.77	0.12	3.07	0.31	0.20	0.00059	2.00	0.01	0.23	0.12	2.78	0.28	0.66	0.0110	2.95	0.03
H2/He	320	0.0366	0.74	0.11	2.97	0.30	0.64	0.00023	2.01	0.01	0.26	0.11	3.10	0.31	0.22	0.0117	2.95	0.03
H2/He	340	0.0459	0.78	0.12	3.13	0.31	0.68	0.00151	2.01	0.01	0.22	0.12	2.60	0.26	0.19	0.0104	2.94	0.03
H2/He	340	0.0490	0.73	0.12	2.93	0.29	0.63	0.00083	2.01	0.01	0.27	0.12	3.20	0.32	0.23	0.0131	2.97	0.04
H2/He	360	0.0660	0.79	0.06	3.15	0.31	0.68	0.03653	2.07	0.04	0.21	0.06	2.56	0.26	0.18	0.0092	2.77	0.02
H2/He	360	0.0660	0.79	0.06	3.15	0.31	0.68	0.03653	2.07	0.04	0.21	0.06	2.56	0.26	0.18	0.0092	2.77	0.02
H2/He	380	0.1388	0.75	0.08	2.98	0.30	0.64	0.04692	2.07	0.08	0.25	0.08	3.06	0.31	0.22	0.0114	2.76	0.02
H2/He	380	0.0534	0.73	0.06	2.91	0.29	0.63	0.04018	2.08	0.04	0.27	0.06	3.26	0.33	0.24	0.0109	2.75	0.01
H2/He	400	0.0735	0.69	0.07	2.76	0.28	0.60	0.0472	2.06	0.09	0.31	0.07	3.72	0.37	0.27	0.0125	2.73	0.01
H2/He	400	0.0441	0.71	0.05	2.85	0.29	0.62	0.0591	1.98	0.04	0.29	0.05	3.44	0.34	0.25	0.0111	2.72	0.01
H2/He	420	0.0368	0.70	0.05	2.79	0.28	0.60	0.04573	2.05	0.04	0.30	0.05	3.64	0.36	0.26	0.0128	2.74	0.02
H2/He	420	0.1166	1.23	0.05	4.93	0.49	0.60	0.04792	2.00	0.04	1.23	0.05	14.79	1.48	-0.20	0.0126	2.62	0.01
H2/He	440	0.0309	0.69	0.05	2.75	0.28	0.60	0.04792	2.00	0.05	0.31	0.05	3.74	0.37	0.27	0.0123	2.74	0.01
H2/He	440	0.0379	0.68	0.05	2.73	0.27	0.59	0.05494	1.97	0.07	0.32	0.05	3.82	0.38	0.28	0.0119	2.74	0.01
H2/He	460	0.0808	0.61	0.09	2.44	0.24	0.53	0.06567	2.04	0.19	0.39	0.09	4.69	0.47	0.34	0.0155	2.75	0.02
H2/He	460	0.0191	0.68	0.04	2.73	0.27	0.59	0.05208	2.00	0.05	0.32	0.04	3.81	0.38	0.28	0.0120	2.72	0.01
H2/He	300	0.0198	0.67	0.04	2.67	0.27	0.58	0.04796	1.98	0.05	0.33	0.04	3.99	0.40	0.29	0.0100	2.75	0.01
H2/He	300	0.0146	0.66	0.04	2.65	0.27	0.57	0.04023	1.98	0.03	0.34	0.04	4.05	0.40	0.29	0.0107	2.76	0.01
He	300	0.6518	0.65	0.05	2.61	0.26	0.56	0.04572	2.02	0.06	0.35	0.05	4.18	0.42	0.30	0.0115	2.77	0.01
He	300	0.0379	0.71	0.05	2.82	0.28	0.61	0.04345	2.01	0.06	0.29	0.05	3.54	0.35	0.26	0.0089	2.75	0.01

3.9.2.5 Pd/Ceria/Alumina catalyst

The fitting model for the Pd/Ceria/Alumina catalyst was distorted at higher k-values at 300 K (Figure 3-63). The quality of the fits increases dramatically during the reduction, with the noise in k^3- weighted data shown to decrease (Figure 3-64 and Figure 3-65) The plots show the quality of the fitting model for the first shells of PdO and Pd metal with the experimental data in the k-range of 2.5-10 $Å^{-1}$ and R-range 1-4 Å. The Fourier transform clearly shows two peaks corresponding to Pd-O and Pd-Pd at ca 1.98 Å and 3.5 Å respectively from the palladium oxide. By 460 K the material has been reduced to metallic Pd with the dominant peak at 2.7 Å being due to Pd-Pd; there is also a large shoulder feature at 2.00 Å, which is due to Pd-O (Figure 3-64). The intensity and sharpness of the Pd-Pd peak increases on cooling back to room temperature and the small shoulder peak at 2.00 Å remains, though with a much lower amplitude. The full table of results for the EXAFS analysis is given in Table 3-16.

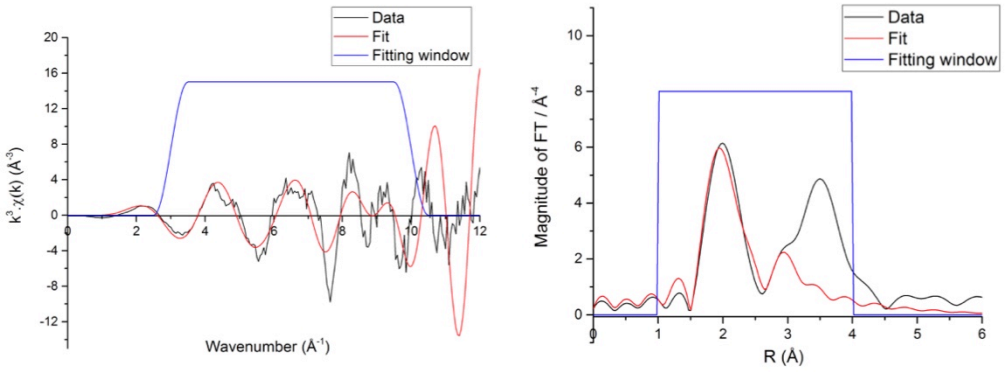

Figure 3-63 - Plot of the k^3 weighted data (left) and the Fourier transform (right) for 2% Pd/ceria/alumina sample at 300K in H_2.

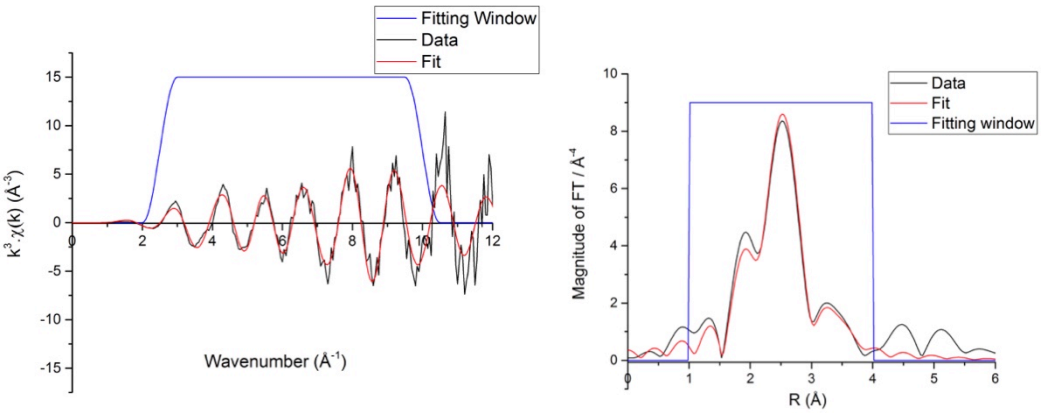

Figure 3-64 - Plot of the k^3 weighted data (left) and the Fourier transform (right) for 2% Pd/ceria/alumina sample at 460K in H_2.

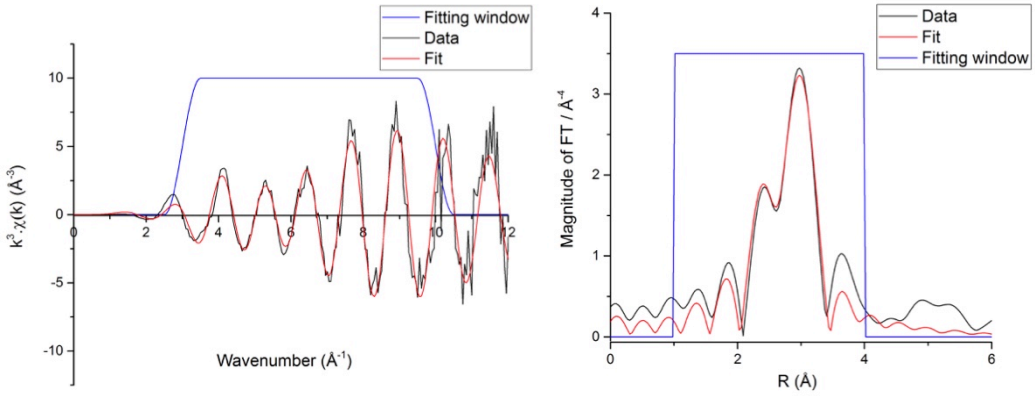

Figure 3-65 - Plot of the k^3-weighted data (left) and the Fourier transform (right) for 2% Pd/ceria/alumina sample at the end of the reduction at 300K in H_2.

The Pd/ceria/alumina catalyst has shown some of the most interesting results; this is likely due to the ceria overlayer. Until 340K the coordination number for the Pd-O shell does not drop, however on increasing temperature it reduces rapidly to a value of ca 1 by 400 K (Figure 3-66). At 360K the Pd metallic phase begins to form as evidenced by the rise in coordination number of Pd-Pd and the reduction in the Pd-O coordination number. The CN rises steadily to a value of 7.6, which rises again to 8 upon returning to room temperature. The final value for the coordination number of the Pd-Pd shell is lower than that expected for the first shell of Pd metal, 8 as opposed to 12, and could indicate the formation of smaller Pd particles on the support. Indeed for all supported materials the value increases only to 8 and doesn't increase further. This may be a support effect, arising from the deposition method however the same effect is seen for the physically mixed Pd silica sample, which indicates it is more likely due to the reduction process.

The bond distance for the Pd-Pd shell does not increase dramatically upon heating, however on cooling it increases from 2.75 to 2.85 Å indicating the formation of a Pd hydride phase (Figure 3-67). The change in the bond distance is caused by hydrogen atoms entering the lattice and causing the bond distance to expand.[10,14] Switching to He atmosphere results in the bond distance decreasing to 2.75, confirming that the increase in bond distance is due to hydride formation. Interestingly this does not occur during the reduction process, which could mean that the two support materials were hindering access to the Pd sites. The reduction of the material combined with the increase in temperature could have caused a rearrangement of the support material, allowing access to the Pd metal sites; this would account for the hydride formation upon cooling. The results of this material are different that the supported alumina and ceria catalysts. For this sample there was no hydride formation at room temperature indicating restricted access to the Pd sites for the H_2 gas, likely due to the SMSI.

Table 3-16 - Results from EXAFS for the Pd/ceria/alumina catalyst.

			Pd Oxide PdO								Pd metal PdPd							
Gas	Temperature (K)	R-factor	x	error	CN	Error	S02	σ2	R	Error	x	error	CN	Error	S02	σ2	R	Error
He	300	0.2541	0.96	0.0900	3.85	0.39	0.83	0.0033	2.03	0.05	0.04	0.09	0.44	0.04	0.03	-0.0045	2.70	0.05
He	300	0.2163	0.99	0.0452	3.95	0.39	0.85	0.0035	2.01	0.05	0.01	0.05	0.15	0.02	0.01	-0.0115	2.71	0.04
H2/He	300	0.2431	0.99	0.0307	3.98	0.40	0.86	0.00221	2.02	0.04	0.01	0.03	0.06	0.01	0.01	-0.0156	2.72	0.05
H2/He	300	0.2543	0.98	0.0673	3.94	0.39	0.85	0.00272	2.01	0.05	0.02	0.07	0.19	0.02	0.01	-0.0089	2.70	0.05
H2/He	300	0.2518	0.98	0.0670	3.92	0.39	0.85	0.00293	2.01	0.05	0.02	0.07	0.25	0.02	0.02	-0.0089	2.70	0.04
H2/He	300	0.2217	0.98	0.0770	3.92	0.39	0.85	0.00149	2.00	0.05	0.02	0.08	0.24	0.02	0.02	-0.0075	2.70	0.04
H2/He	320	0.2229	1.00	0.0217	3.99	0.40	0.86	0.00448	2.03	0.06	0.00	0.02	0.03	0.00	0.00	-0.0167	2.73	0.04
H2/He	320	0.2410	1.00	0.0001	4.00	0.40	0.86	0.00603	2.03	0.05	0.00	0.00	0.00	0.00	0.00	-0.0523	2.73	0.09
H2/He	340	0.1930	1.00	0.0054	4.00	0.40	0.86	0.00751	2.03	0.05	0.00	0.01	0.01	0.00	0.00	-0.0252	2.75	0.04
H2/He	340	0.1930	1.00	0.0054	4.00	0.40	0.86	0.00751	2.03	0.05	0.00	0.01	0.01	0.00	0.00	-0.0252	2.75	0.04
H2/He	360	0.1365	0.75	0.1424	3.01	0.30	0.65	0.0069	1.99	0.03	0.25	0.14	2.96	0.30	0.21	0.0064	2.73	0.03
H2/He	360	0.0805	0.64	0.1273	2.58	0.26	0.31	0.00787	1.99	0.03	0.36	0.13	4.27	0.43	0.56	0.0071	2.74	0.02
H2/He	380	0.0272	0.53	0.0793	2.13	0.21	0.46	0.01659	1.99	0.03	0.47	0.08	5.62	0.56	0.41	0.0076	2.75	0.01
H2/He	380	0.0248	0.48	0.0798	1.92	0.19	0.41	0.02183	2.01	0.04	0.52	0.08	6.25	0.63	0.45	0.0070	2.76	0.01
H2/He	400	0.0174	0.44	0.0732	1.74	0.17	0.38	0.02935	2.00	0.06	0.56	0.07	6.78	0.68	0.49	0.0075	2.75	0.01
H2/He	400	0.0271	0.45	0.0896	1.80	0.18	0.39	0.02984	2.00	0.08	0.55	0.09	6.59	0.66	0.48	0.0073	2.75	0.01
H2/He	460	0.0278	0.36	0.0957	1.45	0.15	0.31	0.02914	2.00	0.08	0.64	0.10	7.64	0.76	0.55	0.0094	2.75	0.01
H2/He	460	0.0278	0.36	0.0957	1.45	0.15	0.31	0.02914	2.00	0.08	0.64	0.10	7.64	0.76	0.55	0.0094	2.75	0.01
H2/He	300	0.0189	0.41	0.0764	1.63	0.16	0.35	0.02721	2.09	0.06	0.59	0.08	7.11	0.71	0.51	0.0072	2.81	0.01
H2/He	300	0.0203	0.33	0.0880	1.33	0.13	0.29	0.04838	2.13	0.21	0.67	0.09	8.02	0.80	0.58	0.0084	2.81	0.01
He	300	0.0186	0.36	0.0814	1.45	0.15	0.31	0.03362	2.10	0.10	0.64	0.08	7.65	0.76	0.55	0.0079	2.81	0.01
He	300	0.0211	0.42	0.0887	1.67	0.17	0.36	0.03173	2.00	0.10	0.58	0.09	7.00	0.70	0.50	0.0058	2.76	0.01

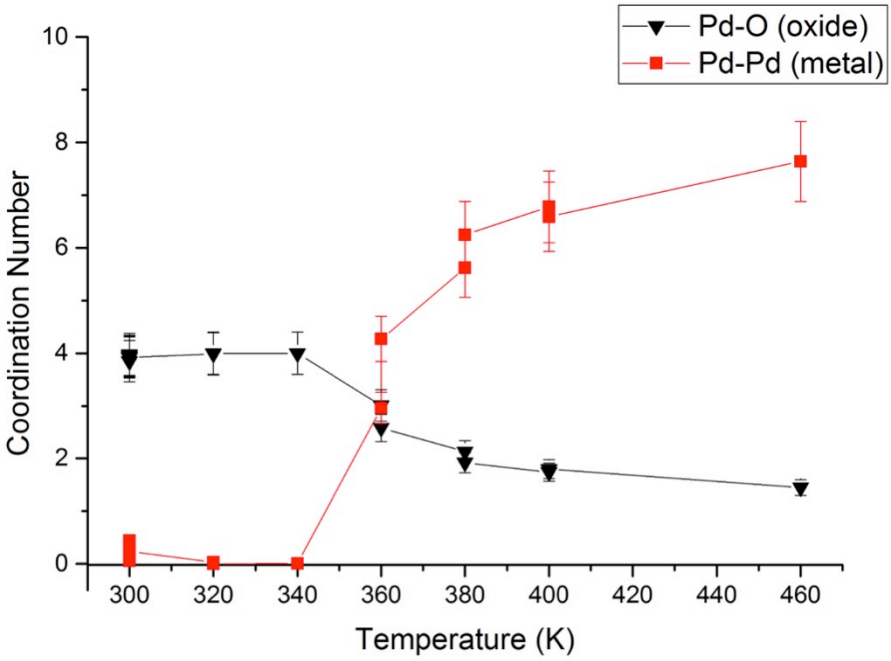

Figure 3-66 - Change in coordination number, from EXAFS fitting, with temperature for Pd/ceria/alumina.

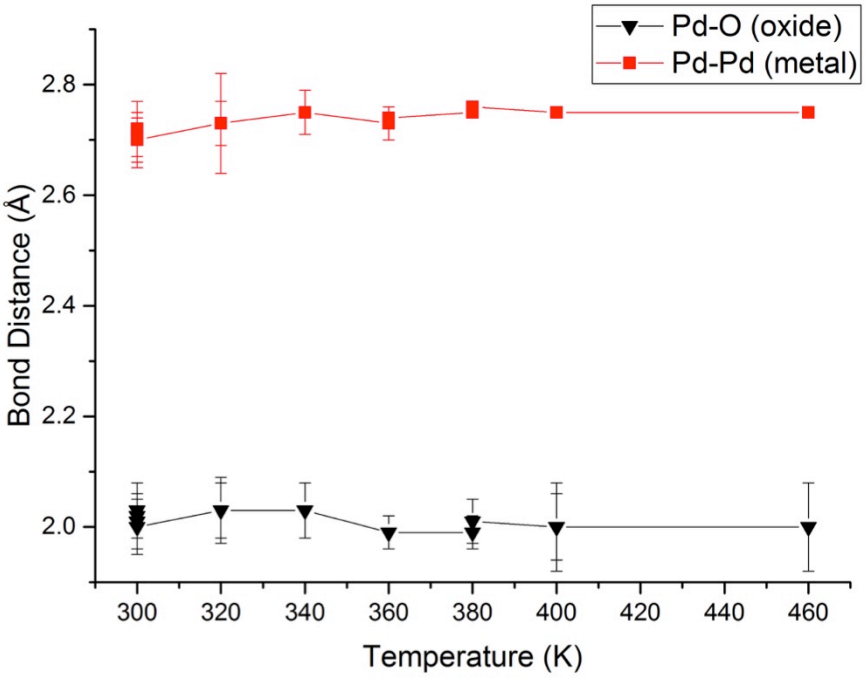

Figure 3-67 - Change in bond distance, from EXAFS fitting, with temperature for Pd/ceria/alumina.

3.10 Conclusions

The formation of Pd hydride was confirmed by use of the Pd L_{III}-edge, through the extra peak present between 3178-3185eV after the edge caused by additional electronic interactions between Pd and H. This effect is not seen in the Pd K-edge due to the nature of the excitations not involving bonding orbitals. K-edge measurements however provided detailed EXAFS measurements of the materials showing the expansion of the bond distance, which occurs in similar temperature regions as Pd hydride formation is observed in the L_{III}-edge.

The different supports were shown to have an impact on the reduction, with silica and alumina supports having less effect than ceria, for which the deposited Pd did not fully reduce. The Pd/ceria/alumina sample appears to be inaccessible to H_2 during the reduction whilst heating, as indicated by the lack of expansion of the Pd-Pd bond distance, showing what can be considered as a SMSI effect hindering the formation of Pd hydride. Interestingly the supported silica sample was shown to have a lower coordination number than either the alumina or ceria/alumina materials. The reasons for this are currently unclear, but may be due to the nature of the Pd sites on the silica surface, such as existing in smaller forms or the fitting model used for the analysis.

This combined L_{III}- and k-edge experiment has proved useful due to the additional electronic information provide from the L_{III}-edge data. This method could be used in future on other platinum group metal systems to investigate reduction or other processes where there are unexpected or unconfirmed results.

Future work in this area could look at the effect of the gaseous environment in other conditions such as during catalysis. This would allow for the changes in the electronic structure during catalysis to be monitored and compared to the catalytic performance. Additionally other platinum group metals and bimetallic nanoclusters could be investigated using this experimental setup.

3.11 References

1) Kumar, A. P.; Kumar, B. P.; Kumar, a. B. V. K.; Huy, B. T.; Lee, Y.-I. *Appl. Surf. Sci.* **2013**, *265*, 500–509.

(2) Astruc, D.; Lu, F.; Aranzaes, J. R. *Angew. Chem. Int. Ed. Engl.* **2005**, *44*, 7852–7872.

(3) Baldwin, T. R.; Burch, R. *Appl. Catal.* **1990**, *66*, 337–358.

(4) Xu, B.; Li, Y.; Qiu, A.; Feng, N.; He, J. M. J.; Chen, Y.; Fan, Y.; Yang, H. *J. Mol. Catal. A Chem.* **2004**, *216*, 107–114.

(5) Arai, M.; Panpranot, J.; Praserthdam, P.; Weerachawanasak, P. *J. Mol. Catal. A Chem.* **2008**, *279*, 133–139.

(6) Witjens, L. C.; Bitter, J. H.; van Dillen, a. J.; de Jong, K. P.; de Groot, F. M. F. *Phys. Chem. Chem. Phys.* **2004**, *6*, 3903.

(7) Liu, Z.; Handa, K.; Kaibuchi, K.; Tanaka, Y.; Kawai, J. *Spectrochim. Acta Part B At. Spectrosc.* **2004**, *59*, 901–904.

(8) Tauster, S. J. *Acc. Chem. Res.* **1987**, *20*, 389–394.

(9) Bunker, G. *Introduction to XAFS A Practical Guide to X-ray Absorption Fine Structure Spectroscopy*; Illinois, 2010.

(10) La, R.; Roma, S. *Solid State Commun.* **1993**, *85*, 863–868.

(11) Laporte, O.; Meggers, W. F. *J. Opt. Soc. Am.* **1925**, *11*, 459–460.

(12) Dong-Ping, M.; Ju-Rong, C. *Commun. Theor. Phys.* **2008**, *43*, 529–538.

(13) Tew, M. W.; Nachtegaal, M.; Janousch, M.; Huthwelker, T.; van Bokhoven, J. a. *Phys. Chem. Chem. Phys.* **2012**, *14*, 5761–5768.

(14) Tew, M. W.; Nachtegaal, M.; Janousch, M.; Huthwelker, T.; van Bokhoven, J. a. *Phys. Chem. Chem. Phys.* **2012**, *14*, 5761–5768.

(15) Colombo, C.; Monhemius, a J.; Plant, J. a. *Ecotoxicol. Environ. Saf.* **2008**, *71*, 722–730.

(16) Jen, H.-W.; Graham, G. .; Chun, W.; McCabe, R. .; Cuif, J.-P.; Deutsch, S. .; Touret, O. *Catal. Today* **1999**, *50*, 309–328.

(17) Juszczyk, W.; Karpiński, Z.; Łomot, D.; Pielaszek, J. *J. Catal.* **2003**, *220*, 299–308.

(18) Hosoya, M.; Shimoda, M. *Appl. Catal. B Environ.* **1996**, *10*, 83–97.

(19) Sankar, G.; Wright, P. A.; Natarajan, S.; Thomas, J. M.; Greave, G. N.; Dent, A. J.; Dobson, B. R.; Ramsdale, C. A.; Jones, R. H. *J. Phys. Chem.* **1993**, *97*, 9550–9554.

(20) Wu, Y.; Zhang, L.; Li, G.; Liang, C.; Huang, X.; Zhang, Y.; Song, G.; Jia, J.; Zhixiang, C. *Mater. Res. Bull.* **2001**, *36*, 253–263.

(21) Faticanti, M.; Cioffi, N.; Rossi, S. De; Ditaranto, N.; Porta, P.; Sabbatini, L.; Bleve-Zacheo, T. *Appl. Catal. B Environ.* **2005**, *60*, 73–82.

(22) Cristoforetti, G.; Pitzalis, E.; Spiniello, R.; Ishak, R.; Giammanco, F.; Muniz-Miranda, M.; Caporali, S. *Appl. Surf. Sci.* **2012**, *258*, 3289–3297.

(23) Gislason, J.; Xia, W.; Sellers, H. *J. Phys. Chem. A* **2002**, *106*, 767–774.

(24) Thirunavukkarasu, K.; Thirumoorthy, K.; Libuda, J.; Gopinath, C. S. *J. Phys. Chem. B* **2005**, *109*, 13272–13282.

(25) Borszeky, K.; B, T. *J. Catal.* **1999**, *166*, 160–166.

(26) Catalysis, A. *Appl. Catal.* **1986**, *22*, 211–219.

(27) Aben, P. *J. Catal.* **1968**, *229*, 224–229.

(28) Chen, J. J.; Ruckenstein, E. *J. Catal.* **1981**, *69*, 254–273.

(29) Hicks, R. F.; Qi, H.; Young, M. L.; Lee, R. G. *J. Catal.* **1990**, *122*, 295–306.

(30) Klm, G. *Ind. Eng. Chem. Prod. Res. Dev.* **1982**, *21*, 267–274.

(31) Shinjoh, H.; Hatanaka, M.; Nagai, Y.; Tanabe, T.; Takahashi, N.; Yoshida, T.; Miyake, Y. *Top. Catal.* **2009**, *52*, 1967–1971.

(32) Wang, J.; Chen, H.; Hu, Z.; Yao, M.; Li, Y. *Catal. Rev.* **2014**, *57*, 79–144.

(33) Badri, A.; Binet, C.; Lavalley, J. *J. Chem. Soc. Faraday Trans.* **1996**, *92*, 1603–1608.

(34) Bredikhin, M N Lokhov, IA Zamaraev, K. *Dokl. Akad. Nauk SSSR* **1988**, *301*, 1124–1128.

(35) Boutonnet, M Kizlin, J Stenius, P. *Colloids and Surfaces* **1982**, *5*, 209–225.

(36) Binet, C.; Jadi, A.; Lavalley, J. *J. Chem. Soc. Trans.* **1992**, *88*, 2079–2084.

(37) Bunluesin, T.; Gottea, R. J.; Grahamb, G. W. *Colloids and Surfaces* **1998**, *15*, 107–114.

(38) Wang, X.; Gorte, R. J.; Wagner, J. P. *J. Catal.* **2002**, *212*, 225–230.

(39) Nolan, M.; Parker, S. C.; Watson, G. W. *Surf. Sci.* **2005**, *595*, 223–232.

(40) Yang, Z.; Lu, Z.; Luo, G.; Hermansson, K. *Phys. Lett. A* **2007**, *369*, 132–139.

(41) Shen, W.; Kobayashi, A.; Ichihashi, Y.; Matsumura, Y.; Haruta, M. *Catal. Letters* **2001**, *73*, 161–165.

(42) Matsumura, Y.; Shen, W.; Ichihashi, Y.; Ando, H. *Catal. Letters* **2000**, *68*, 181–183.

(43) Min, B. .; Santra, a. .; Goodman, D. . *Catal. Today* **2003**, *85*, 113–124.

(44) HALLER, GL RESASCO, D. *Adv. Catal.* **1989**, *36*, 173–235.

(45) Rimer, J. D.; Fedeyko, J. M.; Vlachos, D. G.; Lobo, R. F. *Chemistry* **2006**, *12*, 2926–2934.

(46) Clark, J. H.; Macquarrie, D. J.; Mubofu, E. B. *Green Chem.* **2000**, *2*, 53–56.

(47) Marín-Astorga, N.; Pecchi, G.; Fierro, J. L. G.; Reyes, P. *J. Mol. Catal. A Chem.* **2005**, *231*, 67–74.

(48) Panpranot, J.; Phandinthong, K.; Sirikajorn, T.; Arai, M.; Praserthdam, P. *J. Mol. Catal. A Chem.* **2007**, *261*, 29–35.

(49) Bedford, R. B.; Singh, U. G.; Walton, R. I.; Williams, R. T.; Davis, S. a. *Chem. Mater.* **2005**, *17*, 701–707.

(50) Zaluski, L.; Zaluska, a; Ström-Olsen, J. . *J. Alloys Compd.* **1997**, *253-254*, 70–79.

(51) Fujitani, T.; Saito, M.; Kanai, Y.; Watanabe, T.; Nakamura, J.; Uchijima, T. *Appl. Catal. A Gen.* **1995**, *125*, L199–L202.

(52) He, J. H.; Dechiaro, L. F.; Knies, D. L.; Hubler, G. K.; Grabowski, K. S.; Moser, a. E.; Dominguez, D. D.; Kidwell, D. a.; Hagelstein, P. L. *Int. J. Hydrogen Energy* **2012**, *37*, 12351–12357.

(53) Schlapbach, L.; Züttel, a. *Nature* **2001**, *414*, 353–358.

(54) Kim, H.; Rey, C.; Glimcher, M. J.; Res, J. B. M.; Rosi, N. L.; Eckert, J.; Eddaoudi, M.; Vodak, T.; Kim, J.; Keeffe, M. O.; Yaghi, O. M. *Science (80-.).* **2003**, *300*, 1127–1129.

(55) Jose, D.; Jagirdar, B. R. *Int. J. Hydrogen Energy* **2010**, *35*, 6804–6811.

(56) Houari, A.; Matar, S. F.; Eyert, V. **2014**, *173706*.

(57) Jenewein, B.; Penner, S.; Gabasch, H.; Klötzer, B.; Wang, D.; Knop-Gericke, A.; Schlögl, R.; Hayek, K. *J. Catal.* **2006**, *241*, 155–161.

(58) Vogel, W.; He, W.; Huang, Q. H.; Zou, Z.; Zhang, X. G.; Yang, H. *Int. J. Hydrogen Energy* **2010**, *35*, 8609–8620.

(59) Baranowski, B.; Majchrzak, S.; Flanagan, T. B. *J. Phys. F Met. Phys.* **2002**, *1*, 258–261.

(60) Wolf, R. J.; Lee, M. W.; Ray, J. R. *Phys. Rev. Lett.* **1994**, *73*, 557–560.

(61) Bugaev, a L.; Srabionyan, V. V; Soldatov, a V; Bugaev, L. a; Bokhoven, J. a Van. *J. Phys. Conf. Ser.* **2013**, *430*, 012028.

(62) Fisher, J Stead, L. *ICP-ES Analysis Report*; Sonning Common, 2014.

(63) Isaeva, L. E.; Bazhanov, D. I.; Isaev, E. I.; Eremeev, S. V.; Kulkova, S. E.; Abrikosov, I. a. *Int. J. Hydrogen Energy* **2011**, *36*, 1254–1258.

(64) Sharma, S. *J. Catal.* **2000**, *190*, 199–204.

(65) Fan, L.; Fujimoto, K. *J. Catal.* **1997**, *172*, 238–242.

(66) Suzuki, T.; Souda, R. *Surf. Sci.* **2000**, *448*, 33–39.

(67) Acerbi, N. Chapter 2 Experimental Methods, Oxford University.

(68) Acerbi, N.; Golunski, S.; Tsang, S. C.; Daly, H.; Hardacre, C.; Smith, R.; Collier, P. *J. Phys. Chem. C* **2012**, *116*, 13569–13583.

(69) Bugaev, A. L.; Guda, A. A.; Lomachenko, K. A.; Srabionyan, V. V; Bugaev, L. A.; Soldatov, A. V; Lamberti, C.; Dmitriev, V. P.; Bokhoven, J. A. Van. *J. Phys. Chem. C* **2014**, *118*, 10416–10423.

(70) Ravel, B.; Newville, M. *J. Synchrotron Radiat.* **2005**, *12*, 537–541.

(71) Vaarkamp, M. *Catal. Today* **1998**, *39*, 271–279.

(72) Search, H.; Journals, C.; Contact, A.; Iopscience, M.; Address, I. P. *J. Appl. Phys.* **1993**, *144*, 144–146.

Chapter 4 - Metal Support Interaction of Supported Pd, Rh and Ceria Catalysts

Abstract

The metal support interaction (MSI) between supported metal nanoparticles and inorganic supports is an area of great interest. A growing field of research involves creating materials that take advantage of the MSI effect to improve catalyst stability, through hindering mobility and limiting sintering. In this chapter supported platinum group metals were studied during reduction using combined XAS/XRD. The materials were prepared through sequential deposition on an alumina support of first the platinum group metal then a ceria layer. This layer of ceria was deposited to cover the metal particles; limiting movement and gas transfer processes. It was discovered that despite the additional ceria layer, the material was still exposed to the gas and reduced.

4.1 Introduction

Precious metal/ceria catalysts are used for a variety of applications such as three-way catalysts (TWC)[1,2] and solid oxide fuel cells.[3] The effectiveness of these systems for heterogeneous catalysis is believed to be due to the strong metal support interaction (SMSI).[4,5] This is caused by the interaction between the metal nanoparticles and the ceria, which as a reducible oxide causes a change in the chemisorption properties of the metal particles with regards to CO and H binding making the process more reversible.[6] The SMSI process may be related to electronic, chemical or structural properties of the material.[5]

In this investigation XAS was used to follow the change in the local structure of Pd/Ceria and Rh/Ceria catalysts supported on alumina. These results will be used to shed light on the SMSI between the metal NPs and the support materials.

4.1.1 Background

Palladium and rhodium based catalysts are widely used for a variety of reactions and in particular in the auto-exhaust catalysis area where both of these components, along with other platinum group metals, have been used and studied extensively.[1,6–8] As these are both expensive elements, it is important to maximise the surface area, for catalysis whilst also improving the metal support interaction to improve catalyst reusability. Moisture can have a large effect on the stucture and behaviour of supported metal NPs.[9] It has been shown previously in the literature that the prescence of moisture during Pd NP prepartation can have an influence on the material formed and hinder or enhance the later reduction of the material.[9] While many characterisation methods are commonly used (examples include diffraction, FTIR and electron microscopy), X-ray absorption spectroscopy is advantageous due to the low levels of metal loading and the ability to be employed *in situ* under operating conditions.[10,11]

4.1.1.1 Metal support interaction

Noble metals supported on metal oxides have been known to exhibit interactions between the metal and support known as the strong metal support interaction (SMSI).[12] Indeed metal nanoparticles supported on reducible oxides show significant differences in both catalytic activity and selectivity for hydrogenation reactions; these differences vary depending on the calcination temperature of the support.[13] An effect of the strong metal support interaction is the rapid reduction of absorption capacity for H_2 or CO, without the elevation of pre-reduction temperature.[12] Most of the initial investigations into SMSI focused on the use of titania as a support, with two main theories being proposed for the interaction. The first is a

charge transfer between the metal and the support causing a perturbation in the electronic functionals of the metal.[12] The second is a rearrangement of the support surface, encapsulating the metal NPs and reducing access to the active sites for the gases.[4]

One of the potential drawbacks of using platinum group metals (PGM) in auto-catalysis is their release and uptake into the human body through inhalation of road dust.[1,7] The dissolution of Pt, Pd and Rh in the respiratory tract can lead to the formation of PGM-chlorides which are known to be toxic to biological systems.[7] The dispersion of PGM particulates into the environment can be due to a number of factors such as mechanical attrition and chemical processes, however developing materials which take advantage of the SMSI, the amount of PGM dispersed can be lowered.[1,7]

4.1.1.2 Supported Rhodium Catalysts

The use of rhodium as a catalyst has been known since the 1800s where it was used for the catalytic combination of hydrogen and oxygen to form water.[14] Today Rh can be used for a number of important chemical reactions, with rhodium clusters being explored as potential materials for hydrogen storage and as anticancer treatments.[15] Rh/CeO_2 materials are widely studied for their use in three way catalysts, due to their selectivity for NO_x to N_2 reduction.[16] Rh can be supported on a variety of materials, and can also be successfully ion-exchanged into zeolites, although there are limitations on the effectiveness of these catalysts.[17] The formation and break up of supported Rh clusters has been reported in the literature to bear some similarities to the chemical mechanisms of Ir, with both Rh and Ir clusters shown to breakdown during catalysis with ethane.[18] Formation of Rh clusters on zeolites have shown the importance of the reactive environment for maintaining control of the cluster formation.[18]

Supported Rh is known to oxidise easily at room temperature, this combined with the tendency for a ceria surface to rearrange and encapsulate supported nanoparticles makes TEM imaging of these systems difficult.[16] This is also made more difficult by the relative similarities in contrast for Rh and Ce through TEM, necessitating the use of higher percentage loadings of Rh for imaging.[16] For lower loadings of Rh on ceria, 0.15-0.35%, hydrogenation of benzene can be used to determine the amount of Rh metal accessible on the surface; the amount of metal exposed was found to decrease with increasing reduction temperature due to encapsulation of the Rh by ceria.[16]

Supported rhodium nanoparticles have been studied for the decomposition of N_2O.[19,20] The performance of Rh for nitrous oxide decomposition has been shown to diminish in the presence of oxygen.[20] This is proposed to be due to desorption of oxygen being the rate

limiting step in the decomposition as outlined in the Langmuir-Hinshelwood mechanism.[20] In a study, investigating the effect of the support for Rh NPs on the catalytic activity, it was found that MgO and SiO_2 supports had improved catalytic performance over Rh supported on CeO_2, TiO_2 and Al_2O_3.[20] This effect was related to the particle size, with Rh NPs supported on reducible supports having a smaller particle size.[20] This effect was strong enough to enable Rh/MgO and Rh/SiO_2 materials to decompose N_2O in the presence of oxygen.[20] Supported Rh clusters on MgO have been modified through use of ligands around neighbouring clusters for the selective hydrogenation of 1,3-butadiene.[21] Rh has also been successfully deposited onto mesoporous silica (MCM-41, SBA-15-C, SBA-15-S, KIT-6) for use in N_2O decomposition; mesoporous materials were used due to their high surface area, pore volume and narrow pore-size distribution.[19]

TEM studies of rhodium supported on low surface area ceria showed two mechanisms at work, one in which the Rh particles grow with increasing temperature and the second where the particles get decorated with ceria.[22] Previous investigations have shown that there is evidence of the SMSI for Rh/CeO_2, but only for catalysts reduced at temperatures higher than 973K;[22] these results were obtained for Rh on low surface area ceria.[22]

Understanding the surface geometry and local coordination of the catalyst is an important area of research and can be done computationally using methods such as DFT as well as experimentally.[21] Determining a structure computationally and then proving it experimentally (or vice versa) is a very powerful way to determine the chemistry that occurs at the active sites.[21,23]

4.1.1.3 Supported Palladium Catalysts

Supported palladium catalysts are widely used for hydrogenation reactions and palladium along with other platinum group metals are used as diesel oxidation catalysts.[24] Palladium can be loaded onto the support via a number of methods, the most common being wet impregnation.[8,9,25] Supported Pd catalyst have been discussed in detail in chapter 3, here a short introduction is provided on the SMSI and supported Pd materials.

Most reports of Pd/CeO_2 systems are carried out under dry conditions, however some investigations have been done to investigate the influence of moisture; the presence of moisture was found to promote CO oxidation at lower temperature due to reducing the activation energy for the conversion.[9] The chemistry for Pd/CeO_2 catalysts is slightly different to that for Rh/CeO_2 materials, with decoration of Pd by reduced ceria occurring at the lower temperature 673K compared with 973K reported for Rh.[22] For Pd on high surface area ceria, it

was found that dispersion was high, 70%, but the low stability of the surface lead to encapsulation and deactivation; conversely for low surface area ceria the dispersion was low, 30%, and no encapsulation was observed.[22]

Work by Acerbi et al investigated the effect of depositing a ceria overlayer onto silica or alumina supported PGM catalysts, such as Pd and Rh.[25] It was shown that under reducing atmosphere the PGM formed an electronic junction with the ceria, leading to improved reducibility, rearrangement of the ceria band gap and a variation in the degree of oxygen vacancy formation; all of these properties are dependant upon the work function of the PGM.[25] Raman spectroscopy studies revealed the effect of PGM particles on the redox capabilities of ceria, with a PGM-ceria solid solution being formed in oxidising atmosphere.[25]

4.1.2 Previous XAS investigations

There have been several reported uses of XAS on supported Pd and Rh materials. A selection of these reports will be presented here in order to provide an overview of what is currently being published in the scientific community.

An example of XAS studies on the Rh K-edge is the investigation into Rh/alumina materials for the partial oxidation of methane, which was monitored *in situ* by combined EXAFS and mass spectrometry.[26] This work utilised a capillary cell with the exhaust line connected directly to a mass spectrometer. It was found that upon heating in helium the structure from the Rh carbonyl precursor was maintained, however upon reduction in hydrogen the particles were shown to agglomerate and increase in size.[26] The catalytic activity was found to be related to the residence time, although there was no significant structural change in the catalyst that could be found through the XAS measurements.[26]

Another investigation into the oxidation and reduction kinetics of Rh and Rh_2O_3 was conducted using dispersive EXAFS (DXAFS).[27] This technique allows for better time resolution due to the entire spectrum being recorded at the same time.[10] the advantage of using DXAFS was apparent during the reduction, where a change in he reduction kinetics was discovered at 473 K which was too fast to detect using Surface Enhanced Raman Spectroscopy (SERS).[27] DXAFS has also been used to monitor the hydrothermal aging of Rh/alumina materials; this is again due to the enhanced time resolution arising from the technique.[28]

EXAFS was also used to investigate the deposition of $Rh(PPh_3)Cl_3$ onto phosphinated MCM-41. Here it was shown that the coordination number post reaction was low, 1.3 with a Rh-Rh

bond distance of 2.68.[29] This the Authors took to indicate as the formation of a dimeric species on the surface arising from the binding of monomeric $Rh(PPh_3)Cl_3$ bound on the support agglomerating.[29] The nature of the binding was revealed through fitting of the EXAFS data which showed the presence of a Rh-Si interaction in addition to a Rh-C interaction after the deposition.[29]

This is a sample of some of the uses of Rh K-edge. Whilst there have been several publications looking at supported Rh nanoparticles, there has been little published recently on the metal support interaction or on comparisons between different supported metals.

A report on the aerobic oxidation of cinnamyl alcohol by Pd/alumina catalysts showed how dynamic structural changes in the catalyst could be followed *in situ* using QuEXAFS.[30] Two different *in situ* setups were utilised, a fixed bed reactor and a slurry reactor. Although both were employed successfully it was found that the reaction rates for the slurry reactor were higher, showing that the design of the *in situ* setup will have an impact on the results obtained.[30]

Another common support for Pd is carbon, due to high activities and ease of catalyst recovery.[31,32] The interaction between the carbon support and the Pd was investigated using EXAFS, revealing a Pd-C interaction at 3.6 Å which remains after washing and reduction with $NaBH_4$.[31] However it was found that subsequent hydrogen treatment at increased temperature lead to Pd sintering and the loss of the interaction.[31] Here the use of EXAFS provided information on the nature of the Pd active sites, during various stages of the catalyst preparation, that otherwise may not have been obtained.[31]

Pd/ceria catalysts have a number of uses such as for the hydrogenation of CO and CO_2.[33] In this investigation EXAFS measurements revealed that the decrease in catalytic activity was sue to the sintering of the palladium particles during high temperature reduction; an effect that was not possible to see with diffraction due to the small size of the Pd particles (below 3nm).[33] Additionally it was found that the SMSI between Pd and Ce influenced the hydrogenation. This was accredited to the formation of Ce^{3+} species, which decorated the Pd particles.[33]

One area that has not been investigated extensively in the literature is the formation of Pd hydride using EXAFS. There is a detailed paper from the 1993, which investigates the formation of Pd hydride and carbide phases in supported Pd catalysts; it was noted that only a local probe can be used to successfully determine the difference between interstitial and substitutional alloying.[34] In this work, which utilised the Pd K-edge, it was found that sorption

of hydrogen was suppressed in both carbon and alumina supported Pd catalysts. This could be determined by an expansion of the first shell Pd-Pd bond distance from 2.75 Å to 2.8 Å.[34] Additionally it was found that decomposition of the hydride phase resulted in a Pd-Pd first shell with a coordination number of 9 ± 1.[34] There is very little published on Pd hydride formation in recent years, however there was a recent publication investigating nano-particle size through the Pd-Pd interaction that looked at Pd hydride formation.[35] Here a combination of electron microscopy and K-edge EXAFS were used to determine the ratios of Pd/H at various temperatures and cluster shapes and sizes.[35]

4.1.3 Aim of the work

In this work we investigate the reduction of supported platinum group metals (Pd and Rh) supported on alumina with a ceria overlayer through the use of *in situ* XAS. The main aim of this work was to monitor the changes that occur in the local structure of the material during the reduction and to see if the additional ceria layer offers more stability when compared to standard single layer materials. Additionally the differences between Pd and Rh, two different group VIII metals, will be investigated.

4.2 Experimental

4.2.1 Sample preparation

Supported catalysts were prepared by wet impregnation of either palladium (II) nitrate or rhodium (III) nitrate respectively onto an alumina support followed by deposition precipitation of cerium (IV) nitrate. The catalysts were prepared through a two-step deposition process. First 1wt% of precious metal (PM), either Rh or Pd was deposited through deposition precipitation (DP) or incipient wetness (IW) method onto a γ-alumina support. Once the precursor was deposited on the γ-alumina the catalysts were dried at 105^{o}C for 4 hours and calcined in air at 500^{o}C for 2 hours. Following this a layer of ceria was deposited using the DP method and a cerium (IV) nitrate precursor. Full details are available in a thesis chapter by Nadia Acerbi, with a summary reproduced here for reference.[36]

20g of the catalyst was prepared using 19.8g of alumina support and 0.2g of the precious metal (PM) - calculated from the amount present in the precursor. [36] The precursor was then mixed with MΩ Millipore demineralised water to the volume required to fill the pore volume of the support. [36] The supported catalysts were then dried for 4 hours at 105 ^{o}C and calcined in static air for 2 hours with a ramp rate of 10 ^{o}C/min.

Ceria was added to the material through deposition precipitation.[36] The Cerium nitrate was prepared by reacting Ce(III) hydroxide with nitric acid. For the preparation of 5g of ceria loaded catalyst, 4.25g of the 1% PM loaded alumina was put in a beaker and 18 MΩ Millipore demineralised water was added with stirring at 200 rpm until the volume reached 100 ml. an acid solution, consisting of 1.94 ml of cerium (IV) nitrate, 20 ml of MΩ Millipore demineralised water and 0.5g of nitric acid, and a basic solution consisting of 0.5 M sodium carbonate (Fisher Scientific 95%) were added dropwise to the solution. The pH was monitored using a pH meter and precipitation occurs at 7.5 ± 0.5. The precipitate was then filtered using a Whatman 540 filter and washed several times, to remove Na^{+} arising from the base. The material was then dried for 4 hours at 105 ^{o}C and calcined in static air for 2 hours with a ramp rate of 10 ^{o}C/min.

The materials used in this work are 15% Ceria/ 0.85%Pd/Alumina and 15% Ceria/0.85% Rh/Alumina.

4.2.2 XAS measurements

In situ x-ray absorption measurements were taken at beamline B18 Diamond Light Source (DLS). Samples were loaded into glass capillaries (0.5mm diameter), and mounted into a custom furnace cell with integrated gas rig and mass spectrometer (Figure 4-1). Samples were heated to 573 K at a rate of 5 K/min and monitored using XAS.

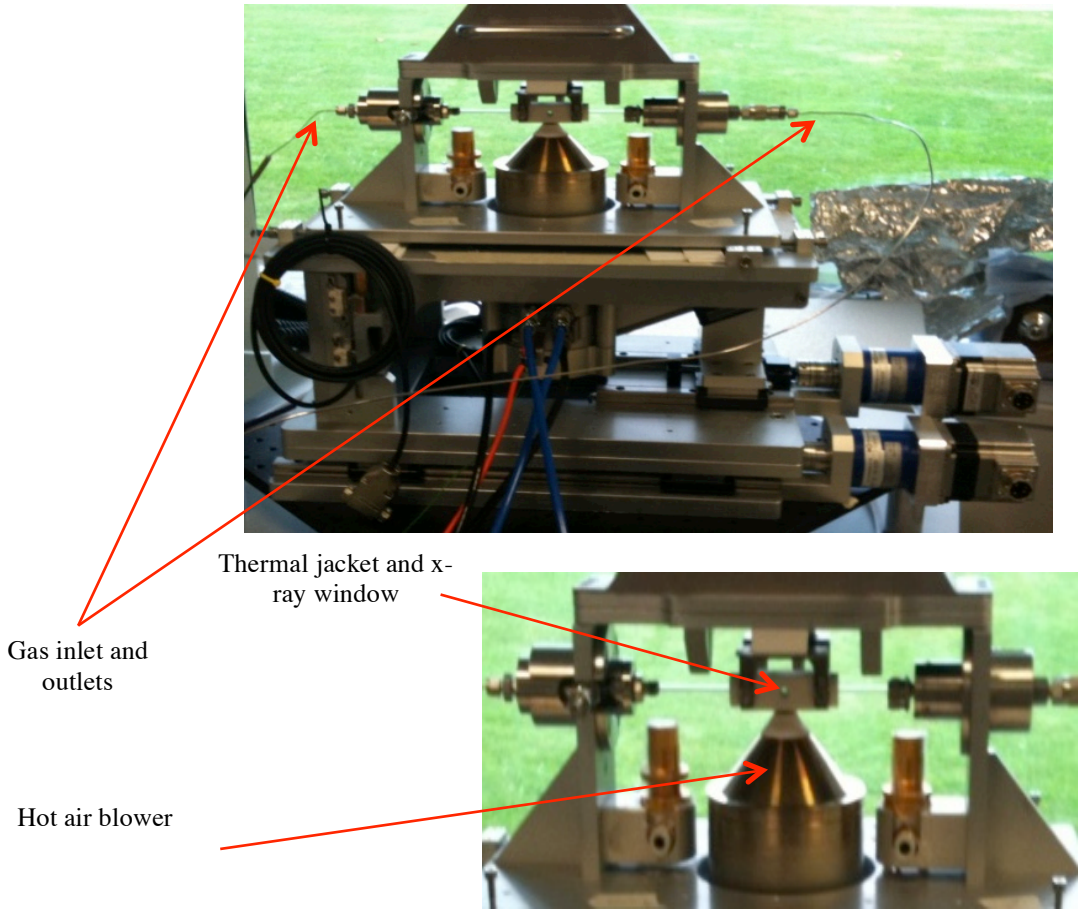

Figure 4-1 - Image of the in situ cell used for the reduction experiments highlighting the key features.

XAS data was collected in QEXAFS mode using a Si (111) monochromator, and the energy was calibrated using Pd and Rh foils for the respective k-edge energies. Data was collected in both fluorescence and transmission using a 9-element Ge detector for the fluorescence measurements. Data was collected in the form of 30 second QEXAFS measurements.

Samples were measured at room temperature in He atmosphere before being reduced at room temperature by a mixture of 5% H_2/He. After the room temperature reduction the samples were heated to 573 K at a rate of 5 K per minute, and held at that maximum for a few minutes before cooling to room temperature at a controlled rate of 20 K/minute.

XAS data was processed using Athena and Artemis software as explained in chapter 2. Amplitude values were obtained by fitting Pd and Rh foil standards using Artemis software. These amplitude values were then used to fit the *in-situ* data on the Pd or $Rh/CeO_2/Al_2O_3$ catalysts. *In-situ* data was fitted using the appropriate shells – Pd-O and Pd-Pd for Pd K-edge and Rh-O, Rh-Rh (second and third shell from the oxide and first shell from the metal) for the Rh K-edge – with fixed coordination number. Additional parameters were added to the amplitude to simulate coordination number variation as explained in chapter 2.

4.3 Pd/Ceria/Alumina Catalysts

Supported Pd/ceria/alumina catalyst was reduced under H_2/He atmosphere at room temperature for 35 minutes before being heated to 573 K at a rate of ca, 5 K/minute. Following this the catalyst was cooled at a controlled rate to room temperature. XAS measurements were taken at room temperature and during the temperature ramp. Combined XAS/XRD measurements were taken whilst the material cooled from 573 K to room temperature.

4.3.1 XANES Analysis

The first 10 minutes of the room temperature scans were taken with the sample under He atmosphere. Almost as soon as the H_2/He is flown over the sample it begins to reduce as evidenced by the change in the post-edge features (Figure 4-2). Whilst the PdO typically has a single peak with a shoulder feature after the edge, in the metallic phase two peaks are formed; this doublet peak can be used as a fingerprint to indicate that a reduction of the Pd has occurred.

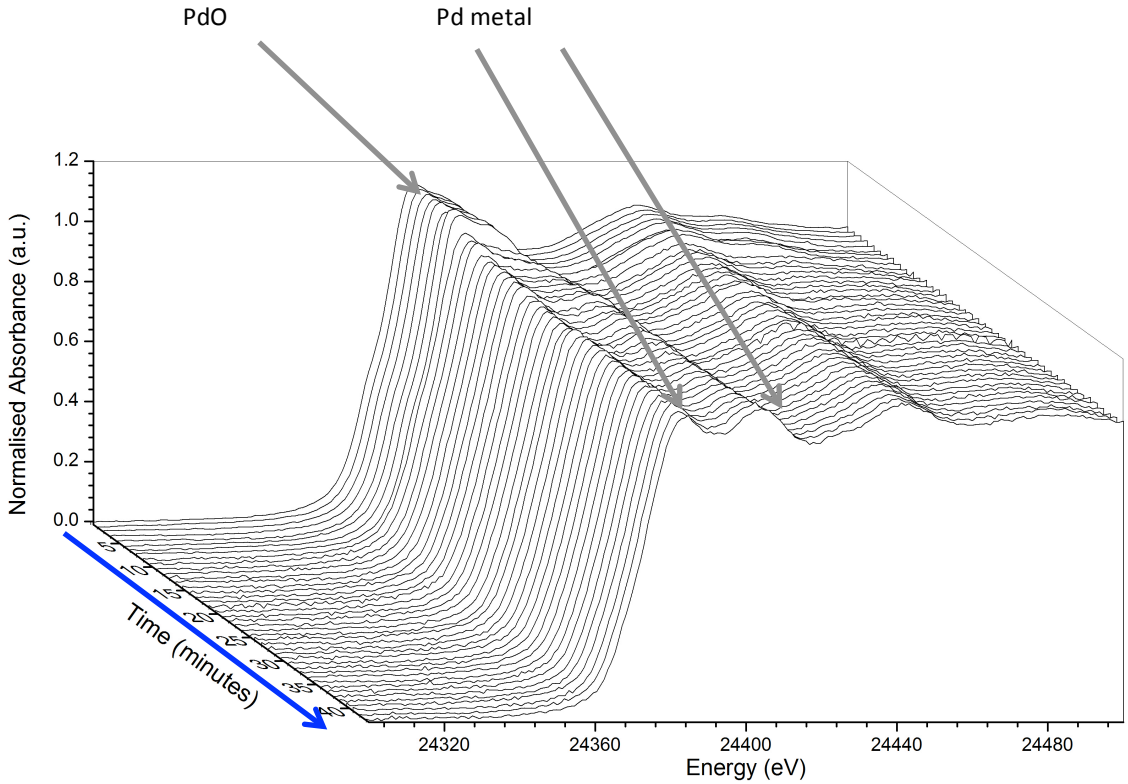

Figure 4-2 - XANES plot of in situ Pd/Ceria/Alumina catalyst at room temperature under H_2/He atmosphere.

There is also a visible decrease in the whiteline intensity from 1.086 to 1.01 after one minute of being exposed to hydrogen (Figure 4-2). The general features then change gradually, with the initial peak after the edge decreasing in size and forming a doublet, which as stated previously, is characteristic of Pd metallic phase. Interestingly the initial material does not possess a sharp defined whiteline peak expected from PdO, which could suggest some Pd-metal contributions in the initial material. These changes are accompanied by a decrease in the edge energy by almost 2eV from ca 24374 to ca 24372 eV. The lower edge energy is the same value as that for the Pd metal foil, providing supporting evidence for a change in oxidation state from Pd^{2+} to Pd^{0}.

This change is also observed in the linear combination fit (LCF) which shows a clear reduction in the amount of the oxide phase present with increasing exposure to H_2, with a 50% conversion to the metal occurring at the end of the room temperature reduction (Figure 4-3). Standards used for this fitting were the Pd foil and a PdO powder mixed with fumed silica. Data was fitted in the range of -20 to +14 eV about the edge position. Visual inspection of the final scan from the room temperature reduction compared to Pd metal reveals that the spectra are quite similar with the main difference being in the region immediately after the whiteline intensity; the second peak is smaller in the spectra at the end of the room temperature reduction than for the Pd foil standard (Figure 4-5).

Closer examination of the fitting model reveals that it may not be entirely accurate. Looking at the individual fits for the datasets reveals that whilst they are fairly accurate for the initial scans, as the reduction proceeds the fits get increasingly more inaccurate (Figure 4-4). This increased inaccuracy may be due to the mixed phase nature of the Pd at this stage, or the use of Pd foil as a standard in the fitting model. Supported NPs will have a different XAS pattern then unsupported materials due to the interaction of the metal orbitals with those on the supporting materials, and these support effects may be responsible for the difference in the LCF fits.

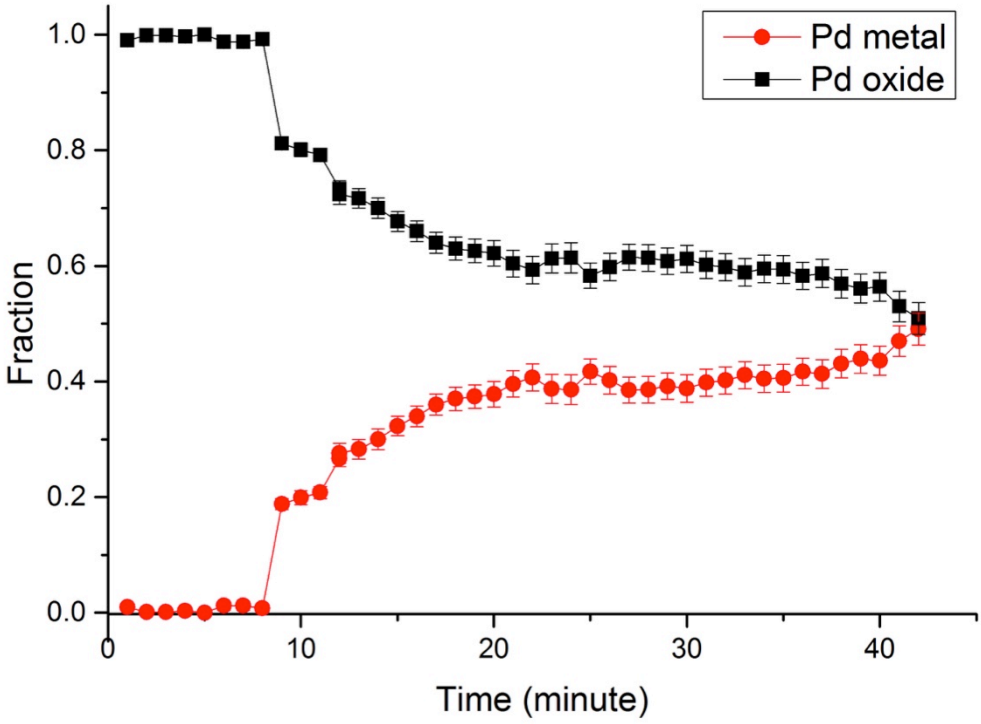

Figure 4-3 - Linear combination fit (LCF) of in situ Pd/Ceria/Alumina catalyst reduced at room temperature under H_2/He.

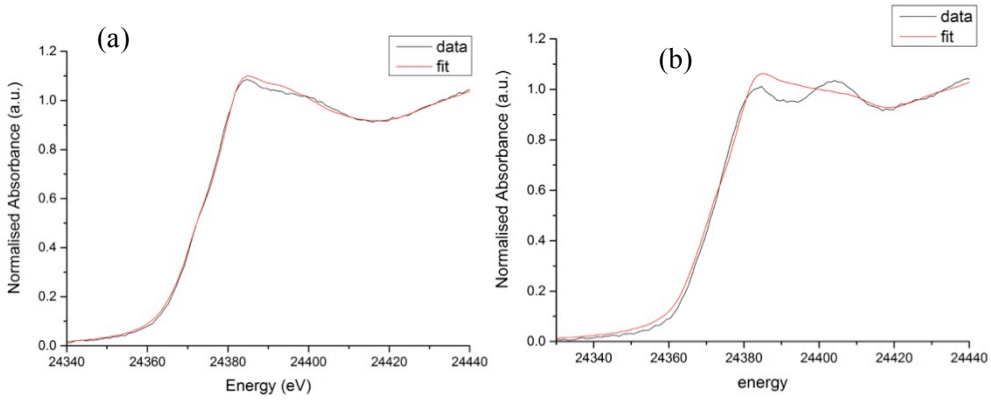

Figure 4-4 - Plot of fit from LCF model for the initial and final scans for room temperature reduction. Fitting range -20 to 14 (relative to E_0 24350 eV).

Similar LCF fitting of data during the temperature ramp to 573 K reveals that full conversion to the metal does not occur, with the material changing from 50% to 62.5% Pd metal by the end of the reduction phase (Figure 4-6). Upon cooling there is no further change in the material according to linear combination analysis, it remains as the Pd metal with no reversion to the oxide (Figure 4-9). It should be noted that once again there are discrepancies in the LCF model between the initial and final scans (Figure 4-7 and Figure 4-10); comparison with the EXAFS fits should shed light on the accuracy of the LCF models.

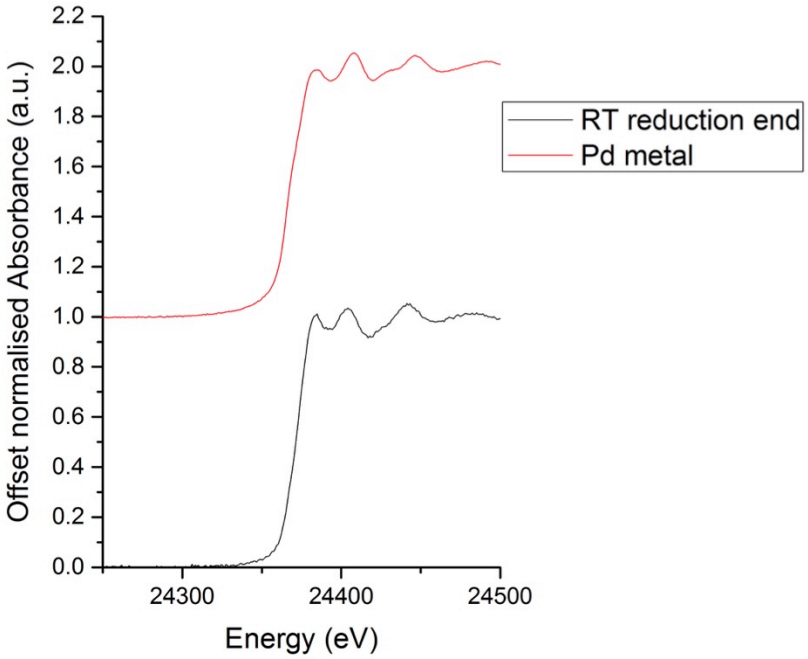

Figure 4-5 - Comparison of normalised XANES spectra for Pd metal standard and material at the end of the room temperature reduction.

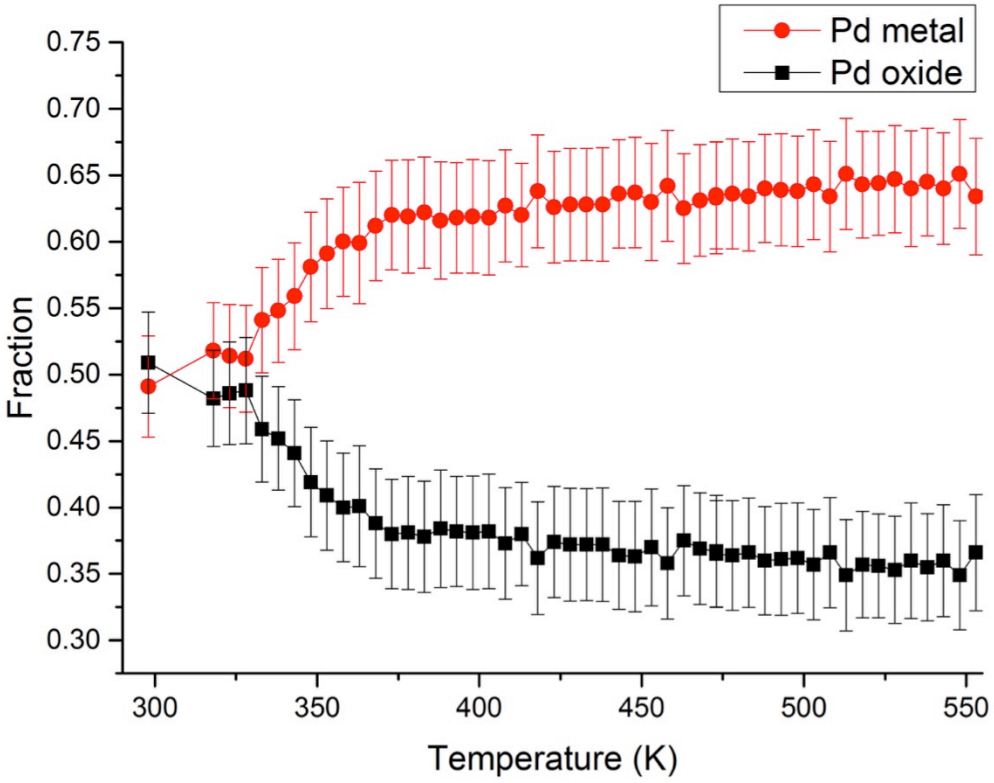

Figure 4-6 - Linear combination fit (LCF) of in situ Pd/Ceria/Alumina catalyst heated to 573 K under H_2/He. Fitting range -20 to 14 (relative to E_0 24350 eV).

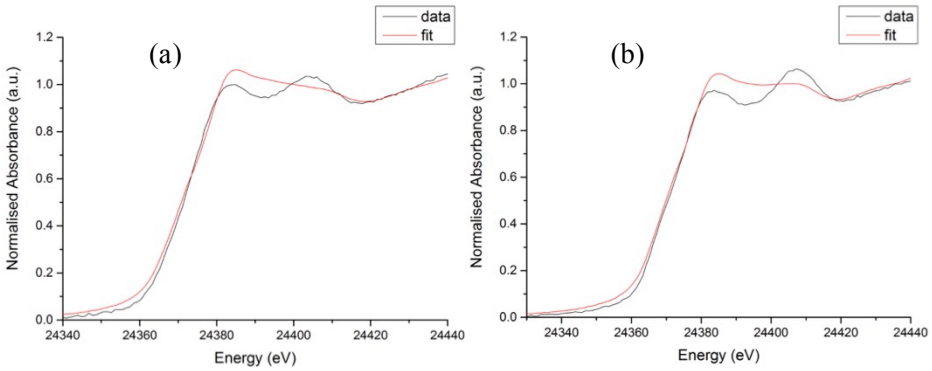

Figure 4-7 - First scan (a) and final scan (b) from LCF fit in the range -20 to 14 relative to E_0 24350 eV.

Comparison of the edge position with standards can be used to estimate the oxidation state of the material (Figure 4-8). The edge position of the material at the end of the room temperature reduction is 24369 eV, which is above the edge energy for palladium oxide (ca 24371 eV). From the LCF fit the majority of the material (62.5%) is in the Pd metal phase, which fits with the change in edge position. However it is still slightly higher than the edge position of the Pd metal (ca 24368 eV), which is indicative of the mixed phase nature of the material. After the reduction ramp to 350^{o}C the edge position shifts again to 24368 eV, whilst after cooling it shifts to 24368.7 eV indicating a complete reduction to the metal. Edge energy analysis is in agreement with LCF findings, and is more reliable due to the minor inaccuracies of some of the LCF models.

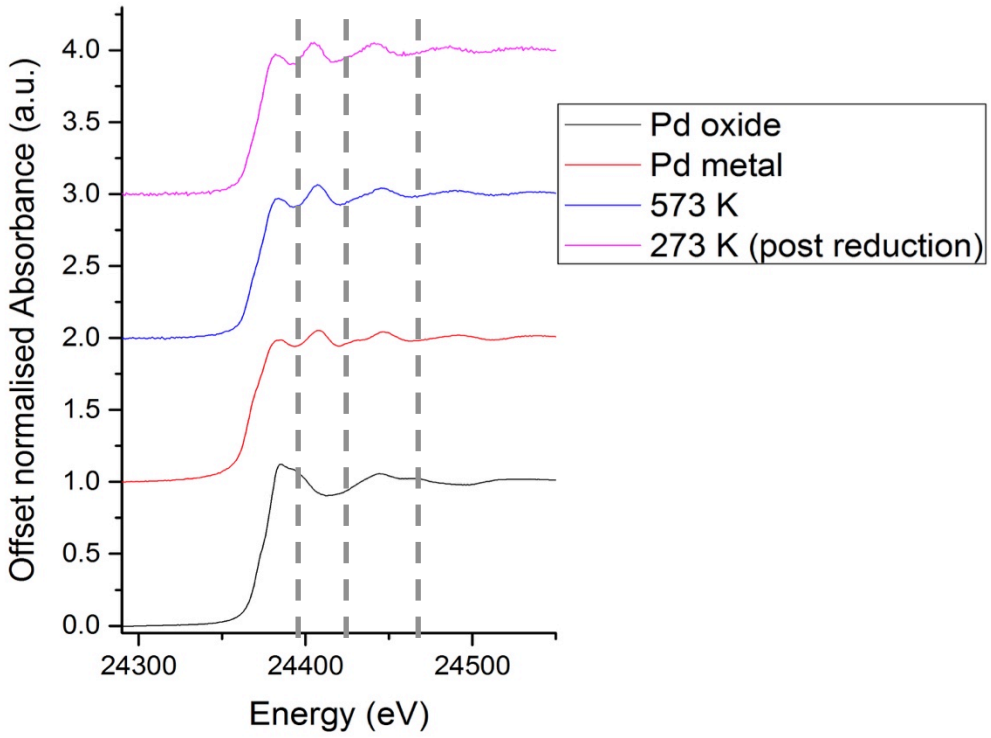

Figure 4-8 - Comparison of the Pd data at the end of the room temperature reduction and at 573K with the PdO and Pd metal standards.

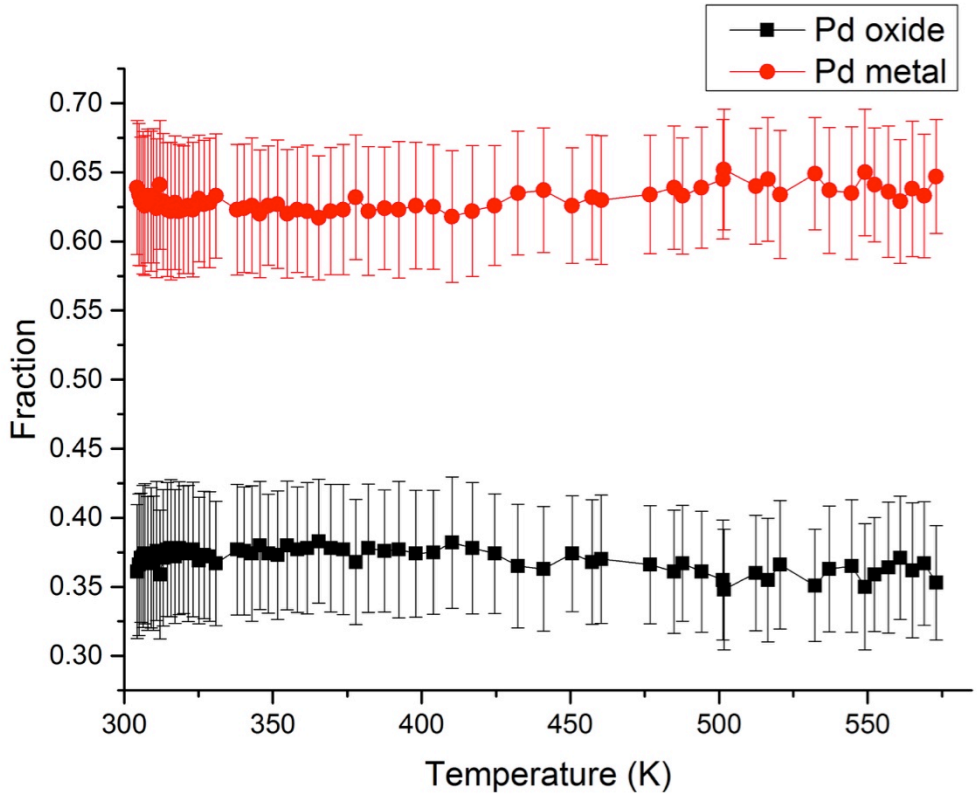

Figure 4-9 - Linear combination fit (LCF) of in situ Pd/Ceria/Alumina catalyst heated to 300°C under H_2/He. Fitting range -20 to 25 (relative to E_0 24350 eV).

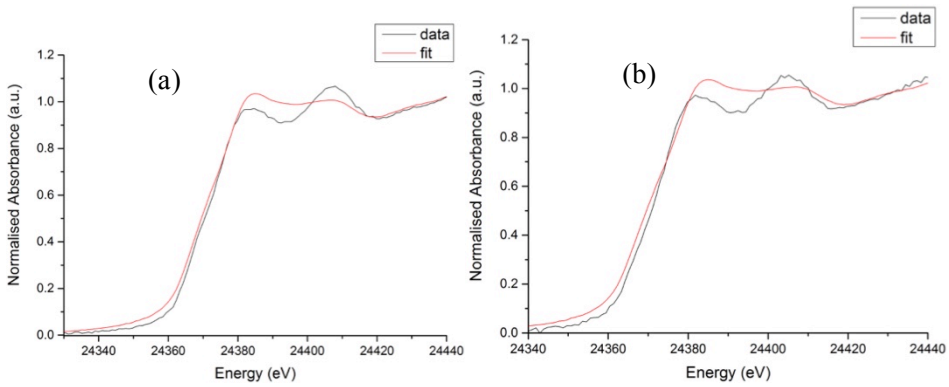

Figure 4-10 - Derivative first scan (a) and derivative final scan (b) from LCF fit in the range -20 to 14 relative to E_0 24350 eV.

From the XANES analysis it can be said that the majority of the reduction proceeds at room temperature, with the maximum reduction of the material occurring by 373 K. Comparison of the edge energy with standards provides additional information that the material doesn't completely reduce. Further comparison with EXAFS analysis will be used to provide more information on the changes in the local structure of the material.

4.4 EXAFS Analysis

In this section the EXAFS analysis will be discussed. In order to help with visualizing and interpreting the data, the various shells for the Pd K-edge analysis discussed in this section are presented below. Figure 4-11 and Figure 4-12 are representative of the PdO first and second shells respectively, with the first shell consisting of oxygen nearest neighbours at a distance of 2 Å and the second shell composed of Pd atoms at a distance of 3 Å. Figure 4-13 and Figure 4-14 are diagrams of the first and second shells of Pd metal. Details on bond distances and coordination numbers are provided in Table 4-1-and Table 4-2.

Table 4-1- Scattering paths and details for PdO.

Shell	Scatterer	Bond distance (Å)	Coordination number
1	O	2.02	4
2	Pd	3.02	4
3	Pd	2.40	8

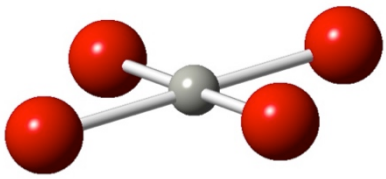

Figure 4-11 - Diagram of the first shell of PdO showing a palladium core, with 4 oxygen nearest neighbours at a distance of 2 Å.

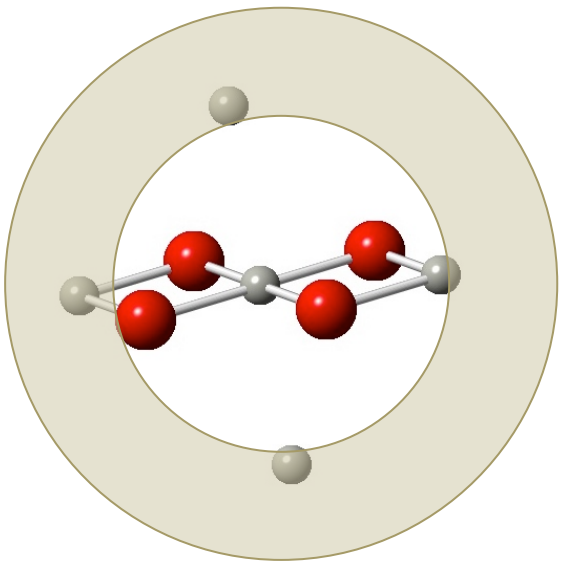

Figure 4-12 - Diagram showing the second shell of PdO, consisting of 4 Pd atoms at a distance of 3 Å.

Table 4-2 - Scattering paths and details for Pd metal.

Shell	Scatterer	Bond distance (Å)	Coordination number
1	Pd	2.75	12
2	Pd	3.88	6

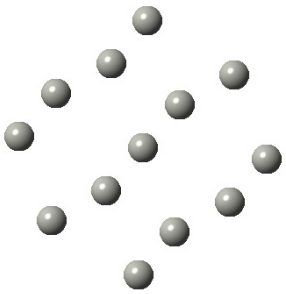

Figure 4-13 - Diagram showing the first shell of Pd metal, which has central Pd atom surrounded by 12 neighbouring Pd atoms at a distance of 2.75 Å.

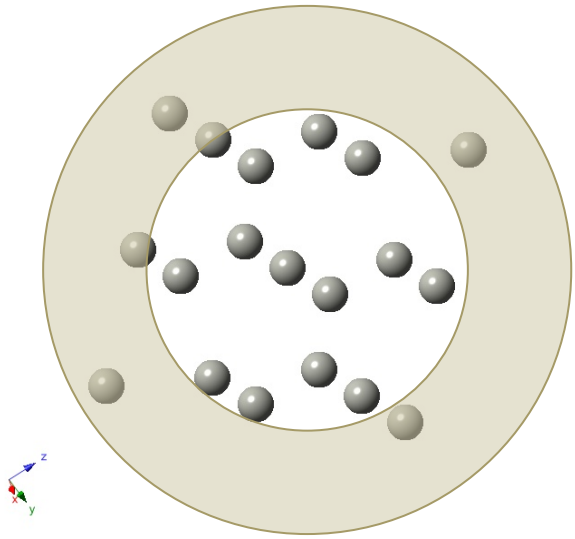

Figure 4-14 - Second shell of Pd metal showing 6 neighbouring Pd atoms at a distance of 3.88 Å.

At room temperature there are several peaks present in the Fourier transform; the k^3-weighted data is reasonably clear in the fitting region, indicating that the multiple peaks are real (Figure 4-15). At the end of the room temperature reduction the material appears reduced with a large peak present at 2.8 Å, there is also a small peak at 2.0 Å indicating the presence of Pd-O and suggesting the reduction has not gone to completion (Figure 4-16). During the reduction the magnitude of the Pd-O peak decreases, whilst the magnitude of the Pd-Pd peak increases (Figure 4-17). By the end of the reduction ramp to 573 K the material appears to be fully reduced with the peak at 2.0 Å lowering to a magnitude of ca, 1 (Figure 4-18). Upon cooling back to room temperature there is no increase in the peak at 2.0 Å, with the material

remaining in the metallic state, there is a small increase amount of noise in the K-space but not large enough for concern (Figure 4-19).

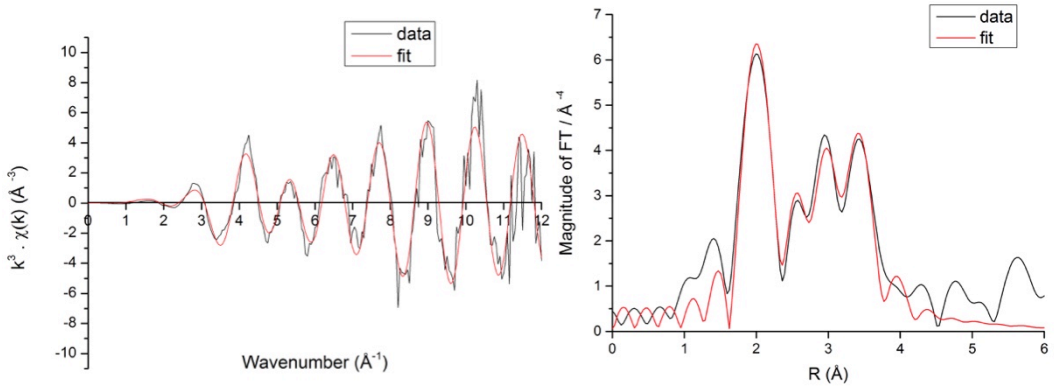

Figure 4-15 - Plot of the k-space k^3 weighted data and the Fourier transform for the material at the beginning of the temperature reduction ramp (303 K).

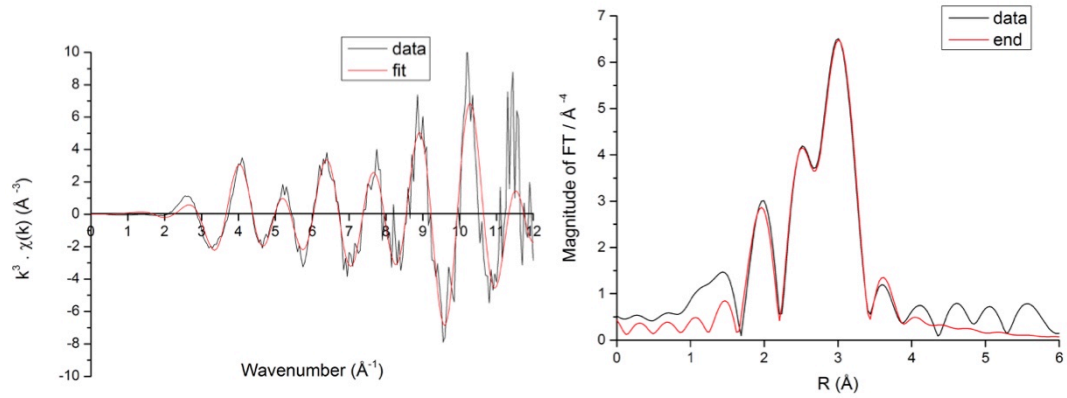

Figure 4-16 – Plot of the k-space k^3 weighted data and the Fourier transform for the material at the end of the room temperature reduction.

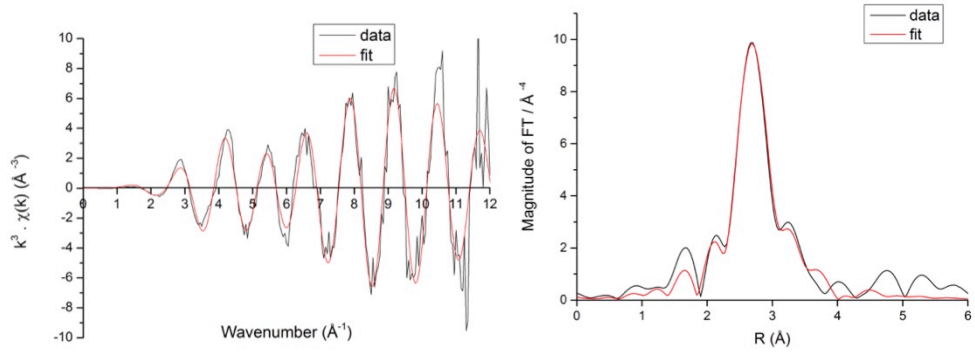

Figure 4-17 - Plot of the k-space k^3 weighted data and the Fourier transform for the material during the temperature reduction ramp (373 K).

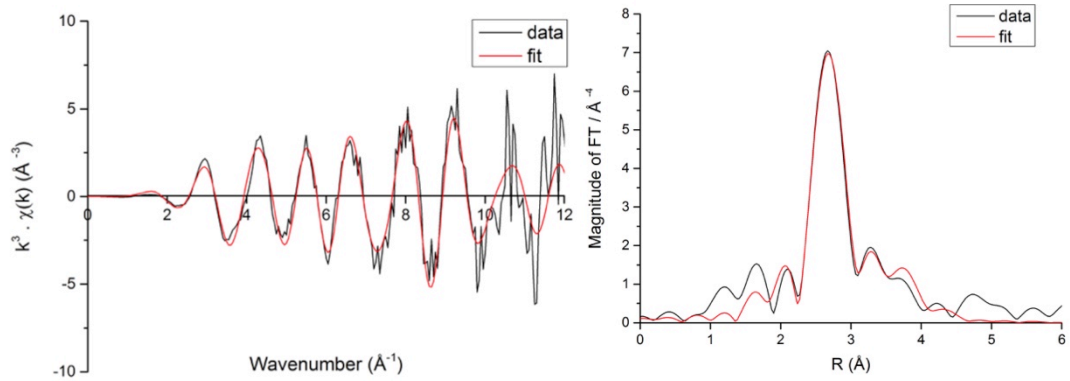

Figure 4-18 - Plot of the k-space k^3 weighted data and the Fourier transform for the material during the reduction at 573 K.

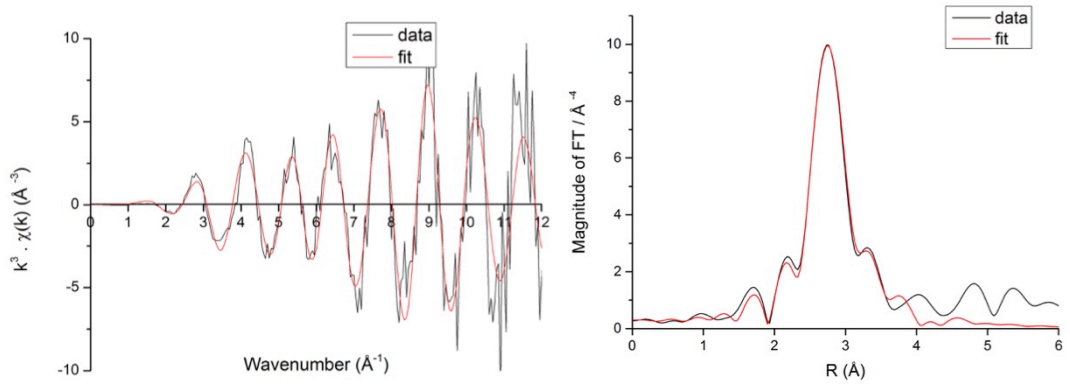

Figure 4-19 - Plot of the k-space k^3 weighted data and the Fourier transform for the material at the end of the cooling step of the reduction (300 K).

The Fourier transform of the data taken during the room temperature reduction, shows a clear change from the initial oxide to a more metallic state (Figure 4-20). However the FT also shows that the conversion is not complete as the peak at ca 1.5Å corresponding to the Pd-O shell is still present at the end of the room temperature reduction, though with a significantly lower magnitude.

This matches the results obtained from the LCF fit. The change in intensity of the Pd-O peak, from 8 to 3.1 is matched by the appearance and increase of the Pd-Pd peak at ca 2.5Å. As the magnitude of the peak is related to number of atoms in the shell, this can be interpreted as the gradual breakdown of the Pd-O followed by the growth of Pd nanoparticles. As the coordination number of the Pd-O shell is 4, assuming the initial material matches the literature value for the first shell, the number of atoms in the shell drops to approximately 1.33. This is a speculative answer but can serve as a basis for more detailed analysis. The full table of results for the room temperature reduction can be found in Table 4-3.

Table 4-3 - Results from EXAFS fitting of room temperature reduction data from Pd catalyst.

				PdO											Pd Metal				
				Pd-O first shell											Pd- Pd first shell				
File	R-factor	E0	error (E0)	x1	error	CN	S02	R	error	ss2	error	x2	error	CN	S02	R	error	ss2	error
72939	0.0092	-1.48	2.399	1.00	0.00	4.00	0.78	2.02	0.0122	0.0007	0.0010	0.00	0.00	0.00	0.00	2.68	0.1620	-0.0552	0.1487
72940	0.0073	-3.70	1.478	0.97	0.11	3.90	0.76	2.00	0.0110	0.0006	0.0014	0.03	0.11	0.31	0.02	2.78	0.2255	0.0024	0.0336
72941	0.0128	-0.60	-0.603	0.90	0.08	3.58	0.70	2.02	0.0073	0.0001	0.0009	0.10	0.08	1.25	0.08	2.93	0.0035	0.0000	0.0357
72942	0.0121	-0.60		0.89	0.07	3.56	0.69	2.01	0.0069	0.0003	0.0009	0.11	0.07	1.32	0.09	2.95	0.0300	0.0003	0.0036
72943	0.0110	0.15	0.937	0.97	0.08	3.88	0.76	2.02	0.0074	0.0003	0.0009	0.03	0.08	0.36	0.02	2.93	0.0395	-0.0067	0.0078
72944	0.0209	-0.13	1.292	1.00	0.00	4.00	0.78	2.03	0.0110	0.0011	0.0009	0.00	0.00	0.00	0.00	2.91	0.0333	-0.0232	0.0247
72945	0.0139	-1.26	1.143	1.00	0.01	4.00	0.78	2.02	0.0091	0.0007	0.0007	0.00	0.01	0.01	0.00	2.89	0.0348	-0.0171	0.0348
72946	0.0456	-0.29	2.016	0.66	0.13	2.64	0.51	2.03	0.0153	0.0006	0.0020	0.34	0.13	4.08	0.27	2.93	0.0432	0.0091	0.0045
72948	0.0213	-2.26	1.397	0.66	0.09	2.64	0.52	2.01	0.0106	0.0072	0.0014	0.34	0.09	4.07	0.26	2.89	0.0270	0.0002	0.0026
72949	0.0344	-2.11	2.004	0.67	0.13	2.67	0.52	2.01	0.0153	0.0006	0.0021	0.33	0.13	3.99	0.26	2.90	0.0380	0.0063	0.0035
72950	0.0540	-5.57	2.399	0.59	0.17	2.37	0.46	1.98	0.0192	0.0014	0.0031	0.41	0.17	4.88	0.32	2.84	0.0396	0.0070	0.0034
72951	0.0676	-5.91	2.863	0.56	0.19	2.24	0.44	1.99	0.0215	0.0011	0.0036	0.44	0.19	5.28	0.34	2.83	0.0215	0.0085	0.0036
72952	0.0468	-2.78	3.826	0.67	0.32	2.67	0.52	2.02	0.0376	0.0034	0.0065	0.33	0.32	3.98	0.26	2.85	0.0582	0.0046	0.0087
72953	0.0468	-2.78	3.826	0.67	0.32	2.67	0.52	2.02	0.0376	0.0034	0.0065	0.33	0.32	3.98	0.26	2.85	0.0582	0.0046	0.0087
72954	0.0405	-5.18	2.161	0.62	0.17	2.47	0.48	2.00	0.02	0.0027	0.0035	0.38	0.17	4.59	0.30	2.83	0.0350	0.0065	0.0030
72955	0.0474	-6.95	2.292	0.50	0.17	2.02	0.39	1.98	0.0183	0.0012	0.0033	0.50	0.17	5.95	0.39	2.82	0.0321	0.0082	0.0026
72956	0.0801	-6.56	3.034	0.58	0.27	2.31	0.45	1.98	0.0301	0.0047	0.0062	0.42	0.27	5.06	0.33	2.82	0.0406	0.0066	0.0036
72957	0.0266	-2.96	1.612	0.48	0.17	1.90	0.37	2.01	0.1713	0.0032	0.0226	0.52	0.17	6.29	0.41	2.84	0.0213	0.0056	0.0032
72958	0.0266	-2.96	1.612	0.48	0.17	1.90	0.37	2.01	0.0226	0.0032	0.0048	0.52	0.17	6.29	0.41	2.84	0.0213	0.0056	0.0032
72959	0.0275	-4.28	3.089	0.53	0.28	2.13	0.42	2.00	0.0331	0.0052	0.0069	0.47	0.28	5.61	0.37	2.84	0.0378	0.0033	0.0056
72960	0.0271	-2.79	5.181	0.42	0.25	1.67	0.33	2.01	0.0464	0.0026	0.0076	0.58	0.25	6.98	0.45	2.85	0.0258	0.0061	0.0049
72961	0.0211	-3.03	4.120	0.44	0.21	1.76	0.34	2.01	0.0365	0.0022	0.0060	0.56	0.21	6.72	0.44	2.84	0.0228	0.0058	0.0041
72962	0.0626	-3.81	2.360	0.50	0.28	1.99	0.39	2.01	0.0368	0.0061	0.0084	0.50	0.28	6.04	0.39	2.84	0.0317	0.0053	0.0052
72963	0.0217	-3.70	1.441	0.48	0.16	1.91	0.37	2.01	0.0214	0.0041	0.0047	0.52	0.16	6.27	0.41	2.83	0.0184	0.0050	0.0031
72964	0.0500	-3.83	2.112	0.45	0.23	1.81	0.35	2.02	0.0321	0.0046	0.0072	0.55	0.23	6.58	0.43	2.84	0.0263	0.0060	0.0043
72965	0.0394	-3.92	1.871	0.45	0.21	1.78	0.35	2.01	0.0299	0.0048	0.0039	0.55	0.21	6.65	0.43	2.84	0.0299	0.0056	0.0068
72966	0.0612	-2.75	2.400	0.39	0.21	1.54	0.30	2.03	0.0314	0.0006	0.0064	0.61	0.21	7.37	0.48	2.85	0.0283	0.0070	0.0043
72967	0.0169	-3.85	1.200	0.47	0.14	1.89	0.37	2.00	0.0178	0.0034	0.0041	0.53	0.14	6.32	0.41	2.84	0.0163	0.0045	0.0028
72968	0.0273	-4.02	1.541	0.45	0.16	1.80	0.35	2.01	0.0190	0.0057	0.0032	0.55	0.16	6.61	0.43	2.84	0.0200	0.0016	0.0043
72969	0.0165	-3.79	1.268	0.40	0.12	1.59	0.31	2.01	0.0168	0.0002	0.0037	0.60	0.12	7.23	0.47	2.84	0.0152	0.0058	0.0025
72970	0.0265	-4.71	1.530	0.43	0.18	1.71	0.33	2.00	0.0245	0.0040	0.0058	0.57	0.18	6.88	0.45	2.83	0.0200	0.0059	0.0033
72971	0.0187	-4.14	1.270	0.40	0.14	1.61	0.32	2.00	0.0180	0.0013	0.0041	0.60	0.14	7.16	0.47	2.84	0.0162	0.0059	0.0027
72972	0.0159	-4.19	1.188	0.44	0.14	1.76	0.34	2.00	0.0184	0.0038	0.0043	0.56	0.14	6.72	0.44	2.83	0.0156	0.0056	0.0026
72973	0.0175	-4.20	1.247	0.36	0.13	1.45	0.28	2.00	0.0190	0.0064	0.0045	0.64	0.13	7.64	0.50	2.84	0.0157	0.0012	0.0025
72974	0.0232	-4.07	1.470	0.39	0.15	1.57	0.31	2.01	0.0214	0.0014	0.0048	0.61	0.15	7.30	0.48	2.84	0.0173	0.0058	0.0028
72975	0.0181	-3.95	1.257	0.36	0.14	1.42	0.28	2.00	0.0199	0.0012	0.0047	0.64	0.14	7.73	0.50	2.84	0.0154	0.0059	0.0025
72976	0.0181	-3.95	1.257	0.36	0.14	1.42	0.28	2.00	0.0199	0.0012	0.0047	0.64	0.14	7.73	0.50	2.84	0.0154	0.0059	0.0025
72977	0.0119	-5.44	1.180	0.33	0.12	1.32	0.26	2.00	0.0181	0.0011	0.0042	0.67	0.12	8.05	0.52	2.82	0.0139	0.0075	0.0023
72978	0.0119	-5.44	1.180	0.33	0.12	1.32	0.26	2.00	0.0181	0.0011	0.0042	0.67	0.12	8.05	0.52	2.82	0.0139	0.0075	0.0023
72979	0.0173	-5.75	1.363	0.20	0.09	0.80	0.16	1.98	0.0152	-0.0056	0.0037	0.80	0.09	9.60	0.62	2.83	0.0168	0.0090	0.0021
72980	0.0130	-5.16	1.097	0.31	0.11	1.23	0.24	1.99	0.0158	-0.0007	0.0038	0.69	0.11	8.30	0.54	2.83	0.0132	0.0070	0.0020
72981	0.0252	-5.59	1.546	0.32	0.23	1.26	0.25	1.99	0.0375	0.0059	0.0105	0.68	0.23	8.21	0.53	2.82	0.0213	0.0067	0.0034

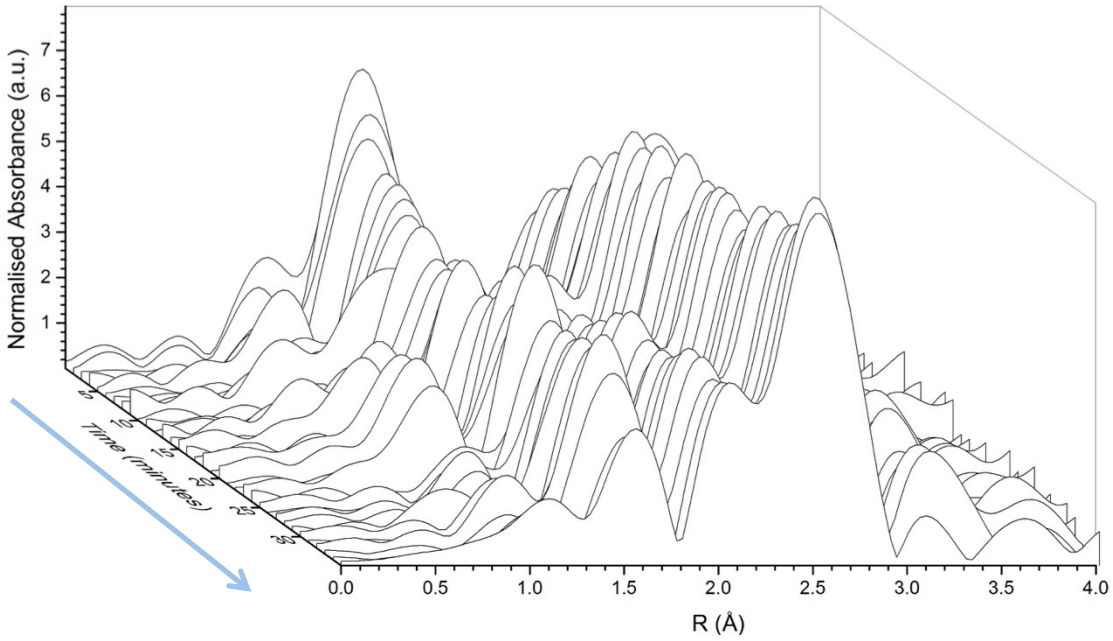

Figure 4-20 - Plot of the Fourier transform of the EXAFS data from the room temperature reduction (not phase-corrected).

Artemis software was used to fit the experimental data and obtain information about the bond lengths and coordination numbers of the PdO and Pd phases. The first shells of PdO and Pd, Pd-O and Pd-Pd respectively were used to fit the data utilising a k-range of 2.5-12 and an R-range of 1-3 Å.

Analysis of the EXAFS region compares favourably with the XANES findings; the material reduces at room temperature, though not completely and reduces further on heating to 573 K. Comparison of the change in bond length of the Pd metal reveals that after the room temperature reduction the bond length is higher than the literature value; 2.84 Å from experimental data compared with 2.75 Å from literature and standard values (Figure 4-21).

During the room temperature reduction the bond distance for the PdO shell remains fairly consistent around the literature value, with a variation of ±0.03Å (Figure 4-21). The value is slightly lower than the literature value at the end of the room temperature reduction, a value of around 1.98 Å. The bond distance for the Pd-Pd shell for the Pd metal phase is fairly large initially. However it should be pointed out that at the initial stage the amount of Pd metal phase present is quite minimal, leading to larger errors in the values obtained. What is far more interesting is once a definite Pd metal phase has been formed the bond distance is found to be higher than that expected for Pd-Pd first shell bond in Pd metal, with a value of 2.84Å as opposed to 2.75Å from literature.

This increased bond distance is however in agreement with the reported bond distance for Pd-Pd in Pd hydride clusters. Palladium hydrides are formed when Pd metal is exposed to hydrogen rich environments. The hydrogen is able to permeate the lattice and fill interstitial spaces, with the extent of hydrogen uptake resulting in either α- or β- hydride formation.

This change in the bond distance could indicate the formation of an intermediate Pd hydride phase, which is lost upon heating as the hydrogen is driven from the structure. Further investigation can be used to reinforce this theory, such as analysis of mass spectroscopy data, which should reveal a small increase in the H_2 signal upon heating if this is the case.

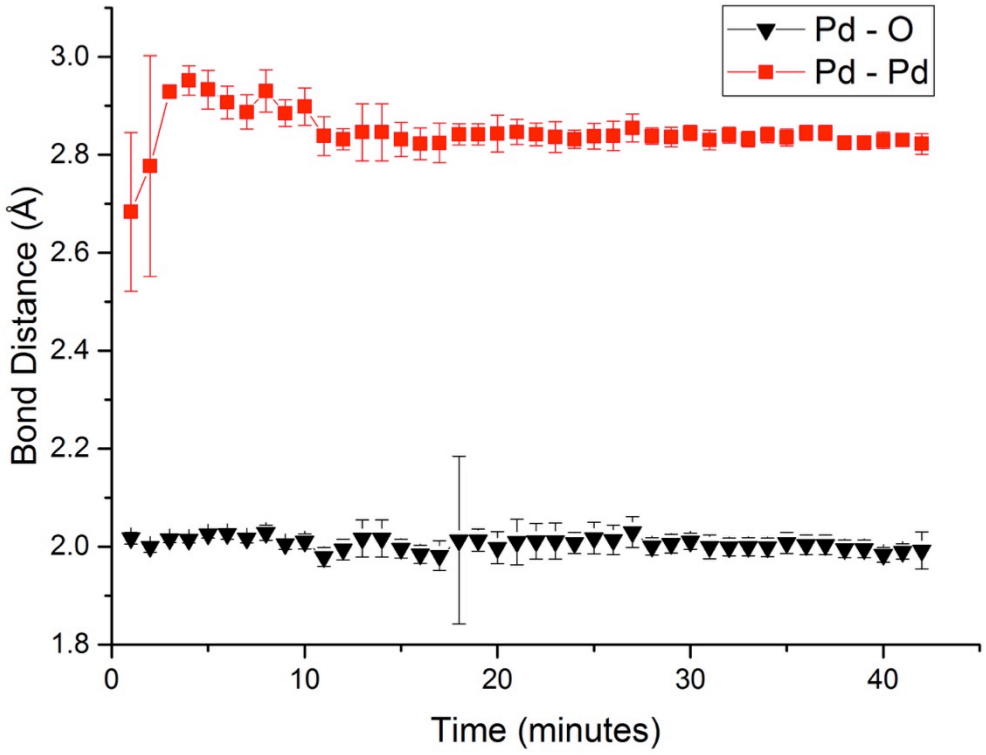

Figure 4-21 - Plot of change in the bond distance against time for the in situ Pd/Ceria/Alumina catalyst under H2/He atmosphere at room temperature.

During the temperature ramp there is a large change in bond distance between 323 – 373 ^{o}C, corresponding to a time difference of 10 minutes (Figure 4-22). This change is evidence of the removal of the Pd hydride phase, as the bond distance returns to the expected value of 2.75 Å, The bond length continues to reduce with increasing temperature, stabilising at around 2.73 Å, though these are expected to be thermal factors influencing the fitting. The full table of results for the temperature ramp are provided in Table 4-4.

Table 4-4 - Results from reduction ramp of Pd catalyst.

	amp	= 0.77972000					PdO								Pd Metal				
							Pd-O first shell								Pd- Pd first shell				
File	R-factor	E0	error (E0)	x1	error	CN	S02	R	error	ss2	error	x2	error	CN	S02	R	error	ss2	error
72981	0.0252	-5.59	1.546	0.32	0.23	1.26	0.25	1.99	0.0375	0.0059	0.0105	0.68	0.23	8.21	0.53	2.82	0.0213	0.0067	0.0034
72986	0.0127	-4.86	2.305	0.31	0.19	1.24	0.24	1.96	0.0317	0.0103	0.0091	0.69	0.19	8.27	0.54	2.77	0.0638	0.0204	0.0057
72987	0.0204	-7.98	2.868	0.05	0.07	0.22	0.04	1.99	0.0334	-0.0101	0.0096	0.95	0.07	11.35	0.74	2.75	0.0817	0.0233	0.0070
72988	0.0166	-3.41	1.017	0.14	0.08	0.57	0.11	1.99	0.0166	-0.0058	0.0040	0.86	0.08	10.29	0.67	2.82	0.0126	0.0075	0.0014
72989	0.0558	-5.25	3.034	0.52	0.46	2.06	0.40	1.96	0.0798	0.0275	0.0200	0.48	0.46	5.82	0.38	2.82	0.1516	0.0125	0.0225
72990	0.0118	-3.45	1.386	0.05	0.04	0.21	0.04	1.95	0.0177	-0.0116	0.0055	0.95	0.04	11.36	0.74	2.80	0.0092	0.0111	0.0017
72991	0.0129	-8.04	1.900	0.00	0.01	0.00	0.00	1.91	0.0461	-0.0295	0.0250	1.00	0.01	11.99	0.78	2.74	0.0509	0.0223	0.0044
72992	0.0112	-4.10	1.414	0.04	0.05	0.16	0.03	1.96	0.0238	-0.0114	0.0074	0.96	0.05	11.51	0.75	2.79	0.0096	0.0111	0.0016
72993	0.0159	-8.89	2.084	0.28	0.28	1.10	0.22	1.91	0.3156	0.0553	0.0859	0.72	0.28	8.69	0.57	2.76	0.0169	0.0080	0.0022
72994	0.0222	-5.73	1.237	0.01	0.00	0.05	-	-	-	-	-	0.99	0.00	11.86	0.91	2.77	0.0163	0.0119	0.0026
72995	0.0175	-5.27	1.007	-0.17	0.22	-0.69	-	-	-	-	-	1.17	0.22	14.06	0.91	2.77	0.0156	0.0113	0.0024
72996	0.0101	-6.13	0.503	0.09	0.07	0.38	-	-	-	-	-	0.91	0.07	10.87	0.71	2.75	0.0046	0.0093	0.0007
72997	0.0125	-6.24	0.543	0.07	0.07	0.28	-	-	-	-	-	0.93	0.07	11.17	0.73	2.75	0.0051	0.0097	0.0007
72998	0.0098	-4.46	0.473	0.06	0.07	0.23	-	-	-	-	-	0.94	0.07	11.31	0.74	2.75	0.0047	0.0100	0.0007
72999	0.0100	-6.38	0.478	0.03	0.07	0.10	-	-	-	-	-	0.97	0.07	11.69	0.76	2.75	0.0046	0.0103	0.0007
73000	0.0117	-6.27	0.529	0.05	0.07	0.18	-	-	-	-	-	0.95	0.07	11.45	0.74	2.75	0.0049	0.0100	0.0007
73001	0.0081	-5.08	0.415	0.05	0.06	0.18	-	-	-	-	-	0.95	0.06	11.45	0.74	2.74	0.0043	0.0104	0.0006
73002	0.0057	-6.39	0.363	0.02	0.05	0.10	-	-	-	-	-	0.98	0.05	11.70	0.76	2.74	0.0037	0.0105	0.0005
73003	0.0086	-6.43	0.444	0.03	0.06	0.13	-	-	-	-	-	0.97	0.06	11.60	0.75	2.74	0.0045	0.0105	0.0006
73004	0.0129	-6.62	0.521	-0.03	0.07	-0.10	-	-	-	-	-	1.03	0.07	12.30	0.80	2.74	0.0055	0.0117	0.0008
73005	0.0125	-4.70	0.541	0.07	0.07	0.27	-	-	-	-	-	0.93	0.07	11.19	0.73	2.74	0.0051	0.0102	0.0008
73006	0.0127	-6.10	0.533	0.04	0.07	0.17	-	-	-	-	-	0.96	0.07	11.48	0.75	2.75	0.0051	0.0100	0.0007
73007	0.0093	-6.72	0.445	0.00	0.06	0.01	-	-	-	-	-	1.00	0.06	11.96	0.78	2.74	0.0046	0.0112	0.0007
73008	0.0053	-6.39	0.362	0.02	0.05	0.10	-	-	-	-	-	0.98	0.05	11.70	0.76	2.74	0.0037	0.0108	0.0005
73009	0.0078	-6.36	0.416	0.01	0.06	0.02	-	-	-	-	-	0.99	0.06	11.93	0.78	2.74	0.0044	0.0113	0.0006
73010	0.0042	-4.80	0.315	0.02	0.04	0.09	-	-	-	-	-	0.98	0.04	11.72	0.76	2.74	0.0033	0.0107	0.0005
73011	0.0143	-6.48	0.534	0.02	0.07	0.08	-	-	-	-	-	0.98	0.07	11.76	0.76	2.74	0.0055	0.0114	0.0008
73012	0.0084	-6.55	0.447	0.09	0.06	0.36	-	-	-	-	-	0.91	0.06	10.91	0.71	2.74	0.0043	0.0102	0.0006
73013	0.0059	-6.80	0.378	0.00	0.05	-0.02	-	-	-	-	-	1.00	0.05	12.06	0.78	0.78	0.0040	0.0117	0.0006
73014	0.0113	-6.37	0.553	0.01	0.08	0.05	-	-	-	-	-	0.99	0.08	11.86	0.77	2.74	0.0052	0.0113	0.0008
73015	0.0086	-5.87	0.483	0.10	0.07	0.42	-	-	-	-	-	0.90	0.07	10.74	0.70	2.73	0.0052	0.0109	0.0008
73016	0.0251	-7.37	0.747	0.06	0.10	0.23	-	-	-	-	-	0.94	0.10	11.30	0.74	2.72	0.0074	0.0111	0.0011
73017	0.0067	5.15	0.407	0.03	0.06	0.13	-	-	-	-	-	0.97	0.06	11.62	0.76	2.74	0.0041	0.0113	0.0006
73018	0.0079	-6.79	0.412	0.03	0.06	0.10	-	-	-	-	-	0.97	0.06	11.70	0.76	2.73	0.0045	0.0117	0.0006
73019	0.0102	-6.57	0.466	0.05	0.07	0.19	-	-	-	-	-	0.95	0.07	11.43	0.74	2.74	0.0050	0.0110	0.0007
73020	0.0139	-6.67	0.513	0.00	0.07	0.00	-	-	-	-	-	1.00	0.07	12.01	0.78	2.73	0.0056	0.0121	0.0008
73021	0.0066	-6.49	0.383	0.07	0.05	0.28	-	-	-	-	-	0.93	0.05	11.16	0.73	2.74	0.0039	0.0109	0.0006
73022	0.0114	-6.51	0.479	0.05	0.07	0.18	-	-	-	-	-	0.95	0.07	11.45	0.74	2.73	0.0053	0.0118	0.0008
73023	0.0135	-6.26	0.487	-0.01	0.07	-0.05	-	-	-	-	-	1.01	0.07	12.14	0.79	2.74	0.0056	0.0125	0.0008
73024	0.0165	-7.02	0.585	0.04	0.08	0.16	-	-	-	-	-	0.96	0.08	11.52	0.75	2.73	0.0062	0.0122	0.0009
73025	0.0141	-5.32	0.485	-0.05	0.07	-0.22	-	-	-	-	-	1.05	0.07	12.65	0.82	2.73	0.0060	0.0136	0.0009
73026	0.0139	-6.94	0.512	-0.04	0.07	-0.17	-	-	-	-	-	1.04	0.07	12.52	0.81	2.73	0.0062	0.0134	0.0009
73027	0.0111	-6.30	0.439	-0.01	0.06	-0.05	-	-	-	-	-	1.01	0.06	12.15	0.79	2.74	0.0052	0.0130	0.0007
73028	0.0237	-6.81	0.690	0.04	0.09	0.16	-	-	-	-	-	0.96	0.09	11.51	0.75	2.73	0.0076	0.0125	0.0011
73029	0.0160	-6.43	0.560	0.02	0.08	0.09	-	-	-	-	-	0.98	0.08	11.73	0.79	2.74	0.0052	0.0130	0.0007
73031	0.0111	-6.30	0.439	-0.01	0.06	-0.05	-	-	-	-	-	1.01	0.06	12.15	0.79	2.74	0.0052	0.0130	0.0007
73032	0.0237	-6.81	0.690	0.04	0.09	0.16	-	-	-	-	-	0.96	0.09	11.51	0.75	2.73	0.0076	0.0125	0.0011
73033	0.0160	-6.43	0.560	0.02	0.08	0.09	-	-	-	-	-	0.98	0.08	11.73	0.76	2.73	0.0063	0.0128	0.0009
73034	0.0252	-6.74	0.681	0.06	0.09	0.25	-	-	-	-	-	0.94	0.09	11.24	0.73	2.73	0.0075	0.0123	0.0011
73035	0.0131	-5.25	0.469	-0.05	0.07	-0.19	-	-	-	-	-	1.05	0.07	12.57	0.82	2.74	0.0058	0.0136	0.0008
73036	0.0136	-5.40	0.510	-0.03	0.07	-0.10	-	-	-	-	-	1.03	0.07	12.31	0.80	2.73	0.0063	0.0136	0.0009
73039	0.0177	-7.26	0.621	-0.05	0.09	-0.19	-	-	-	-	-	1.05	0.09	12.57	0.82	2.72	0.0069	0.0134	0.0010
73040	0.0567	-7.00	1.019	-0.27	0.17	-1.06	-	-	-	-	-	1.27	0.17	15.19	0.99	2.73	0.0146	0.0179	0.0021
73041	0.0233	-6.66	0.645	-0.01	0.09	-0.04	-	-	-	-	-	1.01	0.09	12.12	0.79	2.73	0.0075	0.0129	0.0011
73042	0.0134	-6.53	0.504	0.01	0.07	0.02	-	-	-	-	-	0.99	0.07	11.93	0.78	2.73	0.0062	0.0133	0.0009

Upon cooling the bond distance remains around the expected 2.75 Å value within errors until the temperature reaches 423 K; below this temperature the bond distance increases to 2.82 Å. This is most likely due to a reformation of the hydride phase at room temperature as this is the same value obtained during the initial reduction at room temperature. From this result it can be said that the change in the bond distance can be used as an indicator of hydride phase formation. This can have some use in material characterisation and be used to explain behaviour of palladium catalysts in hydrogen rich environments.

Upon cooling to room temperature the coordination number of the Pd metal first shell remains at approximately 10 (10.38 Å from the fitting model). However the bond length of the material increases, from ca 2.73Å to 2.80 Å (Figure 4-22). This is 0.04 Å less than the bond distance of the initial mixed phased material formed after the room temperature reduction. As mentioned before this could still be used to indicate that there is an intermediate palladium hydride phase present in the material, as this would result in an increase in the Pd-Pd bond distance. Full results from the cooling fits are available in Table 4-5.

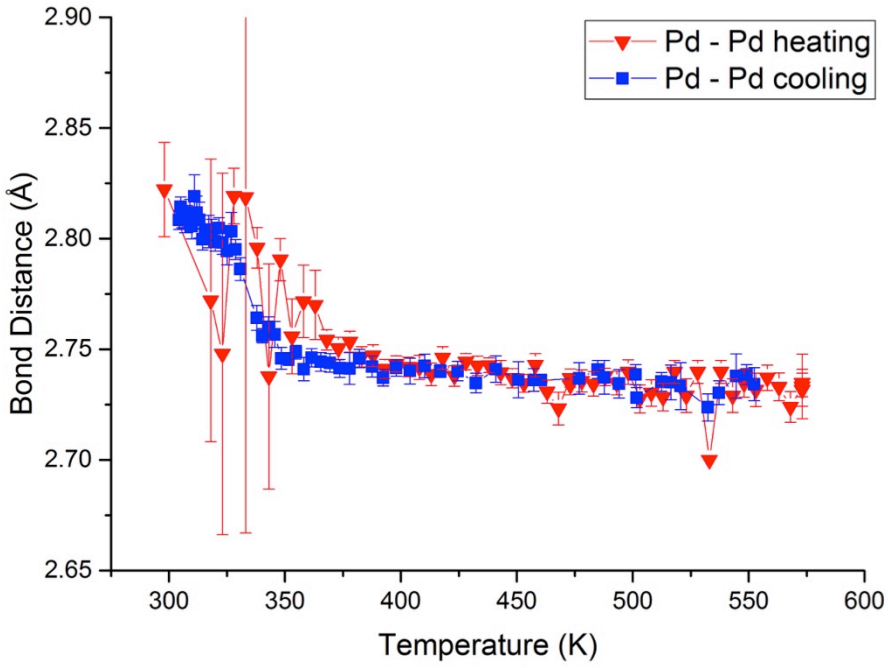

Figure 4-22 - Plot of change in the bond distance of the Pd metal first shell against temperature for the in situ Pd/Ceria/Alumina catalyst under H_2/He atmosphere.

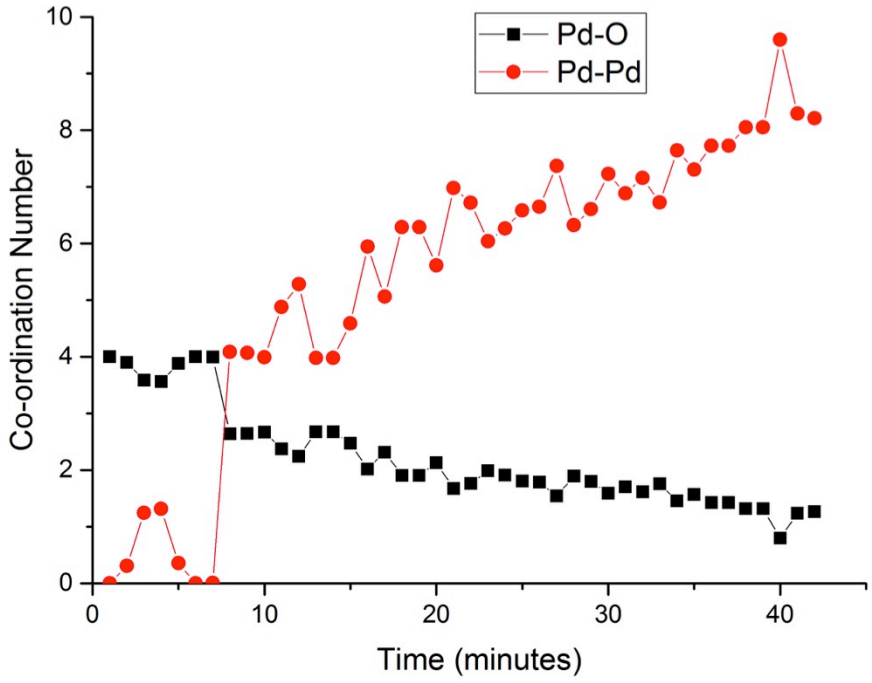

Figure 4-23 - Plot of change in the coordination number against time for the in situ Pd/ceria/alumina catalyst under H_2/He atmosphere.

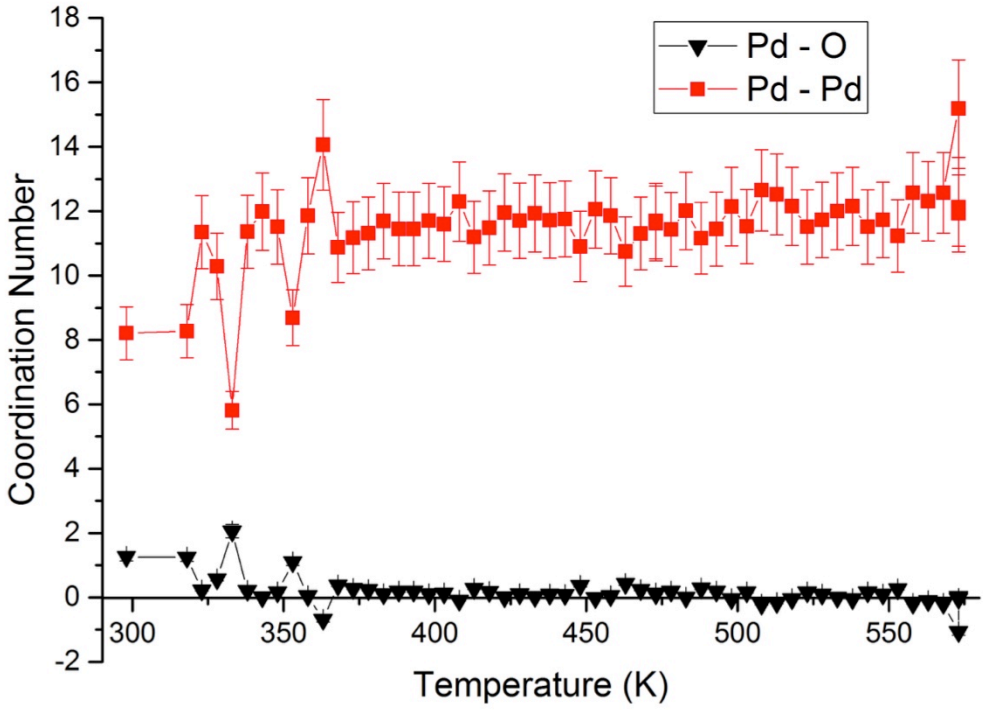

Figure 4-24 - Plot of change in the coordination number against temperature for the in situ reduction of Pd/ceria/alumina catalyst under H_2/He atmosphere.

Table 4-5 - EXAFS results from cooling of Pd catalyst.

				PdO Pd-O first shell										Pd Metal Pd- Pd first shell					
File	R-factor	E0	error (E0)	x1	error	CN	S02	R	error	ss2	error	x2	error	CN	S02	R	error	ss2	error
73043	0.0204	-5.97	0.635	0.00	0.09	0.01	-	-	-	-	-	1.00	0.09	11.96	0.78	2.73	0.0074	0.0130	0.0011
73044	0.0055	-5.89	0.372	-0.10	0.05	-0.38	-	-	-	-	-	1.10	0.05	13.14	0.85	2.74	0.0045	0.0142	0.0006
73045	0.0412	-5.43	0.822	-0.04	0.12	-0.16	-	-	-	-	-	1.04	0.12	12.49	0.81	2.74	0.0100	0.0134	0.0014
73046	0.0103	-5.81	0.486	0.01	0.07	0.04	-	-	-	-	-	0.99	0.07	11.89	0.77	2.73	0.0054	0.0123	0.0008
73047	0.0162	-6.45	0.529	-0.03	0.08	-0.11	-	-	-	-	-	1.03	0.08	12.33	0.80	2.72	0.0061	0.0128	0.0009
73049	0.0500	-6.05	0.937	-0.01	0.14	-0.05	-	-	-	-	-	1.01	0.14	12.16	0.79	2.73	0.0106	0.0126	0.0015
73050	0.0287	-5.80	0.765	0.08	0.10	0.33	-	-	-	-	-	0.92	0.10	11.01	0.72	2.74	0.0079	0.0105	0.0011
73051	0.0068	-5.88	0.345	-0.07	0.05	-0.28	-	-	-	-	-	1.07	0.05	12.83	0.83	2.74	0.0042	0.0132	0.0006
73052	0.0095	-5.18	0.457	-0.03	0.07	-0.10	-	-	-	-	-	1.03	0.07	12.31	0.80	2.73	0.0045	0.0101	0.0006
73054	0.0055	-5.89	0.372	-0.10	0.05	-0.38	-	-	-	-	-	1.10	0.05	13.14	0.85	2.74	0.0045	0.0142	0.0006
73055	0.0185	-5.95	0.566	-0.04	0.09	-0.15	-	-	-	-	-	1.04	0.09	12.46	0.81	2.73	0.0064	0.0122	0.0009
73056	0.0259	-5.72	0.693	-0.01	0.10	-0.06	-	-	-	-	-	1.01	0.10	12.17	0.79	2.74	0.0076	0.0119	0.0011
73058	0.0068	-5.58	0.377	-0.05	0.06	-0.22	-	-	-	-	-	1.05	0.06	12.65	0.82	2.74	0.0041	0.0124	0.0006
73059	0.0235	-5.77	0.711	0.05	0.10	0.19	-	-	-	-	-	0.95	0.10	11.44	0.74	2.74	0.0071	0.0105	0.0010
73060	0.0087	-5.83	0.433	0.02	0.06	0.08	-	-	-	-	-	0.98	0.06	11.77	0.76	2.74	0.0006	0.0108	0.0045
73061	0.0109	-5.76	0.494	0.01	0.07	0.04	-	-	-	-	-	0.99	0.07	11.89	0.77	2.74	0.0051	0.0111	0.0007
73062	0.0331	-5.74	0.780	0.04	0.11	0.17	-	-	-	-	-	0.96	0.11	11.50	0.75	2.74	0.0081	0.0105	0.0012
73063	0.0160	-5.54	0.557	-0.03	0.08	-0.11	-	-	-	-	-	1.03	0.08	12.33	0.80	2.74	0.0060	0.0115	0.0009
73064	0.0087	-5.90	0.443	0.03	0.06	0.11	-	-	-	-	-	0.97	0.06	11.67	0.76	2.73	0.0044	0.0104	0.0006
73065	0.0027	-5.62	0.278	0.01	0.04	0.03	-	-	-	-	-	0.99	0.04	11.90	0.77	2.74	0.0044	0.0107	0.0006
73066	0.0140	-5.63	0.551	0.03	0.08	0.12	-	-	-	-	-	0.97	0.08	11.63	0.77	2.74	0.0028	0.0107	0.0004
73067	0.0166	-5.73	0.551	-0.04	0.08	-0.17	-	-	-	-	-	1.04	0.08	12.50	0.76	2.74	0.0054	0.0102	0.0008
73068	0.0065	-5.65	0.372	0.00	0.05	0.00	-	-	-	-	-	1.00	0.05	11.99	0.81	2.74	0.0059	0.0110	0.0008
73069	0.0063	-5.89	0.389	0.04	0.06	0.17	-	-	-	-	-	0.96	0.06	11.50	0.78	2.74	0.0037	0.0105	0.0005
73070	0.0107	-5.64	0.509	0.03	0.07	0.12	-	-	-	-	-	0.97	0.07	11.65	0.75	2.74	0.0037	0.0094	0.0006
73071	0.0079	-5.38	0.449	0.07	0.06	0.27	-	-	-	-	-	0.93	0.06	11.20	0.76	2.74	0.0047	0.0098	0.0007
73072	0.0253	-5.72	0.787	0.02	0.11	0.08	-	-	-	-	-	0.98	0.11	11.77	0.73	2.75	0.0041	0.0092	0.0006
73073	0.0076	-5.80	0.429	0.01	0.06	0.05	-	-	-	-	-	0.99	0.06	11.85	0.77	2.74	0.0072	0.0098	0.0011
73074	0.0082	-5.66	0.453	0.03	0.06	0.13	-	-	-	-	-	0.97	0.06	11.61	0.77	2.74	0.0041	0.0096	0.0006
73075	0.0076	-5.57	0.444	-0.01	0.06	-0.03	-	-	-	-	-	1.01	0.06	12.10	0.75	2.74	0.0043	0.0096	0.0006
73076	0.0081	-5.55	0.428	0.03	0.06	0.12	-	-	-	-	-	0.97	0.06	11.64	0.79	2.74	0.0042	0.0096	0.0006
73077	0.0139	-5.81	0.602	0.09	0.08	0.37	-	-	-	-	-	0.91	0.08	10.90	0.76	2.75	0.0042	0.0096	0.0006
73078	0.0041	-5.53	0.343	0.04	0.05	0.16	-	-	-	-	-	0.96	0.05	11.51	0.71	2.74	0.0053	0.0088	0.0008
73079	0.0197	-5.83	0.711	0.02	0.10	0.08	-	-	-	-	-	0.98	0.10	11.75	0.75	2.75	0.0031	0.0089	0.0005
73080	0.0035	-5.84	0.310	-0.01	0.04	-0.04	-	-	-	-	-	1.01	0.04	12.12	0.79	2.75	0.0029	0.0095	0.0004
73081	0.0123	-5.81	0.548	0.08	0.08	0.31	-	-	-	-	-	0.92	0.08	11.07	0.72	2.75	0.0050	0.0085	0.0007
73082	0.0179	-5.27	0.639	0.03	0.09	0.14	-	-	-	-	-	0.97	0.09	11.59	0.75	2.76	0.0059	0.0092	0.0009
73083	0.0102	-5.24	0.496	0.03	0.07	0.13	-	-	-	-	-	0.97	0.07	11.60	0.75	2.76	0.0046	0.0092	0.0007
73084	0.0041	-5.54	0.321	0.01	0.05	0.04	-	-	-	-	-	0.99	0.05	11.89	0.77	2.76	0.0031	0.0098	0.0005
73085	0.0154	-5.51	0.611	0.03	0.09	0.11	-	-	-	-	-	0.97	0.09	11.68	0.76	2.76	0.0056	0.0095	0.0008
73088	0.0123	-5.19	0.518	0.02	0.08	0.08	-	-	-	-	-	0.98	0.08	11.76	0.76	2.79	0.0052	0.0103	0.0008
73089	0.0091	-5.29	0.455	0.00	0.06	-0.01	-	-	-	-	-	1.00	0.06	12.04	0.78	2.80	0.0045	0.0105	0.0006
73090	0.0350	-4.88	0.826	-0.06	0.13	-0.25	-	-	-	-	-	1.06	0.13	12.75	0.83	2.80	0.0086	0.0112	0.0013
73091	0.0191	-5.39	0.628	0.05	0.09	0.19	-	-	-	-	-	0.95	0.09	11.42	0.74	2.79	0.0062	0.0100	0.0009
73092	0.0136	-5.35	0.604	0.03	0.09	0.11	-	-	-	-	-	0.97	0.09	11.67	0.76	2.80	0.0054	0.0099	0.0008
73093	0.0103	-5.06	0.513	0.02	0.07	0.06	-	-	-	-	-	0.98	0.07	11.82	0.77	2.80	0.0048	0.0098	0.0007
73094	0.0084	-5.46	0.456	-0.03	0.07	-0.10	-	-	-	-	-	1.03	0.07	12.30	0.80	2.80	0.0043	0.0099	0.0006
73095	0.0106	-5.24	0.480	-0.03	0.07	-0.12	-	-	-	-	-	1.03	0.07	12.36	0.80	2.80	0.0048	0.0104	0.0007
73096	0.0254	-5.33	0.848	0.08	0.12	0.32	-	-	-	-	-	0.92	0.12	11.04	0.72	2.80	0.0073	0.0090	0.0011
73097	0.0062	-5.51	0.370	-0.06	0.06	-0.25	-	-	-	-	-	1.06	0.06	12.76	0.83	2.80	0.0037	0.0109	0.0005
73098	0.0098	-5.87	0.497	-0.04	0.08	-0.18	-	-	-	-	-	1.04	0.08	12.53	0.81	2.80	0.0049	0.0104	0.0007
73099	0.0317	-4.96	0.928	0.08	0.12	0.30	-	-	-	-	-	0.92	0.12	11.09	0.72	2.81	0.0081	0.0089	0.0012
73100	0.0242	-4.82	0.774	0.05	0.11	0.21	-	-	-	-	-	0.95	0.11	11.36	0.74	2.81	0.0075	0.0097	0.0011
73101	0.0428	-4.62	0.986	-0.06	0.15	-0.25	-	-	-	-	-	1.06	0.15	12.74	0.83	2.82	0.0098	0.0109	0.0014
73102	0.0139	-5.42	0.647	0.00	0.09	0.02	-	-	-	-	-	1.00	0.09	11.94	0.78	2.81	0.0059	0.0097	0.0009
73104	0.0195	-5.07	0.725	0.00	0.11	-0.02	-	-	-	-	-	1.00	0.11	12.06	0.78	2.81	0.0065	0.0094	0.0010
73104	0.0173	-5.42	0.647	-0.03	0.09	-0.11	-	-	-	-	-	1.03	0.09	12.33	0.80	2.81	0.0062	0.0100	0.0009
73105	0.0173	-5.42	0.647	-0.03	0.09	-0.11	-	-	-	-	-	1.03	0.09	12.33	0.80	2.81	0.0062	0.0100	0.0009
73106	0.0094	-5.44	0.498	-0.02	0.07	-0.08	-	-	-	-	-	1.02	0.07	12.23	0.80	2.81	0.0049	0.0101	0.0007
73107	0.0094	-5.15	0.521	0.00	0.07	0.01	-	-	-	-	-	1.00	0.07	11.98	0.78	2.81	0.0046	0.0097	0.0007
73108	0.0095	-5.18	0.457	-0.03	0.07	-0.10	-	-	-	-	-	1.03	0.07	12.31	0.80	2.81	0.0045	0.0101	0.0006
73109	0.0079	-5.37	0.448	-0.01	0.07	-0.05	-	-	-	-	-	1.01	0.07	12.16	0.79	2.81	0.0043	0.0099	0.0006

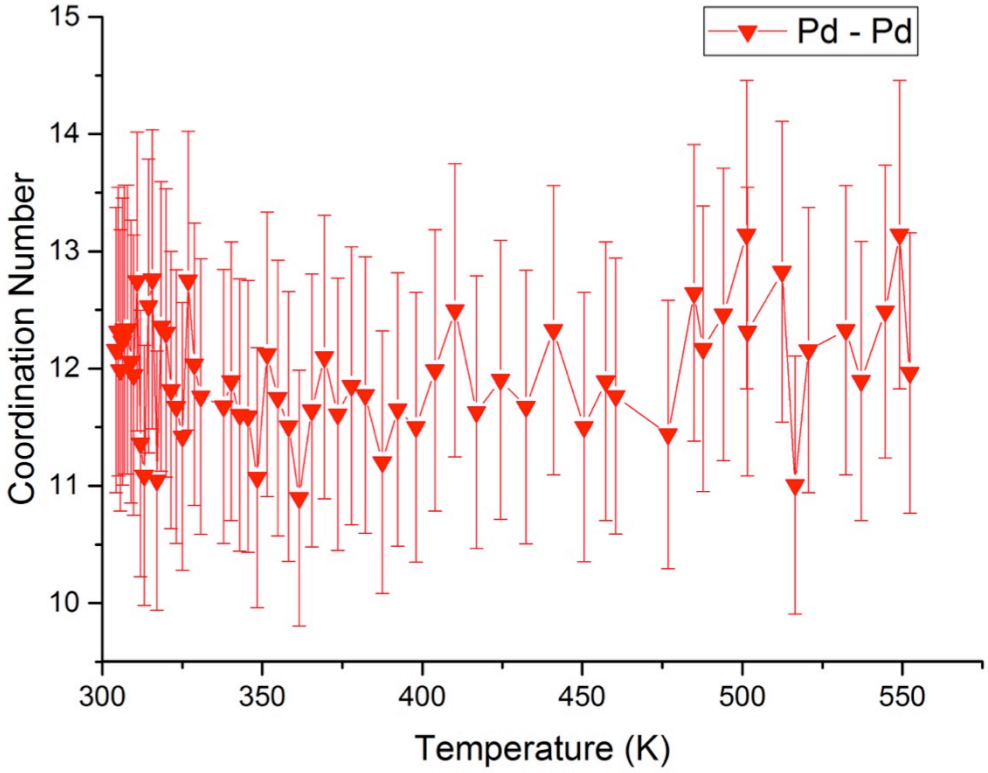

Figure 4-25 - Plot of change in the coordination number against temperature for the in situ cooling of Pd/ceria/alumina catalyst under H_2/He atmosphere.

Artemis modelling was also used to calculate the coordination numbers of the Pd-Pd shell from the metal and the Pd-O shell from the oxide standard (Figure 4-23). The coordination number of the PdO phase decreased as expected from 4.0 to ca 1. At the same time the coordination number of the Pd-Pd shell increase steadily after about 8 minutes from an initial value of 4 to a value close to 8. These values are indicative of a gradual reduction of the PdO to Pd metal. The coordination numbers for the Pd-O shell do not decrease to zero and fitting without the Pd-O path results in a worse fit. This suggests that there is still a contribution from the Pd-O shell.

Upon heating the coordination number for PdO gradually decreases to near zero (Figure 4-24). After 100^{o}C the material can be fitted as just Pd-metal with no further contribution from the Pd-O path. The coordination number for the Pd metal shell increases steadily from the value of 8 at room temperature to between 11 and 12 at 573 K. There is not a great deal of variation in the value of the coordination number for the Pd-Pd shell after 363 K.

Upon cooling to room temperature there is no reformation of the PdO phase meaning the data can be fitted as the pure metal phase. Even so there is a variation in the coordination number during cooling as the value obtained varies between 12.5 and 11.0, although there are large error bars to take into consideration (Figure 4-25). Variation in the coordination number between the

literature value of 12 and those obtained could be due to defects in the structure of the material formed or due to variations in the data. However as the data quality is good it could be perceived that the variations are due to the sample. A previous report also noted a reduced coordination number for the Pd-Pd first shell, and attributed it to being formed from PdO in a hydrogen rich environment.[34]

In summary the supported Pd/ceria/alumina catalyst has been successfully reduced and observed using XAS. Analysis has been used to show that whilst the majority of the material is reduced at room temperature full reduction does not occur until 373 K. Data obtained has also pointed to the existence of an intermediate Pd hydride phase which has not been extensively observed with XAS in the literature.[37,38]

4.5 Rh/ceria/alumina Catalysts

The Rhodium catalysts were calcined to 573 K under H_2/He, with XAS measurements taken at the Rh K-edge. After initially heating the material to 573 K a further ramp to 623 K was employed, a slight variation from the Pd supported catalyst. Whilst according to literature Rh can be reduced at temperatures of 573 K it requires significantly more time than was available during the constraints of the beamtime, hence the extra ramp.[16,39]

4.5.1 XANES Analysis

Initial observations in the XANES region show a clear change in the magnitude of whiteline intensity from the initial rhodium oxide to the material at the end of the reduction (Figure 4-26). This transition also indicates a change in the local coordination of the Rh ions, from the initial 6-coordinate oxide to the 12-coordinate metal. A transition to the 12-coordinate Rh metal state should be indicated by a decrease in intensity of the first peak along with an increase in the intensity of the second peak in addition to an increase of the oscillations in the EXAFS region (Figure 4-31) corresponding to a change in the density of free states; however this is not observed in the fit.

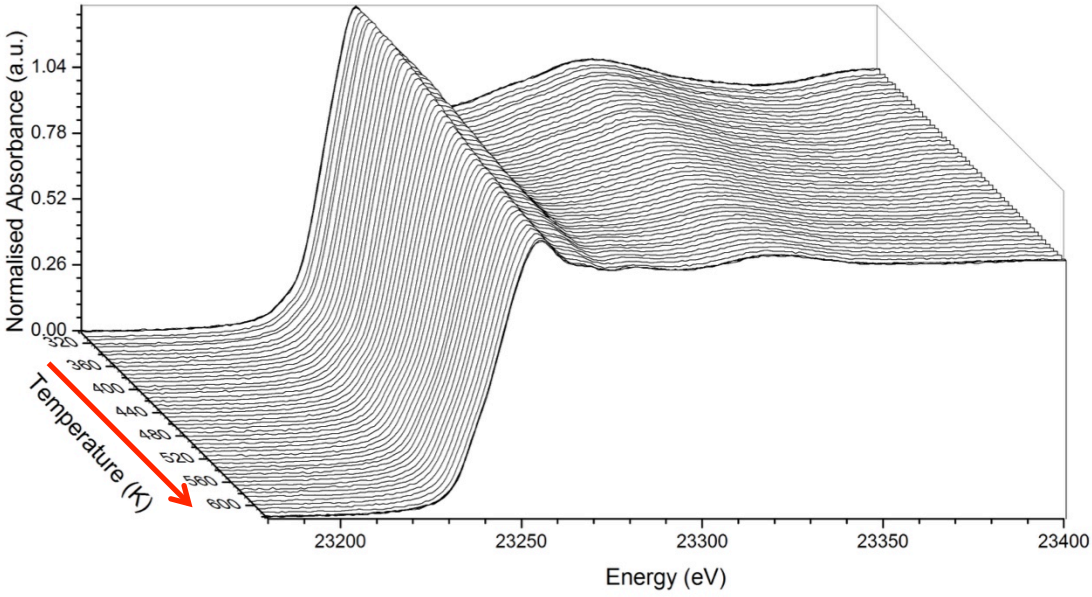

Figure 4-26 - XANES plot of in situ Rh/Ceria/Alumina catalyst heated to 623 K under H_2/He.

From the data the energy of the edge position decreases from 23243.2 eV in the oxide to 23239.0 eV at 578 K; which is the closer in energy to the Rh metal edge, ca 23238.9 eV. Whilst this indicates the material has been reduced to a degree as stated before the features of the

whiteline and XANES region, do not match those of the Rh metal indicating complete reduction has not occurred and instead a mixed phase material has been formed.

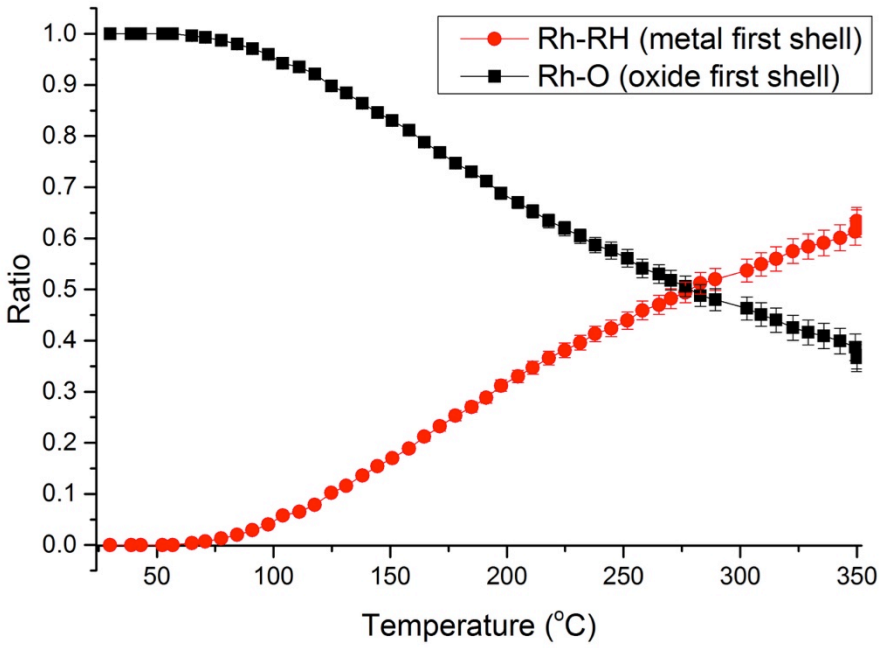

Figure 4-27 - Linear combination fit (LCF) of in situ Rh/Ceria/Alumina catalyst heated to 623 K under H_2/He.

Examples of the LCF fitting model are provided showing the quality of the fit at the beginning of the reduction (Figure 4-28), at 556K (Figure 4-29) and at the end of the reduction (Figure 4-30). Whilst the fit is fairly accurate at room temperature with increasing temperature the quality of the fit decreases rapidly. This is most predominately seen once the Rh metal content increases above 50% (Figure 4-29), where the oscillations after the edge are significantly larger in the fitting model than in the experimental data. This could be due to the standards used as the standard for the Rh metal used for the LCF was from a metal foil and not supported NPs. The data can be used to provide an initial starting point for the analysis, although the LCF results must of course be taken with caution.

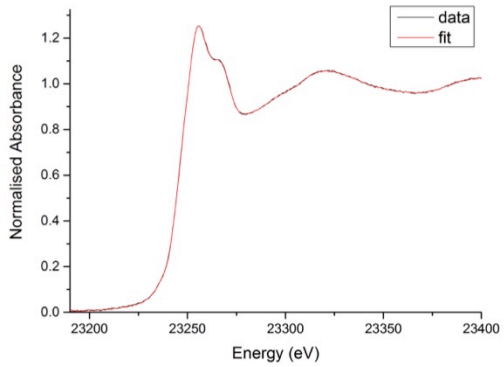

Figure 4-28 - Example of a LCF fit from the start of the reduction experiment at 300 K.

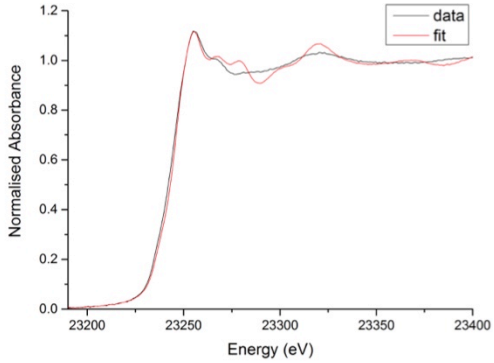

Figure 4-29 - Example of a LCF fit from the middle of the reduction experiment at 556 K where the composition is 50/50.

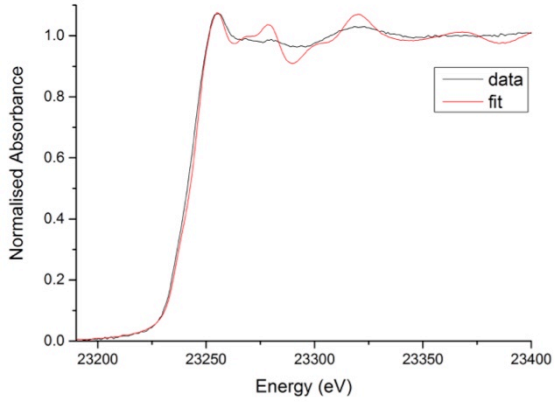

Figure 4-30 - Example of a LCF fit from the end of the reduction experiment.

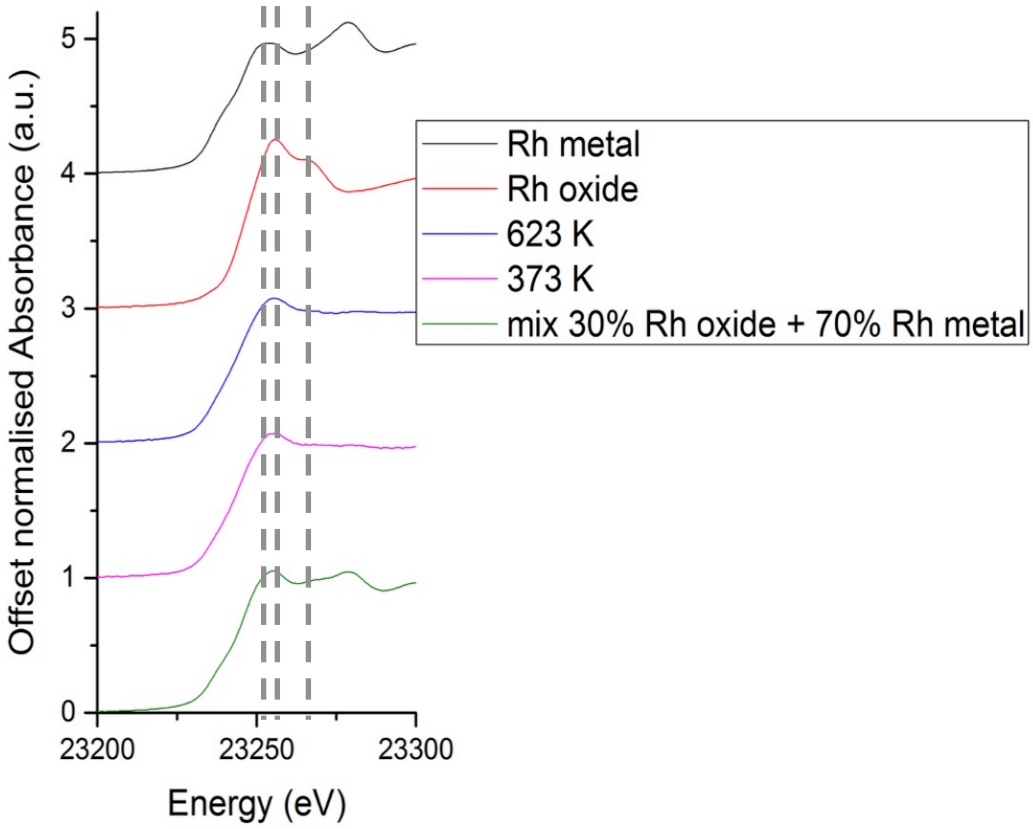

Figure 4-31 - Normalised plots of Rh material at 623 K and at the end of the reduction compared with Rh oxide and Rh metal standards

A linear combination fit (LCF) analysis comparing the XANES data of the *in-situ* experiment to the pure rhodium oxide and pure rhodium metal phases confirms that the reduction does not go to completion (Figure 4-27). The LCF data seems to indicate that at least 30% of the material is still present in the oxide phase at the end of the reduction process, with the conversion to rhodium metal being near 70%. A theoretical XANES plot composed through the combination of 70% Rh metal standard and 30% Rh oxide is shown in Figure 4-31. Comparison with the experimental data reveals reasonable agreement in the area ±10eV about the whiteline intensity. However the amplitude of the oscillations after the edge are considerably higher for the model sample. This is potentially due to the standards being unsupported, with the support effects of the Rh/ceria/alumina material resulting in a dampening of the amplitude. What is also clear from the comparison is that following from the reduction ramp there is very little change in material from 623 K back to room temperature.

4.5.2 EXAFS Analysis

The data was fitted to the first shells of both Rh oxide and Rh metal, which are Rh-O and Rh-Rh paths respectively. Although decoration of M/CeO_2 systems has been confirmed in the literature from TEM studies of materials reduced up to 773K, alloying of the metal NPS with CeO_2 does not occur at these lower reduction temperatures.[40] Hence contributions from Rh-Ce paths were not considered in this analysis.

At room temperature the data could be fitted to the rhodium oxide with little to no contribution from the Rh metal (Figure 4-32). The data was fitted in the k-range of 2.5-0.5 $Å^{-1}$ and R-range of 1-4 Å. At 623 K the amplitude of the oscillations in k-space decreases, as does the magnitude of the peaks in the Fourier transform (Figure 4-33). The shape of the peaks changes, with a peak appearing at 2.4 Å, which is due to the Rh – Rh interaction in addition to the Rh-O peak at 2.0 Å. The Rh-Rh bond shifts to a higher bond distance once cooled to room temperature (Figure 4-34).

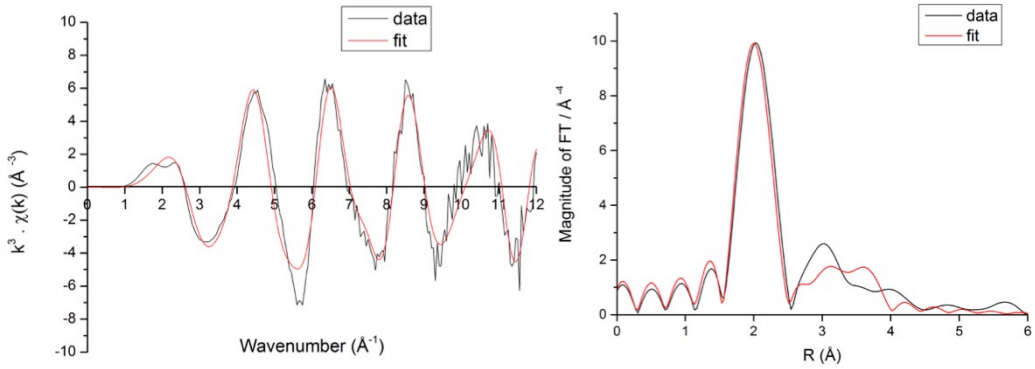

Figure 4-32 - Plot of the k-space k^3 weighted data and the Fourier transform for the material at the beginning of the reduction (303 K).

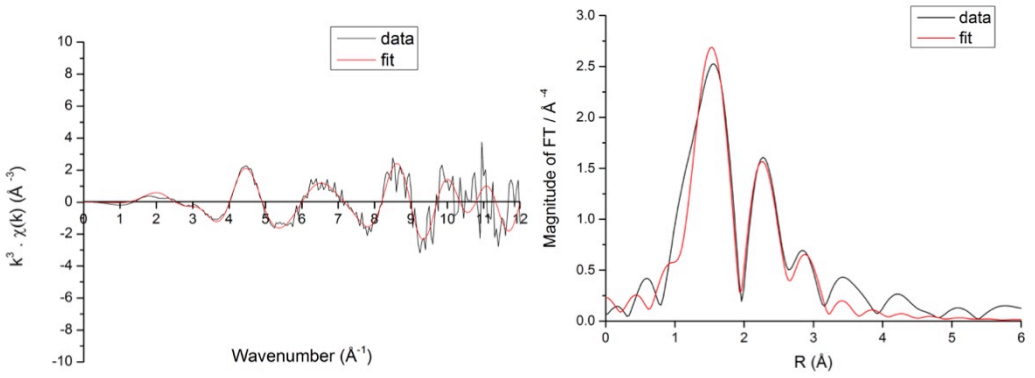

Figure 4-33 - Plot of the k-space k^3 weighted data and the Fourier transform for the material at the end of the reduction ramp (623 K).

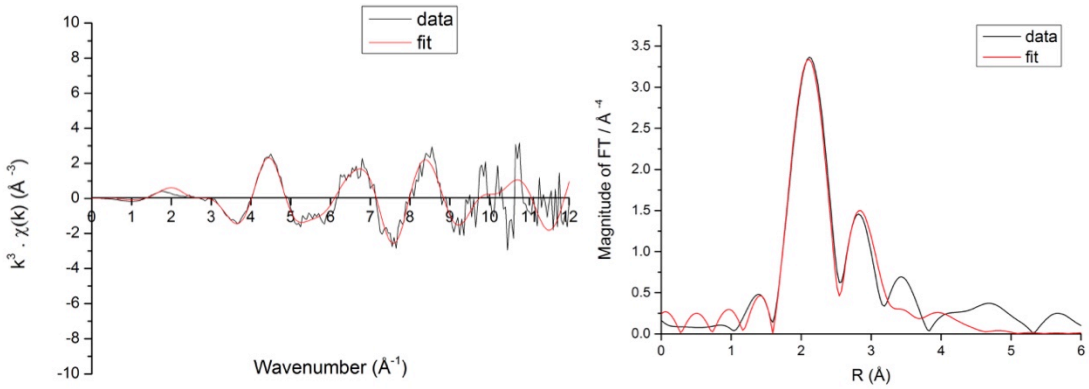

Figure 4-34 - Plot of the k-space k^3 weighted data and the Fourier transform for the material during cooling phase to room temperature (383 K).

Diagrams of the shells used in the fitting model are provided for ease of reference. Figure 4-35 and Figure 4-36 show the first and second shells of Rh oxide, both of which were included in the fitting model. Figure 4-37 and Figure 4-38 show the first and second shells of Rh metal, however only the first shell for the metal was considered in the final fitting model. Details on the bond distances and coordination numbers for the shells are provided in Table 4-6 for Rh oxide and Table 4-7 for Rh metal.

Table 4-6 - Scattering paths and details for Rh oxide.

Shell	Scatterer	Bond distance (Å)	Coordination number
1	O	2.04	6
2	Rh	2.98	4
3	O	3.52	3

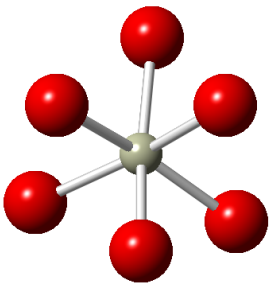

Figure 4-35 - First shell of Rhodium oxide showing the central Rh atom surrounded by 6 oxygen atoms in an octahedral coordination at a distance of 2.0 Å.

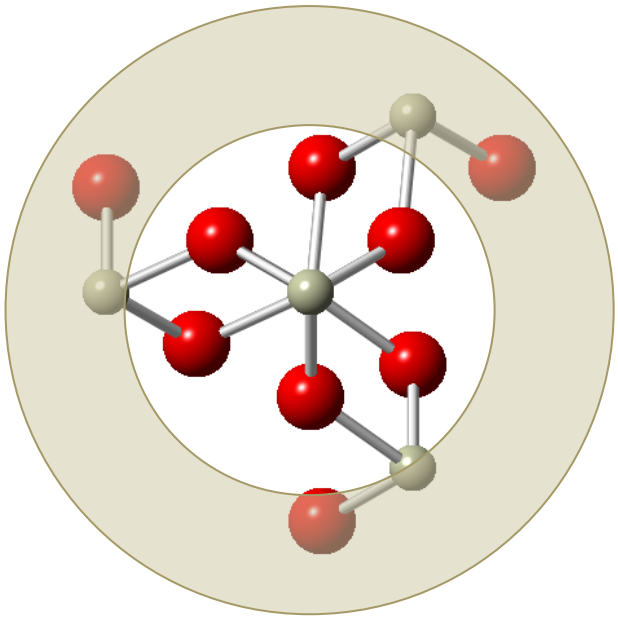

Figure 4-36 - Diagram highlighting the second and third shell of Rhodium oxide consisting of Rh at 2.7 Å and O at 2.98 Å.

Table 4-7 - Scattering paths and details for Rh metal.

Shell	Scatterer	Bond distance (Å)	Coordination number
1	Rh	2.69	12
2	Rh	3.80	6

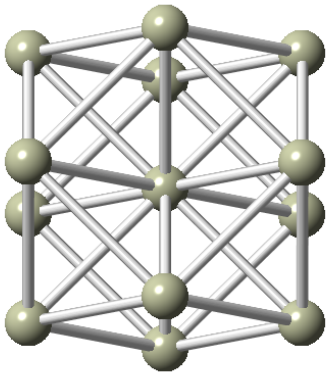

Figure 4-37 - Diagram showing the structure of the Rh metal first shell, which is composed of a central Rh atom surrounded by 10 Rh neighbours at 2.6 A.

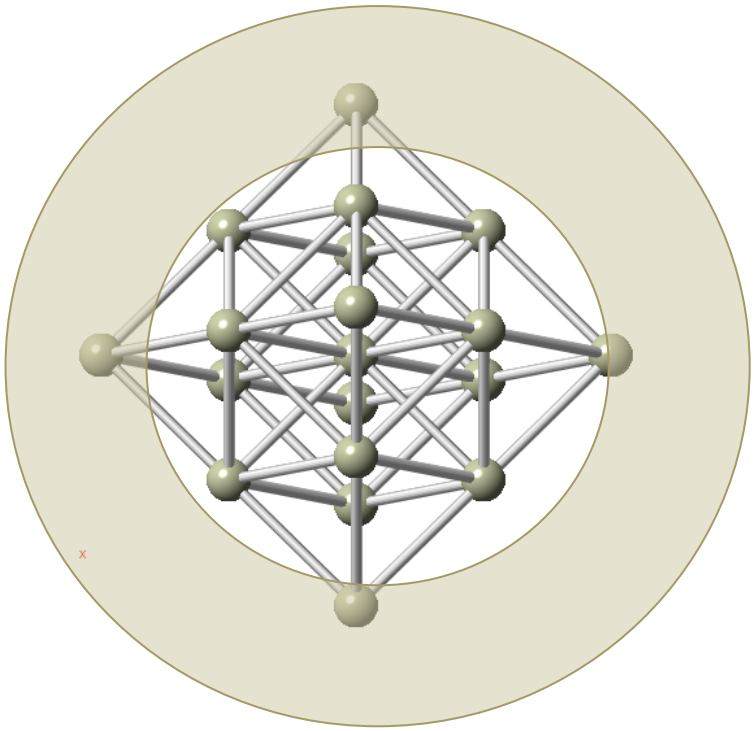

Figure 4-38 - Second shell of Rh metal composed of Rh atoms at 3.29 A.

The change in oxidation state observed in the XANES is reflected in the Fourier transform of the EXAFS region (Figure 4-39). A steady decrease of the magnitude of the Rh-O bond is observed accompanied by minor changes in the bond distance. This supports the theory that the Rh NPs have not been fully reduced from the oxide, as this would be accompanied by a larger change in the bond distance.

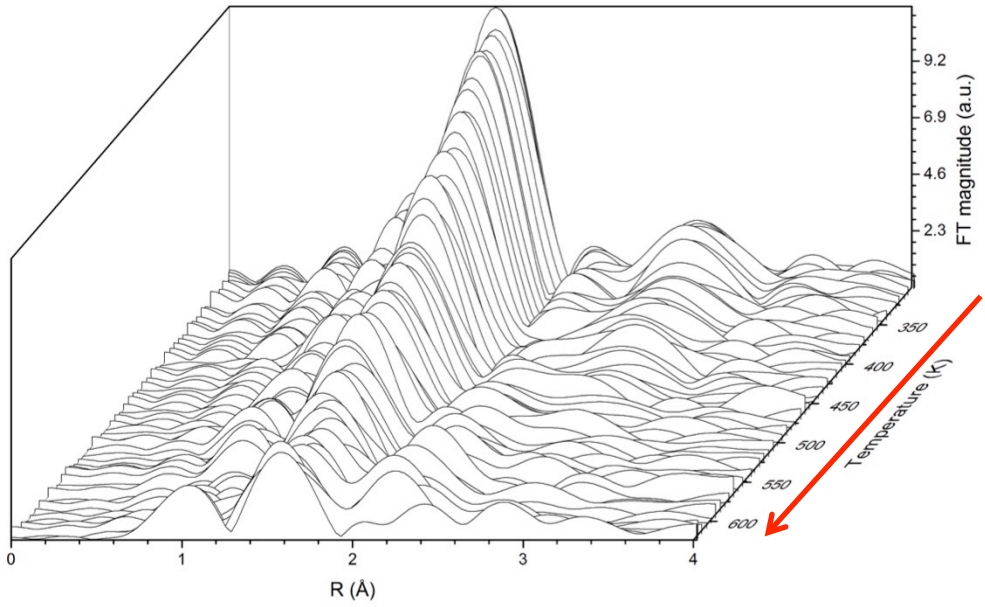

Figure 4-39 - Plot of Fourier Transform (FT) of in situ Rh/Ceria/Alumina catalyst heated to 623 K under H2/He (not phase corrected).

Upon heating the intensity of the Rh-O bond decreases by a factor of 3.5; dropping from 11.5 to 3.4 by 623 K (Figure 4-32 and Figure 4-33). As the magnitude of the intensity can be related to the occupancy, this would correspond to a decrease in the coordination number of the Rh-O shell. By comparison the Rh-Rh bond is none existent at room temperature with the Rh-Rh bond from the Rh oxide at 2.99Å dominating the region. After heating to around 443 K, there is clear evidence of Rh-Rh bond formation with the peak appearing at 2.69 Å with an intensity of 1.73. This peak is not visible at earlier temperatures indicating either there is little to no metallic Rh formation below 448 K or that what ever metallic species is present is in sufficiently low quantities to be masked by the Rh-Rh shell from the Rh oxide phase.

Following the metallic Rh formation the intensity of the Rh-Rh peak increases with increasing temperature, reaching a value of 2.01 by 623 K (Figure 4-33). Upon cooling to room temperature the intensity of the Rh-Rh peak decreases to 1.71, which is very similar to the initial value (Figure 4-34). This helps to confirm that although some reduction has occurred the material is not completely reduced. The change in the intensity of the Rh-Rh bond is potentially due to the rising temperature, rather than any changes in occupancy; fitting of the data will provide confirmation of this.

The fitting of the experimental data, using Artemis software, was focused on using the first shell paths from the oxide and metallic phases to perform a multiphase analysis and determine the composition of the material throughout the reduction. Full tables of results for the EXAFS fitting are available in Table 4-8 and Table 4-9 for the heating and cooling respectively.

The initial material is essentially the pure oxide with a coordination number (CN) of ca 6.5 and is comparable to the expected literature value of 6 for an Rh_2O_3 standard (Figure 4-40). The CN for the Rh metallic phase is close to zero below 100^{o}C; with the few instances where a value is obtained, the CN never rises above 2. This low value taken to be caused by some overlap between the Rh-Rh shell in the metal and the Rh-Rh shell in the oxide, as the Rh-Rh bond-distance reported is higher than expected around 2.8Å, which is 0.1Å higher than the literature value. Upon increasing temperature the bond distance for the oxide first shell decreases steadily from 6 to a minimum of ca, 2.1 by 623 K. The decrease in the oxide shell is matched by a steady rise of the Rh-Rh shell from 2 to ca, 8; this is lower than the literature value but expected due to temperature difference. Upon cooling to room temperature the coordination numbers of the two shells varies only slightly from the values at 623 K, with the Rh-Rh CN returning to a value of 8.5 upon cooling and the Rh-O CN remaining near ca, 2.0 following the reduction (Figure 4-41).

Whilst it is clear that the reduction has not gone to completion it is also clear that the Rh-Rh shell is not complete; with the final coordination value of the shell being ca 9, which is lower than the expected value of 12 for Rh-Rh metal first shell. This indicates the potential existence of defects in the structure or the incomplete growth of the Rh metallic phase. It is known from the literature that supported Rh particles can oxidise easily, and furthermore that the amount of metal formed during reduction is related to the reduction temperature.[16]

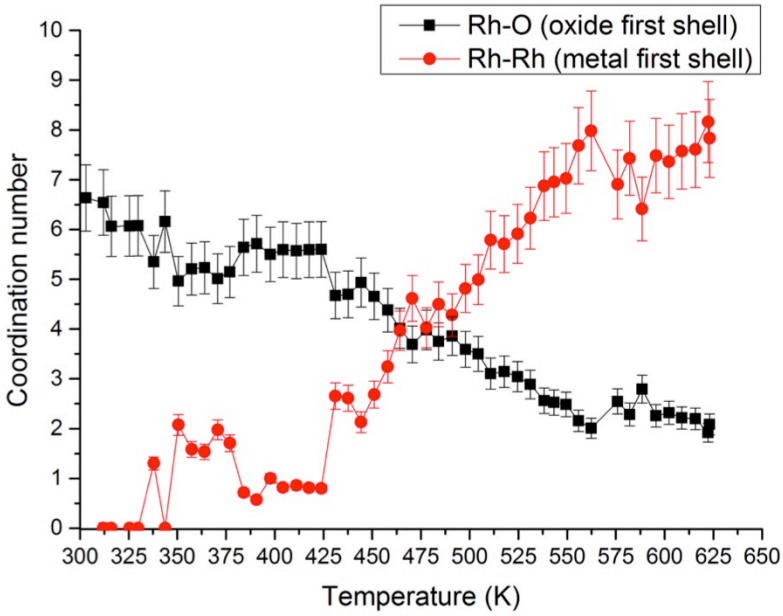

Figure 4-40 - Plot of coordination number from EXAFS fitting against temperature for Rh/Ceria/Alumina catalyst heated to 623 K under H_2/He.

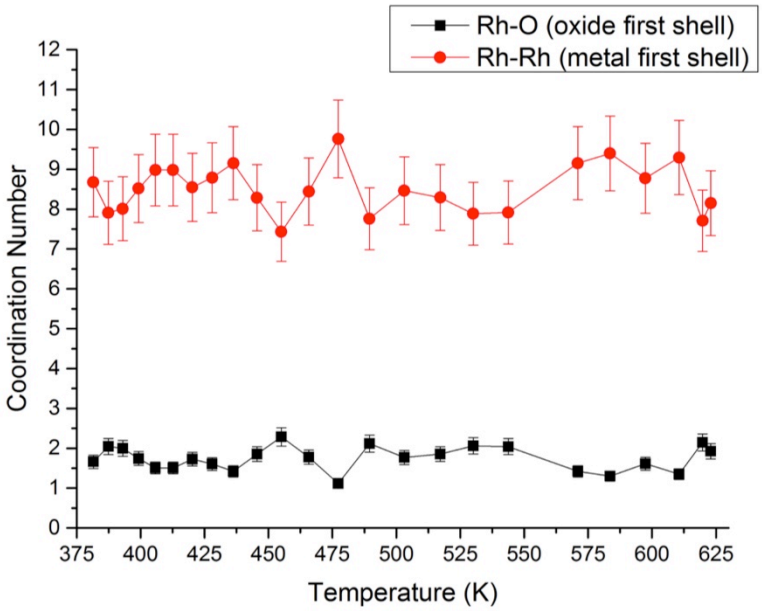

Figure 4-41 - Plot of coordination number from EXAFS fitting against temperature for Rh/Ceria/Alumina catalyst cooling to room temperature under H_2/He.

Table 4-8 - EXAFS results for the Rh catalyst reduction.

		amp	= 0.77972000			Rh2O3										Rh Metal				
						Rh-O first shell										Rh-Rh first shell				
File	temperature	R-factor	E0	error (E0)	x1	CN	CN error	S02	R	error	ss2	error	x2	CN	CN error	S02	R	error	ss2	error
73261	30	0.0557	-3.25	1.658	1.09	6.52	0.65	0.91	2.01	0.0134	0.0035	0.0017	-0.09	-1.04	-0.10	-0.07	3.60	0.0744	0.0041	0.0117
73262	30	0.0652	-3.13	1.748	1.10	6.61	0.66	0.92	2.01	0.0144	0.0037	0.0018	-0.10	-1.23	-0.12	-0.09	3.60	0.0739	0.0045	0.0114
73263	30	0.0652	-3.13	1.748	1.10	6.61	0.66	0.92	2.01	0.0144	0.0037	0.0018	-0.10	-1.23	-0.12	-0.09	3.60	0.0114	0.0045	0.0739
73264	30	0.0602	-3.02	1.712	1.09	6.51	0.65	0.90	2.01	0.0140	0.0035	0.0018	-0.09	-1.03	-0.10	-0.07	3.62	0.0914	0.0048	0.0134
73265	30	0.0602	-3.30	1.648	1.09	6.51	0.65	0.91	2.01	0.0136	0.0036	0.0017	-0.09	-1.03	-0.10	-0.08	3.58	0.0581	0.0030	0.0100
73266	30	0.0595	-3.20	1.713	1.09	6.54	0.65	0.91	2.01	0.0141	0.0037	0.0018	-0.09	-1.08	-0.11	-0.08	3.61	0.0862	0.0048	0.0129
73267	30	0.0615	-3.13	1.724	1.11	6.64	0.66	0.91	2.01	0.0143	0.0037	0.0018	-0.11	-1.27	-0.13	-0.08	3.61	0.0732	0.0048	0.0113
73268	39	0.0657	-2.98	1.795	1.09	6.54	0.65	0.91	2.01	0.0147	0.0038	0.0019	-0.09	-1.09	-0.11	-0.08	3.59	0.0821	0.0045	0.0132
73269	43.1	0.0612	-2.56	1.762	1.01	6.06	0.61	0.84	2.02	0.0145	0.0033	0.0014	-0.01	-0.13	-0.01	-0.01	3.58	0.0860	-0.0051	0.0323
73270	52.4	0.0597	-2.76	1.706	1.01	6.07	0.61	0.84	2.02	0.0136	0.0030	0.0013	-0.01	-0.14	-0.01	-0.01	3.59	0.0931	-0.0041	0.0315
73271	56.8	0.0645	-2.78	1.802	1.01	6.08	0.61	0.84	2.02	0.0146	0.0033	0.0014	-0.01	-0.15	-0.02	-0.01	3.58	0.1011	-0.0037	0.0328
73272	65	0.0662	-2.69	1.819	0.89	5.35	0.53	0.85	2.02	0.0035	0.0151	0.0015	0.11	1.30	0.13	-0.01	3.58	0.0771	-0.0037	0.0250
73273	70.8	0.0585	-2.84	1.740	1.03	6.16	0.62	0.86	2.02	0.0142	0.0035	0.0015	-0.03	-0.32	-0.03	-0.02	3.60	0.0723	-0.0018	0.0185
73274	77.6	0.0565	-1.30	1.342	0.83	4.96	0.50	0.78	2.03	0.0106	0.0018	0.0010	0.17	2.08	0.21	0.05	2.62	0.0319	0.0032	0.0060
73275	84.4	0.0565	-2.14	1.506	0.87	5.21	0.52	0.72	2.02	0.0108	0.0015	0.0012	0.13	1.59	0.16	0.11	2.46	0.0590	0.0158	0.0124
73276	91	0.0504	-2.29	1.420	0.87	5.23	0.52	0.73	2.02	0.0103	0.0015	0.0012	0.13	1.53	0.15	0.11	2.46	0.0533	0.0149	0.0112
73277	97.8	0.0921	-2.67	1.827	0.84	5.01	0.50	0.70	2.02	0.0128	0.0014	0.0016	0.16	1.98	0.20	0.14	2.53	0.0745	0.0179	0.0167
73278	104	0.0565	-2.13	1.458	0.86	5.15	0.51	0.71	2.02	0.0106	0.0018	0.0013	0.14	1.71	0.17	0.12	2.48	0.0584	0.0171	0.0131
73279	111.1	0.0529	-1.86	1.484	0.94	5.64	0.56	0.78	2.03	0.0117	0.0022	0.0011	0.06	0.72	0.07	0.05	2.61	0.0287	0.0023	0.0056
73280	117.7	0.0436	-2.48	1.407	0.95	5.71	0.57	0.79	2.02	0.0108	0.0025	0.0010	0.05	0.57	0.06	0.04	2.61	0.0314	0.0024	0.0063
73281	124.8	0.0407	-2.63	1.422	0.92	5.50	0.55	0.76	2.02	0.0106	0.0019	0.0010	0.08	1.00	0.10	0.07	2.36	0.0351	0.0048	0.0045
73282	131.2	0.0564	-1.51	1.467	0.93	5.59	0.56	0.78	2.02	0.0116	0.0025	0.0011	0.07	0.82	0.08	0.06	2.62	0.0397	0.0051	0.0073
73283	138.1	0.0470	-1.83	1.402	0.93	5.57	0.56	0.77	2.02	0.0111	0.0029	0.0011	0.07	0.86	0.09	0.06	2.62	0.0332	0.0051	0.0062
73284	144.6	0.0453	-2.09	1.412	0.93	5.59	0.56	0.78	2.02	0.0113	0.0032	0.0011	0.07	0.81	0.08	0.06	2.61	0.0393	0.0059	0.0074
73285	150.9	0.0454	-1.97	1.395	0.93	5.60	0.56	0.78	2.02	0.0113	0.0037	0.0011	0.07	0.80	0.08	0.06	2.61	0.0444	0.0068	0.0083
73286	158.1	0.0686	-1.73	1.552	0.78	4.67	0.47	0.65	2.02	0.0115	0.0023	0.0014	0.22	2.65	0.27	0.17	2.52	0.0414	0.0197	0.0102
73287	164.6	0.0406	-2.16	1.547	0.78	4.69	0.47	0.65	2.02	0.0119	0.0031	0.0014	0.22	2.61	0.26	0.18	2.51	0.0419	0.0208	0.0108
73288	171.3	0.0672	-1.18	1.593	0.82	4.93	0.49	0.69	2.03	0.0126	0.0036	0.0017	0.18	2.13	0.21	0.15	2.67	0.1972	0.0348	0.0651
73289	178	0.0708	-1.20	1.608	0.78	4.66	0.47	0.65	2.03	0.0123	0.0255	0.0016	0.22	2.68	0.27	0.19	2.69	0.0971	0.0035	0.0292
73290	184.9	0.0529	-1.36	1.639	0.73	4.38	0.44	0.61	2.03	0.0120	0.0035	0.0017	0.27	3.24	0.32	0.23	2.56	0.1380	0.0259	0.0249
73291	191.2	0.0394	-0.81	1.821	0.67	4.02	0.40	0.57	2.03	0.0153	0.0029	0.0020	0.33	3.97	0.40	0.20	2.55	0.0474	0.0228	0.0125
73292	197.5	0.0554	-1.23	1.551	0.62	3.69	0.37	0.52	2.03	0.0136	0.0011	0.0017	0.38	4.62	0.46	0.26	2.57	0.0488	0.0294	0.0143
73293	204.8	0.0647	-0.57	1.96	0.66	3.99	0.40	0.51	2.03	0.0147	0.0021	0.0021	0.34	4.03	0.40	0.26	2.59	0.0520	0.0297	0.0151
73294	211.1	0.0642	-0.38	1.963	0.63	3.75	0.38	0.48	2.03	0.0148	0.0020	0.0022	0.37	4.50	0.45	0.29	2.62	0.0583	0.0360	0.0174
73295	218	0.0820	-0.37	2.187	0.64	3.86	0.39	0.50	2.03	0.0169	0.0031	0.0025	0.36	4.28	0.43	0.28	2.61	0.0609	0.0339	0.0181
73296	224.8	0.0557	-0.51	1.808	0.60	3.59	0.36	0.46	2.03	0.0134	0.0023	0.0020	0.40	4.81	0.48	0.31	2.63	0.0481	0.0357	0.0137
73297	231.4	0.0628	-0.07	1.910	0.58	3.50	0.35	0.45	2.04	0.0145	0.0027	0.0022	0.42	4.99	0.50	0.32	2.64	0.0523	0.0379	0.0150
73298	237.8	0.0646	0.85	1.893	0.52	3.11	0.31	0.40	2.04	0.0139	0.0014	0.0021	0.48	5.79	0.58	0.37	2.67	0.0521	0.0412	0.0142
73299	244.7	0.0518	0.60	1.755	0.52	3.15	0.31	0.41	2.04	0.0130	0.0020	0.0019	0.48	5.71	0.57	0.37	2.68	0.0493	0.0425	0.0134
73300	251.6	0.0619	0.62	1.930	0.51	3.04	0.30	0.39	2.04	0.0140	0.0019	0.0021	0.49	5.91	0.59	0.38	2.68	0.0435	0.0435	0.0145
73301	258.1	0.0585	0.50	1.774	0.48	2.89	0.29	0.37	2.03	0.0132	0.0018	0.0020	0.52	6.23	0.62	0.40	2.69	0.0441	0.0421	0.0111
73302	265.2	0.0980	1.58	2.261	0.43	2.56	0.26	0.33	2.05	0.0164	0.0005	0.0025	0.57	6.87	0.69	0.44	2.71	0.0622	0.0484	0.0161
73303	270.3	0.0485	0.76	1.692	0.42	2.52	0.25	0.33	2.04	0.0116	0.0003	0.0017	0.58	6.95	0.70	0.45	2.70	0.0440	0.0466	0.0109
73304	276.5	0.0724	0.68	2.030	0.41	2.49	0.25	0.32	2.04	0.0141	0.0006	0.0021	0.59	7.03	0.70	0.45	2.71	0.0499	0.0454	0.0118
73305	282.9	0.0418	0.00	1.361	0.36	2.16	0.22	0.28	2.03	0.0104	0.0002	0.0016	0.64	7.68	0.77	0.50	3.43	0.0381	0.0264	0.0058
73306	289.3	0.0223	2.76	2.331	0.33	2.01	0.20	0.26	2.04	0.0152	-0.0010	0.0020	0.67	7.98	0.80	0.50	3.64	0.1272	0.0540	0.0327
73308	302.9	0.0131	-1.89	1.248	0.42	2.55	0.25	0.33	2.02	0.0086	0.0026	0.0013	0.58	6.91	0.69	0.45	2.66	0.0189	0.0329	0.0042
73309	309	0.0152	-0.15	1.248	0.38	2.28	0.23	0.30	2.03	0.0083	0.0017	0.0013	0.62	7.43	0.74	0.48	2.69	0.0354	0.0017	0.0044
73310	315.4	0.0168	3.16	2.660	0.47	2.79	0.28	0.36	2.05	0.0136	0.0040	0.0051	0.53	6.41	0.64	0.42	2.88	0.0436	0.0353	0.0144
73311	322.6	0.0107	0.08	1.428	0.38	2.26	0.23	0.29	2.04	0.0103	0.0027	0.0016	0.62	7.49	0.75	0.48	2.71	0.0286	0.0356	0.0056
73312	329.2	0.0050	-1.68	1.037	0.39	2.32	0.23	0.30	2.02	0.0074	0.0030	0.0011	0.61	7.36	0.74	0.48	2.68	0.0194	0.0346	0.0036
73313	335.8	0.0115	-0.34	1.524	0.37	2.21	0.22	0.29	2.03	0.0111	0.0021	0.0015	0.63	7.57	0.76	0.49	2.63	0.0305	0.0288	0.0060
73314	342.8	0.0118	0.68	1.056	0.37	2.20	0.22	0.29	2.05	0.0077	0.0038	0.0014	0.63	7.61	0.76	0.50	2.71	0.0182	0.0328	0.0031
73315	349.3	0.0045	-0.75	0.948	0.32	1.92	0.19	0.25	2.04	0.0070	0.0021	0.0010	0.68	8.16	0.82	0.53	2.72	0.0178	0.0321	0.0030
73316	350.1	0.0082	0.60	1.292	0.35	2.08	0.21	0.27	2.05	0.0106	0.0045	0.0015	0.65	7.83	0.78	0.51	2.69	0.0328	0.0306	0.0075
73317	350	0.0074	-1.09	1.303	0.33	2.01	0.20	0.26	2.03	0.0102	0.0037	0.0015	0.67	7.99	0.80	0.52	2.69	0.0236	0.0281	0.0034
73318	350	0.0292	-3.26	1.811	0.39	2.31	0.23	0.30	2.01	0.0130	0.0057	0.0022	0.61	7.38	0.74	0.48	2.65	0.0273	0.0301	0.0042
73319	350	0.0122	-1.64	1.175	0.30	1.78	0.18	0.23	2.02	0.0076	0.0025	0.0014	0.70	8.44	0.84	0.55	2.69	0.0188	0.0325	0.0025

Table 4-9 - EXAFS results for the cooling of Rh catalyst.

					Rh2O3									Rh Metal							
					Rh-O first shell									Rh-Rh first shell							
File	temperature	R-factor	E0	error (E0)	x1	CN	CN error	S02	R	error	ss2	error	x2	CN	CN error	S02	R	error	ss2	error
73330	350	0.0058	-3.27	1.487	0.36	2.13	0.21	0.28	2.02	0.0118	0.0055	0.0014	0.64	7.73	0.77	0.50	2.64	0.0199	0.0234	0.0038
73330	350	0.0146	-2.52	2.051	0.27	1.65	0.16	0.21	2.02	0.0021	0.0022	0.0145	0.73	8.71	0.87	0.57	2.71	0.0276	0.0311	0.0043
73330	350	0.0270	1.72	2.150	0.27	1.59	0.16	0.21	2.05	0.0161	0.0028	0.0026	0.73	8.82	0.88	0.58	2.74	0.0367	0.0285	0.0045
73330	350	0.0104	1.23	1.672	0.32	1.92	0.19	0.25	2.05	0.0140	0.0059	0.0022	0.68	8.15	0.82	0.53	2.70	0.0297	0.0240	0.0035
73330	346.8	0.0074	-3.60	-3.597	0.36	2.15	0.21	0.28	2.01	0.0069	0.0063	0.0014	0.64	7.71	0.77	0.50	2.66	0.0133	0.0271	0.0019
73330	337.6	0.0078	-3.85	1.213	0.23	1.35	0.14	0.18	2.01	0.0062	-0.0019	0.0010	0.77	9.30	0.93	0.61	2.68	0.0194	0.0344	0.0022
73330	324.4	0.0196	-3.25	1.569	0.27	1.61	0.16	0.21	2.01	0.0095	0.0015	0.0018	0.73	8.78	0.88	0.57	2.67	0.0254	0.0304	0.0030
73330	310.6	0.1119	0.00	0.000	0.22	1.30	0.13	0.17	2.03	0.0000	-0.0013	0.0000	0.78	9.40	0.94	0.61	2.76	0.0000	0.0458	0.0000
73330	298	0.0310	-0.03	2.330	0.24	1.42	0.14	0.19	2.04	0.0157	0.0027	0.0029	0.76	9.15	0.92	0.60	2.84	0.0607	0.0496	0.0067
73330	270.8	0.0286	0.10	2.268	0.34	2.04	0.20	0.27	2.04	0.0172	0.0059	0.0030	0.66	7.92	0.79	0.52	2.79	0.0654	0.0479	0.0075
73331	257.1	0.0392	-0.27	2.474	0.34	2.06	0.21	0.27	2.04	0.0188	0.0063	0.0033	0.66	7.88	0.79	0.51	2.79	0.0676	0.0455	0.0075
73332	244.2	0.0188	-0.39	1.766	0.31	1.85	0.19	0.24	2.04	0.0127	0.0041	0.0022	0.69	8.29	0.83	0.54	2.79	0.0498	0.0479	0.0056
73333	230.1	0.0269	0.27	2.097	0.29	1.77	0.18	0.23	2.04	0.0145	0.0035	0.0024	0.71	8.46	0.85	0.55	2.81	0.0574	0.0461	0.0060
73334	216.5	0.0413	2.66	2.330	0.35	2.12	0.21	0.28	2.06	0.0189	0.0074	0.0039	0.65	7.76	0.78	0.51	2.87	0.0567	0.0396	0.0068
73335	204.3	0.0187	1.52	2.305	0.19	1.12	0.11	0.15	2.04	0.0120	-0.0048	0.0020	0.81	9.76	0.98	0.64	2.77	0.0368	0.0286	0.0037
73336	192.8	0.0223	-1.84	2.992	0.30	1.78	0.18	0.23	2.03	0.0190	0.0013	0.0023	0.70	8.44	0.84	0.55	2.66	0.0697	0.0303	0.0107
73337	182	0.0460	-4.83	3.487	0.38	2.28	0.23	0.30	2.00	0.0274	0.0067	0.0044	0.62	7.43	0.74	0.48	2.67	0.0429	0.0254	0.0068
73338	172.5	0.0302	-2.29	1.995	0.31	1.86	0.19	0.24	2.02	0.0127	0.0029	0.0021	0.69	8.29	0.83	0.54	2.70	0.0340	0.0323	0.0038
73339	163.3	0.0100	1.21	1.503	0.24	1.42	0.14	0.19	2.05	0.0097	-0.0012	0.0016	0.76	9.15	0.92	0.60	2.77	0.0253	0.0263	0.0027
73340	155	0.0134	-0.27	1.693	0.27	1.61	0.16	0.21	2.03	0.0119	0.0017	0.0019	0.73	8.79	0.88	0.57	2.76	0.0296	0.0296	0.0035
73341	147.2	0.0325	0.26	2.275	0.29	1.73	0.17	0.23	2.04	0.0151	0.0018	0.0023	0.71	8.55	0.85	0.56	2.82	0.0659	0.0483	0.0072
73342	139.7	0.0325	0.26	2.275	0.25	1.51	0.15	0.23	2.04	0.0151	0.0018	0.0023	0.75	8.98	0.90	0.56	2.82	0.0659	0.0483	0.0072
73343	132.8	0.0125	0.57	1.692	0.25	1.51	0.15	0.20	2.04	0.0109	-0.0004	0.0018	0.75	8.98	0.90	0.59	2.75	0.0261	0.0256	0.0028
73344	126.2	0.0214	1.55	1.972	0.29	1.74	0.17	0.23	2.05	0.0146	0.0030	0.0026	0.71	8.52	0.85	0.56	2.76	0.0329	0.0242	0.0034
73345	120	0.0406	-4.29	3.289	0.33	2.00	0.20	0.26	2.01	0.0231	0.0035	0.0037	0.67	8.01	0.80	0.52	2.68	0.0426	0.0238	0.0053
73346	114.4	0.0380	-0.40	2.743	0.34	2.04	0.20	0.27	2.04	0.0202	0.0058	0.0032	0.66	7.91	0.79	0.52	2.81	0.0834	0.0470	0.0082
73347	108.5	0.0151	1.39	1.931	0.28	1.66	0.17	0.22	2.04	0.0129	0.0008	0.0018	0.72	8.68	0.87	0.57	2.79	0.0569	0.0484	0.0065

Results from the Artemis fitting of the coordination number correspond with the observations from the XANES data, which suggested that the material has not been fully reduced. This is strongly indicated by the steady decrease in the coordination number of the oxide, and from the change in the coordination number of the Rh metal (Figure 4-40). These results indicate that complete reduction did not occur, perhaps necessitating a higher temperature or longer reduction time is required for the material. The results are in reasonable agreement with the XANES analysis, by also suggesting a 30% conversion from the LCF fitting.

Comparing the mixing parameter from EXAFS fitting with the LCF results confirms that there is a reasonable agreement between the two fitting methods (Figure 4-42). One area of note are the region between 323 – 373 K which shows some Rh metal, however this has already been explained as correlation with the Rh oxide second shell. A second area of interest is between 548 – 573 K where the material passes the 50% reduction point in both XANES and EXAFS models. In this region the amount of conversion from the EXAFS model rises higher than the XANES, this again is potentially due to correlation with higher shells in the fitting model. Overall the model is in good agreement giving a 65% conversion from EXAFS and a 70% conversion from XANES; a 5% difference is well within the accepted errors for the model.

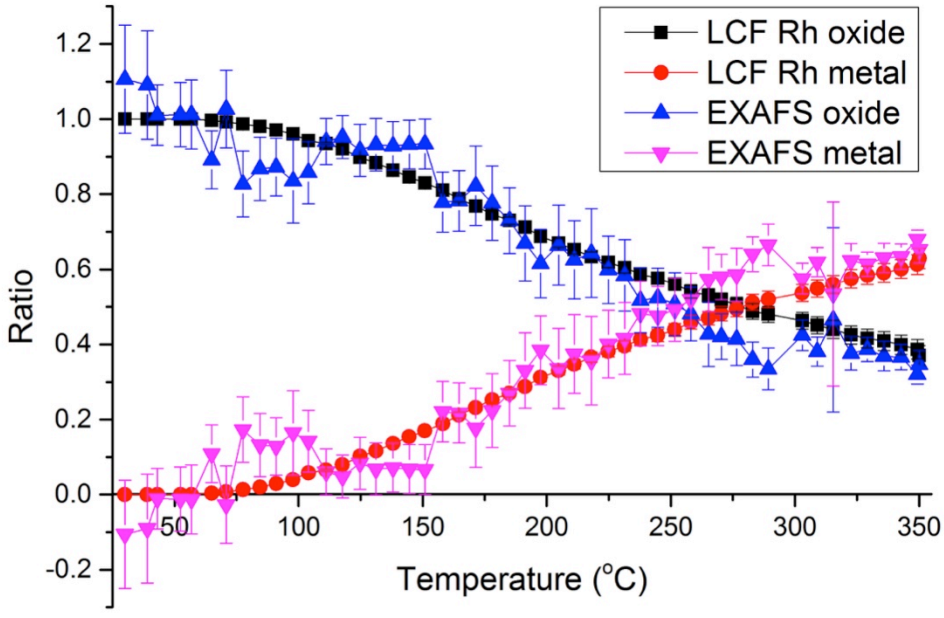

Figure 4-42 - Comparison of Artemis and LCF fitting models to Rh oxide and Rh metal standards.

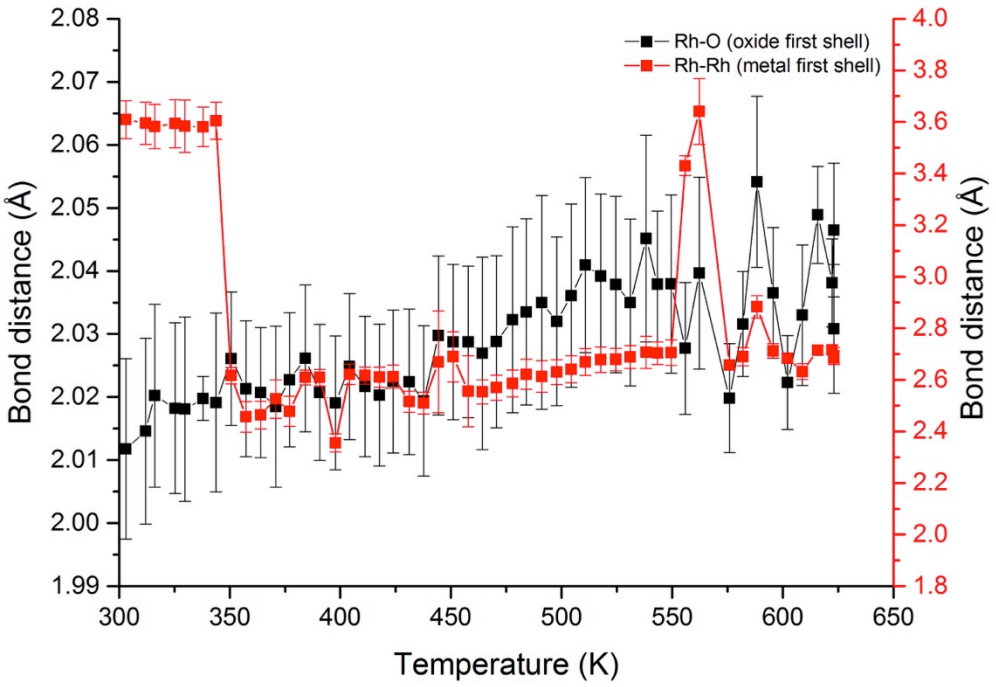

Figure 4-43 - Plot of bond distance from EXAFS fitting against temperature for Rh/Ceria/Alumina catalyst heated to 623 K under H_2/He.

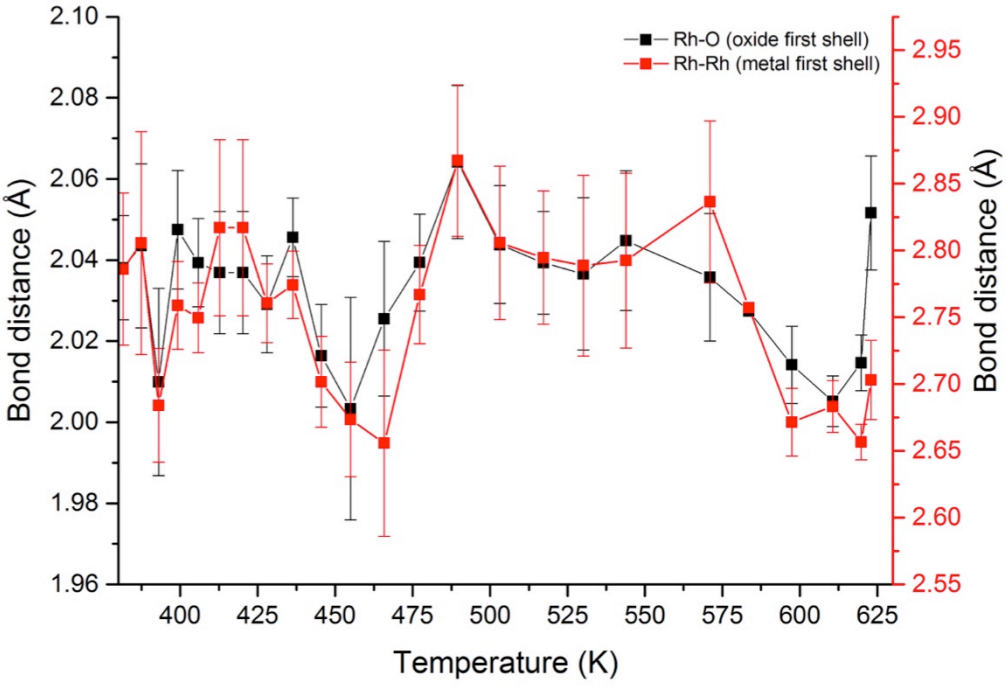

Figure 4-44 - Plot of bond distance from EXAFS fitting against temperature for Rh/Ceria/Alumina cooling to room temperature under H_2/He.

By following the change in the bond distance it can be seen that the initial instances of Rh-Rh presence below 348 K are actually due to correlation with the Rh-Rh second shell in the oxide

(Figure 4-43). This is confirmed through the bond distance of 3.6 Å, which is considerably larger than the value of 2.69 Å reported in the literature. At 75^{o}C onwards the value for the bond distance drops to ca 2.7 Å close to the expected value for the Rh-Rh first shell. The Rh – O shell has a slowly increasing bond distance with increasing temperature, until reaching a value of 2.04 Å. The variance in the value for this shell is much smaller than that for the Rh-Rh shell. This could be due to the greater stability of the Rh-O shell and the larger amount of the material present.

Upon cooling the bond distance for the Rh-Rh shell increases from the expected value of 2.7 Å to an enlarged value of 2.8 Å; this 0.1 Å increase whilst with in the error for the shell is still of interest (Figure 4-44). Again the variance in the Rh – O bond distance is by comparison very small.

Of interest is the lack of complete reduction in the material despite the increased reduction in temperature and time. One potential explanation is that the oxygen in the Ceria is able to diffuse into the Rh_2O_3 structure, or the oxygen is trapped by the surrounding ceria and simply cannot escape the structure; confirmation of this would require a similar investigation on pure ceria and alumina supports to gauge the different support effects.

To summarise the results from XANES and LCF suggest that there is a 65% conversion to the metal phase and this is confirmed by EXAFS analysis. Complete reduction did not occur after heating to 623 K, indicating either a longer reduction time or higher temperatures are required for the reduction to go to completion. Additionally there could potentially be some oxygen donation from the Ceria overlayer into the Rh species.

4.6 Conclusions

Both support Pd and Rh catalysts have been investigated using *in-situ* XAS. Both materials showed signs of reduction, the level of reduction for Rh being much lower than for Pd, which appeared to reduce completely. Supported palladium material showed an interesting expansion of the bond distance at low temperature, from 2.75 Å to 2.80 Å, attributed to Pd hydride formation.[38] The lower level of Rh reduction can be linked to the reduction capabilities of Rh_2O_3. The use of ceria as an over layer does not prevent the gases from accessing the active sites of Pd and Rh and causing reduction, which is in contrast to some of the earlier theories on the SMSI.[12]

Although the Pd material was reduced to near completion the reduction for Rh did not, with a maximum conversion to Rh metal of ca, 65% discovered. Whilst this could be mere coincidence due to incomplete reduction, it could also be evidence to another effect of the support materials. It is possible that the complete reduction of the material is impeded by the ceria support. It is well documented that ceria possesses a remarkable oxygen storage capacity; this stored oxygen could be transferred to the metal NPs during the reduction.[8] This effect would be limited to metal clusters within a specific distance to the ceria, or impeded in defect sites in the ceria structure. The fact that this is not seen with Pd could be due to the synergistic properties exhibited by Pd/ceria materials.[41] Further data is required to confirm this theory.

Whilst characterisation on these materials has been conducted and published,[25] a re-examination of the material using techniques such as combined TGA/MS and TEM would be beneficial to the analysis. Further analysis of EXAFS data combined with changes in the lattice parameter from XRD and mass spectroscopy data would be required in order to confirm these results.

4.7 References

(1) Ash, P. W.; Boyd, D. a; Hyde, T. I.; Keating, J. L.; Randlshofer, G.; Rothenbacher, K.; Sankar, G.; Schauer, J. J.; Shafer, M. M.; Toner, B. M. *Environ. Sci. Technol.* **2014**, *48*, 3658–3665.

(2) Kwon, H. J.; Baik, J. H.; Kwon, Y. T.; Nam, I.-S.; Oh, S. H. *Chem. Eng. J.* **2008**, *141*, 194–203.

(3) Antolini, E. *Energy Environ. Sci.* **2009**, *2*, 915.

(4) Arai, M.; Panpranot, J.; Praserthdam, P.; Weerachawanasak, P. *J. Mol. Catal. A Chem.* **2008**, *279*, 133–139.

(5) Bowker, M.; Stone, P.; Morrall, P.; Smith, R.; Bennett, R.; Perkins, N.; Kvon, R.; Pang, C.; Fourre, E.; Hall, M. *J. Catal.* **2005**, *234*, 172–181.

(6) Shinjoh, H.; Hatanaka, M.; Nagai, Y.; Tanabe, T.; Takahashi, N.; Yoshida, T.; Miyake, Y. *Top. Catal.* **2009**, *52*, 1967–1971.

(7) Colombo, C.; Monhemius, a J.; Plant, J. a. *Ecotoxicol. Environ. Saf.* **2008**, *71*, 722–730.

(8) Jen, H.-W.; Graham, G. .; Chun, W.; McCabe, R. .; Cuif, J.-P.; Deutsch, S. .; Touret, O. *Catal. Today* **1999**, *50*, 309–328.

(9) Li, G.; Li, L.; Yuan, Y.; Shi, J.; Yuan, Y.; Li, Y.; Zhao, W.; Shi, J. *Appl. Catal. B Environ.* **2014**, *158-159*, 341–347.

(10) Bunker, G. *Introduction to XAFS A Practical Guide to X-ray Absorption Fine Structure Spectroscopy*; Illinois, 2010.

(11) Sankar, G.; Thomas, J. M. *Top. Catal.* **1999**, *8*, 1–21.

(12) Tauster, S. J. *Acc. Chem. Res.* **1987**, *20*, 389–394.

(13) Yang, M.; Feng, L.; Chen, Y.; Li, Y.; Yang, H.; Fan, Y.; Xu, B. *Chem. Phys. Lett.* **2003**, *372*, 160–165.

(14) Robertson, B. A. J. B.; Thnard, L. J. *Platin. Met. Rev.* **1975**, *19*, 64–69.

(15) Hogarth, G.; Kabir, S. E.; Nordlander, E. *Dalton Trans.* **2010**, *39*, 6153–6174.

(16) Fajardie, F. *Catal. Letters* **1998**, *54*, 187–193.

(17) Davis, M. E. *Ind. Eng. Chem. Res.* **1991**, *30*, 1675–1683.

(18) Kulkarni, A.; Lobo-Lapidus, R. J.; Gates, B. C. *Chem. Commun. (Camb).* **2010**, *46*, 5997–6015.

(19) Hussain, M.; Fino, D.; Russo, N. *J. Hazard. Mater.* **2012**, *211-212*, 255–265.

(20) Beyer, H.; Emmerich, J.; Chatziapostolou, K.; Köhler, K. *Appl. Catal. A Gen.* **2011**, *391*, 411–416.

(21) Dixon, D. a.; Katz, A.; Arslan, I.; Gates, B. C. *Catal. Letters* **2014**, *144*, 1785–1789.

(22) Badri, A.; Binet, C.; Lavalley, J. *J. Chem. Soc. Faraday Trans.* **1996**, *92*, 1603–1608.

(23) Scott, M.; Waterhouse, G.; Söhnel, T. *34th Annu. Condesend Matter Mater. Meet.* **2010**.

(24) Hosoya, M.; Shimoda, M. *Appl. Catal. B Environ.* **1996**, *10*, 83–97.

(25) Acerbi, N.; Golunski, S.; Tsang, S. C.; Daly, H.; Hardacre, C.; Smith, R.; Collier, P. *J. Phys. Chem. C* **2012**, *116*, 13569–13583.

(26) Grunwaldt, J. *J. Catal.* **2001**, *200*, 321–329.

(27) Newton, M. a; Fiddy, S. G.; Guilera, G.; Jyoti, B.; Evans, J. *Chem. Commun. (Camb).* **2005**, 118–120.

(28) Marchionni, V.; Newton, M. a.; Kambolis, A.; Matam, S. K.; Weidenkaff, A.; Ferri, D. *Catal. Today* **2014**, *229*, 80–87.

(29) Chang, J. R.; Lin, H. M.; Cheng, S. W.; Tseng, C. K.; Tzou, D. L.; Shyu, S. G. *J. Mol. Catal. A Chem.* **2010**, *329*, 27–35.

(30) Grunwaldt, J.; Keresszegi, C.; Mallat, T.; Baiker, A. **2003**, *213*, 291–295.

(31) Lin, S. D.; Hsu, Y.; Jen, P.; Lee, J. **2005**, *238*, 88–95.

(32) Tew, M. W.; Nachtegaal, M.; Janousch, M.; Huthwelker, T.; van Bokhoven, J. a. *Phys. Chem. Chem. Phys.* **2012**, *14*, 5761–5768.

(33) Shen, W.; Ichihashi, Y.; Ando, H.; Matsumura, Y.; Okumura, M.; Haruta, M. *Appl. Catal. A Gen.* **2001**, *217*, 231–239.

(34) McCaulley, J. a. *J.Phys.Chem.* **1993**, *97*, 10372–10379.

(35) Wang, J.; Wang, Q.; Jiang, X.; Liu, Z.; Yang, W.; Frenkel, A. I. *J. Phys. Chem. C* **2015**, *119*, 854–861.

(36) Acerbi, N. Chapter 2 Experimental Methods, Oxford University.

(37) La, R.; Roma, S. *Solid State Commun.* **1993**, *85*, 863–868.

(38) Tew, M. W.; Nachtegaal, M.; Janousch, M.; Huthwelker, T.; van Bokhoven, J. a. *Phys. Chem. Chem. Phys.* **2012**, *14*, 5761–5768.

(39) Weng, W.; Pei, X.; Li, J.; Luo, C.; Liu, Y.; Lin, H.; Huang, C.; Wan, H. *Catal. Today* **2006**, *117*, 53–61.

(40) Bernal, S.; Calvino, J. J.; Cauqui, M. A.; Gatica, J. M.; Cartes, C. L.; Omil, J. A. P.; Pintado, J. M. *Catal. Today* **2003**, *77*, 385–406.

(41) Yang, Z.; Lu, Z.; Luo, G.; Hermansson, K. *Phys. Lett. A* **2007**, *369*, 132–139.

Chapter 5 - Multi-edge XAS Analysis of AuCu Bimetallic Clusters

Abstract

Bimetallic clusters have a variety of uses in catalysis due to synergistic properties and improved catalytic performance. In this chapter we explore the characterisation of AuCu bimetallic clusters during reduction, calcination and under catalysis for the oxidation of propene. Multi-edge analysis was utilised to investigate the material at both the Au- and Cu-edges, with the information combined to enhance the characterisation of the clusters. The catalyst activation mechanism was investigated using *in situ* XAS.

5.1 Introduction

$AuCu/SiO_2$ catalysts have been shown to be both active and selective for the catalytic synthesis of acrolein from propene. The nature of the catalyst and variables such as composition, species present (e.g. Cu metal or CuO), loading method, reduction method and calcination procedure can influence the catalytic activity and selectivity. Adjusting these variables, through variations in the particle size, dispersion and oxidation state can be used to improve the catalytic potential of the material. It has been shown that the combination of copper and gold to improved selectivity, with the CuO providing higher selectivity at higher temperature and Au being active at lower temperature. Careful selection of the synthesis method and activation procedure can tailor the performance of the catalyst.

5.1.1 Background

A bimetallic structure can be compromised of a variety of different nanostructures such as a core-shell structure, random alloy or mixed monometallic nanoparticles.[1] Also of importance is the surface composition of the bimetallic clusters; this can be affected by the intrinsic properties of the metals such as bond strengths and surface energies, and external conditions such as temperatures and environment during catalyst pre-treatment and reaction.[1,2]

Au based bimetallics are effective catalysts for a variety of applications such as CO oxidation, epoxidation of propene, selective oxidation of alcohols and hydrogenation reactions.[3–6] The designing of catalysts for selective oxidation represents a significant research challenge. Bimetallic copper-gold systems are of interest due to the number of bulk phases that can be formed and the complex structures of small particles. AuCu bimetallic catalysts have been shown to be active for a number of selective oxidation reactions, with the oxidation of CO, propene and toluene being good examples.[1,7–10] A previous publication by Sinfelt reported the characterisation of bimetallic $AuCu/SiO_2$ clusters for the oxidation of propene to acrolein using XAS.[11]

Both the Cu and Au components are active for the catalysis. Copper catalysts such as Cu_2O, CuO and Cu metal have been successfully used for the oxidation of propene with the major product being acrolein[12,13]. One of the main issues with Cu catalysts is controlling the dispersion of the Cu nanoparticles during reduction and catalysis reactions.[14]Au nanoparticles have been shown to be active for a number of reactions such as the oxidation of CO, with the breakthrough paper by Haruta demonstrating their use as catalysts for propene oxidation.[15] Supported Au catalysts on reducible supports such as titania or iron oxide have been utilised in the selective oxidation of propene to propane oxide, usually with hydrogen as a co-

reductant.[16–18] Bimetallic clusters have been shown to exhibit better catalytic performances then their monometallic analogues.[7,19]

Currently the chlorohydrin route is the most prevalent method for the production of propene oxide; however this method generates significant quantities of chlorinated waste.[20] Hence greener and sustainable alternatives, such as AuCu catalysis are active areas of research. The oxidation of propene, in a mixed H_2/O_2 environment, can produce a number of products dependent upon the reaction conditions and the selectivity of the catalyst (Figure 5-1).[21] Therefore there is a need to develop active and selective catalysts for the oxidation of propene to acrolein.

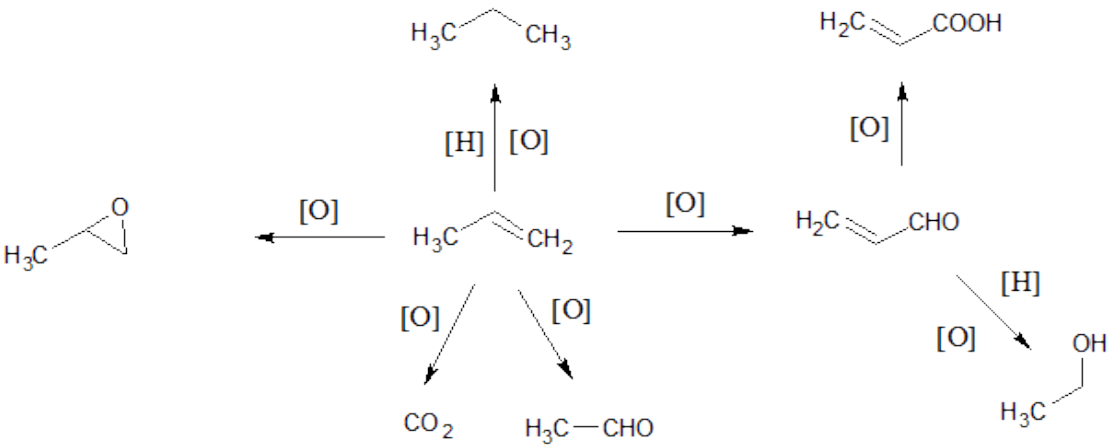

Figure 5-1 - Reaction scheme for the various oxidation reactions of propene (based on reaction scheme from Bracey et al).[21]

There are a number of methods for AuCu bimetallic cluster formation, such as a two-step reduction process involving Au and Cu ions in a micro emulsion solution.[1]Co-impregnation of Au and Cu precursors or deposition are also viable methods for creating AuCu catalysts.[7,11]

Previous investigations by Sinfelt into the structure of bimetallic clusters made extensive use of XAS techniques as a characterisation tool.[22] The materials looked at were bimetallic AgCu and AuCu formed through co-impregnation methods, using gold chloride and copper nitrate for the latter.[22] Interestingly despite the miscibility of gold and copper the EXAFS results revealed that there was extensive segregation of the two metals.[22] One of the main aims of this study was to ascertain whether the components of bimetallic metals are miscible in bulk or will they segregate with one component concentrating on the surface. For the AuCu clusters it was found that the Cu-Cu bond distance was longer than expected (2.61 Å as opposed to the literature value of 2.56 Å), meanwhile the Au-A distance was shorter than expected (2.8 as opposed to 2.884).[22–24] There is also a difference in the coordination numbers

with the number of nearest neighbours about the Au atom found to be 11 as opposed to 12 for the Cu atom; both metals have a first shell coordination number of 12 for the metallic phase.[22] The authors took this as an indication that the gold-rich region is present on the on the surface, which is supported by other published investigations into AuCu bimetallic materials.[25,26] It has also been noted in the literature that fitting the two components simultaneously allows for physical conditions about regarding the system to be taken into account, improving the accuracy of the results.[11]

A recent publication by our research group and JM looked into the impact of catalyst preparation on the structure and catalytic performance of $AuCu/SiO_2$ catalysts for the oxidation of propene to acrolein.[18] This work was based on patent from Sinfelt, which reported that a co-impregnated $AuCu/SiO_2$ catalyst could convert up to 40% of propene with 50-70% selectivity for acrolein.[27] The preparation method they used following impregnation or deposition was first reduction, with either hydrogen or $NaBH_4$, followed by high temperature calcination.[18]

It was found that for the coimpregnated materials reduction by hydrogen produced materials with a high amount of AuCu alloying, whilst reduction with $NaBH_4$ produced smaller particles with negligible interaction between the Au and Cu.[18] Subsequent calcination at high temperature (675^{o}C) resulted in the destruction of the AuCu phase, though some interaction was still observed through transmission electron microscopy (TEM).[18] The material formed through sequential deposition exhibited smaller particle sizes, observed through broader and weaker peaks in the XRD patterns, with most of the gold present in the metallic phase and most of the copper present as Copper(II) oxide.[18] Catalysts after reduction (without calcination), and after the high temperature calcination (reduced and calcined) were used for the oxidation of propene.

The reduced only catalysts were observed to have mixed selectivity due to a number of varied active sites whilst the reduced-calcined catalysts exhibited more selectivity towards acrolein.[18] The reduced deposited catalysts showed a higher activity than any of the impregnated catalysts with a much higher selectivity for acrolein; indicating that one type of active site is dominant in the material.[18] However the reduced and calcined catalyst exhibited the reduced and calcined deposited catalyst exhibited the highest activity of any reported in the paper (10% conversion) with good selectivity for acrolein (89%). This is in spite of the material having no detectable AuCu interaction, which is believed to be destroyed by the calcination procedure.[18] This report shows the importance of the preparation procedure as the

deposited catalysts exhibit much higher activity than their impregnated counter parts, in some cases by as much as 30%.[18]

5.1.2 Aim of the work

The principle aim of this investigation is study the structural changes of $AuCu/SiO_2$ bimetallic catalysts, during catalyst activation as well as during the oxidation of propene. The extent and the nature of the AuCu interaction, whether the metals are truly bimetallic, alloyed or have limited interaction will also be compared. The investigations will focus on *in situ* XAS measurements on both the Au L_{III}- and Cu K-edges, during reduction with hydrogen, calcination to 600^{o}C and for the catalytic oxidation of propene. *In situ* measurements during propene oxidation will be performed on both the reduced only and reduced-calcined catalysts to follow the differences, if any are observable, between the two catalysts.

The reduction mechanism expected for the Au L_{III}-edge is a change from the 4-coordinate $NaAuCl_4$ precursor to Au metal, whilst on the Cu K-edge the reduced material is expected to be Copper (II) oxide, rather than Cu metal.[18] Upon calcination there are changes expected in the material with the loss of the AuCu interaction expected to be visible in the EXAFS. This information can then be used to help interpret results from catalytic testing and help to tailor the synthesis of these catalysts for future use.

5.2 Experimental

5.2.1 Sample preparation

Samples were prepared using the impregnation procedure on a silica support. First the pore volume of the silica was measured by adding water until the incipient wetness point was reached, with the change in mass during the addition being monitored. A solution of copper nitrate hemipentahydrate and tetrachloroauric acid was prepared using an appropriate volume of water to fill the pores of the support and give the desired concentration and ratio of metals in the final product. The material was then dried at 105^{o}C for three hours.

Samples were also prepared through deposition procedure, with the Cu and Au precursors being added sequentially; the Cu precursor was added first. Full details of catalyst preparation are available in publications by Dr Peter Ellis of Johnson Matthey, and reproduced here for reference.[18,21] The copper and gold were deposited sequentially with the Cu being deposited first.[18] This was done through the addition of a solution made from basic copper carbonate (7.5g, 85 mmol Cu), ammonium hydroxide (85 ml) and water (75 ml) was added to the silica support (Grace P432, reference SP550-SP10022, BET surface area 340 m^2 g^{-1}).[18] The suspension was then heated to boiling, following which the ammonia was removed via distillation, resulting in the deposition of Cu onto the silica. The product was then collected via filtration, washed and dried at 105^{o}C for 3 hours. [18]

The Au was then added to this material by first re-suspending the Cu/SiO_2 in water (400ml) at 65^{o}C. Au was then added through deposition precipitation using tetrachloroauric acid (0.89 g solution, 1.9 mmol) and sodium hydroxide (0.1 M solution). [18] The pH was maintained around 9 for the deposition by monitoring the addition of the Au solution and base. The product was removed via filtration and dried at 105 ^{o}C for three hours.[18]

Ex-situ reduction was carried out in a tube furnace with 5% H_2/N_2, ramping to 40 ^{o}C at 2 ^{o}C/min and held for 30 minutes to purge the tube.[18] A further ramp to 315 ^{o}C at a rate of 10 ^{o}C/min was then employed holding at temperature for 2 hours before cooling to room temperature. A higher calcination at 675 ^{o}C was also used on some of the materials.[18]

5.2.2 XAS measurements

X-ray Absorption spectroscopy measurements were performed on the SAMBA beamline at Synchrotron Soleil, Paris, France. Data was collected on both Au L_{III}- and Cu K-edges separately under identical conditions on each edge, with data recorded in QuEXAFS mode with scans taken every second and merged; typically 50 spectra were combined to give the data used for the analysis. Samples were loaded into a purpose built reaction cell, with gas inlets and outlets and a furnace for controlling temperature (Figure 5-2 and Figure 5-3). Spectra were processed using Athena and Artemis software utilising Cu and Au foils as standards.

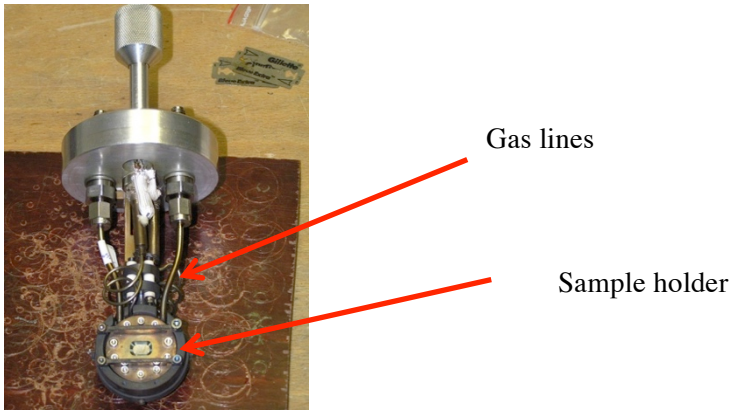

Figure 5-2 - Image of the sample holder from reaction cell showing the sample holder gas inlets and outlets.

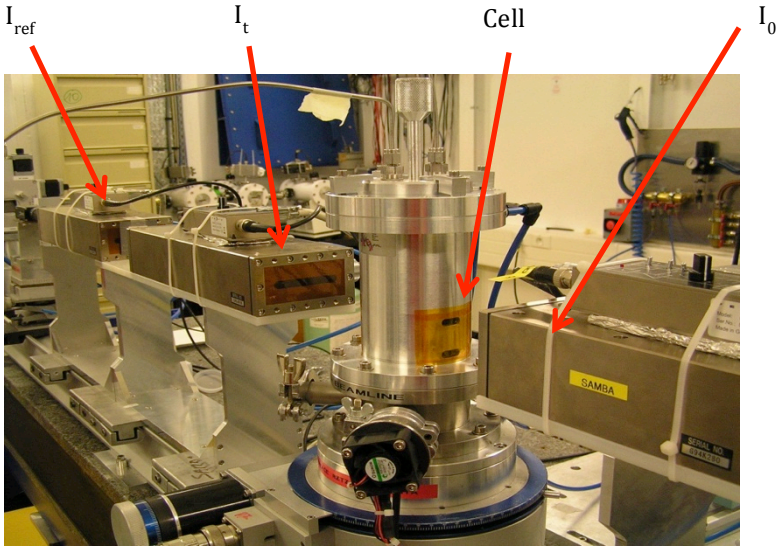

Figure 5-3 – Image of the beamline set up showing the position of the cell and ion chambers, I_0, It and I_{ref}.

5.2.3 Experiments

Three main experiments were investigated in the course of this work:

1. **Reduction**: the supported AuCu materials were reduced in flow of hydrogen 10 ml/min *in situ* and heated to 300 ^{o}C on the beamline.
2. **Calcination**: the reduced catalyst was then calcined *in situ* up to a temperature of ca 600^{o}C.
3. **Catalysis:** the materials were tested for their catalytic potential for the oxidation of propene to acrolein. The experiments were performed using the both the reduced only (from the end of experiment 1) and reduced-calcined (from the end of experiment 2) catalysts respectively. The reaction vessel was heated to 200 ^{o}C, then in steps to 320 ^{o}C using 40 ^{o}C increments. Data was collected at each temperature.

5.3 Reduction

In this experiment the deposited metal precursors are reduced to leave the active components of the catalyst. Materials were deposited in the lab and the reduction carried out in situ on the beamline in a flow of hydrogen (10ml/min) and with moderate heating (up to ca 573 K). Data was recorded on both the Cu K-edge and Au L_{III}-edge with two different samples in separate experiments, under the same reaction conditions.

5.3.1 Au edge

Data was normalised using Athena software and analysed using Artemis. The fitting windows used were, 2.5-10 in k-space k^3 weighted and 1.5-4 $Å^{-1}$. For this experiment data was first fitted in a combined measurement to include an AuCu path to determine the extent of the bimetallic interaction. However as initial scans showed no interaction between the metals each set of data, Cu k-edge and Au L_{III}-edge respectively was fitted separately.

5.3.1.1 XANES Analysis

Analysis of the XANES data during the reduction after Au deposition shows a clear change from the precursor to the Au metal - highlighted by a change in whiteline intensity from 1.25 to 0.74 at ca 373-448 K (Figure 5-4). This is also visible by a change in the edge feature of the XANES from the 4-coordinate AuOH precursor to the metal, as indicated by the loss of the whiteline and the emergence of a double peak feature after the edge. AuOH was used for this fitting model, as it is believed that the $NaAuCl_4$ undergoes hydrolysis on following deposition on the surface.[18]

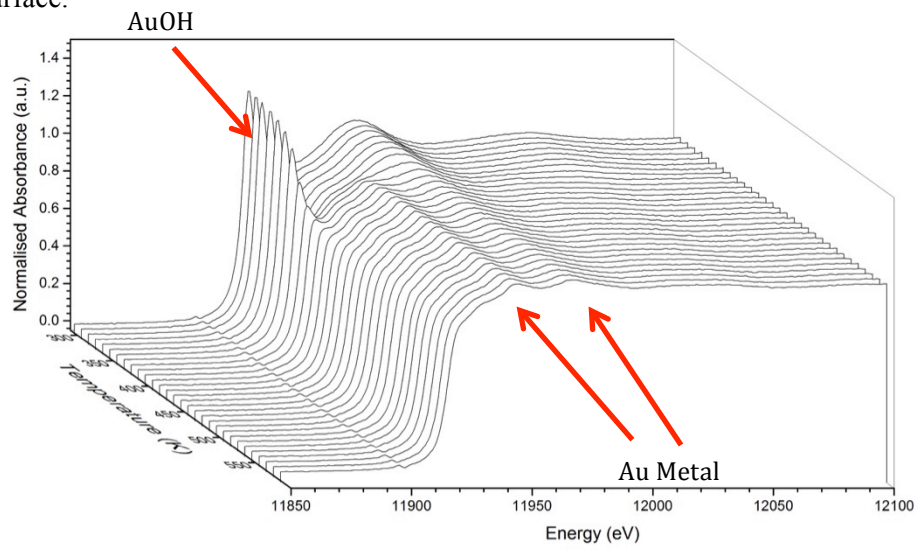

Figure 5-4 –Au l_3-edge XANES plot of the reduction of Au precursor.

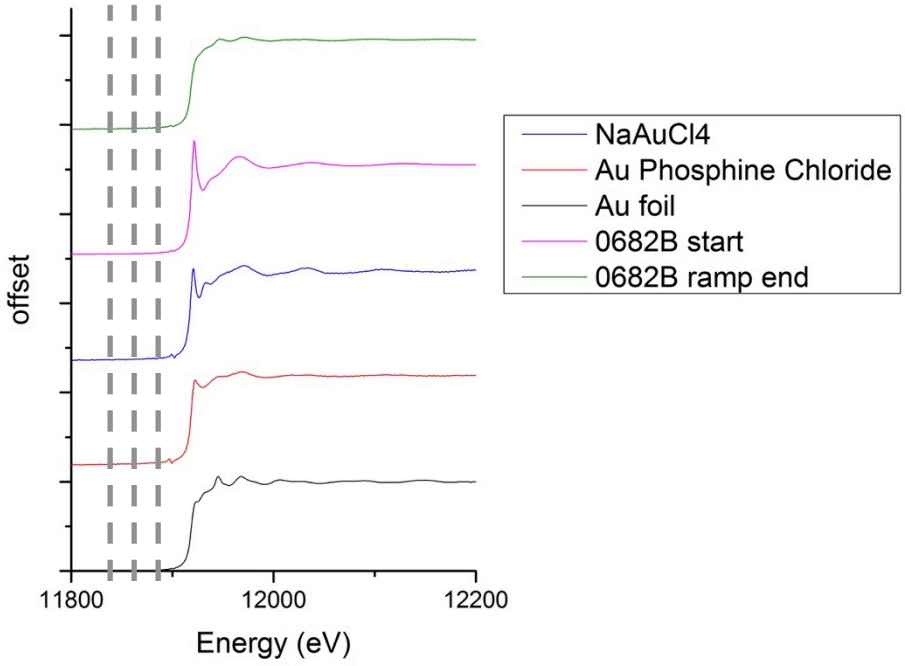

Figure 5-5 - Comparison of the XANES for the start and end of the reduction ramp with Au standards.

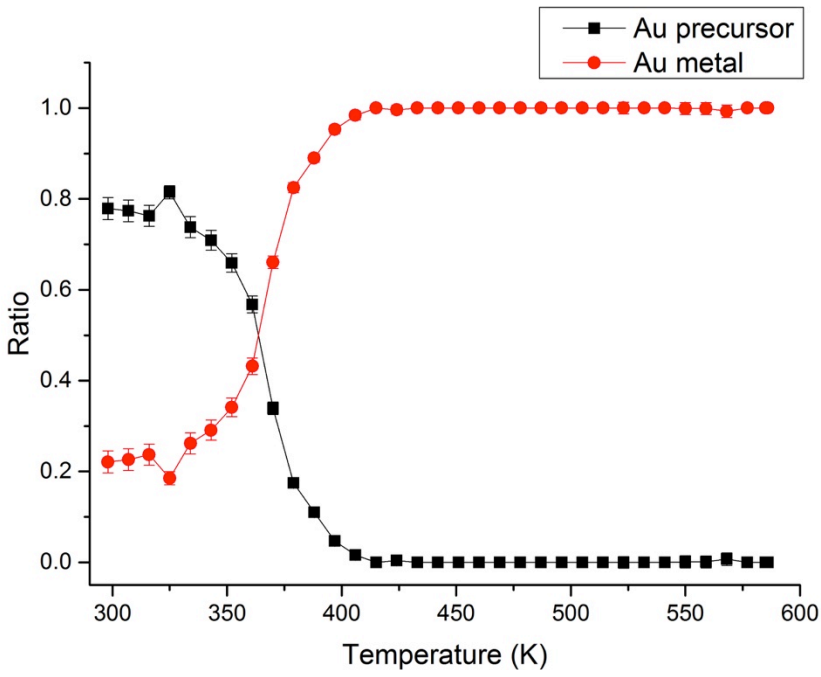

Figure 5-6 - Linear combination fit of Au metal and AuOH standards with 0682B reduction data for the Au L_3 edge.

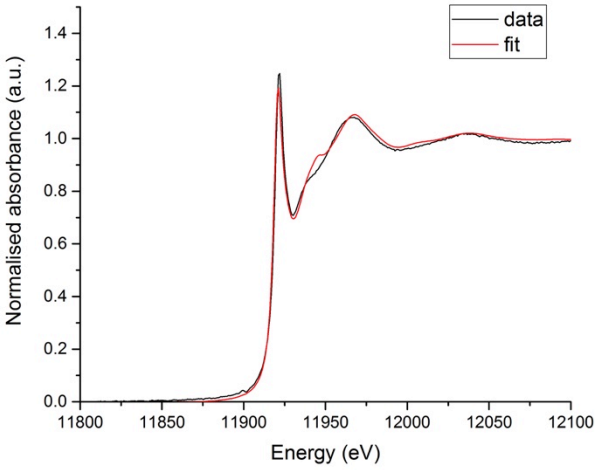

Figure 5-7 - Example of LCF fitting for the Au-edge data at the beginning of the reduction.

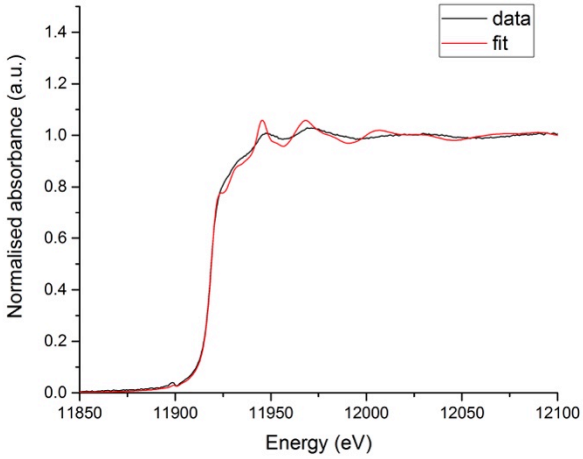

Figure 5-8 - Example of the LCF fitting of Au-edge data at the end of the reduction.

Closer comparison of the XANES from the beginning and end of the ramp shows a change in edge position from 11918.2 eV to 11920 eV (Figure 5-5). This change in energy can be linked to the change in oxidation state of the Au content as it goes from +2 to 0; this change can also be used to confirm the transformation from the 4-coordinate precursor to the metal phase. At the end of the temperature ramp the material resembles Au metal though with reduced amplitude of the post-edge features (Figure 5-5). This indicates that although the material exists mostly as the pure metal, there are other factors influencing the data such as potential Cu alloying support or temperature effects.

Linear combination fitting of the data was performed using Athena software, using the AuOH and Au foil scans as standards (Figure 5-6). The results clearly show the transition from the

precursor to the metal, occurring in a similar temperature region to that observed visually in the XANES, ca 348-448 K. the LCF shows a total reduction to the metal occurs by 423 K, with no further changes occurring upon increased heating, which matches again with initial visual inspection of the data.

Examples of the fit quality for the LCF of the reduction process are provided in Figure 5-7 and Figure 5-8. Prior to reduction the data shows a large whiteline intensity, consistent with a 4-coordinate Au system such as AuOH. After the reduction the data matches the standard for Au metal (Figure 5-8). The amplitude of the oscillations, in the post-edge region, is higher for the standard at room temperature after the reduction than the experimental data. This potentially due to the standard being unsupported, hence it is unperturbed by support effects.

5.3.1.2 EXAFS Analysis

In order to aid understanding of the following EXAFS results, diagrams for the shells used in the fitting are provided, bond distances and other details are provided in Table 5-1. The first shell of $NaAuCl_4$ and Au metal are provided in Figure 5-9 and Figure 5-10 respectively. The shells for $NaAuCl_4$ are presented here as a reference for a 4-coordinate gold system, however during fitting an $Au(OH)_3$ first shell was used, as it was believed the Au precursor underwent hydrolysis during the reaction.

Table 5-1 - Bond distances and details for the Au metal model used in the fits.

Shell	Scatterer	Bond distance (Å)	Coordination number
1	Au	2.75	12
2	Au	3.88	6

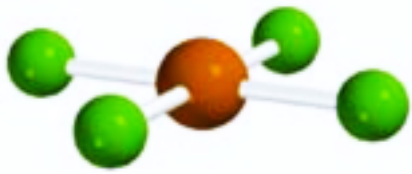

Figure 5-9 - Diagram of the first shell of $NaAuCl_4$, showing the Au centre and surrounding CL atoms in a planar structure.

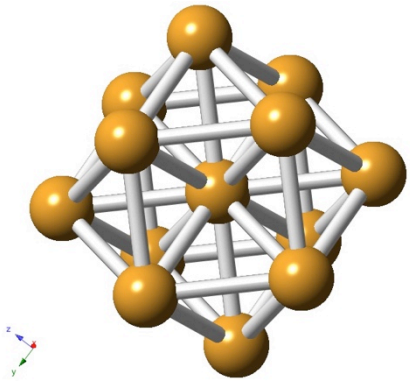

Figure 5-10 - Diagram of the first shell of Au metal, which has a central Au atom surrounded by 12 neighbouring Au atoms in an FCC crystal structure.

Data was processed with Artemis software using a standard Au metal Cif file and a quick first shell fit for the AuOH Au-O shell. Attempts to model the material with an AuCu shell were unsuccessful; hence the material was fitted purely as a combination of Au metal and AuOH (Figure 5-11).

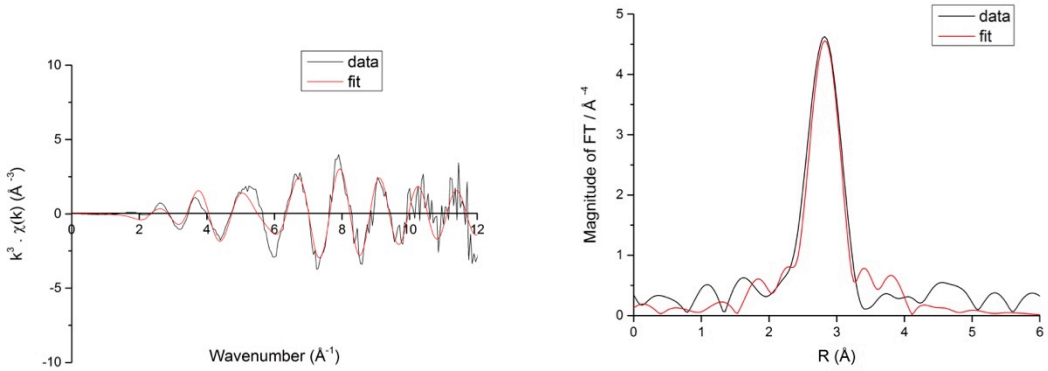

Figure 5-11 - Example of data showing k^3-weighted EXAFS data (left) and the Fourier transform of EXAFS data (right) collected on the Au L_{III}-edge at the end of the reduction.

Comparison of the data with the standards shows a clear change from the initial 4-coordinate precursor to Au metal (Figure 5-12), which has been previously noted in the XANES analysis. What should be noted here is the large change in intensity from the starting material (c) to the end of the ramp (d); this change may simply be due to temperature effects or may indicate a much smaller cluster size. Also of note is although the shape of the peak in (d) resembles the Au metal standard it is shifted to lower energy. The significance of this feature needs to be explored, as it could be an effect of loading the particle on the silica support or of some other factor. It should be noted that the edge energies for the data were of by about 20 eV. The monochromator on the beamline used in this experiment oscillates at a high frequency during QuEXAFS measurement, and can slowly shift out off alignment over time.

This can be remedied through normalising to a standard Au foil (which was done), however this could also be an explanation for the observed shift in the Fourier transform.

As can be seen in Figure 5-13 the bond distances for the Au-O shell varies only slightly during the ramp, remaining around ca 2.00 Å before dropping to 1.95 Å at around 125°C. The bond distance for the metal phase is initially much higher than the expected value (3.14 compared with 2.88) at 348 K.[22] The Au-Au distance then drops to ca 2.8 Å at 378 K before lowering again to 2.78 Å between 438-508 K. The initial high bond distance for the metal phase could be due to the low amount of Au metal species present, potentially leading to correlation with the Au-Au interaction from the AuOH. As this path has not been included in the fitting model it cannot be discounted at this time. However the effects are minimal, as soon as the Au metal species increases in concentration the bond distance decreases to the expected value (ca 2.8) and the errors decrease dramatically.

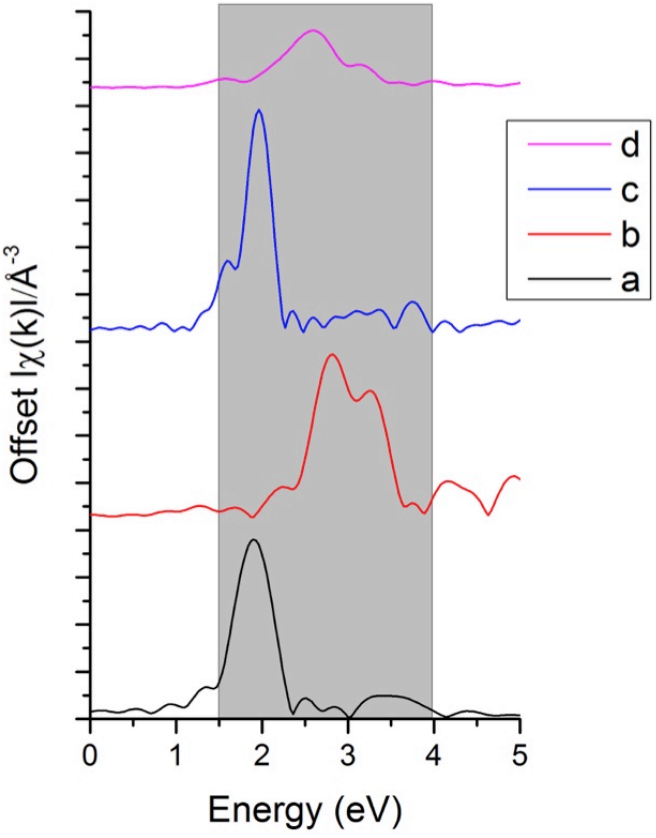

Figure 5-12 - Comparison of Fourier transforms of Au L_{III}-edge EXAFS data where a) Au metal, b) AuOH, c) material at start of ramp (298 K), d) material at the end of the ramp (588 K).

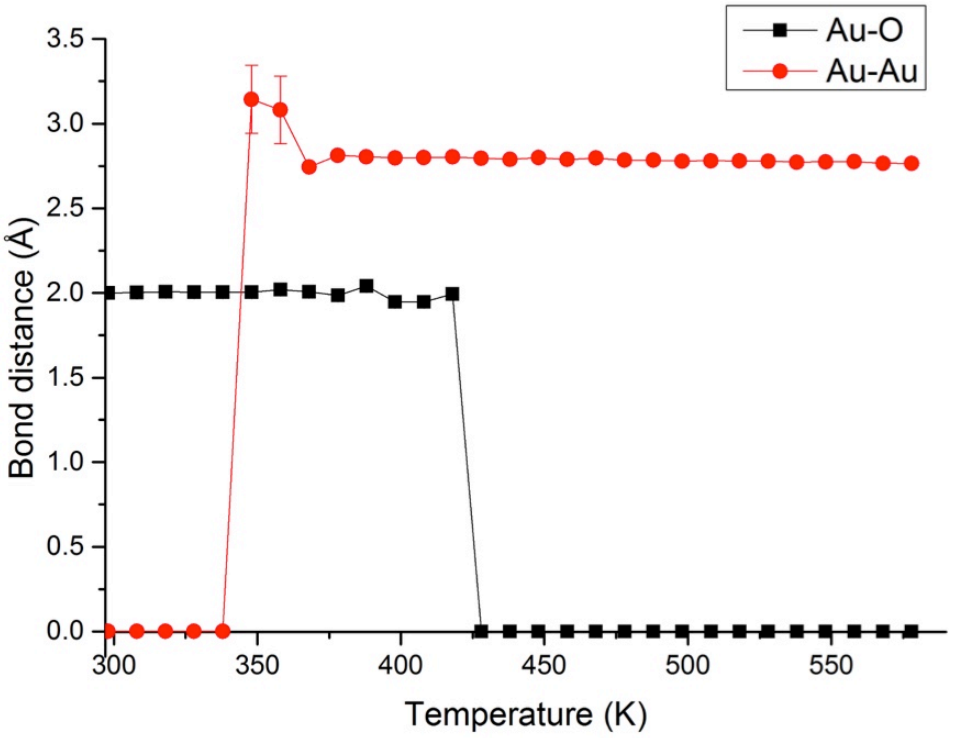

Figure 5-13 - Change in bond distance with temperature for Au edge data.

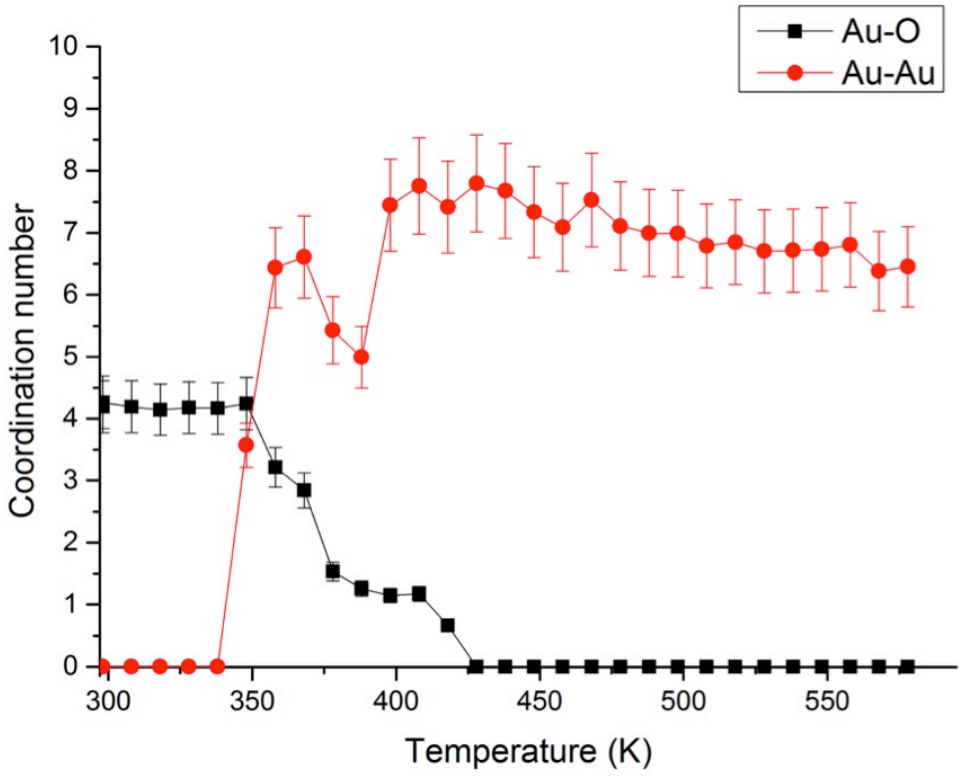

Figure 5-14 - Change in coordination number with temperature for Au edge data.

The coordination number (CN) for the Au-O shell drops from ca 4.0 to 0.7 in the temperature range of 85-135^{o}C (Figure 5-14), whilst the Au-Au CN rises from 3.6 to 7.8 in the same region. This clearly shows the transformation of the precursor to the metal, and correlates with the earlier findings from XANES and LCF. The Au-Au CN decreases to 6.8 in the temperature region 408-573 K, which could be an effect of reducing particle size at higher temperature. What should be noted is that the reduction is completed by 423 K, as indicated by XANES analysis, there is a rapid decrease in the coordination number for the Au-O shell from 348 K where the reduction begins to occur. However there is no such change in the bond distance. The lower coordination number of 7 for the Au-Au shell matches with the decreased intensity of the Au-Au peak observed in the XANES (Figure 5-5). Both support the formation of small Au particles which can grow with time.[21]

The results from both the XANES and EXAFS analysis indicates that the Au content of the catalyst has been successfully reduced to the metallic state, however the clusters are not perfect Au particles.

Table 5-2 - Results from Artemis fitting of the Au-L_{III}-edge data for reduction experiment.

		AuOH						Au						
		2.06 Au-O standard						2.88 Au-Au standard						
File	emperature (oC	R-factor	r	error	SO2	xAuOH	CN	error	r	error	SO2	xAu	CN	
1	25	0.0058	2.00	0.02	0.79	1.05	4.2	0.4	0.00	0.00	0.00	0.00	0.0	0.0
7	25	0.0054	2.00	0.02	0.80	1.07	4.3	0.4	0.00	0.00	0.00	0.00	0.0	0.0
9	35	0.0057	2.00	0.02	0.79	1.05	4.2	0.4	0.00	0.00	0.00	0.00	0.0	0.0
10	45	0.0064	2.01	0.02	0.78	1.04	4.1	0.4	0.00	0.00	0.00	0.00	0.0	0.0
11	55	0.0052	2.00	0.02	0.78	1.04	4.2	0.4	0.00	0.00	0.00	0.00	0.0	0.0
12	65	0.0056	2.01	0.02	0.78	1.04	4.2	0.4	0.00	0.00	0.00	0.00	0.0	0.0
13	75	0.0048	2.01	0.02	0.80	1.06	4.2	0.4	3.14	0.20	0.24	0.30	3.6	0.4
14	85	0.0005	2.02	0.02	0.60	0.80	3.2	0.3	3.08	0.20	0.43	0.54	6.4	0.6
15	95	0.0088	2.01	0.02	0.53	0.71	2.8	0.3	2.74	0.02	0.04	0.55	6.6	0.7
16	105	0.0135	1.99	0.02	0.29	0.38	1.5	0.2	2.81	0.02	0.36	0.45	5.4	0.5
17	115	0.0083	2.04	0.02	0.24	0.31	1.3	0.1	2.80	0.02	0.34	0.42	5.0	0.5
18	125	0.0058	1.95	0.02	0.22	0.29	1.1	0.1	2.80	0.02	0.50	0.62	7.4	0.7
19	135	0.0170	1.95	0.02	0.22	0.29	1.2	0.1	2.80	0.02	0.52	0.65	7.8	0.8
20	145	0.0052	1.99	0.02	0.12	0.17	0.7	0.1	2.80	0.02	0.50	0.62	7.4	0.7
21	155	0.0424	0.00	0.00	0.00	0.00	0.0	0.0	2.80	0.02	0.52	0.65	7.8	0.8
22	165	0.0057	0.00	0.00	0.00	0.00	0.0	0.0	2.79	0.02	0.52	0.64	7.7	0.8
23	175	0.0323	0.00	0.00	0.00	0.00	0.0	0.0	2.80	0.02	0.49	0.61	7.3	0.7
24	185	0.0323	0.00	0.00	0.00	0.00	0.0	0.0	2.79	0.02	0.48	0.59	7.1	0.7
25	195	0.0410	0.00	0.00	0.00	0.00	0.0	0.0	2.80	0.02	0.51	0.63	7.5	0.8
26	205	0.0449	0.00	0.00	0.00	0.00	0.0	0.0	2.78	0.02	0.48	0.59	7.1	0.7
27	215	0.0460	0.00	0.00	0.00	0.00	0.0	0.0	2.78	0.02	0.47	0.58	7.0	0.7
28	225	0.0547	0.00	0.00	0.00	0.00	0.0	0.0	2.78	0.02	0.47	0.58	7.0	0.7
29	235	0.0607	0.00	0.00	0.00	0.00	0.0	0.0	2.78	0.02	0.46	0.57	6.8	0.7
30	245	0.0545	0.00	0.00	0.00	0.00	0.0	0.0	2.78	0.02	0.46	0.57	6.9	0.7
31	255	0.0524	0.00	0.00	0.00	0.00	0.0	0.0	2.78	0.02	0.45	0.56	6.7	0.7
32	265	0.0638	0.00	0.00	0.00	0.00	0.0	0.0	2.77	0.02	0.45	0.56	6.7	0.7
33	275	0.0632	0.00	0.00	0.00	0.00	0.0	0.0	2.77	0.02	0.45	0.56	6.7	0.7
34	285	0.0637	0.00	0.00	0.00	0.00	0.0	0.0	2.78	0.02	0.46	0.57	6.8	0.7
35	295	0.0589	0.00	0.00	0.00	0.00	0.0	0.0	2.77	0.02	0.43	0.53	6.4	0.6
36	305	0.0712	0.00	0.00	0.00	0.00	0.0	0.0	2.77	0.02	0.43	0.54	6.5	0.6

5.3.2 Cu edge

Cu edge data was processed using Athena and analysed using Artemis. The fitting windows for the EXAFS analysis were 2.5-10 $Å^{-1}$ k^3-weighted and 1-3 Å.

5.3.2.1 XANES Analysis

Initial observations of the XANES region, shows a clear change in the whiteline intensity from the catalyst at room temperature to the final temperature at 573 K. The features also change from a clear single peak at the edge to a doublet characteristic of Cu metal. Comparison of the Cu-edge data shows a clear change from the initial material at room temperature, which resembles the CuO standard, and the material at the end of the ramp (Figure 5-16). At the end of the ramp the material appears to be more of a mixture between CuO and Cu metal with the second peak after the edge resembling Cu metal whilst the whiteline intensity lacks the doublet expected from metallic Cu. Instead this region bears closer resemblance to CuO, though with much reduced intensity.

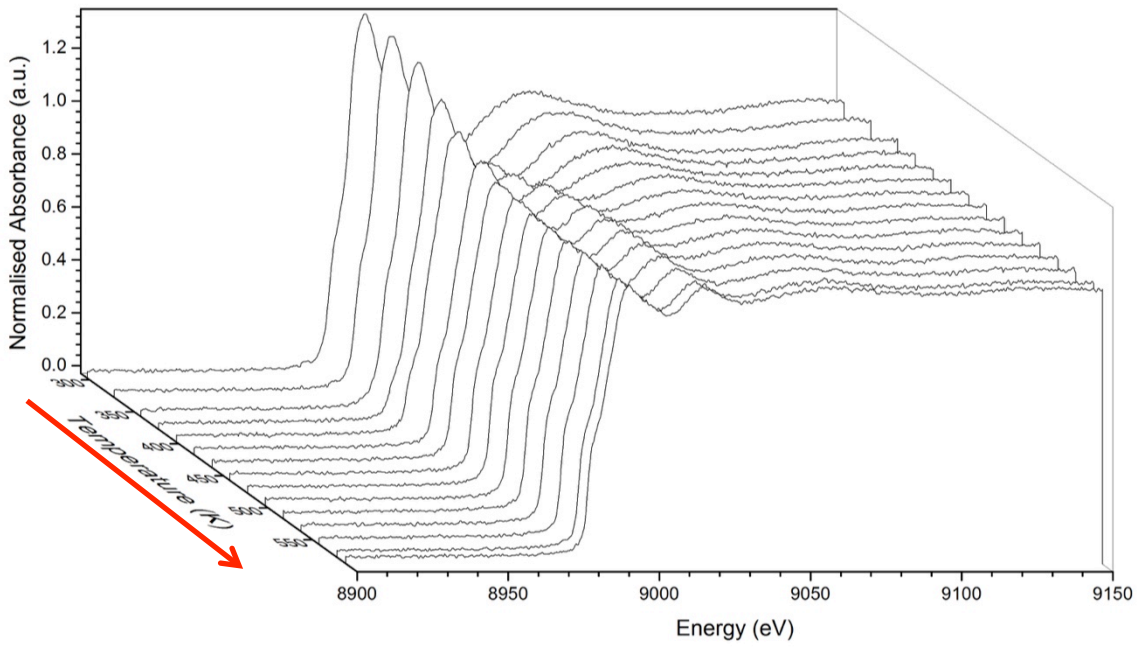

Figure 5-15 - XANES plot of the reduction experiment on the Cu k-edge.

Upon cooling back to room temperature further changes are observed in the XANES, though less dramatic than those observed for the heating process (Figure 5-16). The whiteline intensity increases slightly and the first two oscillations become sharper. The third peak observed for Cu metal, but not CuO, also increases in definition on cooling, indicating a possible increase in Cu metal character. Of interest as well in the edge feature, this is known

to be caused by p-d orbital mixing and to be sensitive to changes in the local structure.[28] It is observed to be less pronounced in the experimental data than for the standard, which may be due to changes in the structure resulting from being loaded onto a silica support.

LCF fitting of the data reveals that the material at the beginning of the ramp exists purely as CuO, and gradually converts with increasing temperature, fully converting by 423 K. What is interesting to note is after this point in the region from 473-573 K the material becomes a mix of oxide and metallic phases again, with over 70% of the Cu present in the metallic phase. The reason for this is unclear, what should be noted is that the LCF fits are not exact, due to the Cu metal standard being a Cu foil and not nanoparticles on an SiO_2 support. Closer inspection of the fitting model reveals that for the data at the beginning of the reduction the quality of the fit is poor (Figure 5-18). At higher temperatures towards the end of the reduction the quality still appears poor (Figure 5-19), however the oscillations in the EXAFS region for the fit match loosely those seen in the experimental data; although they still have much higher amplitude.

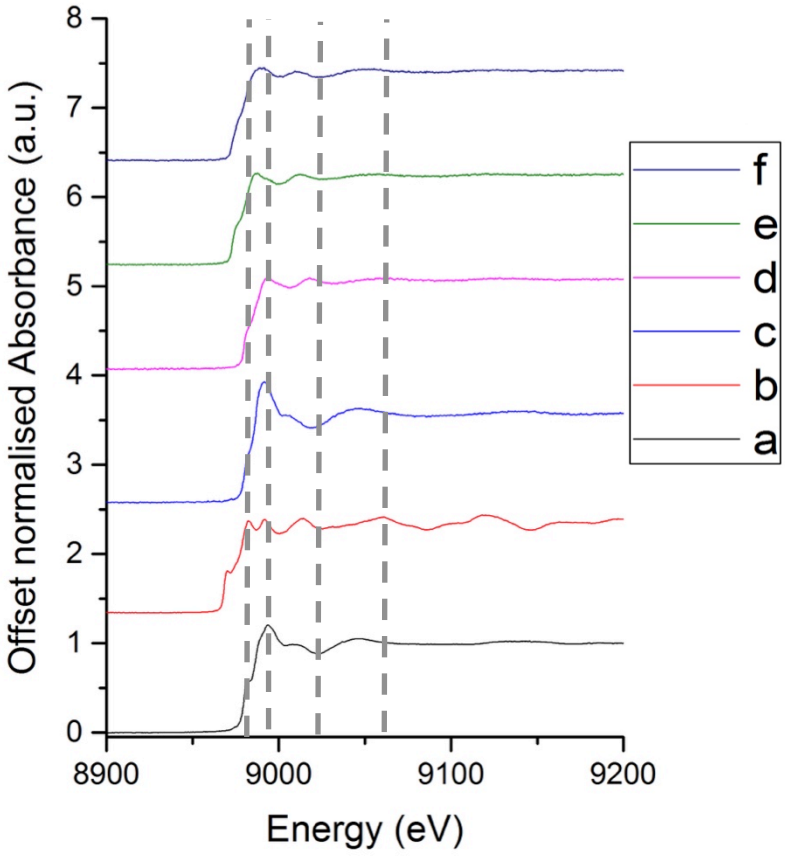

Figure 5-16 - Comparison of XANES data for the Cu K-edge compared with standards. Where a) CuO/SiO_2, b) Cu metal, and the catalyst during the reduction at c) 298 K, d) 588 K, e) cooling 588 K and f) 298 K.

The use of a metal foil as a standard rather than a can have an effect as the subtle variations, caused through smaller particle size and support interactions, are not taken into account.[29,30] However as the LCF measurements are used merely as a guide to the reduction processes this is not a serious issue; EXAFS analysis should reveal all the necessary information. Attempts to use Cu_2O as a standard were unsuccessful, which suggests the material is a mixture of CuO and Cu.

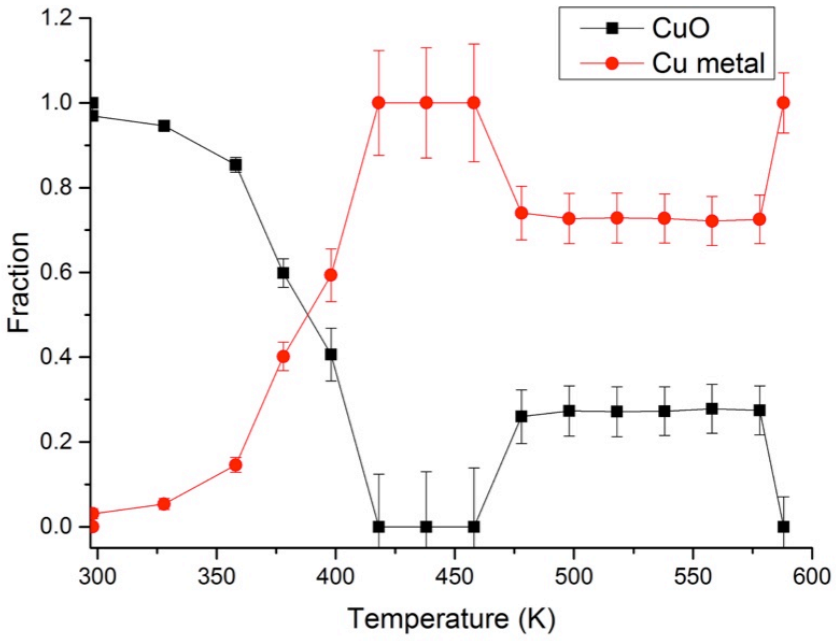

Figure 5-17 - LCF of ramp data using CuO and Cu metal standards.

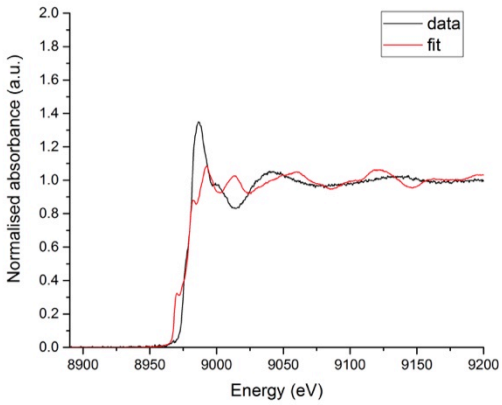

Figure 5-18 - Example of LCF fit from the beginning of the reduction.

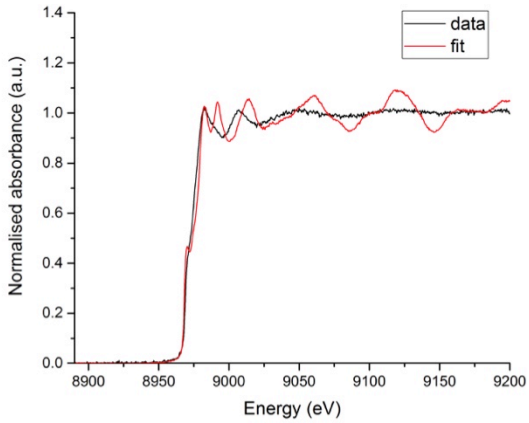

Figure 5-19 - Example of LCF fit from the end of the reduction.

5.3.2.2 EXAFS Analysis

The following diagrams are provided to show visually the Cu and CuO shells used in the fitting model. It was found that the copper oxide existed in the Cu(II) oxide form as CuO rather than as Cu_2O, hence these shells were used in all subsequent fits. Details of the shells, bond distances and coordination numbers are provided in Table 5-3 for CuO, Table 5-4 for Cu_2O and Figure 5-5 for Cu metal.

Table 5-3 - Table showing bond distances and other parameters for CuO used in the fitting model

Shell	Scatterer	Bond distance (Å)	Coordination number
1	O	1.95	6
2	Cu	3	12

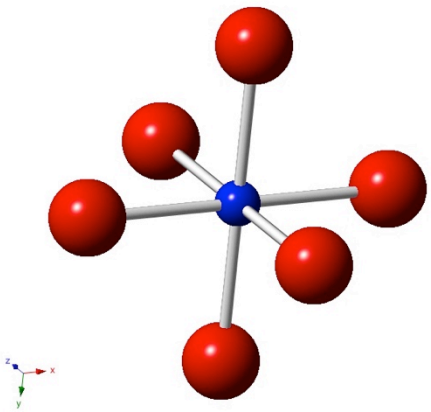

Figure 5-20 - Diagram for the first shell of CuO, showing a central Cu ion (blue) surrounded by 6 oxygen atoms.

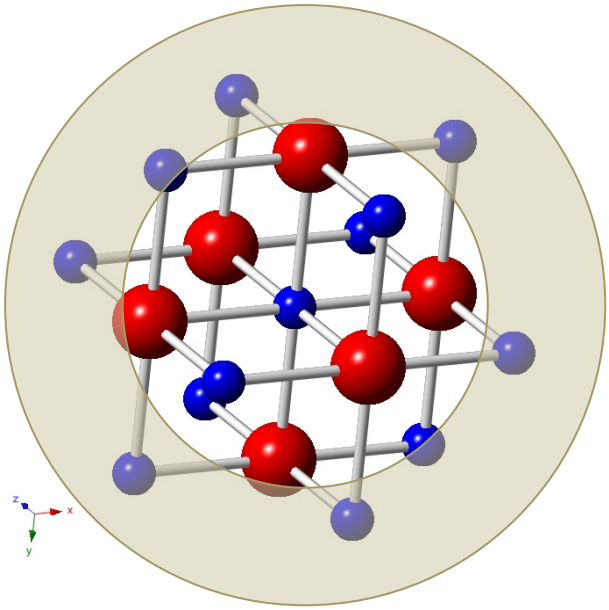

Figure 5-21 - Image with the second shell of CuO, showing the neighbouring Cu atoms highlighted.

Table 5-4 - Table showing bond distances and other details for the Cu_2O oxide shells used in the fitting model

Shell	Scatterer	Bond distance (Å)	Coordination number
1	O	1.83	4
2	Cu	2.98	12

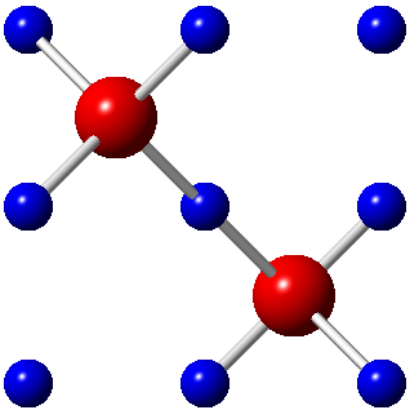

Figure 5-22 - Image showing the first shell of Cu_2O

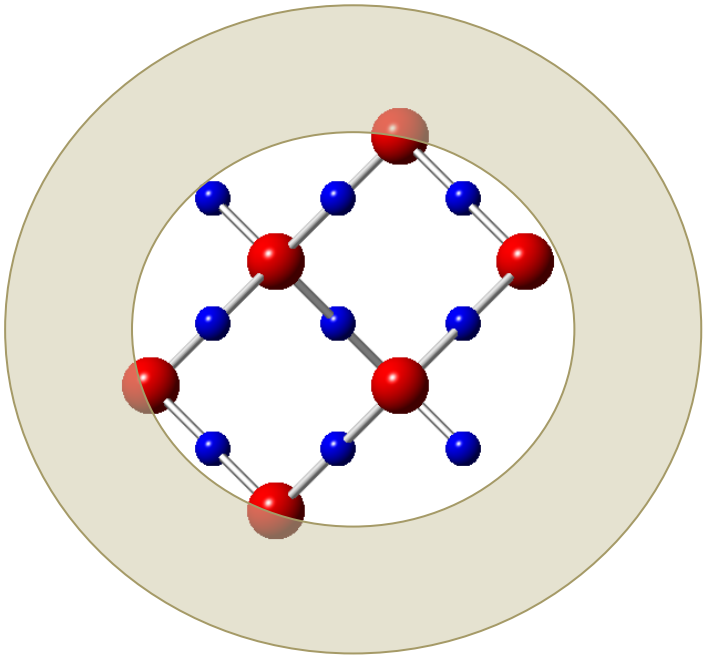

Figure 5-23 - Image showing the second shell of Cu_2O

Table 5-5 - Table showing bond distance and other details for the Cu metal first shell

Shell	Scatterer	Bond distance (Å)	Coordination number
1	Cu	2.56	12

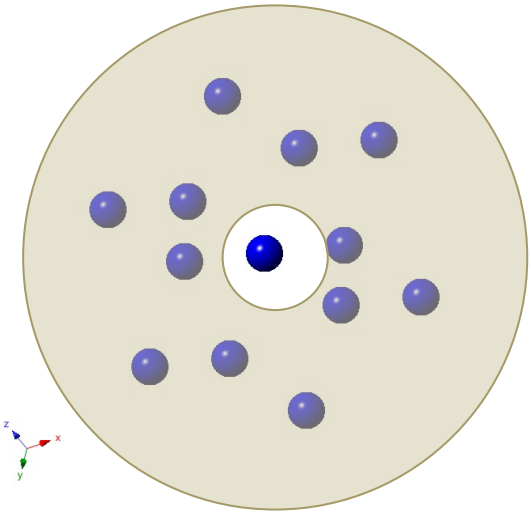

Figure 5-24 - Image of the first shell of Cu metal, showing a central Cu atom surrounded by 12 Cu neighbours.

Artemis fitting was used to follow the changes in the CN and bond distances of the Cu-O and Cu-Cu shells from the copper oxide and metal respectively. Fitting with a Cu-Au shell, created using the first shell theory method was unsuccessful, suggesting there is little to no

interaction between the Cu and Au metals on the SiO_2 surface. The full table of results are available in the Table 5-6. With in the fitting window of 2.5-10 $Å^{-1}$ the quality of the fit was acceptable; there were some errors outside of this range due to only considering the first shell contributions in the fitting model (Figure 5-25).

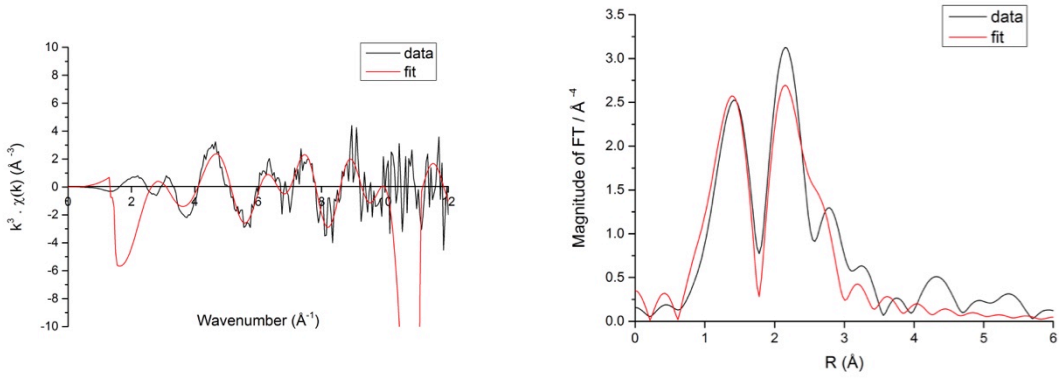

Figure 5-25 - Example of data from the fitting model showing k^3-weighted EXAFS data (left) and the Fourier transform of EXAFS data (right) for Cu-edge data for the material at the end of the reduction process.

The coordination number for the Cu-O shell drops sharply after 448 K, from 3.8 to 0.3 this is accompanied by an increase in the Cu-Cu CN from ca 0.3 to 7.5 (Figure 5-27); this a higher temperature region for the reduction than that shown by LCF and XANES Analysis. There is also a reduction in the bond distance between 373-473 K, with a reduction of the Cu-Cu bond distance in the same region (Figure 5-28). There is a discrepancy in the CNs between 433-456 K, with values of 1.7 for the Cu-Cu shell and 1.2 for the Cu-O shell being returned from the fit. This is accompanied by a lowering of the bond distances for both shells. This could be due to the increased disorder from the low amounts of Cu metal present or due to the fitting model used in the analysis. Low amounts of Cu metal would result in reduced amplitude of the Cu-Cu peak, making the fitting more inaccurate due to the lower signal to noise ration.

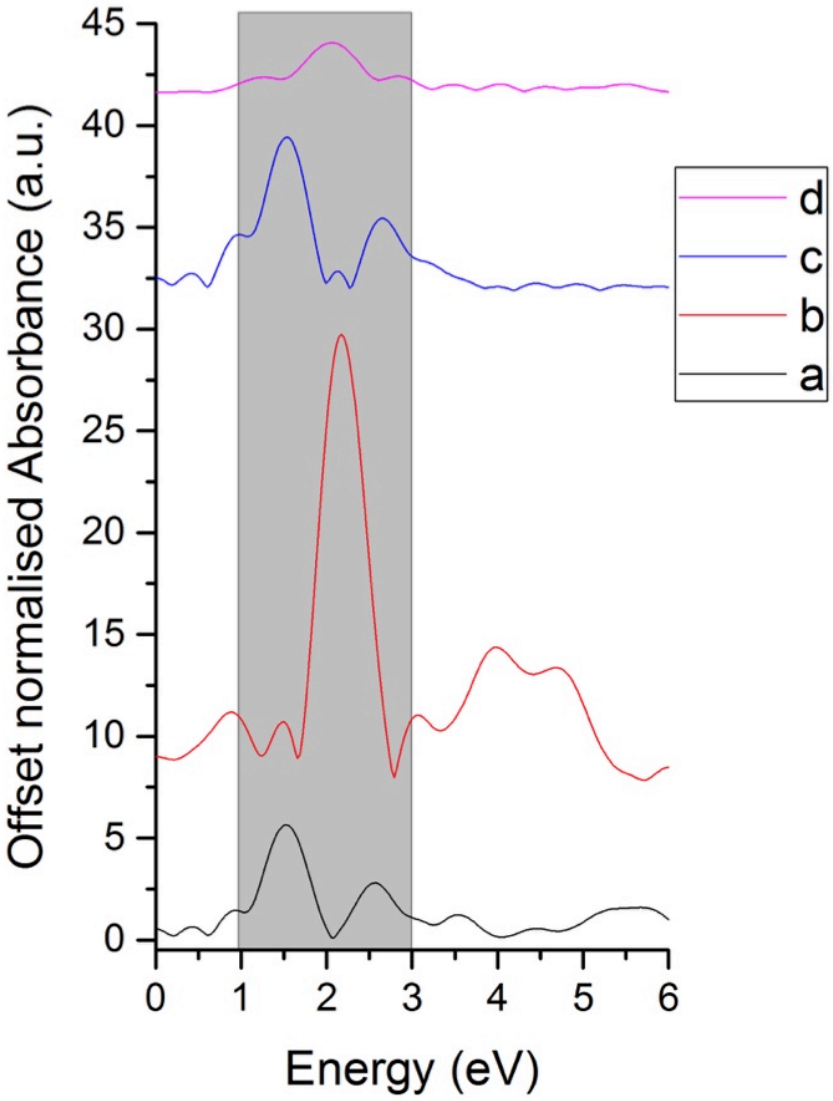

Figure 5-26 - Comparison of the Fourier transform of Cu k-edge data for, a) CuO/SiO_2, b) Cu metal, c) catalyst at 298 K, d) catalyst at 588 K.

Table 5-6 - Results from Artemis fitting of the Cu k-edge data for reduction experiment.

		CuO 1.9508 Cu-O standard								CuCu reff= 2.5562						
File	temperature	R-factor	r	error	SO2	ss	xCuO	CN	error	r	error	SO2	ss	xCu	CN	error
1	25	0.02506	1.96	0.05	0.84	0.0054	0.94	3.8	0.4	2.60	0.05	0.00	-0.0125	0.00	0.0	0.0
5	55	0.02508	1.95	0.05	0.89	0.0069	1.00	4.0	0.4	2.60	0.08	0.00	-0.0247	0.00	0.0	0.0
10	85	0.02141	1.95	0.04	0.85	0.0063	0.95	3.8	0.4	2.60	0.09	0.00	-0.0294	0.00	0.0	0.0
15	105	0.02393	1.96	0.05	0.75	0.0052	0.83	3.3	0.3	2.57	0.07	0.01	-0.0028	0.02	0.1	0.0
20	125	0.02954	1.98	0.06	0.67	0.0092	0.75	3.0	0.3	2.62	0.07	0.01	-0.0021	0.02	0.1	0.0
25	145	0.01769	1.98	0.04	0.50	0.0084	0.55	2.2	0.2	2.62	0.04	0.01	-0.0093	0.01	0.0	0.0
30	165	0.03116	2.03	0.05	0.45	0.0217	0.50	2.0	0.2	2.64	0.03	0.02	0.0003	0.03	0.2	0.0
35	185	0.0482	2.03	0.07	0.47	0.0185	0.49	2.0	0.2	2.63	0.04	0.03	0.0003	0.03	0.2	0.0
40	205	0.14892	1.85	0.13	0.32	0.0116	0.35	1.4	0.1	2.51	0.09	0.05	0.0030	0.05	0.4	0.0
45	225	0.06646	1.83	0.11	0.13	0.0031	0.14	0.6	0.1	2.53	0.10	0.22	0.0167	0.25	2.0	0.2
50	245	0.03084	1.79	0.05	0.07	0.0003	0.08	0.3	0.0	2.50	0.06	0.64	0.0291	0.72	5.7	0.6
55	265	0.03021	1.78	0.03	0.00	-0.0204	0.00	0.0	0.0	2.48	0.03	0.88	0.0338	0.98	7.8	0.8
60	285	0.04721	1.79	0.10	0.00	-0.0167	0.01	0.0	0.0	2.48	0.06	0.76	0.0300	0.85	6.8	0.7
65	305	0.02895	1.97	0.03	0.16	0.0314	0.18	0.7	0.1	2.50	0.03	0.74	0.0306	0.82	6.6	0.7
70	315	0.12477	1.99	0.16	0.16	-0.0165	-0.01	0.0	0.0	2.49	0.08	0.59	0.0267	0.66	5.3	0.5

In these fits the extra term added to fit coordination numbers for the Cu-O and Cu-Cu shell are tied together by assuming that that any copper present in the system must be in the form of either CuO or CuCu. This forced summation to one phase or another may have introduced a similar error to that observed from LCF fitting. As such the data was also analysed fitting the coordination number terms independently from each other.

Fitting of the coordination numbers independently gives a rather different story to that previously established. The Cu-O decomposes gradually with increasing temperature falling from ca 3.8 to 2.0 by 558 K. Further reduction leads to the removal of the CuO and leaves Cu metal (Figure 5-29). The metal does not appear at 423 K as suggested by LCF of the XANES measurement, but instead appears much later at 473 K. The growth of the metal phase is a rather slow process. Although the coordination number for the Cu-O shell drops dramatically the increase in the Cu-Cu coordination number before 573 K is negligible. Comparison with the sigma-squared terms reveals negative values indicating that the path might not be present in the material before 523 K. These changes in the coordination number compare better with the observed change in intensity, and hence the occupancy, of the paths from visual analysis of the Fourier transforms.

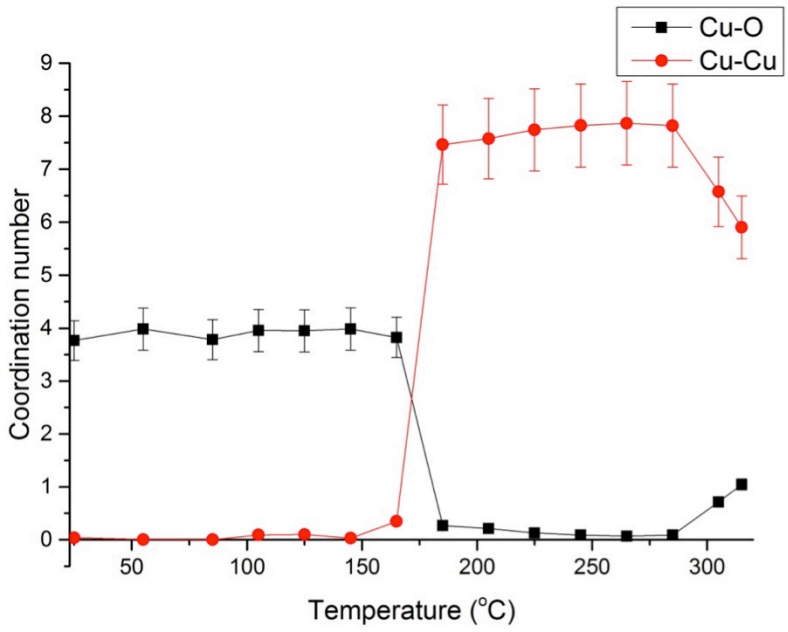

Figure 5-27 - Change in coordination number with increasing temperature for the Cu-O and Cu-Cu first shells.

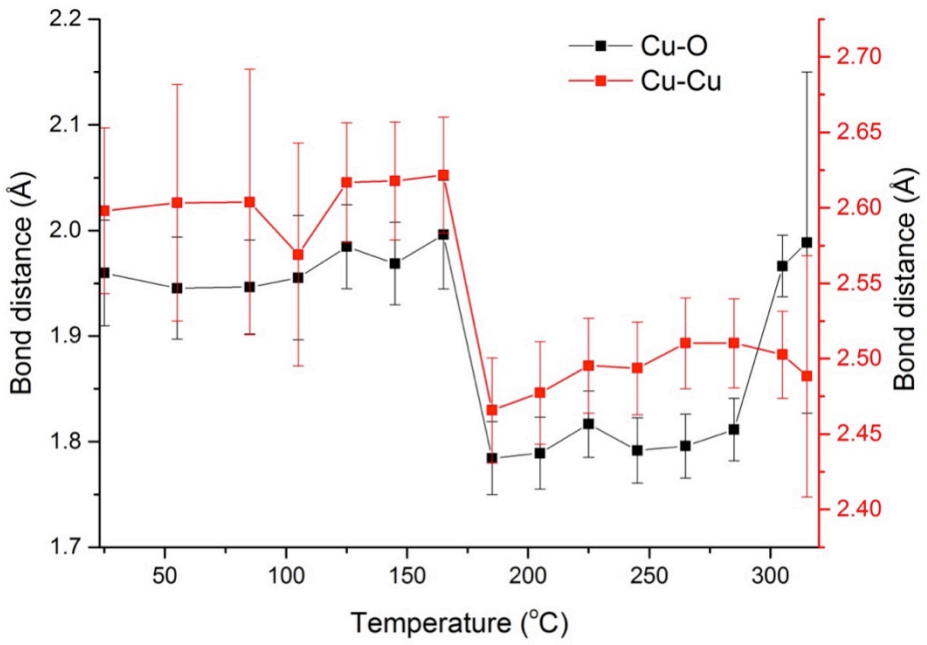

Figure 5-28 - Change in bond distance of the Cu-O and Cu-Cu first shells.

The bond distance for the Cu-O shell decreases sharply after 458 K, from 2.3 Å to ca 1.8 Å; this is an increase from the literature value of 1.95 Å (Figure 5-30).[18,22] This may be due to the disorder of the materials, as they undergo the transition from oxide to metal. The bond distance for the Cu-Cu shell is also larger than expected (by ca 0.1-0.15 Å) for the scans where the amount of Cu-Cu present is low. This indicates that the accuracy of fitting the Cu-Cu shell is dependent on the amount of Cu metallic phase present in the sample. As the amount of Cu metal present in the sample increases the value of the bond distance begins to more closely resemble the literature value.[18,22]

Upon cooling the Cu-O bond distance decreases from 1.99 Å to 1.92 Å (literature value 1.95 Å for CuO)[18,22], whilst the Cu-Cu bond distance increases from 2.49 Å to 2.53 Å (literature value 2.55 Å for Cu-Cu).[18,22] The change in coordination number is much less uniform; however there is a general increase from 1.6 to 2.7 and from 1.2 to 1.4 for the Cu-O and Cu-Cu shells respectively.

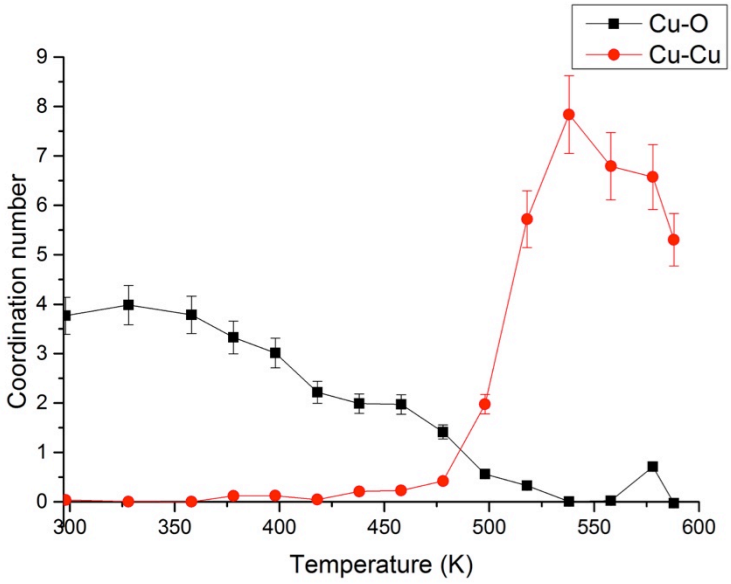

Figure 5-29 - Change in coordination number with increasing temperature for the Cu-O and Cu-Cu first shells floating the coordination parameter for Cu-O and Cu-Cu.

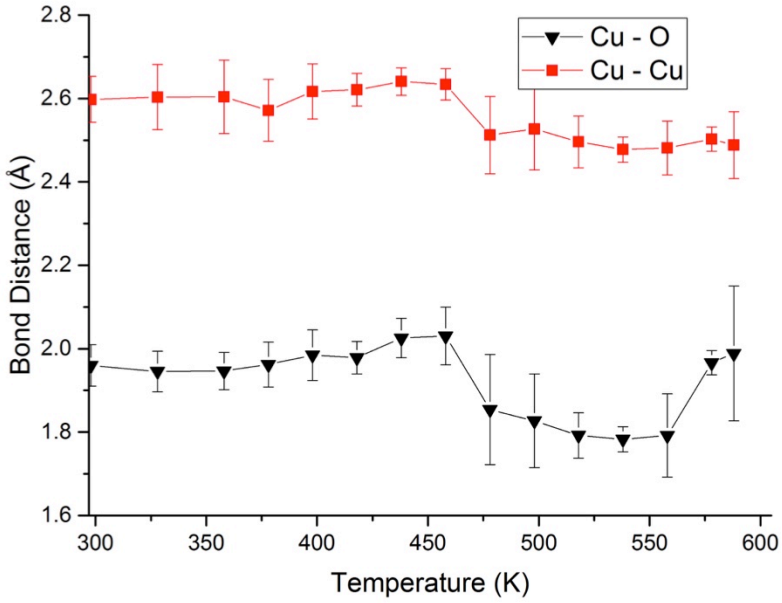

Figure 5-30 - Change in bond distance of the Cu-O and Cu-Cu first shells floating the coordination parameter for Cu-O and Cu-Cu.

5.3.3 Discussion

Both the Cu and Au edges indicate that reduction of the sample is occurring with differing levels of success. Reduction on the Au edge leads to a complete removal of the Au-O phase, causing a total reduction to the metal. The metal particles formed are not large as indicated by the reduced coordination number. The bond distance is slightly lower than expected, being 0.1 Å lower than the expected value of 2.88 Å for Au-Au metal. This error may be due to the increased disorder of the system at higher temperature, and the changes to the structure that occur with increasing temperature due to lattice expansion.

The Cu k-edge data reveals that a full reduction doesn't occur until higher temperatures, ca 498 K. This process is also shown to be reversible as upon cooling the copper oxide is reformed.

On both edges no interaction between the metals could be determined, indicating prior to and during the reduction step the metals exist as separate species on the silica support.

Published work on these $AuCu/SiO_2$ catalysts have also stated that the gold is fully reduced after the reduction step, with the Cu(I) oxide being formed in preference to the Cu(II) oxide or Cu metal states.[18] however no evidence was found the CuAu interaction, previously established through XRD characterisation.[18]

5.4 Calcination

Calcination data was fitted using a multi-edge model comprising of the Au L_{III}-edge and the Cu K-edge and using the Au-O, Au-Au, Au-Cu and Cu-O, Cu-Cu and Cu-Au, paths respectively. The same parameters were used for the AuCu and CuAu paths with the exception of the coordination number term as this was found to decrease the quality of the fit. Fitting ranges used are k-range 2.5-10 $Å,^{-1}$ R-range 1-3 Å for the Cu k-edge and k-range 2.5-10 $Å^{-1}$, R-range 1.5-4 Å for the Au L_{III}-edge.

5.4.1 XANES Analysis

Initial observations of the Au XANES reveal minimal changes in the shape of the oscillations with increasing temperature (Figure 5-31). The material starts and ends as Au metal, with the intensity of the post-edge feature decreasing only slightly from 1.022 to 1.02. As there are no pre-edge features for Au metal, the XANES does not provide a lot of information on any structural transformations, other than confirming that the Au content remains in the metallic state.

The Cu XANES shows a decrease in the whiteline intensity upon increasing temperature, dropping from 1.24 to 1.16 (arbitrary intensity units) (Figure 5-32). This indicates there is a change in the density of states for the Cu species; possibly linked to a change the number of nearest neighbours, as the change is not dramatic enough to have been caused by a change in oxidation state. Visual observations also confirm that the material resembles the CuO, from the shape and features of the EXAFS region, rather than the Cu metal.

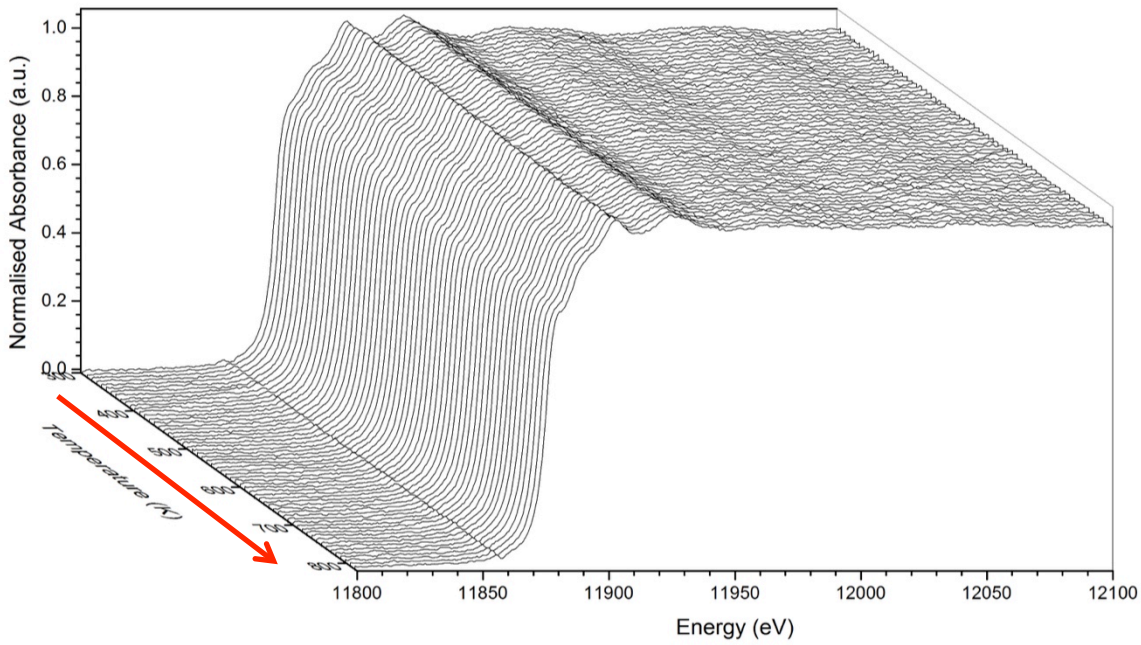

Figure 5-31 - Plot of XANES form Au L_{III}-edge against temperature for the calcination of AuCu catalyst.

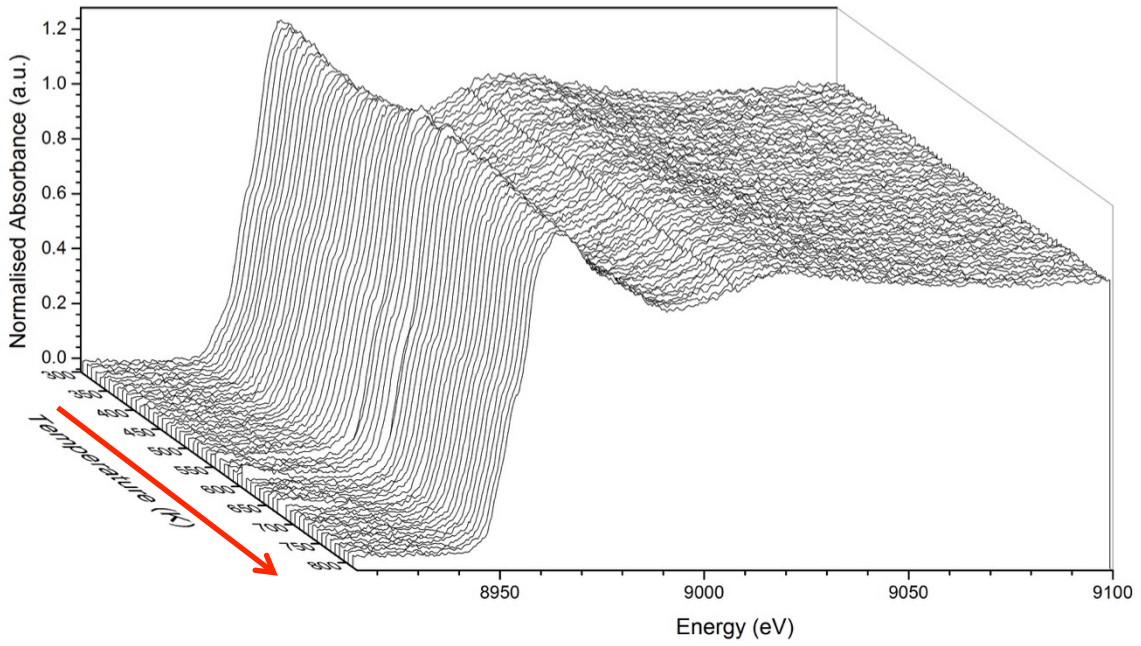

Figure 5-32 - Plot of XANES form Cu k-edge against temperature for the calcination of AuCu catalyst.

5.4.2 EXAFS Analysis

As there are minimal visual changes in the XANES, EXAFS analysis is crucial to understanding the changes occurring during the calcination of the reduced catalyst. The fitting model utilised fixed values for the Cu-Cu and Au-Cu bond variations to preserve the integrity of the fitting model. Comparisons between the floated term model and the forced summation model with visual inspection of the EXAFS peak intensities have confirmed that the floated model is more accurate for determining the coordination numbers of the system. The full EXAFS results for the Cu edge can be found in Table 5-7 and for the Au-edge in Table 5-8.

Visual comparison of the data shows that at the beginning (Figure 5-33) and end of the catalysis (Figure 5-34) the material exists as Au-metal, with only subtle changes. By comparison the Cu edge data has considerably more noise in k-space and this translates to difficulties in obtaining high quality fits to the experimental data (Figure 5-35).

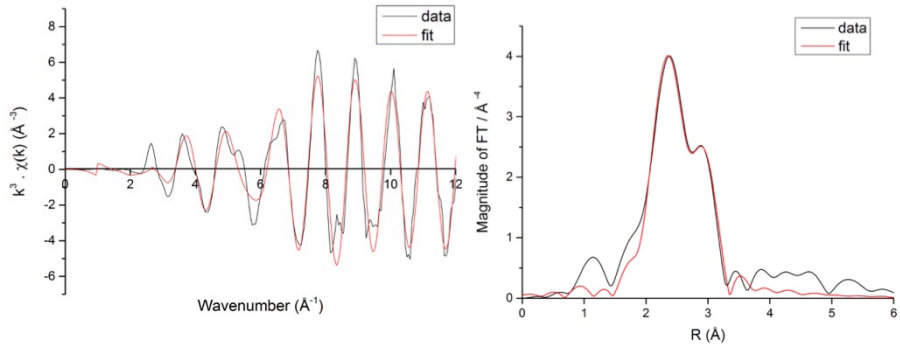

Figure 5-33 - Example of data showing k^3-weighted data (left) and the Fourier transform (right) for Au-edge data at the beginning of the calcination.

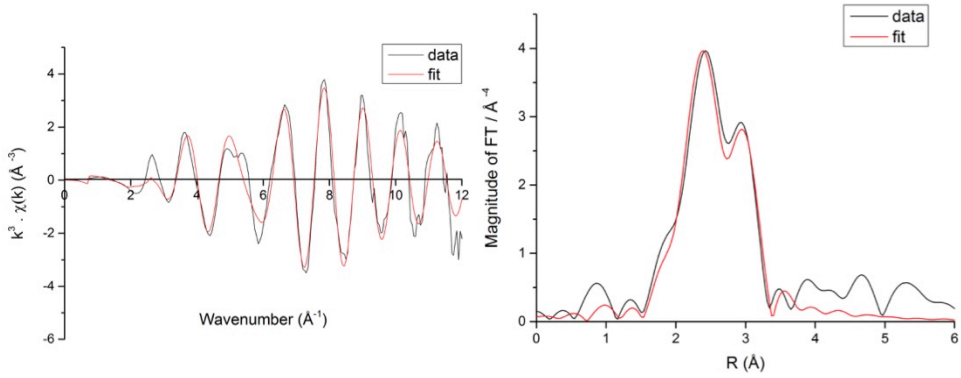

Figure 5-34 - Example of data showing k^3-weighted data (left) and the Fourier transform (right) for Au-edge data after the calcination process.

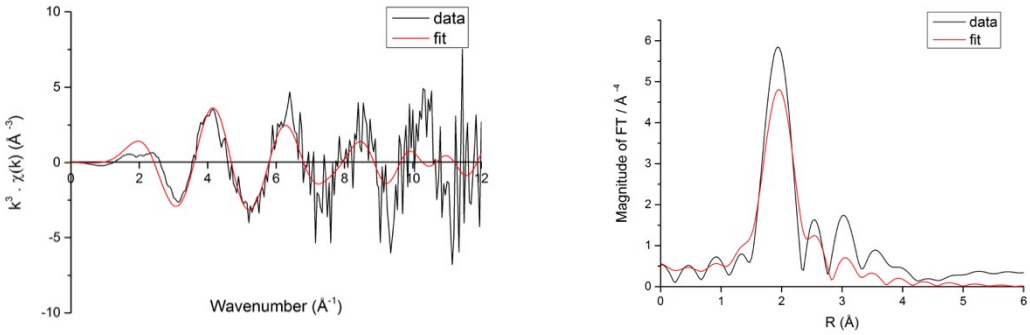

Figure 5-35 - Example of data showing k^3-weighted data (left) and the Fourier transform (right) for Cu-edge data at the start of the calcination process.

The bond distances of the first shell Au-Au and Cu-O shells were allowed to vary. The fits reveal interesting information about the Cu-O bond distance, which increases dramatically above 373 K from 1.9Å to 2.0 Å between 373-473 K within error the value is close to the literature value for the Cu-O shell (1.96 Å),[18,22] however the increase in value requires some explanation.[18] It was not possible to fit this model with a Cu-Au path so correlation with that shell is unlikely; instead it is possible that the rise in intensity may be due to the data quality at this point in the experiment which was noisy for the Cu K-edge data (Figure 5-35).

The Au-Au bond distance remains near 2.8 Å, within error values, for the majority of the calcination. This is 0.08 Å lower than the expected value for the Au-Au first shell. Upon reaching a reaction temperature of ca 773 K the Au-Au bond distance rises to 3.0, well above the expected value. The reason for these discrepancies is unclear; the high temperature variation may simply be due to the reduced data quality from working at higher temperature. The lower start values are not due to another interaction, as the only other species present on the Au-edge is the Au-Cu and this was included in the fitting model.

Table 5-7 - Cu k-edge results for fitting of calcination data.

	CuO 1.9508 Cu-O standard								CuCu reff= 2.5562		CuCu					CuAu reff= 2.5562						
temperature	R-factor	r	error	SO2	ss	xCuO	CN	error	r	error	SO2	ss	xCu	CN	error	r	error	SO2	ss	xCuAu	CN	error
30	0.02	1.93	0.03	0.73	0.0054	0.81	3.24	0.32	**2.56**	-	0.00	0.0030	0.01	0.05	0.00	**2.71**	-	0.01	0.0030	0.00	0.00	0.00
50	0.04	1.93	0.04	0.74	0.0056	0.83	3.31	0.33	**2.56**	-	0.01	0.0030	0.02	0.13	0.01	**2.71**	-	0.09	0.0030	0.00	0.00	0.00
75	0.04	1.92	0.03	0.62	0.0034	0.70	2.79	0.28	**2.56**	0.00	-0.03	0.0030	-0.03	0.00	0.00	**2.71**			0.0030	0.00	0.00	0.00
100	0.04	1.96	0.03	0.59	0.0030	0.66	2.64	0.26	**2.56**	-	-0.04	0.0030	-0.04	0.00	0.00	**2.71**	-	0.00	0.0030	0.00	0.00	0.00
125	0.04	2.01	0.02	0.43	0.0026	0.48	1.90		**2.56**	0.00	0.00	0.0030	0.00	0.01	0.00	**2.71**			0.0030	0.00	0.00	0.00
150	0.07	1.99	0.04	0.61	0.0114	0.48	1.91	0.19	**2.56**	-	-0.01	0.0030	0.00	0.00	0.00	**2.71**	-	-0.06	0.0030	-0.06	0.00	0.00
175	0.07	2.01	0.04	0.54	0.0063	0.61	2.43	0.24	**2.56**		0.00	0.0030	-0.02	0.00	0.00	**2.71**			0.0030	0.00	0.00	0.00
200	0.07	1.99	0.04	0.61	0.0114	0.68	2.71	0.27	**2.56**	-	-0.01	0.0030	-0.01	0.00	0.00	**2.71**	-	-0.06	0.0030	-0.07	0.00	0.00
250	0.07	1.90	0.04	0.58	0.0070	0.64	2.57	0.26	**2.56**	-	-0.01	0.0030	-0.01	0.00	0.00	**2.71**	-	0.00	0.0030	0.00	0.00	0.00
275	0.07	1.94	0.04	0.01	0.0059	0.66	2.63	0.26	**2.56**	-	0.02	0.0030	0.03	0.21	0.02	**2.71**	-		0.0030	0.00	0.00	0.00
300	0.14	1.89	0.03	0.41	0.0001	0.46	1.85	0.18	**2.56**	-	0.02	0.0030	0.02	0.14	0.01	**2.71**	-	-0.03	0.0030	-0.03	0.00	0.00
325	0.06	1.88	0.04	0.57	0.0018	0.64	2.55	0.25	**2.56**	-	0.02	0.0030	0.00	0.00	0.00	**2.71**	-	0.00	0.0030	0.00	0.00	0.00
350	0.08	1.88	0.06	0.57	0.0066	0.63	2.54	0.25	**2.56**	-	0.00	0.0030	0.00	0.00	0.00	**2.71**	-	0.00	0.0030	0.00	0.00	0.00
375	0.07	1.88	0.04	0.57	0.0014	0.63	2.53	0.25	**2.56**	-	-0.01	0.0030	-0.01	0.00	0.00	**2.71**	-		0.0030	0.00	0.00	0.00
400	0.11	1.86	0.10	0.69	0.0042	0.77	3.09	0.31	**2.56**	-	-0.02	0.0030	-0.02	0.00	0.00	**2.71**	-	-0.03	0.0030	-0.04	0.00	0.00
450	0.08	1.86	0.04	0.37	0.0108	0.42	1.66	0.17	**2.56**	-	0.03	0.0030	0.04	0.30	0.03	**2.71**	-	-0.05	0.0030	-0.06	0.00	0.00
475	0.08	1.94	0.04	0.38	0.0020	0.43	1.71	0.17	**2.56**	-	0.03	0.0030	0.04	0.29	0.03	**2.71**	-	0.00	0.0030	0.00	0.00	0.00
500	0.12	1.94	0.04	0.55	0.0103	0.61	2.44	0.24	**2.56**	-	0.01	0.0030	0.01	0.09	0.01	**2.71**	-	0.01	0.0030	0.01	0.14	0.01
545	0.11	1.97	0.04	0.53	0.0124	0.59	2.35	0.23	**2.56**	-	0.09	0.0227	0.02	0.15	0.01	**2.71**	-	0.00	0.0030	0.00	0.00	0.00

Table 5-8 - Au L_{III}-edge results for fitting of calcination data.

	Au-Cu							Au-Au						
		n=12		reff= 2.7100					n=12		reff= 2.8600			
temperature	x value	CN	error	R value	error	so2	ss2	x value	CN	error	R value	error	so2	ss2
30	0.05	0.57	0.06	2.71	-	0.03	0.0030	0.84	10.03	1.00	2.82	0.02	0.60	0.0124
50	0.05	0.59	0.06	2.71	-	0.04	0.0030	0.86	10.38	1.04	2.82	0.03	0.63	0.0143
75	0.01	0.17	0.02	2.71	0.02	0.01	0.0030	0.84	10.05	1.01	2.81	0.02	0.61	0.0126
100	0.02	0.21	0.02	2.71	-	0.01	0.0030	0.80	9.58	0.96	2.81	0.02	0.58	0.0118
125	0.00	0.00	0.05	2.71	-	0.00	0.0030	0.80	9.64	0.96	2.81	0.02	0.58	0.0113
150	0.01	0.11	0.01	2.71	-	0.00	0.0030	0.96	11.46	1.15	2.82	0.03	0.68	0.0148
175	0.00	0.00	0.00	2.71	-	0.05	0.0030	1.00	12.03	1.20	2.86	0.03	0.88	0.0246
200	-0.02	0.00	0.00	2.71	-	-0.02	0.0030	0.73	8.74	0.87	2.80	0.02	0.53	0.0104
250	-0.02	-0.19	-0.02	2.71	-	-0.01	0.0030	0.84	10.10	1.01	2.82	0.03	0.61	0.0147
275	0.01	0.12	0.01	2.71	-	0.01	0.0030	0.93	11.17	1.12	2.82	0.04	0.67	0.0201
300	-0.01	0.00	0.00	2.71	-	0.00	0.0030	0.63	7.60	0.76	2.77	0.03	0.59	0.0133
325	0.00	0.02	0.00	2.71	-	0.00	0.0030	0.61	7.28	0.73	2.77	0.03	0.44	0.4387
350	0.01	0.12	0.01	2.71	-	0.01	0.0030	0.68	8.21	0.82	2.79	0.06	0.49	0.0157
375	0.00	0.00	0.00	2.71	-	-0.02	0.0030	0.83	9.92	0.99	2.83	0.03	0.60	0.0196
400	-0.08	0.00	0.00	2.71	-	-0.06	0.0030	0.64	7.67	0.77	2.81	0.02	0.46	0.0107
450	0.03	0.40	0.04	2.71	-	0.02	0.0030	0.62	7.43	0.74	2.80	0.06	0.45	0.0173
475	0.00	0.00	0.00	2.71	-	0.00	0.0030	0.69	8.27	0.83	2.79	0.03	0.50	0.0161
500	0.12	1.42	0.14	2.71	-	0.09	0.0030	0.55	6.60	0.66	3.00	0.02	0.40	0.0113
545	0.13	1.57	0.16	2.71	-	0.09	0.0030	0.57	6.88	0.69	3.00	0.02	0.41	0.0100

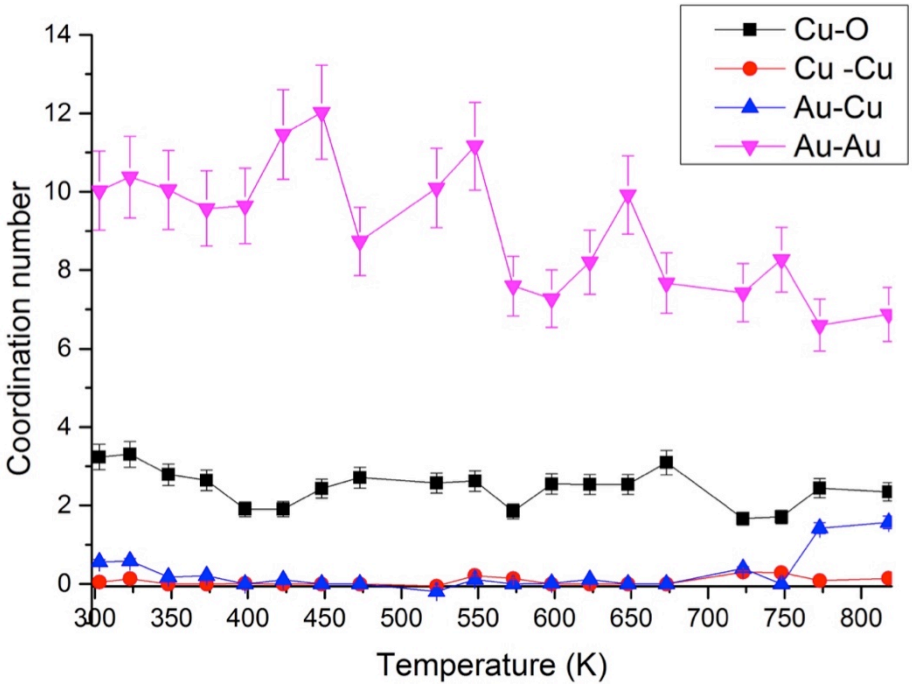

Figure 5-36 - Plot of the change in coordination number with increasing temperature for the calcination of the catalyst on both the Cu K-edge and the Au L_{III}-edge.

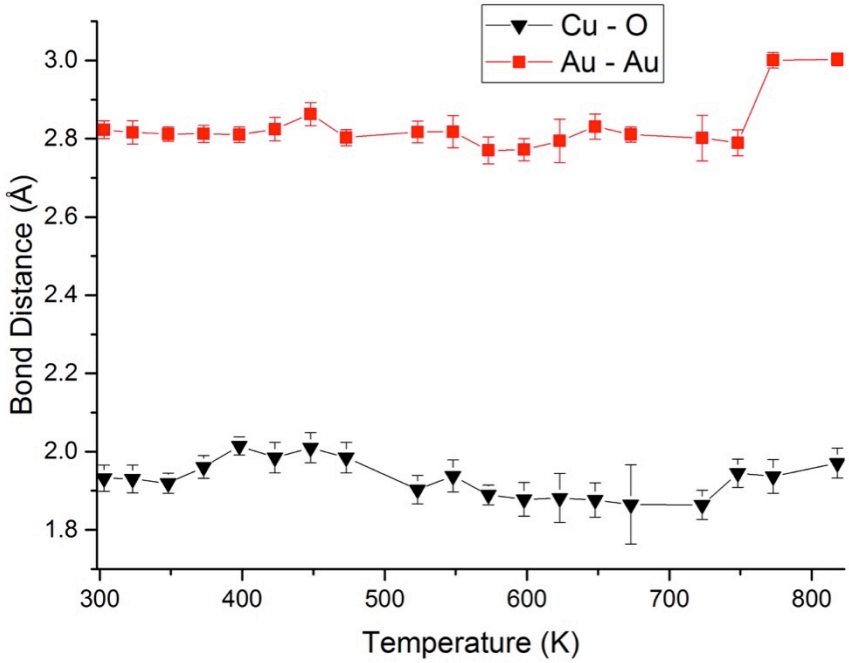

Figure 5-37 - Plot of the change bond distance with increasing temperature for the calcination of the catalyst on both the Cu K-edge and the Au L_{III}-edge.

The change in coordination number for the Cu-edge data reveals that only the CuO species is present in any significant amount during the calcination (Figure 5-36). The coordination number for the Cu-O shell drops steadily from 3.23 to 2.34 at 818 K, whilst the coordination number for the Cu-Cu shell rises to 0.3 at its maximum during the calcination. Additionally the Cu-Cu shell frequently had significantly low or negative σ^2 values, indicating the presence of the phase is unlikely. The negative result did not impact the integrity of the model as fits were run both with and without the Cu-Cu shell and the change in the numbers was not apparent to within 2 significant figures.

The coordination number for the Au-Au shell begins at 10 and finishes at a lower value of 6.8. However the value for the Au-Au shell fluctuates more than any other value during the calcination, reaching a maximum of 11.8 at some points (Figure 5-36). This may be due to the quality of the back group subtraction and the noise present in the data at certain scans. It is not due to other contributions as both the Au-Cu paths, which is likely to contribute, and the Au-O path, which is unlikely to contribute, have been included with no improvement on the fit. The general trend is a lowering of the Au-Au coordination number with increasing temperature. This is matched by the reducing intensity of the Au-Au peak in the Fourier transform plots of the EXAFS data.

There is a minimal Au-Cu interaction in the Au-edge data; however none was present on the Cu edge. It should be noted that the values for the CuAu coordination number obtained were significantly low, as are the σ^2 terms. This indicates that there may be minimal to no interaction actually present in the material. Corresponding evidence for this is the lack of a CuAu interaction on the Cu-edge.

5.4.3 Discussion

The material at the end of the calcination should be directly comparable to the reduced and calcined catalyst used in the catalysis. A comparison of the XANES of the two materials is presented in Figure 5-38, as can be seen the data aligns very well between the two materials. The values for the coordination numbers and bond distances for the material are also in agreement (Table 5-9). This shows that the calcination is reproducible *in situ* XAS experiment to a good degree, when compared to a laboratory prepared sample.

Both XANES and EXAFS analysis confirm that the material changes only slightly from the initial reduced catalyst. On the Cu-edge the metal content never reaches any substantial amount, with the significant majority of the material present in the CuO phase. On the gold edge the majority of the material is present as Au metal. Attempts to fit a CuAu shell on the

Cu k-edge data were unsuccessful; attempts on the Au-edge were moderately more successful. Although it was possible to fit an CuAu shell to the data the CN numbers generated were exceptionally low, below one until 773 K. An interaction has been reported for the $AuCu/SiO_2$ reduced and calcined catalyst in the literature, however it was not possible to determine the extent of that with this data.[18,22]

Table 5-9 - Values for the reduced only and reduced calcined catalyst from the EXAFS analysis of the Au l_{III}-edge data.

temperature	R-factor	Au-Au x value	CN	error	2.86 R value	error	so2	ss2
Reduced Calcined catalyst	0.05	0.99	11.91	1.19	2.88	0.01	0.72	0.0075
reduced only catalyst	0.03	1.02	12.21	1.22	2.86	0.01	0.74	0.0106

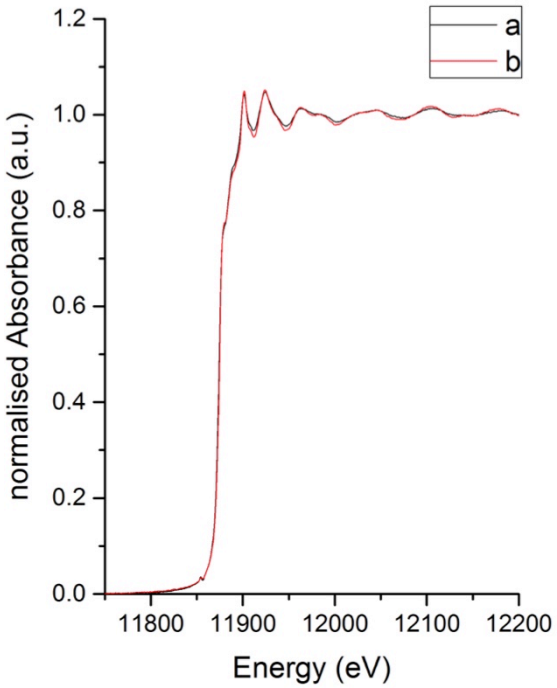

Figure 5-38 - Plot of the XANES for the reduced only (a) and reduced-calcined catalysts (b) on the Au L_{III}-edge.

5.5 Catalysis

In situ selective oxidation of propene to acrolein was performed in the reaction cell using the reduced only, and the reduced-calcined materials as catalysts, in separate experiments. Measurements were performed on both the Au L_{III}-edge and the Cu k-edge. The Fitting ranges are k-range 2.5-10 $Å^{-1}$, R-range 1-3 Å for the Cu k-edge and k-range 2.5-10 $Å^{-1}$, R-range 1.5-4 Å for the Au L_{III}-edge. The conversion of propene was followed using mass spectrometry, however only the XAS measurements are reported here as the characterisation of the support material is the focus of this investigation.

5.5.1 Reduced only catalyst

This material was formed from the deposition of Cu and Au precursors and reduced to leave the metallic phases. It has not been calcined and hence should exhibit different structure and behaviour to the calcined catalyst.

5.5.1.1 XANES Analysis

Analysis of the XANES data in comparison with Au standards reveals that the catalyst does not change substantially during the catalysis. The features of the post-edge region become more pronounced with increasing temperature during the reaction. This indicates that the catalyst is being calcined during the catalysis, potentially leading to increased Au particle size and variations in the catalysis.[21] No equivalent stepwise heating program was carried out in the absence of the catalysis, meaning comparisons of the uncalcined material need to be done with the previous calcination data, or for information. However as this particular investigation is bout the effect of catalyst pre-treatment prior to catalysis, it will be directly compared to the reduced and calcined catalyst. The Cu k-edge data shows subtle variations in the XANES region, mainly through the formation of an edge feature that appears 513 K upon heating and remains for the rest of the catalysis experiment (Figure 5-40).

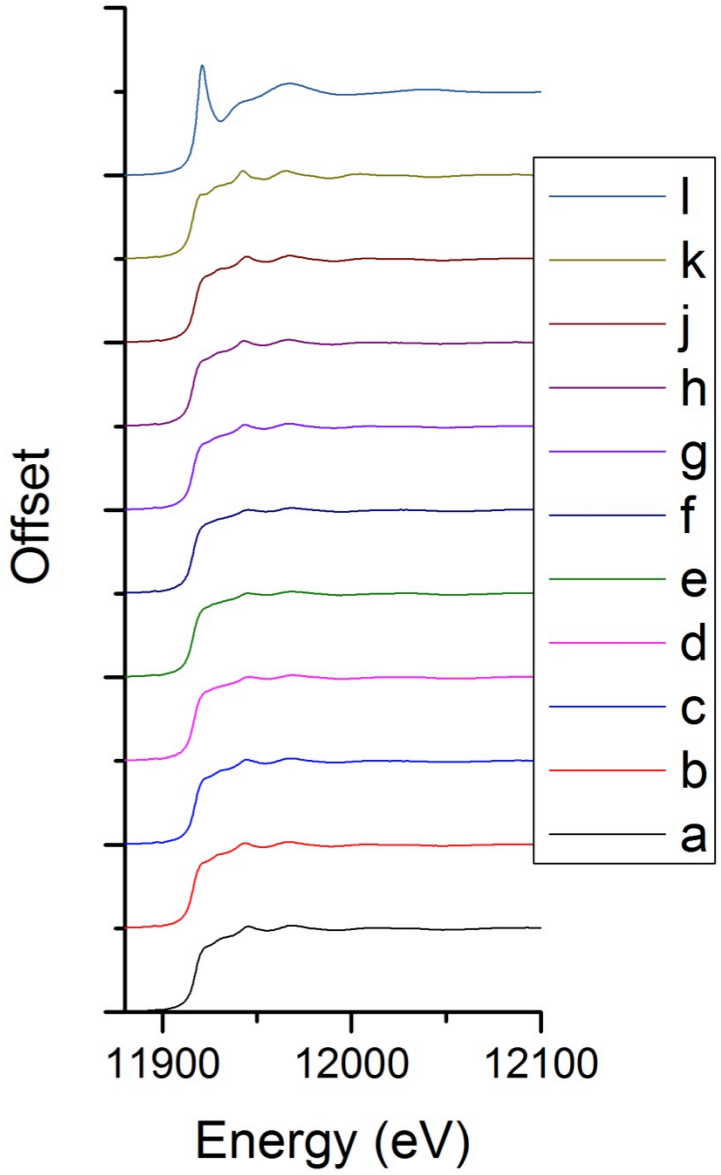

Figure 5-39 - Au edge XANES for the reduced only catalyst, where a) catalyst at room temperature before heating, b) at 473 K, c) at 513 K, d) at 553 K, e) at 593 K , f) cooling 553 K, g) cooling 513 K, h) cooling 473 K, j) room temperature after heating, k) Au metal standard l) Au(OH) standard.

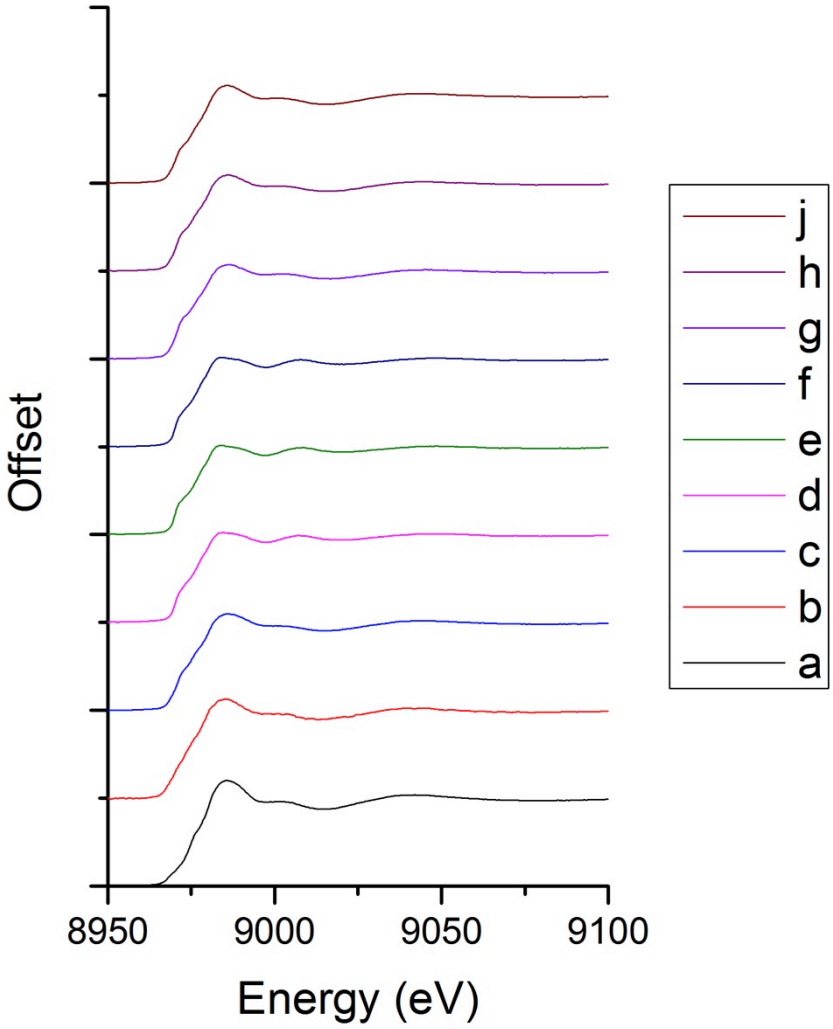

Figure 5-40 - Cu edge XANES for the reduced only catalyst, where a) catalyst at room temperature before heating, b) at 473 K, c) at 513 K, d) at 553 K, e) at 593 K , f) cooling 553 K, g) cooling 513 K, h) cooling 473 K, j) room temperature after heating.

5.5.1.2 EXAFS Analysis

The Au-edge data was fitted using the Au-Au and Au-Cu shells, the latter was left out due to the lack of Au-Cu in the material (Figure 5-41 and Figure 5-42). After the catalysis the material appears again as Au metal, however the amplitude of the noise oscillations at higher R values appears to increase.

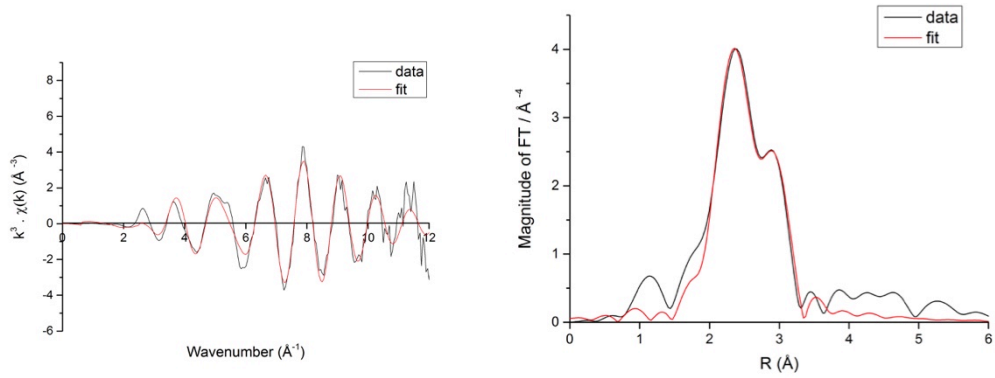

Figure 5-41 - Example of data showing k^3-weighted data (left) and the Fourier transform (right) for Au-edge data at the beginning of the catalysis.

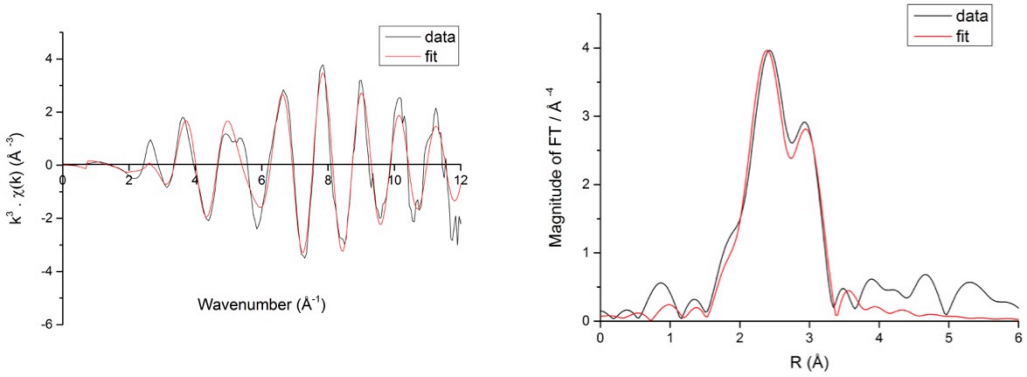

Figure 5-42 - Example of data showing k^3-weighted data (left) and the Fourier transform (right) for Au-edge data at the end of the catalysis.

Visual comparison of the Fourier transformed EXAFS data for the Au-edge, shows striking similarities between the experimental data and Au metal standard, with reduced intensity of the Au-Au peak (Figure 5-43). The intensity of the Au-Au peak increases with increasing temperature, mirroring the observations from XANES regarding the increased sharpness of the oscillations. The full table of results for the Au L_{III}-edge data is given in Table 5-10.

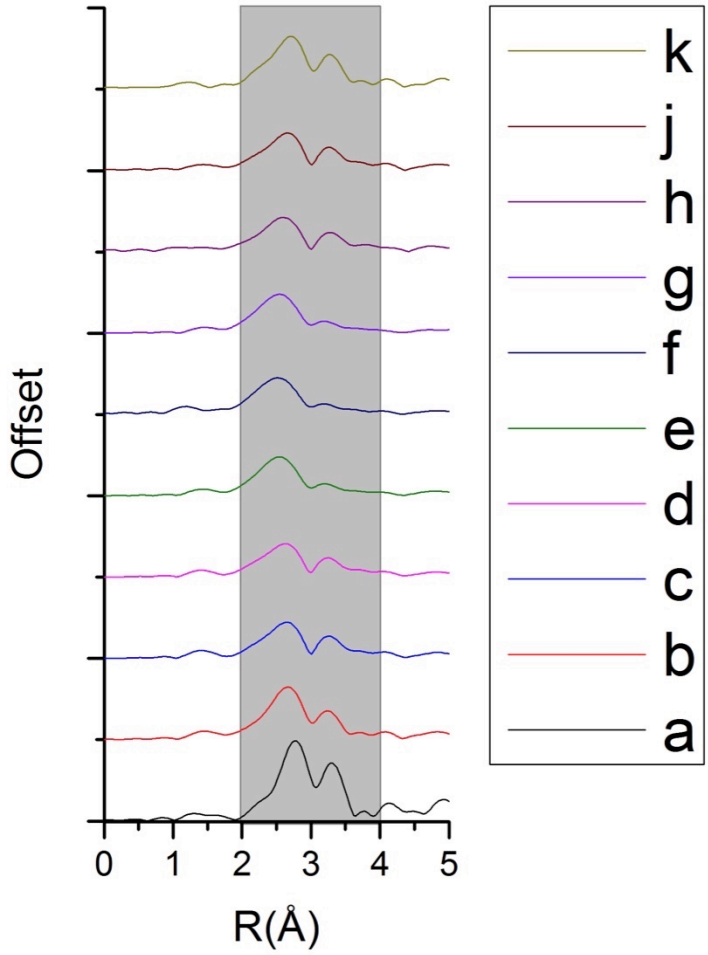

Figure 5-43 - Plot of the Fourier Transformed data for the Au-edge for the reduced only material used for propene catalysis. Where a) Au metal standard, b) the catalyst at room temperature, c) at 473 K, d) at 513 K, e) at 553 K, f) at 593 K, g) cooling 553 K, h) cooling 513 K, j) cooling 473 K, k) cooling room temperature. Grey region indicates the fitting window. Arrow indicates direction for plots from a to k.

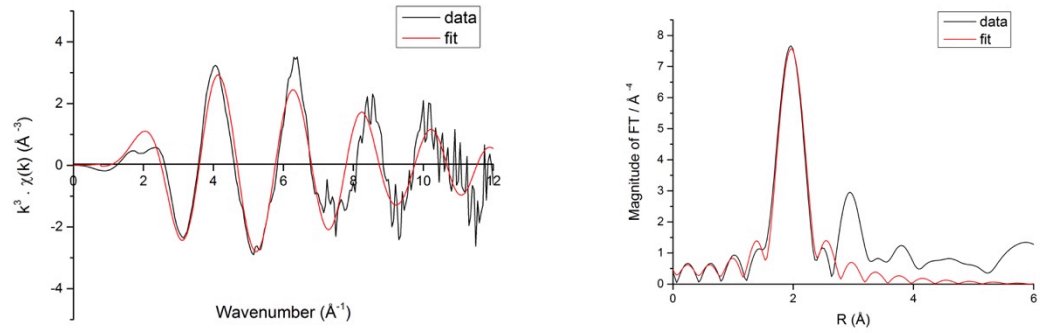

Figure 5-44 - Example of data showing k^3-weighted data (left) and the Fourier transform (right) for Cu-edge at the beginning of the catalysis.

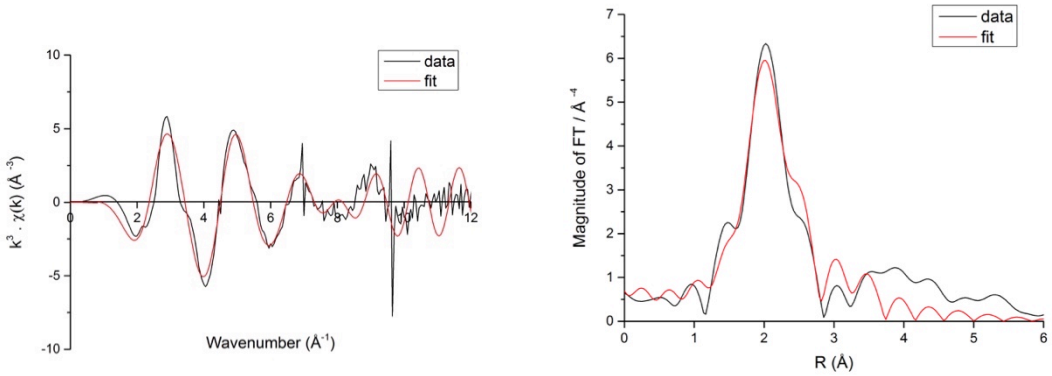

Figure 5-45 - Example of data showing k^3-weighted data (left) and the Fourier transform (right) for Au-edge data at the end of the catalysis.

Visual interpretation of the Cu-edge data shows that the material exists predominately as CuO, indicated by the peak at ca 2 Å (Figure 5-44). This also changes in the EXAFS region after the catalysis with the peak at ca, 3 Å disappearing at the end of the catalysis (Figure 5-45).

The Cu-edge data strongly resembles the CuO standard, though with reduced magnitude. Upon increasing temperature the magnitude of Cu-O peak decreases; it rises again to a similar magnitude upon cooling (Figure 5-46). The full table of results for the Cu K-edge are given in Table 5-11.

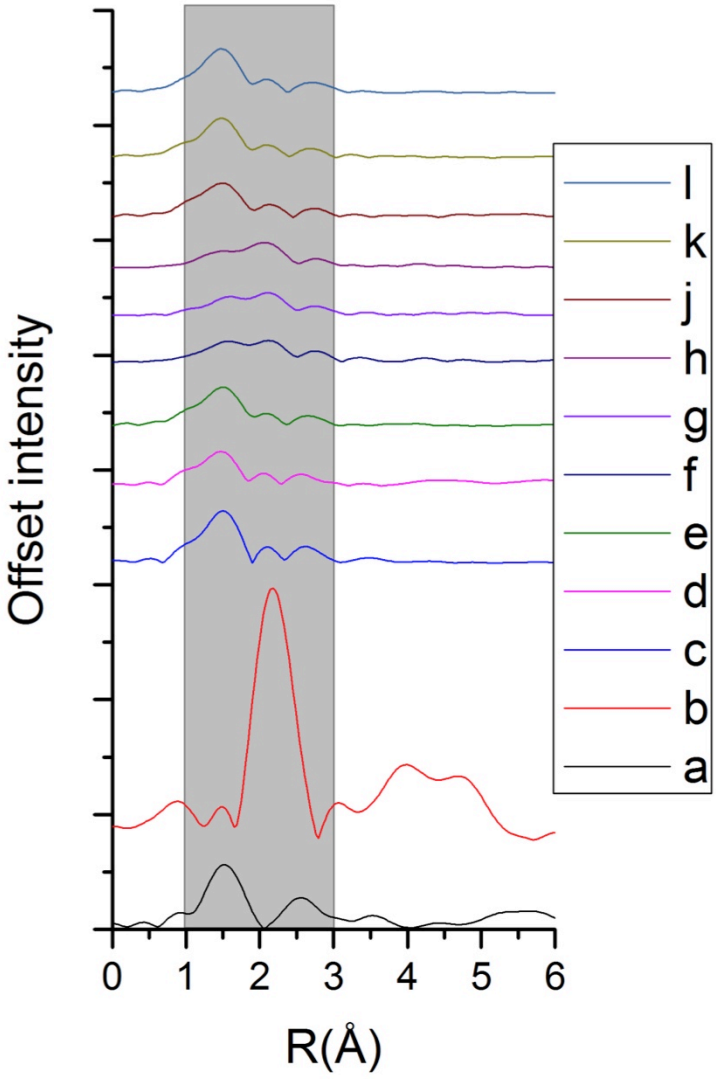

Figure 5-46 - Plot of the Fourier Transformed data for the Cu k-edge reduced only material used for propene catalysis. Where a) CuO, b) Cu foil standard, c) catalyst at room temperature, d) at 473 K, e) at 513 K, f) at 553 K, g) at 593 K, h) cooling 553 K, j) cooling 513 K, k) cooling 473 K, l) cooling room temperature. Grey region indicates the fitting window.

Table 5-10- Au L_{III}-edge results for fitting of propene catalysis data using reduced only catalyst

		Au-Cu							Au-Au							
			n=12		reff= 2.7100					n=12		reff= 2.8600			
temperature	R-factor	x value	CN	error	R value	error	so2	ss2	x value	CN	error	R value	error	so2	ss2
25	0.03	0.00	0.00	0.00	2.71	0.00	0.00	0.0030	0.82	9.78	0.98	2.82	0.01	0.59	0.0101
200	0.05	0.00	0.00	0.00	2.71	0.00	0.00	0.0030	0.88	10.56	1.06	2.82	0.02	0.64	0.0151
240	0.05	0.01	0.00	0.00	2.71	0.00	0.01	0.0030	0.81	9.74	0.97	2.81	0.02	0.59	0.0159
280	0.18	0.02	0.00	0.00	2.71	0.00	0.02	0.0030	0.68	8.19	0.82	2.75	0.03	0.49	0.0146
320	0.14	0.02	0.00	0.00	2.71	0.00	0.00	0.0030	0.64	7.70	0.77	2.74	0.04	0.46	0.0140
280	0.14	0.02	0.00	0.00	2.71	0.00	0.00	0.0030	0.68	8.16	0.82	2.75	0.18	0.49	0.0143
240	0.03	0.00	0.00	0.00	2.71	0.00	0.00	0.0030	0.86	10.31	1.03	2.82	0.02	0.62	0.0162
200	0.04	0.01	0.00	0.00	2.71	0.00	0.00	0.0030	0.89	10.62	1.06	2.83	0.02	0.64	0.0149
25	0.03	0.01	0.00	0.00	2.71	0.00	0.01	0.0030	0.95	11.43	1.14	2.84	0.02	0.69	0.0113

Table 5-11 - Cu k-edge results for fitting of propene catalysis data using reduced only catalyst

		Cu-O							Cu-Cu							Cu-Au							
			n=4		reff= 1.9500					n=12		reff= 2.5600					n=12		reff= 2.7100			
temperature	R-factor	x value	CN	error	R value	error	so2	ss2	x value	CN	error	R value	error	so2	ss2	x value	CN	error	R value	error	so2	ss2
25	0.03	0.81	3.23	0.32	1.96	0.09	0.72	0.0081	0.00	0.05	0.00	2.56	-	0.00	0.0030	0.02	0.25	0.02	2.71	0.00	0.00	0.0030
200	0.05	0.58	2.34	0.23	1.98	0.13	0.52	0.0105	0.00	0.05	0.00	2.56	-	0.00	0.0030	0.01	0.08	0.01	2.71	0.00	0.02	0.0030
240	0.05	0.50	2.00	0.20	1.89	0.04	0.45	0.0076	0.00	0.00	0.00	2.56	-	0.00	0.0030	0.05	0.55	0.05	2.71	0.00	0.04	0.0030
280	0.18	0.35	1.39	0.14	1.88	0.23	0.31	0.0155	0.02	0.18	0.02	2.56	-	0.01	0.0030	0.07	0.89	0.09	2.71	0.00	0.07	0.0030
320	0.14	0.33	1.33	0.13	1.88	0.30	0.30	0.0174	0.02	0.23	0.02	2.56	-	0.02	0.0341	0.00	0.00	0.00	2.71	0.00	0.00	0.0030
280	0.14	0.43	1.72	0.17	1.90	0.26	0.38	0.0204	0.02	0.28	0.03	2.56	-	0.02	0.0030	0.06	0.76	0.08	2.71	0.00	0.00	0.0030
240	0.03	0.59	2.38	0.24	1.92	0.04	0.53	0.0124	0.00	0.00	0.00	2.56	-	0.01	0.0030	0.00	0.00	0.00	2.71	0.00	0.00	0.0030
200	0.04	0.57	2.26	0.23	1.92	0.04	0.51	0.0101	0.00	0.03	0.00	2.56	-	0.00	0.0030	0.00	0.00	0.00	2.71	0.00	0.00	0.0030
25	0.03	0.65	2.58	0.26	1.92	0.04	0.58	0.0101	0.00	0.03	0.00	2.56	-	0.00	0.0030	0.00	0.00	0.00	2.71	0.00	0.00	0.0030

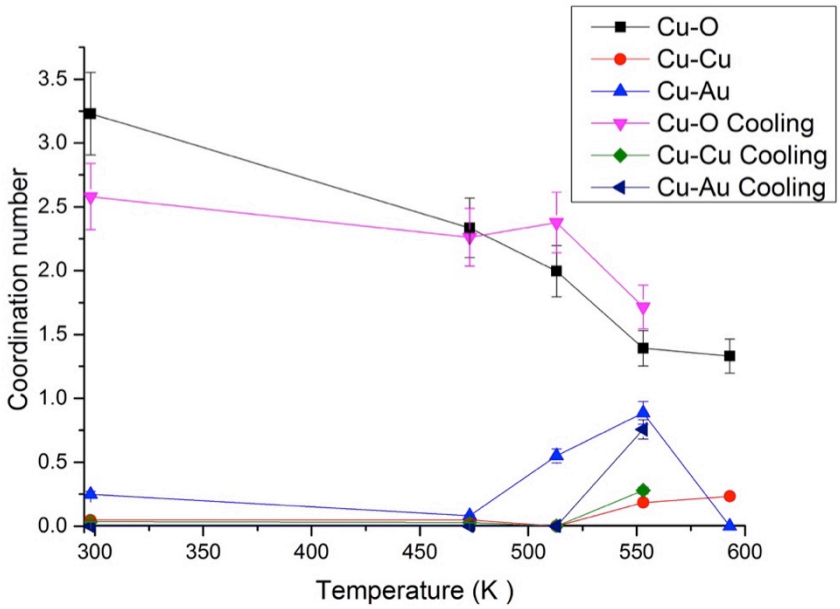

Figure 5-47 - Plot of change in coordination number with temperature for Cu k-edge data.

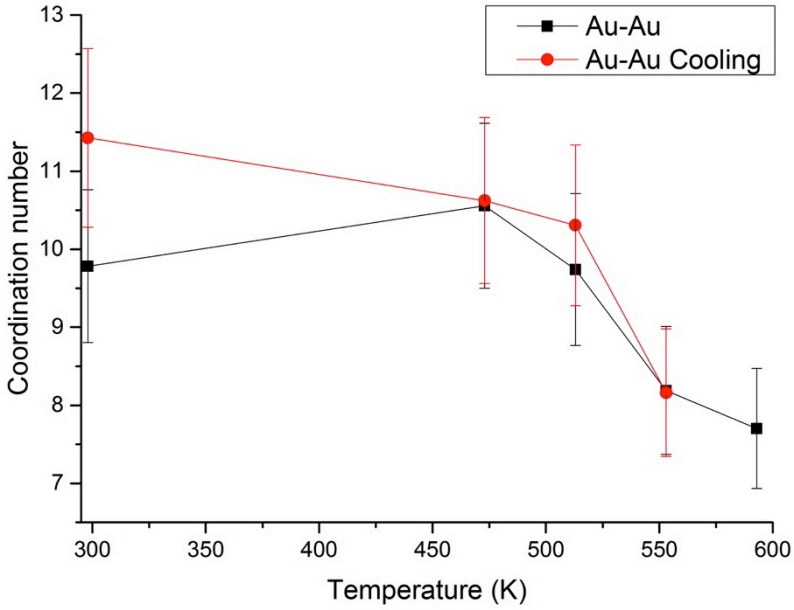

Figure 5-48 - Plot of change in coordination number with temperature for Au L_{III}-edge data.

The coordination number for the Cu-O shell decreases with increasing temperature, dropping from 3.23 to 1.33 (Figure 5-47). Upon cooling back to room temperature there is a discrepancy in the coordination number with the value at 297 K determined as being 1.39 on heating and 1.72 on cooling however this can be reconciled through the error values. The rest of the values for the coordination number are in good agreement. The coordination number for the Cu-Cu shell barely rises above 0.25 throughout the catalysis, indicating there is minimal contribution from Cu-Cu to the structure. There appears to be a large amount of Au-

Cu present in the catalyst at temperatures above 473 K on the Cu-edge; however the Au-Cu path could not be fitted on the Au edge data.

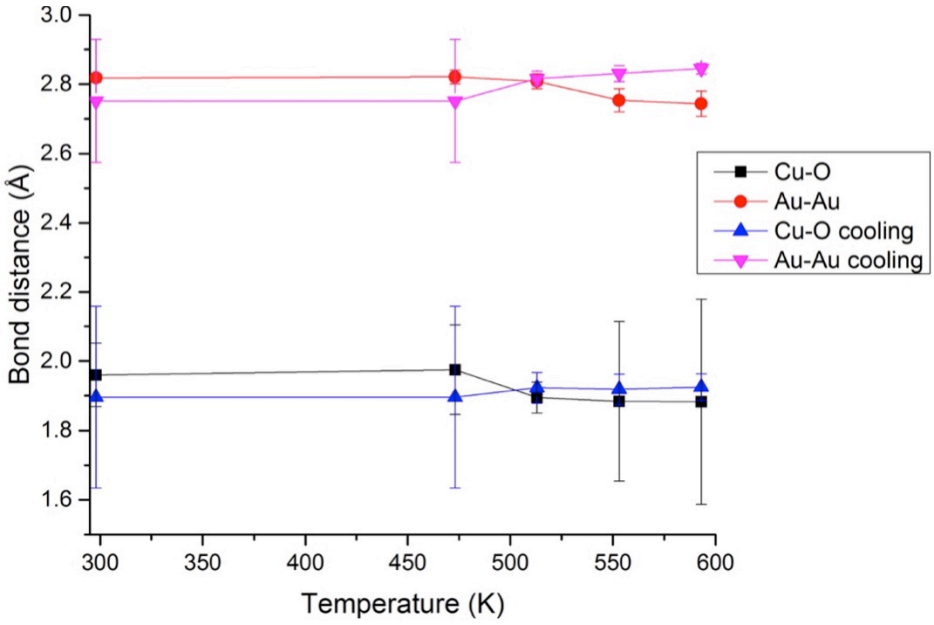

Figure 5-49- Change in bond distance with temperature for the Cu-O and Au-Au shells during the selective oxidation of propene using reduced only catalyst.

The bond distances apart from the first shell were fixed in the fitting model to lower the number of independent variables and improve the integrity of the model. The bond distance for the Au-Au shell is lower than the literature value of 2.86 Å, being around 2.8 Å until reaching 553 K where it decreases further to a value of 2.75 Å. Unsurprisingly this low value for the bond distance has the highest error values. After cooling the value for the bond distance increases to 2.84, matching the trend for increasing values with the coordination number for the shell. The bond distance for the Cu-O shell decreases upon increasing temperature, reaching a minimum of 1.88 at 593 K. Upon cooling the bond distance does not return to near the literature value of 1.95 Å but slightly lower at 1.92Å.

The coordination number for the Au-Au shell decreases with increasing temperature, falling from 10 to 7.70 at the maximum temperature of 593 K (Figure 5-48). Upon cooling the coordination number does not return to the same value, rising to 11.5; this value is within errors in the same region as the starting value. This could indicate that a change has occurred in the Au component of the catalyst, as the amount of metal present has increased. This change is potentially due by the catalyst becoming calcined during this reaction leading to changes that make it more comparable to the reduced-calcined material.

5.5.2 Reduced and calcined catalyst

The last material is a reduced and calcined catalyst, where the catalyst is both reduced and fully calcined prior to use in the propene oxidation reaction. The materials were show to have different catalytic activity in the literature, so the study of the local coordination is of interest.[18,21]

5.5.2.1 XANES Analysis

The Cu-edge data shows that the reduced and calcined catalyst exists with the Cu primarily in the metallic state (Figure 5-50). Comparison with the Cu standards confirms that the material is in the Cu(II) oxide form, however the intensity of the edge feature is significantly reduced.[18] As this feature is caused by p-d orbital mixing, it is sensitive to changes in structure, thus indicating that the supported CuO is different to the bulk standard; either through particle size or local structure. Further fitting of the EXAFS region should reveal which one is the cause.

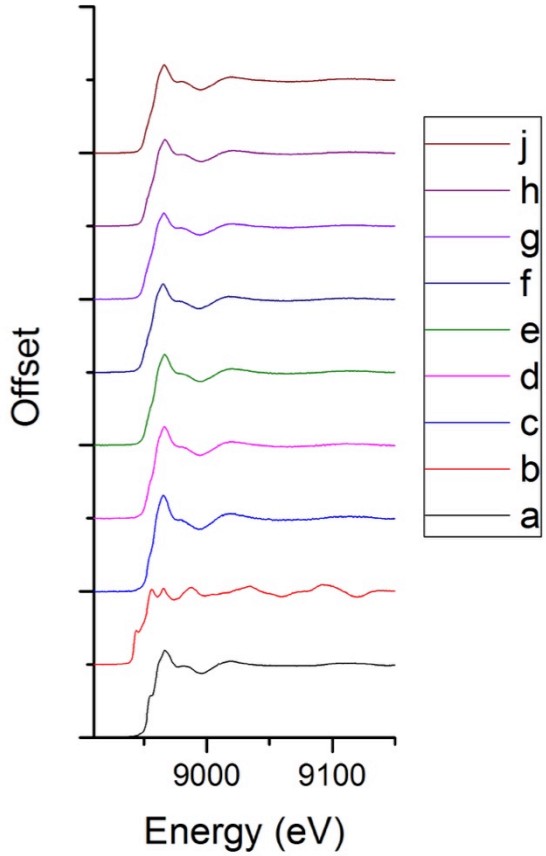

Figure 5-50 - XANES on the Cu k-edge of the reduced and calcined catalyst for propene oxidation, where a) CuO on silica, b) Cu foil standard, c) catalyst at room temperature, d) catalyst at 473 K, e) at 513 K, f) at 553 K, g) at 593 K, h) cooling at 553 K, j) cooling at room temperature.

The reduced and calcined catalyst exists with the Au primarily in the metallic state. Through out the catalysis reaction there are few changes in the XANES for the Au-edge data (Figure 5-51). Comparison with the Au standards confirms that the material is in the metallic form, although the intensity of the post edge features are lower than for the Au foil; this is potentially due to support effects.

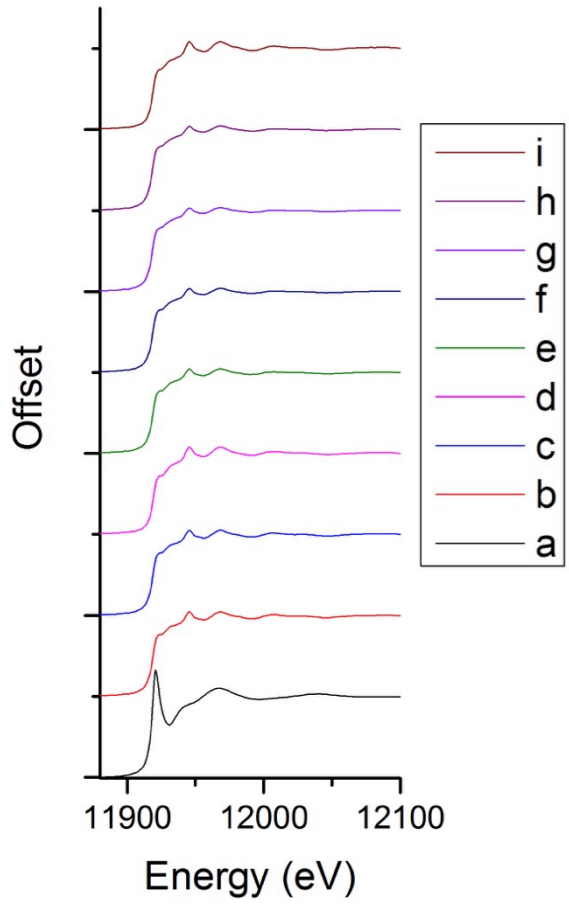

Figure 5-51 - XANES of Au L_{III} - edge for catalysis of propene with reduced and calcined catalyst. Where a) AuOH standard, b) Au metal standard, c) catalyst at room temperature, d) at 473 K, e) at 513 K, f) at 553 K, g) at 593 K, h) cooling to 553 K, j) cooling to room temperature.

5.5.2.2 EXAFS Analysis

The Au-edge data for the reduced calcined catalyst shows higher amplitudes for the k-space oscillations than for the calcined only catalyst (Figure 5-52). By the end of the catalysis the material exists purely as Au metal with little to no contribution from other phases (Figure 5-53). The full table of results for the Au L_{III}-edge is given in Table 5-12.

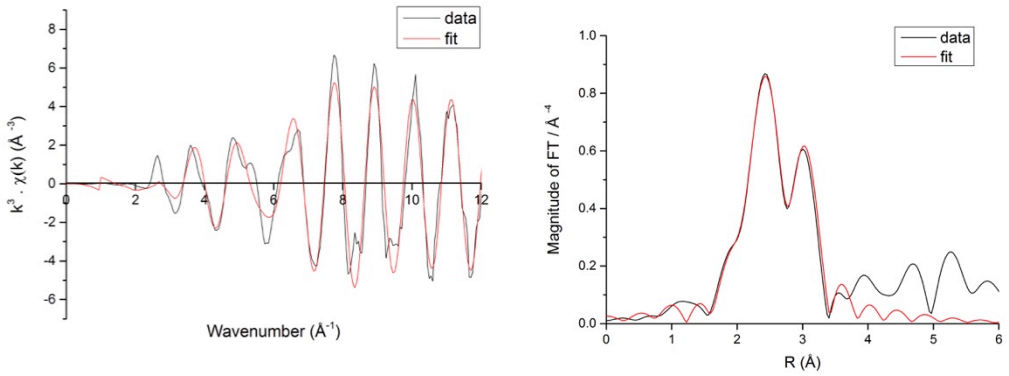

Figure 5-52 - Example of data showing k^3-weighted data (left) and the Fourier transform (right) for Au-edge data for the reduced-calcined catalyst at the start of the propene catalysis.

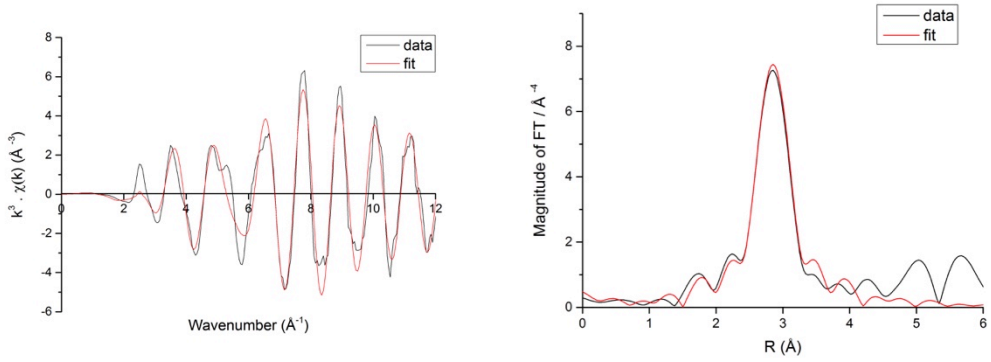

Figure 5-53 - Example of data showing k^3-weighted data (left) and the Fourier transform (right) for Au-edge data for the reduced-calcined catalyst after propene catalysis.

Comparison of the Fourier transform of the EXAFS region for the reduced-calcined catalyst data with standards reveals that the material exists primarily as Au metal (Figure 5-56). Upon increasing temperature the intensity of the Au-Au peak decreases reaching a minimum at 320°C, and returning to a similar magnitude at the end of the experiment. The intensity of the Cu-O peak changes only slightly with increasing temperature. The noise in the data increases upon cooling, visible in the region between 0-2 Å. Comparison with the standards reveals the material exists primarily as CuO. There is a small peak around 2 Å, which could potentially be due to Cu-Cu formation.

Inspection of the data for the reduced-calcined catalyst reveals that the material reveals that the material begins as Cu oxide, with a large amount of noise at higher k-range (Figure 5-54). At the end of the catalysis the material remains as the Cu oxide, with the peak near 3 Å due to Cu-Cu decreasing slightly in magnitude (Figure 5-55).

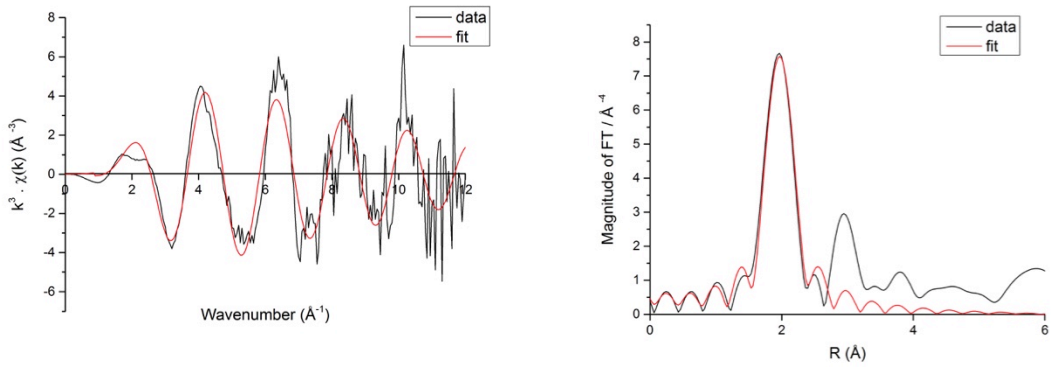

Figure 5-54 - Example of data showing k^3-weighted data (left) and the Fourier transform (right) for Cu-edge for the reduced-calcined catalyst at the start of the propene oxidation.

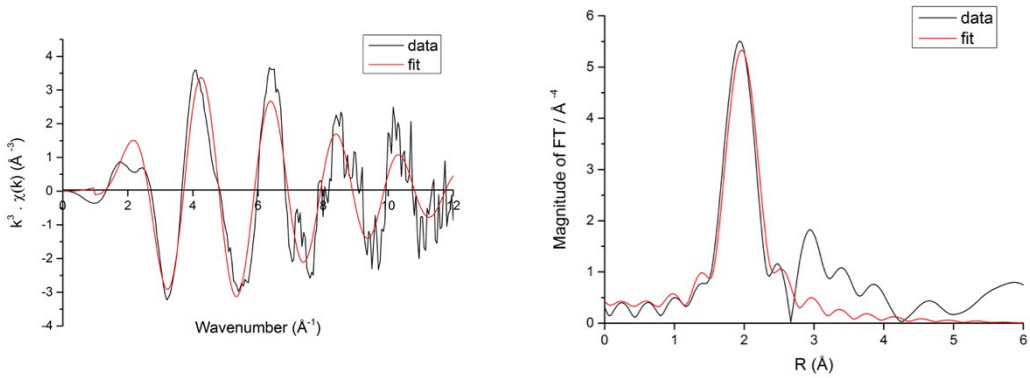

Figure 5-55 - Example of data showing k^3-weighted data (left) and the Fourier transform (right) for Cu-edge data for the reduced-calcined catalyst after propene oxidation.

The coordination numbers for the Cu-O shell in the Cu k-edge data decreases steadily with increasing temperature; dropping from 3.15 to 2.75 (Figure 5-58). On cooling it rises again to 2.83, slightly lower than the initial value. This mirrors the results from the reduced only catalyst, which also had a lower Cu-O coordination number after the reaction. The coordination number for the Cu-Cu shell never rises above 0.35, falls with increasing temperature, lowering to 0.11 at 320^{o}C and reaches a value of zero upon cooling to room temperature. This suggests that the material exists as CuO only with little to no metallic Cu present.

EXAFS fitting of the Au-edge data has shown that the coordination number decreases from 12 to 10.51; on cooling it rises back to 12 (Figure 5-59). Within errors the coordination number change on heating and cooling are consistent and support the same trend. The full table of results for the Au L_{III}-edge are provided in Table 5-10 and Cu K-edge data is given in Table 5-13.

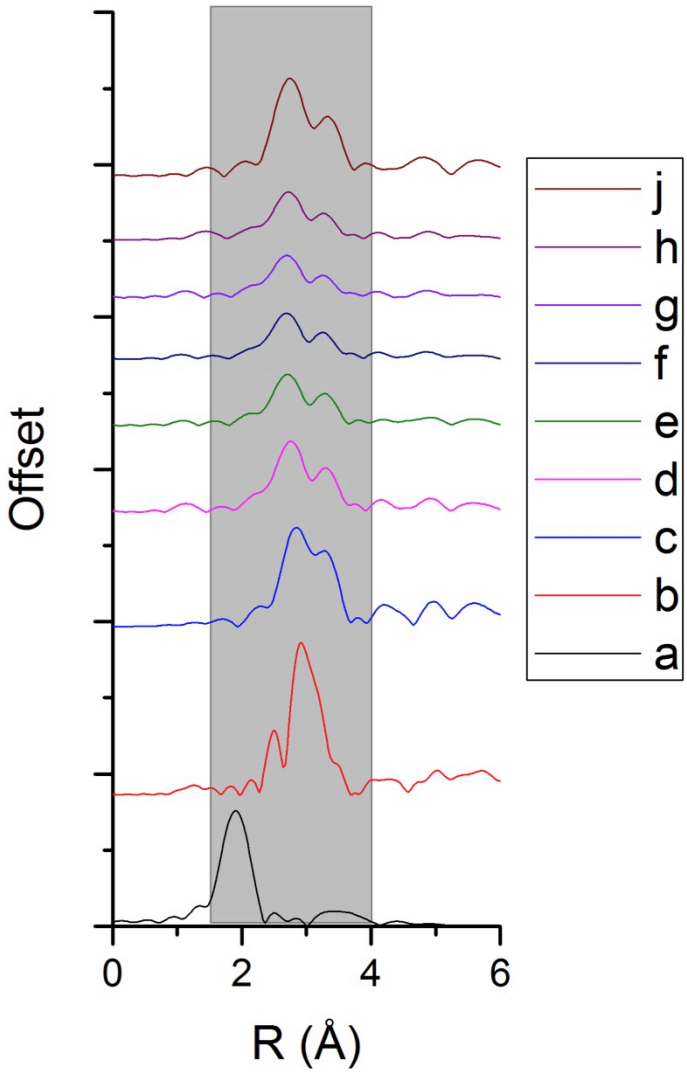

Figure 5-56 - Fourier transform of EXAFS data on the Au L_{III}-edge for the catalysis of propene using reduced and calcined catalyst. Where a) AuOH standard, b) Au metal standard, c) the catalyst at room temperature, d) at 473 K, e) at 513 K, f) at 553 K, g) at 593 K, h) cooling at 553 K, j) cooling at room temperature. Grey region indicates the fitting window.

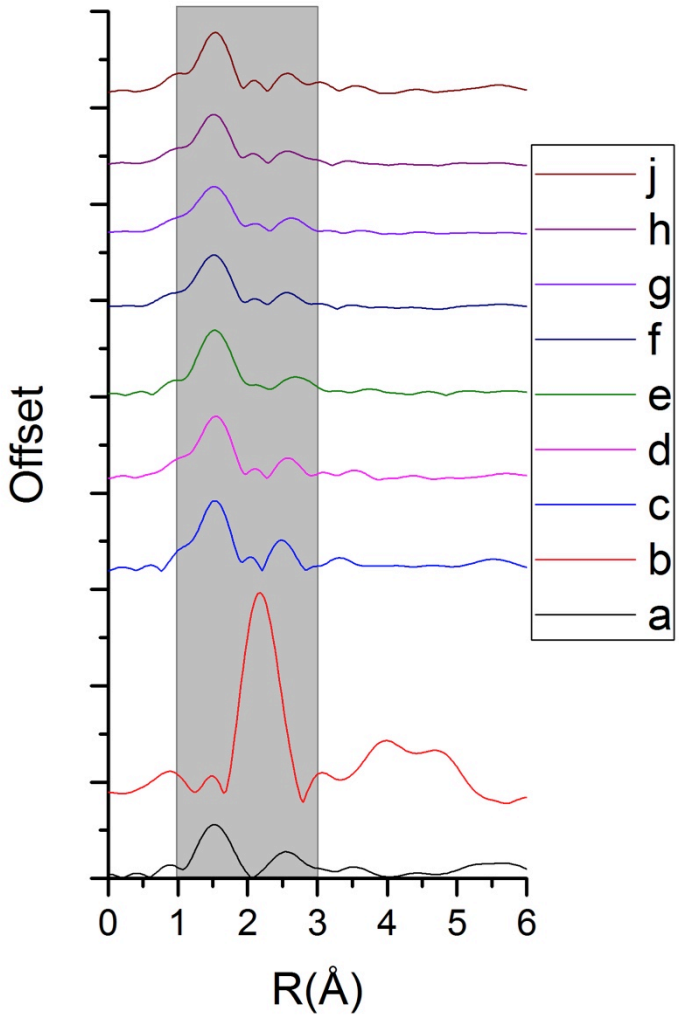

Figure 5-57 - Fourier transform of EXAFS data on the Cu k-edge for the catalysis of propene using reduced and calcined catalyst. Where a) CuO, b) Cu foil standard, c) the catalyst at room temperature, d) at 473 K, e) at 513 K, f) at 553 K, g) at 593 KC, h) cooling at 553 K, j) cooling at room temperature. Grey region indicates the fitting window.

Table 5-12 - Au L_{III}-edge results for fitting of propene catalysis data using reduced-calcined catalyst.

		Au-Cu							Au-Au			2.86			
temperature	R-factor	x value	CN	error	R value	error	so2	ss2	x value	CN	error	R value	error	so2	ss2
25	0.05	0.00	0.00	0.00	0.00	0.00	0.00	0.0000	0.99	11.91	1.19	2.88	0.01	0.72	0.0075
200	0.03	0.00	0.00	0.00	0.00	0.00	0.00	0.0000	1.03	12.41	1.24	2.86	0.01	1.02	0.0136
240	0.03	0.00	0.00	0.00	0.00	0.00	0.00	0.0000	0.97	11.69	1.17	2.86	0.16	0.70	0.0132
280	0.03	0.00	0.00	0.00	0.00	0.00	0.00	0.0000	0.94	11.30	1.13	2.85	0.01	0.68	0.0141
320	0.03	0.00	0.00	0.00	0.00	0.00	0.00	0.0000	0.88	10.51	1.05	2.84	0.02	0.63	0.0143
280	0.04	0.00	0.00	0.00	0.00	0.00	0.00	0.0000	0.89	10.74	1.07	2.85	0.02	0.65	0.0133
25	0.03	0.00	0.00	0.00	0.00	0.00	0.00	0.0000	0.99	11.90	1.19	2.85	0.01	1.05	0.0104

Table 5-13 - Cu k-edge results for fitting of propene catalysis data using reduced-calcined catalyst.

		Cu-O			1.95				Cu-Cu							Cu-Au						
temperature	R-factor	x value	CN	error	R value	error	so2	ss2	x value	CN	error	R value	error	so2	ss2	x value	CN	error	R value	error	so2	ss2
25	0.05	0.79	3.15	0.03	1.96	0.02	0.71	0.0031	0.03	0.35	0.03	2.56	-	0.02	0.0030	0.00	0.00	0.00	0.00	0.00	0.00	0.0000
200	0.03	0.71	2.83	0.00	1.95	0.02	0.66	0.0058	0.02	0.18	0.02	2.56	-	0.02	0.0030	0.00	0.00	0.00	0.00	0.00	0.00	0.0000
240	0.03	0.75	2.99	0.48	1.95	0.04	1.08	0.0105	0.01	0.11	0.01	2.56	-	0.01	0.0030	0.02	0.00	0.00	0.00	0.00	0.00	0.0000
280	0.03	0.69	2.75	0.00	1.96	0.04	0.62	0.0071	0.01	0.11	0.01	2.56	-	0.01	0.0030	0.00	0.00	0.00	0.00	0.00	0.00	0.0000
320	0.03	0.65	2.62	0.00	1.96	0.03	0.59	0.0085	0.01	0.13	0.01	2.56	-	0.01	0.0030	0.00	0.00	0.00	0.00	0.00	0.00	0.0000
280	0.04	0.64	2.56	0.00	1.95	0.04	0.57	0.0079	0.01	0.11	0.01	2.56	-	0.01	0.0030	0.00	0.00	0.00	0.00	0.00	0.00	0.0000
25	0.03	0.71	2.83	0.00	1.95	0.02	0.63	0.0063	0.02	0.00	0.00	2.56	-	0.01	0.0030	0.00	0.00	0.00	0.00	0.00	0.00	0.0000

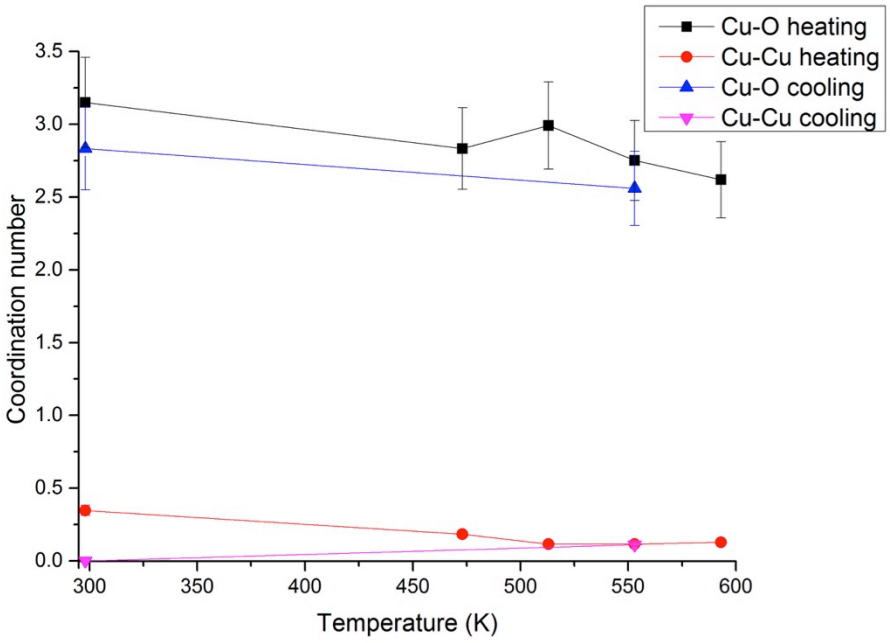

Figure 5-58 - Plot of change in coordination number with temperature for Cu k-edge data.

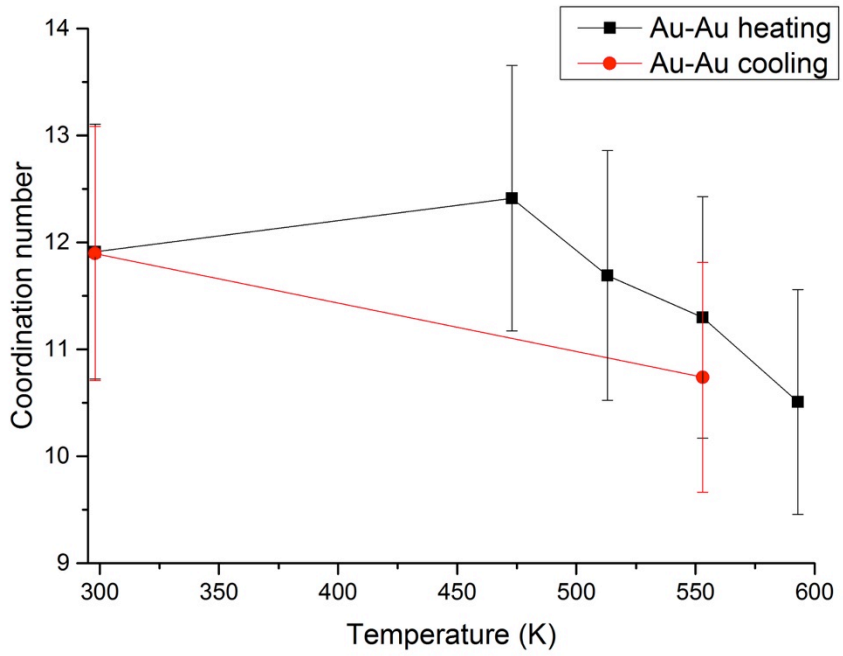

Figure 5-59 - Plot of change in coordination number with temperature for Au L_{III}-edge data.

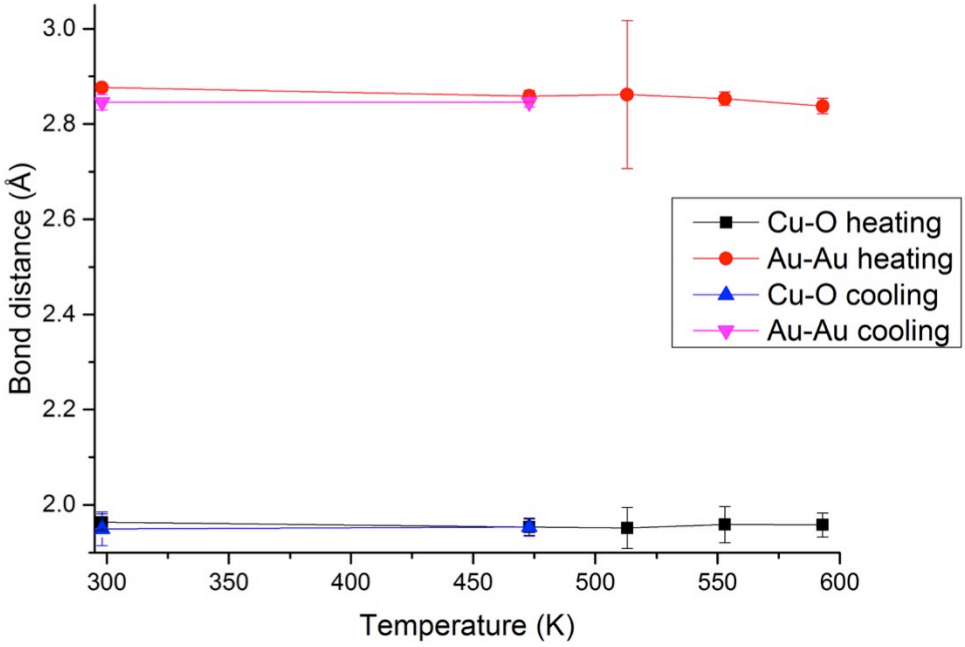

Figure 5-60 - Plot of change in bond distance with temperature for Au L_{III}-edge and Cu k-edge data.

The bond distance for the Au-Au shell starts at 2.86 Å, slightly higher than the literature value of 2.86 Å. This value decreases slightly with increasing temperature, lowering to a value of 2.85 Å. The bond distance for the Cu-O shell changes only slightly throughout the experiment 1.96 Å. The Cu-Cu bond distance was kept constant during the fit.

5.5.3 Discussion

The Cu-Au interaction observed from the Cu-edge fits, may not be reliable. The main reason for this statement is the lack of an interaction on the Au edge data. If the AuCu phase were to be present in the materials used for catalysis, the interaction should be visible on both metal edges. Additionally as it has been shown in the literature that the interaction between metals in a bimetallic cluster leads to charge transfer, if the interaction is present it should be visible on both edges.[31] As Au data utilises the L_{III}-edge it should be more sensitive to interactions with the bonding orbitals, the absence of the AuCu in the fitting leads to the conclusion that it is either not present or the interaction is of sufficiently low value to be ignored from the fitting model.

In the report by Sinfelt the AuCu interaction was supported by both bond distance measurements and slight variations in the coordination numbers (CN), with the Au-Au first shell having a CN of 11 and the Cu-Cu first shell having a coordination number of 12. However in the current analysis the coordination numbers for the AuCu interaction are not

consistent and the R-factors for the fits including the shell are not as good as those where t is left out. However it has previously been stated in the literature that the interaction is present in these materials, using EXAFS analysis as confirmation.[18] It is here that the differences between fitting models must be addressed. In the previous work the total amount of each metal was assumed to only be able to exist in one of three phases, the pure metal, the oxide or the bimetallic. In the case of the Cu edge this would mean either Cu metal, CuO or CuAu. The fitting model was therefore constructed as with an additional term to the amplitude term, formed using an equation with three inter-related unknowns and a maximum value of 1.[18] As such the system was restricted into putting the metals into one of three states. When replicating these measurements, it was found that a large amount of noise was being assigned to the AuCu shell in the fitting model; indeed this is seen with the Cu-edge data for the reduced-only catalyst to some extent.

In the present work a different approach was taken. The three terms for the coordination numbers of the different shells was allowed to float and remain independent of each other. The results were different to the ones reported and showed interesting features, such as the potential Cu(I)O formed during the catalytic oxidation with the reduced-calcined catalyst.[18] Whilst the results are different, it should be noted that EXAFS analysis is down to interpretation and the integrity of the model.

Comparison of the Fourier transforms of the catalysts on the Au-edge shows that the reduced-calcined catalyst has more defined peaks with larger magnitude (Figure 5-39 and Figure 5-51). This correlates well with the results from EXAFS fitting which shows that the reduced-calcined catalyst has a higher coordination number than the reduced only catalyst (Figure 5-48 and Figure 5-58).

The Cu-O bond distances for both catalysts in the range from 1.92-1.96 are consistent with Cu(II) –oxygen interactions.[18] The lowered bond distance of 1.88Å between 240 and 593 K could be potential evidence of Cu(I)-oxygen formation; this would be more of a mixed phase as the bond distance is not as low as for a pure Cu_2O first shell (1.83Å). In both cases there are changes on the Cu-edge as the coordination number lowers after the catalysis. It may be possible to reverse this effect by re-calcining the catalyst; this needs be further explored.

Relating the materials back to catalysis results, the reduced and calcined catalyst shows higher conversion rates than the reduced only material (5.6 as opposed to 2.0).[18] The reduced calcined material shows slightly lower selectivity towards acrolein, having 84% selectivity compared with 93% for the reduced on catalyst, and also forms more oxygenates.[18] This

means the phases present and their properties are directly influencing the catalyst, with the calcination step altering the structure of the catalyst enough to cause a sizable change in the activity.[18] Due to the tendency for Au catalysts to make propene oxide during propene oxidation and Cu catalysts to form acrolein, it is assumed that the active site is Cu-based.[18] It was noted in a previously reported investigation that a pure Cu/SiO_2 material has lower conversion (0.22%), whilst maintain a comparable selectivity for acrolein (85%). This indicates that the presence of Au in the catalyst is in some way aiding the conversion. One theory is that the catalyst preparation procedure results in well dispersed CuO active sites as a result of the Au content.[18] The reduced-calcined material also showed a slight formation of Cu(I)O which is reported in the literature to be an active species for the oxidation of propene.[18] while there is no conclusive proof of the presence of this species it is a potential reason for the difference in the catalytic activity.

5.6 Conclusions

$AuCu/SiO_2$ catalysts are active for the oxidation of propene and are selective towards acrolein. The activation process has been followed *in situ* using EXAFS to provide insights into the changes occurring on the local structure. Reduction of the Au and Cu precursors is required in order to form AuCu alloys. Whilst the catalyst was successfully reduced, no interaction in the local structure between the metals could be determined. Calcination of the catalyst leads to the growth of Au metal and CuO species with little interaction between the metals.

5.7 References

(1) Liu, X.; Wang, A.; Li, L.; Zhang, T.; Mou, C.-Y.; Lee, J.-F. *J. Catal.* **2011**, *278*, 288–296.

(2) Liu, X.; Wang, A.; Zhang, T.; Su, D.-S.; Mou, C.-Y. *Catal. Today* **2011**, *160*, 103–108.

(3) Miyamura, H.; Matsubara, R.; Miyazaki, Y.; Kobayashi, S. *Angew. Chem. Int. Ed. Engl.* **2007**, *46*, 4151–4154.

(4) Letters, C.; Catalysts, N. G.; Monoxide, C.; Haruta, M.; Kobayashi, T.; Sano, H.; Yamada, N. **1987**, 405–408.

(5) Bond, G. C.; Thompson, D. T. *Catal. Rev.* **1999**, *41*, 319–388.

(6) Enache, D. I.; Edwards, J. K.; Landon, P.; Solsona-Espriu, B.; Carley, A. F.; Herzing, A. a; Watanabe, M.; Kiely, C. J.; Knight, D. W.; Hutchings, G. J. *Science* **2006**, *311*, 362–365.

(7) Bracey, C. L.; Ellis, P. R.; Hutchings, G. J. *Chem. Soc. Rev.* **2009**, *38*, 2231–2243.

(8) Bauer, J. C.; Toops, T. J.; Oyola, Y.; Parks II, J. E.; Dai, S.; Overbury, S. H. *Catal. Today* **2014**, *231*, 15–21.

(9) Chimentão, R. J.; Medina, F.; Fierro, J. L. G.; Llorca, J.; Sueiras, J. E.; Cesteros, Y.; Salagre, P. *J. Mol. Catal. A Chem.* **2007**, *274*, 159–168.

(10) Llorca, J.; Dominguez, M.; Ledesma, C.; Chimentao, R.; Medina, F.; Sueiras, J.; Angurell, I.; Seco, M.; Rossell, O. *J. Catal.* **2008**, *258*, 187–198.

(11) Via, G. H.; Drake, K. F.; Meitzner, G.; Lytle, F. W.; Sinfelt, J. H. *Catal. Letters* **1990**, *5*, 25–34.

(12) Vaughan, O.; Kyriakou, G.; Macleod, N.; Tikhov, M.; Lambert, R. *J. Catal.* **2005**, *236*, 401–404.

(13) Scotti, N.; Ravasio, N.; Zaccheria, F.; Psaro, R.; Evangelisti, C. *Chem. Commun. (Camb).* **2013**, *49*, 1957–1959.

(14) Basile, a; Parmaliana, a; Tosti, S.; Iulianelli, a; Gallucci, F.; Espro, C.; Spooren, J. *Catal. Today* **2008**, *137*, 17–22.

(15) Hayashi, T.; Tanaka, K.; Haruta, M. **1998**, *575*, 566–575.

(16) Uphade, B. S.; Tsubota, S.; Hayashi, T.; Haruta, M. *Chem. Lett.* **1998**, 1277.

(17) Mul, G. *J. Catal.* **2001**, *201*, 128–137.

(18) Belin, S.; Bracey, C. L.; Briois, V.; Ellis, P. R.; Hutchings, G. J.; Hyde, T. I.; Sankar, G. *Catal. Sci. Technol.* **2013**, *3*, 2944.

(19) Liao, X.; Chu, W.; Dai, X.; Pitchon, V. *Appl. Catal. B Environ.* **2013**, *142-143*, 25–37.

(20) Nijhuis, T. A.; Makkee, M.; Moulijn, J. a.; Weckhuysen, B. M. *Ind. Eng. Chem. Res.* **2006**, *45*, 3447–3459.

(21) Bracey, C. L.; Carley, A. F.; Edwards, J. K.; Ellis, P. R.; Hutchings, G. J. *Catal. Sci. Technol.* **2011**, *1*, 76.

(22) Meitzner, G.; Via, G. H.; Lytle, F. W.; Sinfelt, J. H. *J. Chem. Phys.* **1985**, *83*, 4793.

(23) Grandjean, D.; Castricum, H. L.; van den Heuvel, J. C.; Weckhuysen, B. M. *J. Phys. Chem. B* **2006**, *110*, 16892–16901.

(24) Guo, N.; Fingland, B. R.; Williams, W. D.; Kispersky, V. F.; Jelic, J.; Delgass, W. N.; Ribeiro, F. H.; Meyer, R. J.; Miller, J. T. *Phys. Chem. Chem. Phys.* **2010**, *12*, 5678–5693.

(25) McDavid, J. M. *J. Vac. Sci. Technol.* **1975**, *12*, 351.

(26) Potter, H. C. *J. Vac. Sci. Technol.* **1975**, *12*, 279.

(27) Barnett, A. E.; JohnI.Sinfelt. Novel Gold-Copper Catalysts for the Partial Oxidation of Olefins. 3989674, 1976.

(28) Silversmit, G.; Poelman, H.; Balcaen, V.; Heynderickx, P. M.; Olea, M.; Nikitenko, S.; Bras, W.; Smet, P. F.; Poelman, D.; De Gryse, R.; Reniers, M.-F.; Marin, G. B. *J. Phys. Chem. Solids* **2009**, *70*, 1274–1284.

(29) Frenkel, A. *Zeitschrift für Krist.* **2007**, *222*, 605–611.

(30) Li, Z.-R.; Yan, W.; Wei, S. *AIP Conf. Proc.* **2007**, *882*, 767–770.

(31) Liu, Z.; Handa, K.; Kaibuchi, K.; Tanaka, Y.; Kawai, J. *Spectrochim. Acta Part B At. Spectrosc.* **2004**, *59*, 901–904.

Chapter 6 - Thermal Decomposition of Nano-sized Zinc Oxide by Thermal Decomposition of Zinc Peroxide Followed with *In situ* XAS and XRD

Abstract

Zinc oxide nanoparticles are important for a variety of applications due to their semi-conductor properties; these properties are linked to the nanoparticle size. One way to produce zinc oxide nanoparticles of controlled size is through the thermal decomposition of zinc peroxide. In this chapter the decomposition of zinc peroxide is investigated using XAS and XRD to follow the changes in the long range and local structures. It was discovered that the material reaches a point (around 150^{o}C) where it undergoes a rearrangement in the local structure, from hexagonal to tetragonal. Following this the zinc oxide clusters grow steadily with increasing temperature.

6.1 Introduction

Zinc oxide nanoparticles are useful for a variety of different applications, due to the electronic and structural properties of the material. As with other metal oxide nanoparticles the structure morphology and size of the particles have a large impact on their properties and uses.[1] Here we outline a method to synthesize zinc oxide nanoparticles from a zinc peroxide precursor resulting in the formation of nanoparticles with a narrow size distribution. By investigating the decomposition we aim to understand the changes occurring in both the local- and long-range structure; this will alter the tailoring of the calcination procedure to potentially control the growth of the material.

6.1.1 Background

Zinc oxide has been used for thousands of years from ancient Egypt, where it was used in skin cream, to the Roman empire and beyond.[2] Zinc oxide is widely used in the modern world with some examples being its use in the vulcanisation process,[3] as a form of control in lattices,[4] as a pigment,[5] and as an additive in lubricating oils.[6] Zinc oxide is a semiconductor material, namely an n-type semi-conductor, useful for a range of applications such as solar cells[7] and chemical sensors.[8,9]

The photocatalytic applications for ZnO nanoparticles are linked to the particle size, and have been shown to be applicable for environmental applications such as the decomposition of drugs in water supplies.[10] ZnO has also shown antimicrobial properties on the nanoscale, and as such has been used in food packaging and for other antimicrobial purposes.[11] The suitability of ZnO nanoparticles for food packaging applications comes from its activity toward a wide variety of microorganisms, thermal and mechanical resistance and the ability to be incorporated into polymeric matrices.[11] ZnO nanoparticles also show potential for use in cancer treatment for the selective destruction of tumour cells.[12] The ZnO nanoparticles show interesting properties on the nanoscale such as the generation of reactive oxidative species, which are essential for medical applications.[12] All of the applications for ZnO nanoparticles are linked to the properties of the material which are in turn determined by the particle size and morphology; this means developing a reliable and effective method for producing ZnO nanoparticles is an important area of research.

There are two main commercial processes for forming zinc oxide; the French process and the American process.[13] In the French process zinc metal is vaporised through external heating, the vapour is carried off into an adjoining chamber where it is burned in air to form zinc oxide powder.[5] In the American process, sulphide concentrates are oxidised and roasted with

anthracite coal in a flat bed furnace. This produces metallic vapours of zinc; these are further burned under controlled conditions to form zinc oxide and led to a bag house where the particles are collected. The main disadvantages of these two processes are the need for high temperatures (in excess of 1000^{o}C) and the remaining unreacted zinc metal.[14]

Forming ZnO nanoparticles with narrow size distribution and controlled morphology can sometimes require more exotic synthesis methods. Zinc oxide can be formed by using supercritical water as a reaction medium and zinc acetate and hydrogen peroxide as the reactants.[6] The water and hydrogen peroxide are preheated before they reach the mixing point; this is essential in order to maintain the supercritical condition. The rapid decomposition of zinc acetate at the mixing point leads to the formation of fine particles. The decomposition is mainly due to reaction with the supercritical water and occasionally with oxygen dissolved in the water.[6] The particles are formed within a minute and are soft and fluffy; this can lead the particles to agglomerate over time.[6]

Zinc oxide nanoparticles can also be synthesised at room temperature without the presence of an amine through the use of a double-jet precipitation method.[15] The morphology size of the nanoparticles can be tailored by adjusting the zinc salt used, leading to the formation either of star-shaped particles or ellipsoids.[15]

Zinc peroxide decomposition is another method to make zinc oxide nanoparticles, through thermal decomposition. It was found that the material decomposed at 473K contained O_2^{2-} ions.[16] As the photoluminescence property and the electrical conductivity of ZnO is dependent on the oxygen vacancies, developing a method to control these defects is essential.[16] This can be clearly seen by the colour of zinc oxide particles with oxygen deficiencies which are yellow rather than the usual white colour of zinc oxide.[16] It has been determined that the oxygen deficiency decreases with increasing calcination temperatures, and this is followed by the change in lattice parameter of the ZnO seen in XRD.[6] Heating at higher temperatures such as 513K results in the loss of O_2^{2-} ions and the formation of oxygen vacancies in the material.[16]

The structure and properties of zinc oxide nanoparticles can be modified by adding materials to the reaction mixture such as poly(vinlypyrrolidone) also known as PVP.[17] These PVP stabilised zinc oxide nanoparticles were found to be more stable than their non-capped equivalents and also had a narrower particle size distribution.[17] When no PVP is added the amount of particle interaction is increased leading to aggregation and reduced stability.[17]

It was found that the presence of water and acetate in the reaction mixture considerably increased the rate of particle growth during ZnO particle synthesis.[18] Zinc oxide can be used as an example system to obtain a more detailed understanding of the sol-gel synthesis and growth of oxidic nanoparticles.[18] The authors modified the synthesis procedure by cooling to 0^{o}C instead of refluxing for a few hours as done previously in the literature.[19,20] The synthesis was further modified by using zinc acetate in place of zinc dehydrate.[18] A washing method was developed which was based on the repeated precipitation by addition of alkanes and redispersion in ethanol. The chemical composition of the films developed was found to be useful for studies of electrical and optical properties of ZnO nanoparticle films.[9] It was found that the other products of the reaction, namely the Lithium acetate, would hinder particle growth.[9]

ZnO nanoparticles, specifically zinc oxide nanorods are used in combination with polymers to form photovoltaic devices.[21,22] This based on the advantages of using metal oxides as electron acceptors, with features such as rigid nanocrystalline structures in addition to the intrinsic properties of zinc oxide such as high electron mobility.[23] The most attractive feature however is the low temperature synthesis and potential for morphology control through simple solution chemistry, essentially making the manufacture of these nanoparticles more cost effective than other potential materials.[23]

The authors utilised poly(3-hexylthiophene) polymer (P3HT) as the interface layer for vertically orientated ZnO nanorods. This arrangement was shown to have a power conversion efficiency up to four times greater than for the corresponding ZnO nanoparticle device. This highlights the importance of controlling the nanoparticle morphology to tailor materials to specific needs.

Another method for preparing highly dispersed and uniform ZnO particles of different shapes and sizes through the slow addition of zinc salts and sodium hydroxide to aqueous solutions of Arabic gum.[24] Control of the temperature was shown to be critical in controlling the size and morphology of the material formed.[24]

6.2 Aim of the work

As you can see from the literature, zinc oxide nanoparticles are useful for a variety of purposes. Their usefulness is linked to their semi-conductor properties, which are in turn related to the size and shape of the zinc oxide nanoparticles. In this work we will investigate the formation of zinc oxide nanoparticles through the thermal decomposition of zinc peroxide, as this has been shown to produce zinc oxide nanoparticles of narrow size distribution. This work will focus solely on the decomposition process, with the potential applications and benefits of these materials left to other projects. The zinc peroxide was thermally decomposed and monitored *in situ* using combined XAS/XRD; this allows for investigation of both the local and long-range structures during the decomposition process.

6.3 Experimental Section

6.3.1 Sample preparation

Zinc peroxide samples can be prepared via a zinc acetate precursor following the method described by Tsur *et al*. The method is relatively straightforward and can be carried out in glass beakers at ambient conditions (room temperature and pressure). In the first step zinc acetate is dissolved in a mixture of distilled water and H_2O_2, and to this solution PEG 200 was added with stirring. The solution was stirred for two hours, forming a clear yellowish or colourless solution. NaOH was added to this solution in order to precipitate the nanoparticles. The NaOH was added until the pH of the solution was lowered to 11.5, this changing the previously clear solution into a white suspension. The precipitate was separated by centrifugation and washed with NaOH followed by distilled water until a pH of at least 8.4 was achieved. The precipitate was then dried at 80 ^{o}C for 2 hours in an oven.

6.3.2 Synchrotron radiation measurements

Combined XRD/XAS data were collected on the Zinc K-edge at the B18 beamline, Diamond Light Source (UK), using a Si (111) monochromator for XAS whilst diffraction data was collected using a 9 element Ge detector. Quick-EXAFS data was collected in transmission mode, using a zinc reference foil to calibrate the energy. X-Ray Diffraction data was recorded using a wavelength of 1.305Å, just above the Zn K-edge in terms of energy.

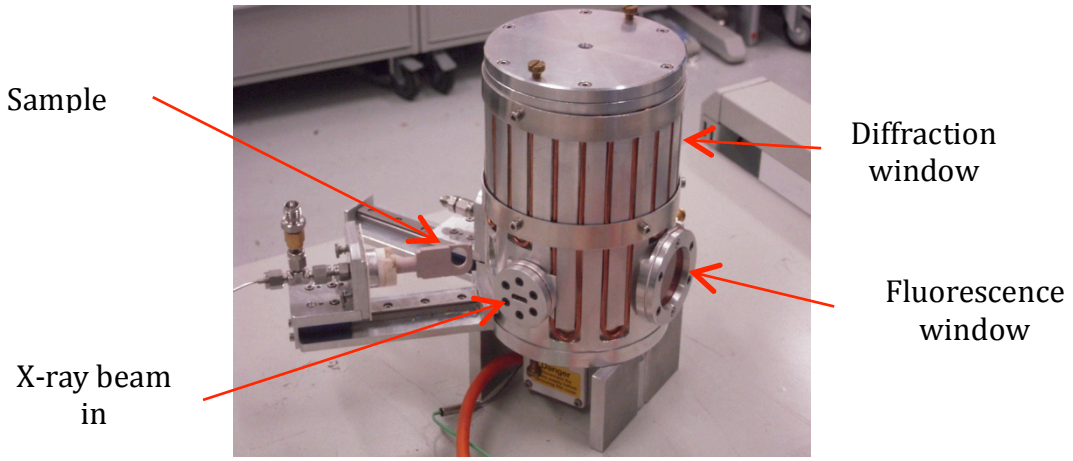

Figure 6-1 - Image of the in situ cell utilised in this work showing the important features such as X-ray windows and sample holder.

The zinc peroxide sample was made using a mixture of ZnO_2 (20mg) and fumed silica (130 mg) which was subsequently pressed into a 13 mm pellet before loading into a high temperature furnace cell that is custom built for taking combined measurements (Figure 6-1).

For these experiments a flow of air at 10ml/min was used. The zinc peroxide pellets were then heated up to 500^{o}C at a rate of 5^{o}C/min, in air, whilst diffraction and absorption data were recorded sequentially.

QuEXAFS data was normalised in Athena and fitted using Artemis software running with IFEFFIT11[5]. Refinement was carried out using k^3 weighting in the range 2.5-11.5Å^{-1}. A value for the Zn amplitude term was obtained by fitting of a zinc foil standard with fixed coordination number. This parameter was used in subsequent analysis of the *in situ* data using Artemis software (Demeter package), utilising the first shell of zinc oxide and zinc peroxide, Zn-Zn and Zn-O respectively. Further fitting of the first shell and further analysis of coordination number was performed using Excurve (version 9.3).

6.3.3 Raman spectroscopy experiments

Raman Spectroscopy measurements were performed on a Renishaw inVia Raman Microscope, using a 514.5 nm laser. *In situ* measurements were done in a purpose built Linkam cell, which was water-cooled and had gas valves for flowing air into the sample.

The experiments were designed to provide complimentary information to the EXAFS data. The data was collected in a stepwise process, ramping at 5 ^{o}C in 50 ^{o}C steps to 150 ^{o}C. Then in 10 degree steps from 180 ^{o}C to 220 ^{o}C, and returning to 50 degree steps from 250 ^{o}C to 500 ^{o}C.

6.3.4 Thermogrametric analysis measurements

Thermogravimetric analysis (TGA) with an integrated mass spectrometer (MS) was used to measure the change in mass of the peroxide and monitor the waste gases being produced. The measurements were performed using a 2 ^{o}C/min ramp to 600 ^{o}C with data being measured constantly during the experiment. The MS was connected to the exhaust line to monitor the gases and waste materials coming of the sample.

6.4 Results and Discussion

A combination of techniques were utilised to monitor the thermal decomposition of zinc peroxide into zinc oxide. Whilst the main experiment involved the use of synchrotron radiation for a combined XAS/XRD experiment, complimentary laboratory techniques were also employed to extract more information out of the transformation.

6.5 Thermogravimetric Analysis

Thermogravimetric analysis was used to follow the decomposition of the zinc peroxide and monitor the products being expelled. It was shown that the change in structure from the peroxide to the oxide is accompanied with a dramatic change in the mass from 99% to 86% a change of approximately 13% which is equivalent to the theoretical mass change for the decomposition. By using an integrated mass spectrometer the products produced during the decomposition were analysed, it was shown that the major product was oxygen. Additionally the slight change in mass below 180 ^{o}C is due to the removal of water. Although the sample was dried it is not always possible to remove all the water contained within.

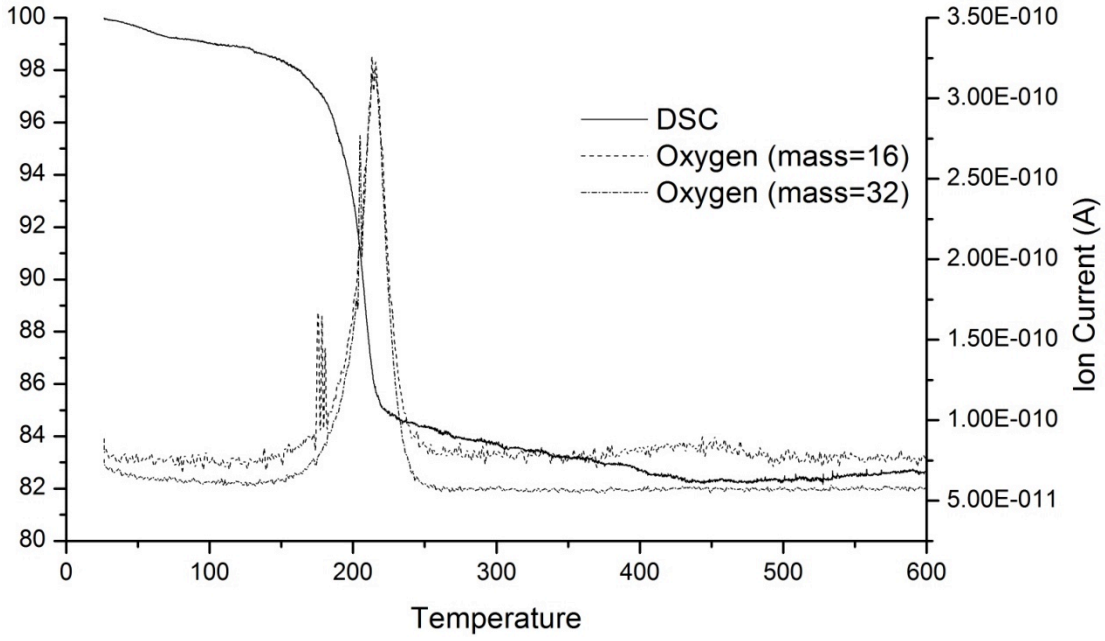

Figure 6-2 - TGA showing the change in mass of the zinc peroxide sample with increasing temperature; also showing are the two oxygen MS paths.

Using differential scanning calorimetry (DSC) it was shown that the change in structure is sharp and exothermic with the whole process being completed by 210 ^{o}C. What this apparently suggests is that the entire transformation can be completed at a much lower temperature. However the effect on particle growth and morphology needs to be investigated.

6.6 XRD Analysis

X-ray diffraction was used to monitor the changes occurring in the long-range structure of the material. As zinc oxide and zinc peroxide have quite distinct structures it is possible to easily distinguish between the two patterns. Figure 6-3 shows the different patterns for both zinc peroxide and zinc oxide, in addition to showing the various corresponding Bragg reflections.

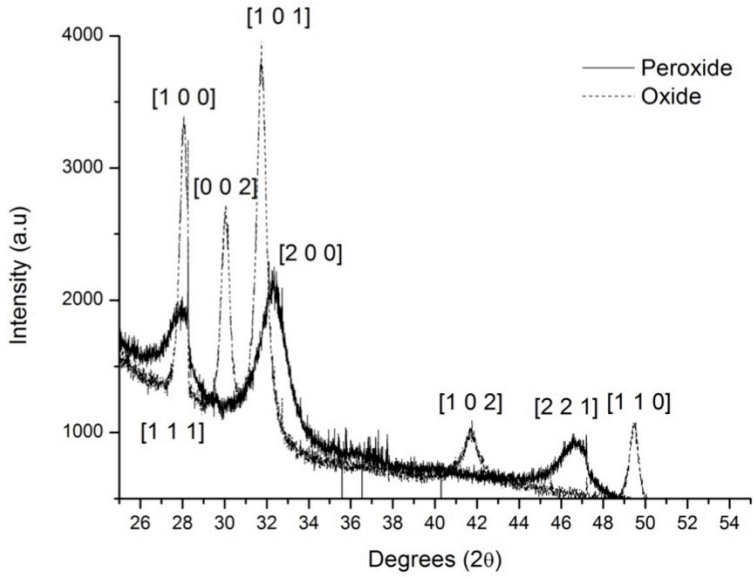

Figure 6-3 - XRD pattern for the first and last scan of the in situ data showing the corresponding Bragg reflections.

In situ X-ray diffraction was collected in combination with the XAS data. The data shows a clear transition from the initial peroxide to zinc oxide upon heating to 500^{o}C (Figure 6-4). The material undergoes transformation in the region from 140^{o}C to 270^{o}C, shown by the decrease in intensity of the peroxide peaks and the emergence of the oxide peaks. Close inspection of the peaks in the phase change region reveals that this area is much harder to analyse in detail than initial viewing suggests. This is due to the overlapping peaks between 27 – 33 degrees 2 θ (the oxide [100], [002] and [101] are in the same general area as the peroxide [111] and [200] peaks). As such there is no true amorphous phase, as is usually expected when a material undergoes a phase change, where no peaks are visible. Instead there

is a region between 190-250 ^{o}C where there are faint oscillations in a broader hump, which could potentially be from either structure.

Looking at higher 2θ it is possible to see more clearly where the amorphous region lies. By taking the [221] peak which has no neighbouring peak in the oxide pattern it is possible to follow the gradual decomposition of the peroxide phase which appears to occur at 210^{o}C.

Following the intensity of the peroxide [2 2 1] and the oxide [1 0 2] reflections in comparison to the whiteline intensity from XANES reveals some interesting information (Figure 6-5). The decrease in intensity of the peroxide [221] reflection closely matches the change in the whiteline intensity. The corresponding oxide [110] reflection slowly increases in intensity from 200^{o}C up to 500^{o}C. However there is a significant region with low peak intensity, which would indicate and support a slow growth of the zinc oxide structure, as opposed to a rapid rearrangement of the structure.

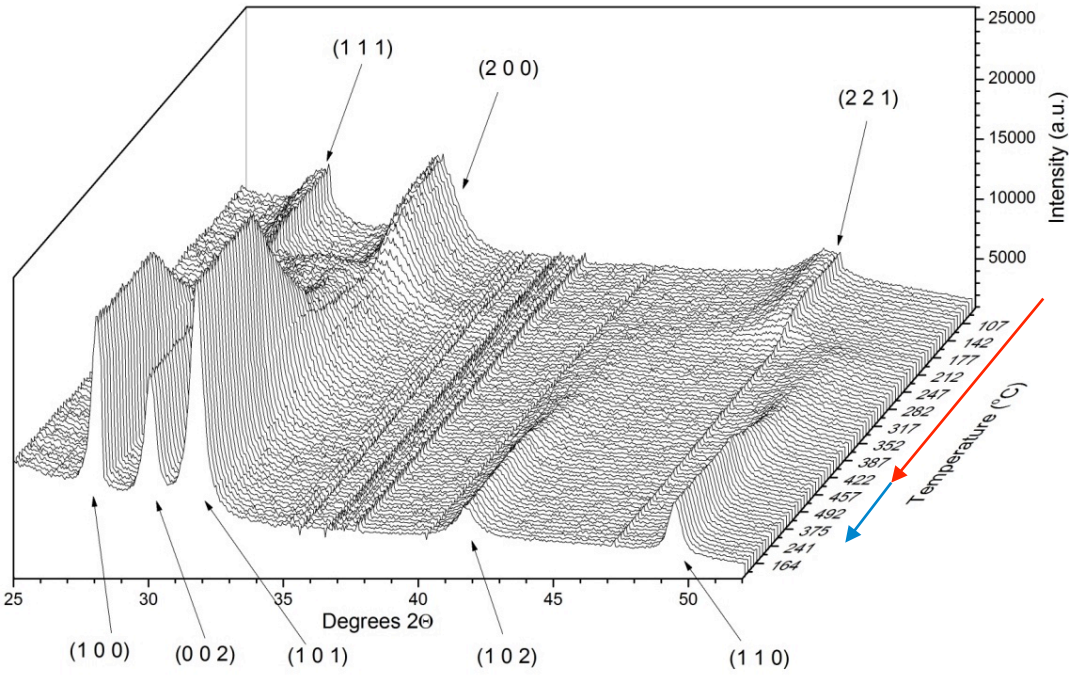

Figure 6-4 - Plot of diffraction patterns against temperature obtained in situ at B-18 at diamond light source. Arrows indicating direction of heating (red) and cooling (blue).

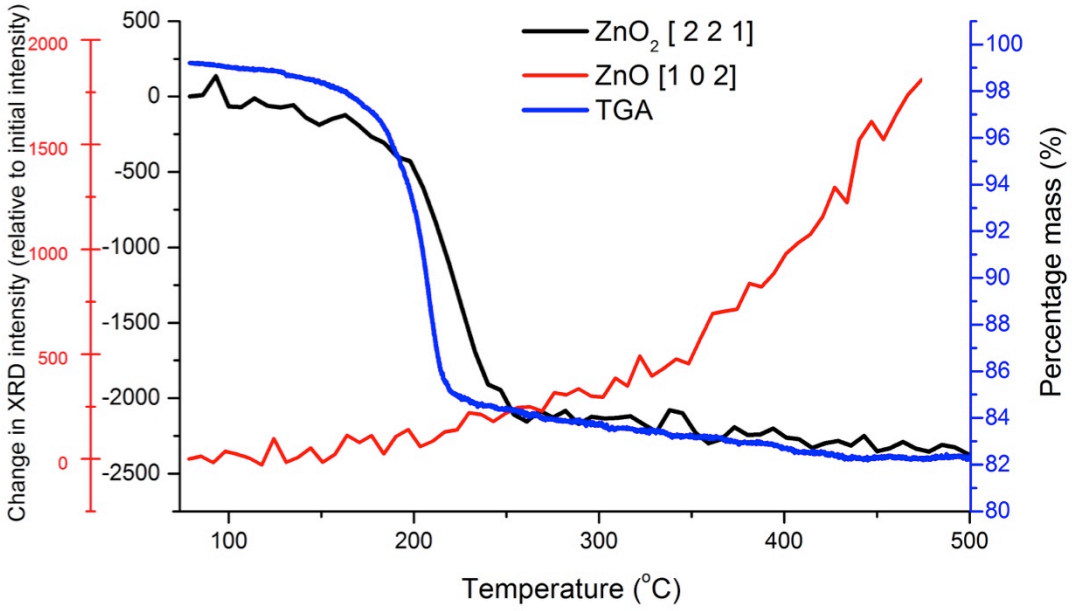

Figure 6-5 - Comparison of the whiteline intensity with the change in intensity of the ZnO [1 0 2] and ZnO_2 [2 2 1] peaks from XRD.

6.7 XANES analysis

X-ray absorption near edge spectroscopy (XANES) can be used to follow changes in the structure and oxidation state of materials through the variations in the whiteline intensity and the edge position respectively. As such the transformation from zinc peroxide to zinc oxide can be followed using XANES. The differences between the initial and final structures of the material can be clearly seen by plotting the normalised absorbance (Figure 6-6). As zinc is a group 12 element it has a filled d-orbital and hence no pre-edge peak arising from disallowed s→d transitions is apparent with either the zinc peroxide or zinc oxide. As such the XANES analysis will focus on variations in the whiteline intensity and the edge positions of the sample with increasing temperature. The shoulder feature present on the edge of the spectra ZnO, is caused by the nature of the transitions. The Zn K-edge is caused by transitions from s to p orbitals, any change in the edge features can therefore be related to a variation in one of these orbitals, it has also been noted that changes in the absorption edge are particularly sensitive to changes in the coordination number.[25,26] The change in coordination from octahedral to tetrahedral, leads to a disruption in the symmetry of the molecule, such that mixing of p and d orbitals becomes allowed; the Laporte rule no longer applying.[25] It is this increase in orbital mixing that leads to the shoulder feature observed in for the ZnO spectra.

The white line intensity, which is related to the density of free states available, is shown to decrease between 155 °C to 180 °C, from 1.75 to 1.46 (Figure 6-7). This decrease correlates well with a change from 6-coordination in the local structure about the zinc centre in the

peroxide to 4-coordinate in the oxide. This is linked to the change in the number of free states available for the excited photon. The whiteline is related to the number of available free states that an electron can move into.[26] For the 6-coordinate peroxide there are more available energy levels on the neighbouring oxygens than for the 4-coordinate oxide; hence a decrease of the whiteline intensity is observed. [26]

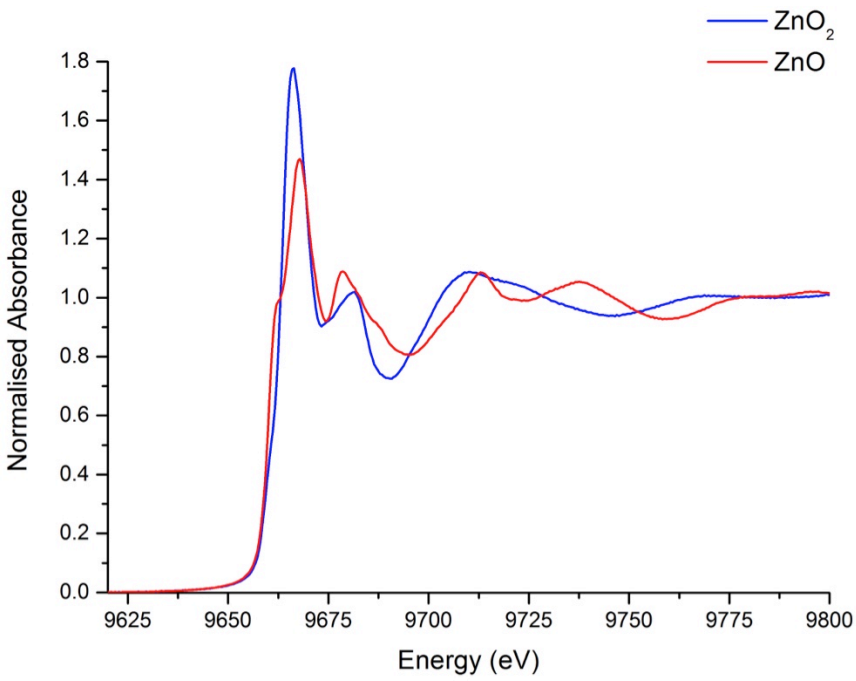

Figure 6-6 - Normalised absorbance plot of initial (peroxide) and final (oxide) scans highlighting the changes in the whiteline region and EXAFS oscillations.

Plotting the XANES spectra against temperature makes the change in the local coordination more apparent (Figure 6-7). At 142°C the magnitude of the whiteline intensity begins to decrease steadily from 1.74 till reaching the lower value of 1.47 at 190°C. After reaching 500°C the value of the whiteline intensity does not change as dramatically, only lowering to 1.46; a change of 0.1. Upon cooling down to room temperature at the end of the reaction the value raises slightly to 1.5.

What is of more interest is the sharpness of the oscillations; they are much sharper and more clearly defined after the edge at 500°C then at the phase change region (Figure 6-8). Upon cooling to room temperature the oscillations become even sharper. This can be interpreted as an indication of the increasing size and definition of the zinc oxide particles.

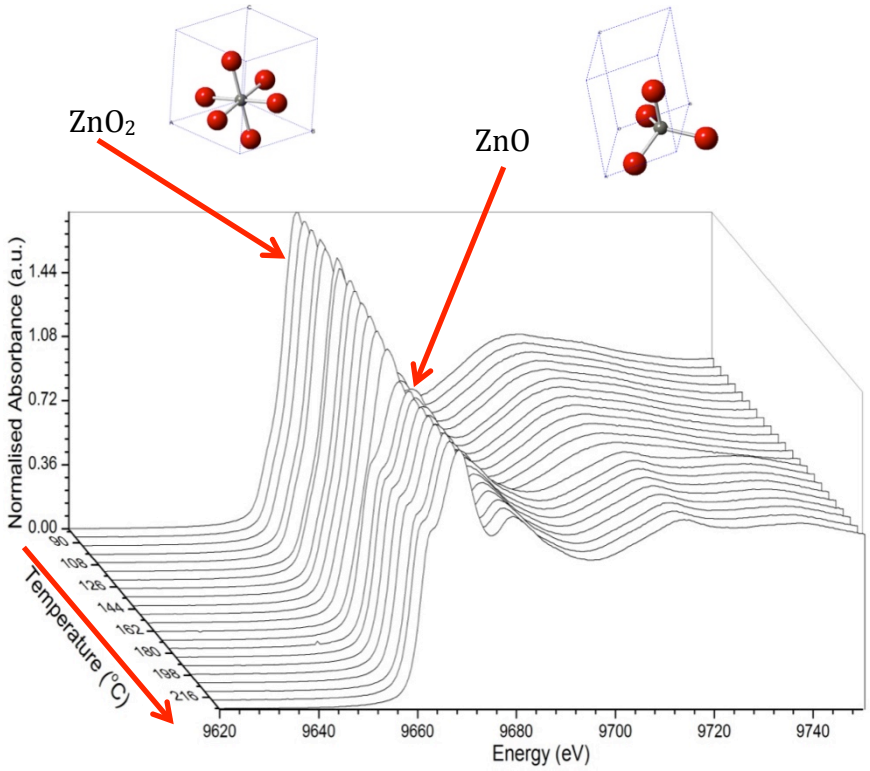

Figure 6-7 - Plot of the change in the XANES with temperature for the temperature ramp.

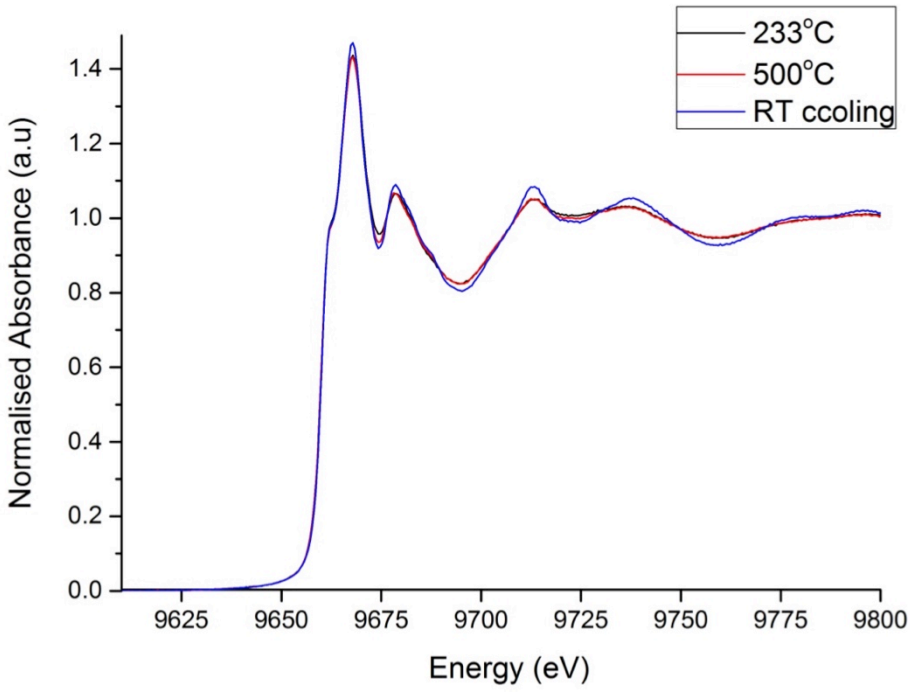

Figure 6-8 - Comparison of material at the end of the phase change region (233 °C), at the end of the heating process (500 °C) and after cooling down to room temperature at the end of the experiment.

Linear combination fitting (LCF) was used to get an approximation of the change in the local structure with respect to temperature from the XANES data (Figure 6-9). Zinc oxide and zinc peroxide scans were used as standards for this analysis, fitted in the region of -20 to +30 eV about the e0 position of the data.

The LCF revealed that the material undergoes a rapid transformation in the region 180-250^{o}C. At higher temperatures, and after cooling, the material remains as ZnO with no further reduction or reoxidation back to the peroxide. This information is of interest as from XRD there is no indication of the change in the local structure. There is just a region between 190-230^{o}C with no clearly defined peaks for the oxide or peroxide. Following this there is then a gradual increase in the oxide peak heights and sharpness. This change is believed to be an indication of what is occurring with the peak sharpness; as the particles grow in size and crystallinity, the definition of the ZnO peaks increases.

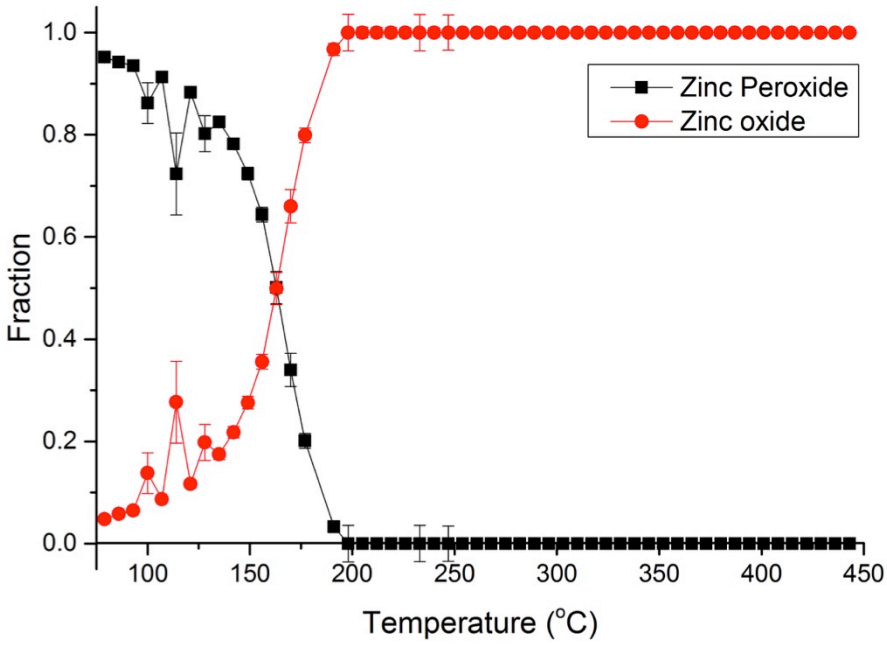

Figure 6-9 - Phase composition from linear combination fit of experimental data with Zinc peroxide and Zinc Oxide standards data obtained through Athena software.

6.8 EXAFS analysis

Initial data processing was done using Athena software, before the normalised data was fitted using Artemis. First the initial scan was fitted to zinc peroxide standard in order to obtain parameter values for the various shells and the amplitude term. Following on from that and to verify the integrity of the model, the rest of the experimental data was fitted using these refined parameters. These parameters were subsequently used as a starting point in the fitting model.

The various shells discussed in the following sections are outlined here for clarity. For zinc peroxide the first three shells utilised are the Zn-O shell at 2.1 Å (Figure 6-10), the Zn-O second shell at 2.92 (Figure 6-11) and the Zn-Zn third shell at 3.44 Å (Figure 6-12). Further details are available in Table 6-1.

For zinc oxide the three shells used are the Zn-O first shell at 1.98Å (Figure 6-13), the Zn-Zn second shell at 3.2 Å (Figure 6-14), and the Zn-Zn third shell at 3.25 Å (Figure 6-15); all are combined into a single shell for the these fits. Further details are available in Table 6-2.

Table 6-1 - Scattering paths and details for Zinc Peroxide.

Shell	Scatterer	Bond distance	Coordination number
1	O	2.10	6
2	O	2.92	6
3	Zn	3.44	12

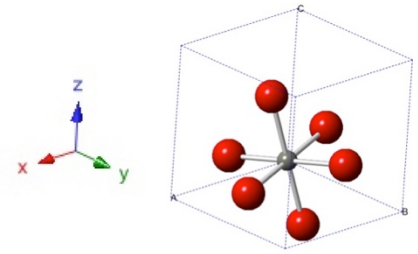

Figure 6-10 - Zinc peroxide 1st shell.

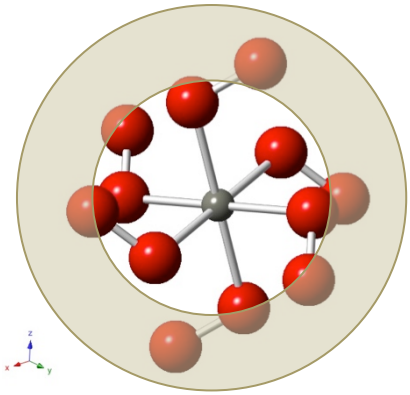

Figure 6-11 - Zinc peroxide 1st shell and 2nd shell, with the 2nd shell highlighted.

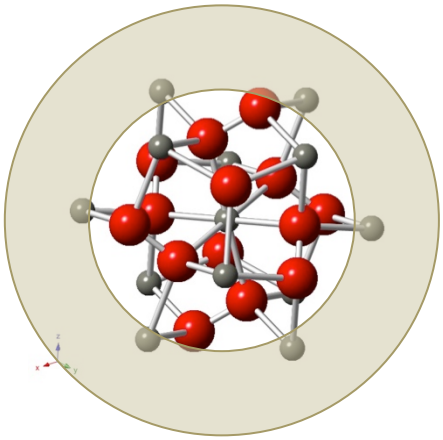

Figure 6-12 - Zinc peroxide 1st shell, 2nd shell and 3rd shell, with the 3rd highlighted.

Table 6-2 - Scattering paths and details for zinc oxide.

Shell	Scatterer	Bond distance	Coordination number
1	O	1.98	4
2	Zn	3.21	6
3	Zn	3.25	6

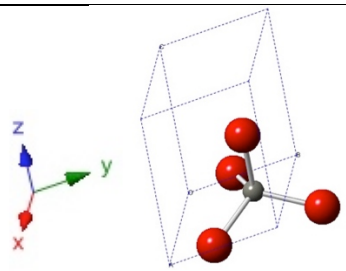

Figure 6-13 - Zinc oxide 1st shell.

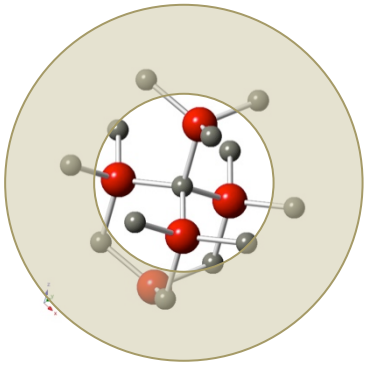

Figure 6-14 - Zinc oxide 1st shell and 2nd shell, with the 2nd highlighted.

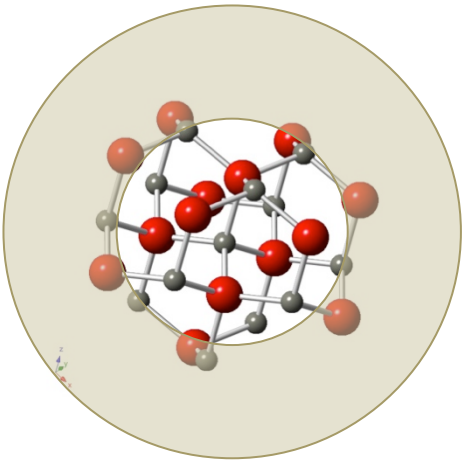

Figure 6-15 - Zinc oxide 1st shell, 2nd shell and 3rd shell, with the 3rd shell highlighted.

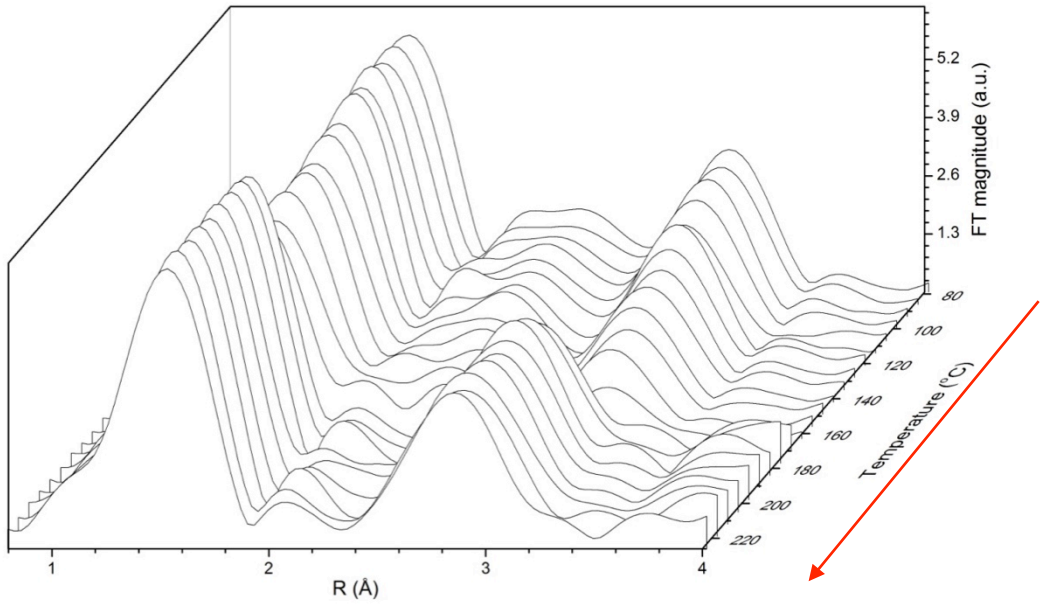

Figure 6-16 - Fourier transform of experimental data against temperature.

Plotting the Fourier transformed data against temperature reveals that material gradually loses its peroxide character below 160 ^{o}C as shown from the gradual decrease in intensity of the Zn-Zn at 3.44 Å from 3.8 to 1.1, disappearing entirely around 170 ^{o}C. Following this point there is a sharp change to the oxide Zn-O second shell at 3.2 Å. The magnitude of this oscillation does not vary much with increasing temperature, instead remaining more or less consistent around 2.5. The second shell Zn-O resulting from the peroxo species gets gradually smaller with increasing temperature, before disappearing entirely after 190 ^{o}C. These changes in the features indicate that while there is a gradual change in the coordination number of the higher shells with increasing temperature, the change in local structure is actually a rapid process.

6.8.1 Decomposition of Zinc Peroxide

Data was fitted with using the first shell paths for zinc peroxide and zinc oxide, and the fit is agreeable within the 1-3 Å range of interest (Figure 6-17). After the phase change region the quality of the fit decreases slightly, there are doublets in k-space that the fitting model doe not take into account (Figure 6-18). However given the quality of the FT fit, it is possible that these features are due to higher shells or interactions that are not necessary for the level of fit being conducted.

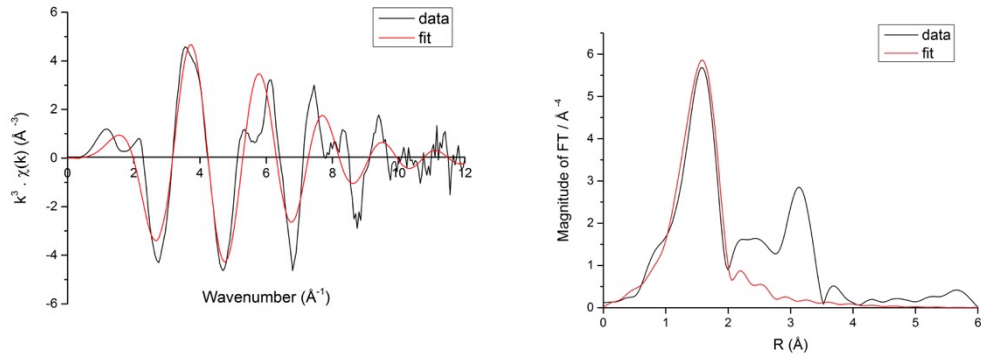

Figure 6-17 - Plots showing the k^3-weighted data (left) and the Fourier transform (right) for the ZnO first shell at the beginning of the calcination.

.

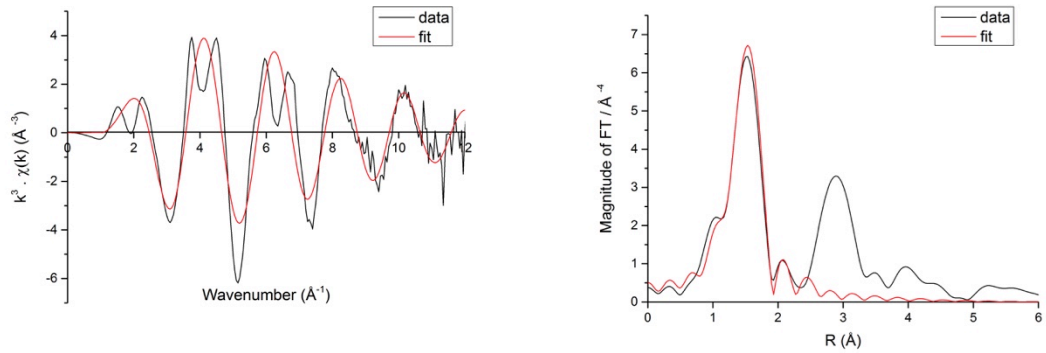

Figure 6-18 - Plots showing the k^3-weighted data (left) and the Fourier transform (right) for the ZnO first shell at the end of the phase change region (220°C).

Fitting the data using just the zinc peroxide paths revealed some interesting information with regards to the way the decomposition occurs. The Zn-Zn bond distance begins at near 3.45 Å, which is consistent with the Zn-Zn distance in zinc peroxide (Figure 6-19). However at 170°C this value decreases rapidly to 3.24Å close to the value of 3.2 Å expected for a Zn-Zn distance in zinc oxide. This value is then maintained during subsequent scans. The Zn-O bond distance decreases less sharply from the 2.05 Å expected from Zn-O in the peroxide to 1.97 Å close to the expected value for Zn-O in the oxide. The change in the bond distance occurs over the temperature range 130 °C to 190 °C, whilst the change in the Zn-Zn bond distance occurs over a narrower 20 °C region between 160-180 °C. This indicates that the structural changes occurring are beginning with the oxygen shells, which is to be expected as the decomposition involves the liberation of oxygen from the structure.

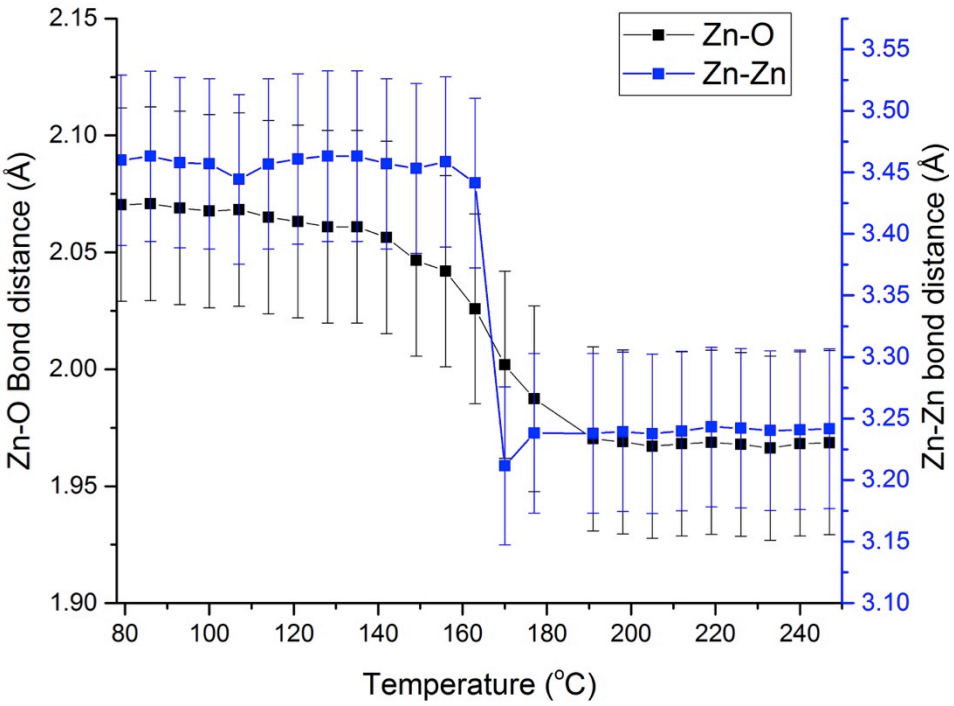

Figure 6-19 - Plot of the change in bond distance with temperature for the zinc peroxide Zn-O first shell and the Zn-Zn shell (2nd shell for the metal or 3rd for the oxide).

The coordination numbers for the first 3 shells were also fitted using Artemis. The results for the fitting model show a steady value of 6 for the coordination of the first shell Zn-O. This decreases rapidly above 160 °C, stabilising at ca 4 by 190 °C. The coordination number for the second shell Zn-O which is the peroxo species also decreases dramatically in the phase change region from 6 to 1 by 200 °C. This value is far below that acceptable for the shell to be in existence. The Zn-Zn shell decreases steadily on increasing temperature, reaching its lowest value of 2 at 170 °C. After this the coordination number of the Zn-Zn shell increases rapidly over the next 40 °C to return to the literature value of 12. The coordination number for this shell is the same in both zinc oxide and zinc peroxide. What can be interpreted from these results is that the zinc peroxide particles decrease in size, as demonstrated form the decreasing coordination numbers and the decreasing peak intensities in the XRD data. Overall the data shows that that the first shell undergoes a rearrangement to 4-coorination, similar to what is seen in XRD and XANES; this is accompanied by the loss of the second shell of oxygen and the gradual reduction in the Zn-Zn coordination number.

The disorder of the higher shells was fixed and made constant; the value for the first shell was allowed to vary in the fits. This value increased with increasing temperature reaching a maximum around 160 °C in the phase change region, and then dropping sharply to a value of

around ca 0.006. This indicates the change from the more stable oxide structure from the initial peroxide material.

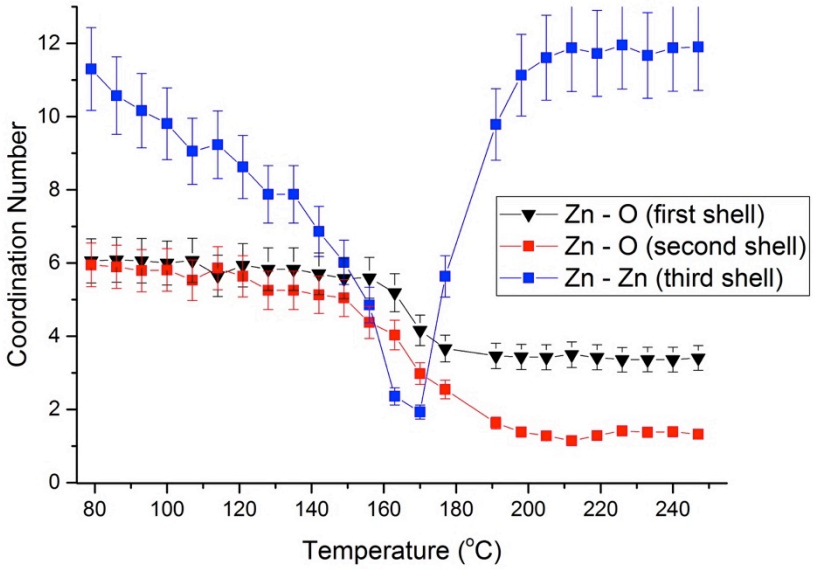

Figure 6-20 - Plot of coordination number against temperature for zinc peroxide paths.

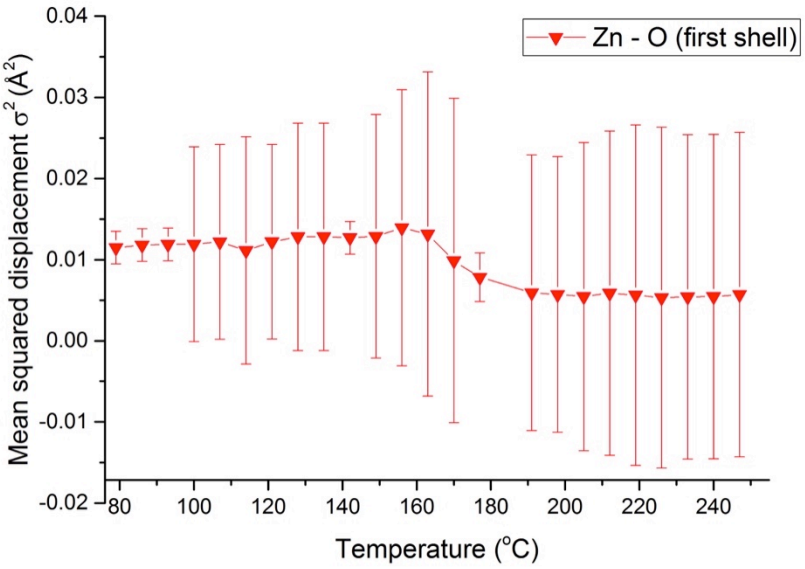

Figure 6-21 - Disorder against temperature for the zinc peroxide first shell path.

6.8.2 Comparison of Excurve and Artemis Fitting Models

In order to validate the values obtained from Artemis fitting, the data for the first shell was compared with fits from Excurve software. As Excurve is not dependant on the crystal structure, it has a much more flexible structural model; any changes in the structure should easily be able to be interpreted. The fitting model was set up using the first shell of zinc peroxide and the Zn-Zn second shell from the peroxide. As the structural model is not fixed the changes in the bond distance and coordination number would be related to a change in the morphology of the material. An example of the fit quality is given in Figure 6-22, this shows the material at the beginning of the decomposition whilst it is still predominately ZnO_2. The quality of the fit is maintained through out the decomposition, even when the material changes phase from the peroxide to the oxide the integrity of the fit is still good (Figure 6-23).

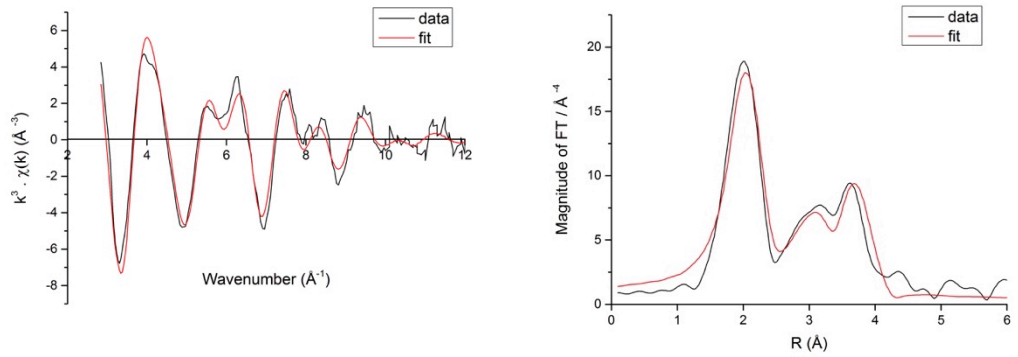

Figure 6-22 - Plots showing the k^3-weighted data (left) and the Fourier transform (right) for the ZnO first shell at the beginning of the calcination fitted with Excurve software.

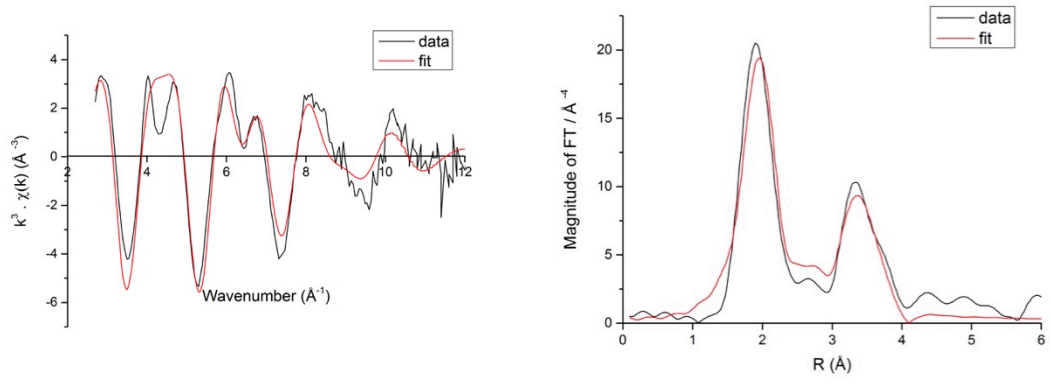

Figure 6-23 - Plots showing the k^3-weighted data (left) and the Fourier transform (right) for the ZnO first shell at the end of the phase change region (220°C) fitted with Excurve software.

Comparison of the bond distance from the two different fits revealed that they are consistent within errors (Figure 6-24). This shows that the changes determined from Artemis fitting of the first shell are real, and that the fitting model used to obtain them is valid.

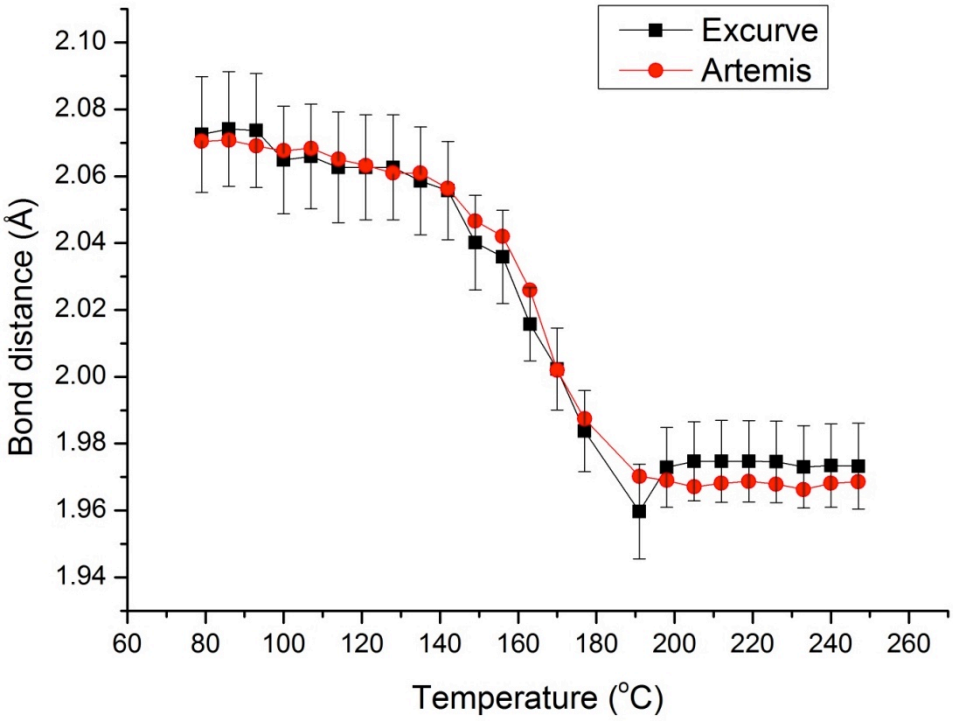

Figure 6-24 - Change in the bond distance of the first shell of zinc peroxide against temperature for both Excurve and Artemis fitted software.

The fitting of coordination numbers is simpler using Excurve due to the flexibility of the theoretical model in comparison to Artemis which uses fixed structures based on crystallographic data (Figure 6-25). Even so the coordination numbers for the first shell fit reasonably well within error below the phase change region. However the values obtained through Excurve fitting are lower than those from Artemis by a value of 1. Once the temperature reaches 150°C the value for the Excurve coordination number drops from 4.5 to 2.5 by 180°C; the corresponding Artemis values for the coordination umber in this region is 3.5. However upon reaching 190°C the value for both fitting models is 3.5, close to the value of 4 expected for the Zn-O shell in zinc oxide. This fitting shows that Excurve may be more sensitive to the subtle changes in the coordination number, when compared to the Artemis fitting model use – although it should be noted that the Excurve model has larger error in the values and that when these are included the Artemis fits are in agreement.

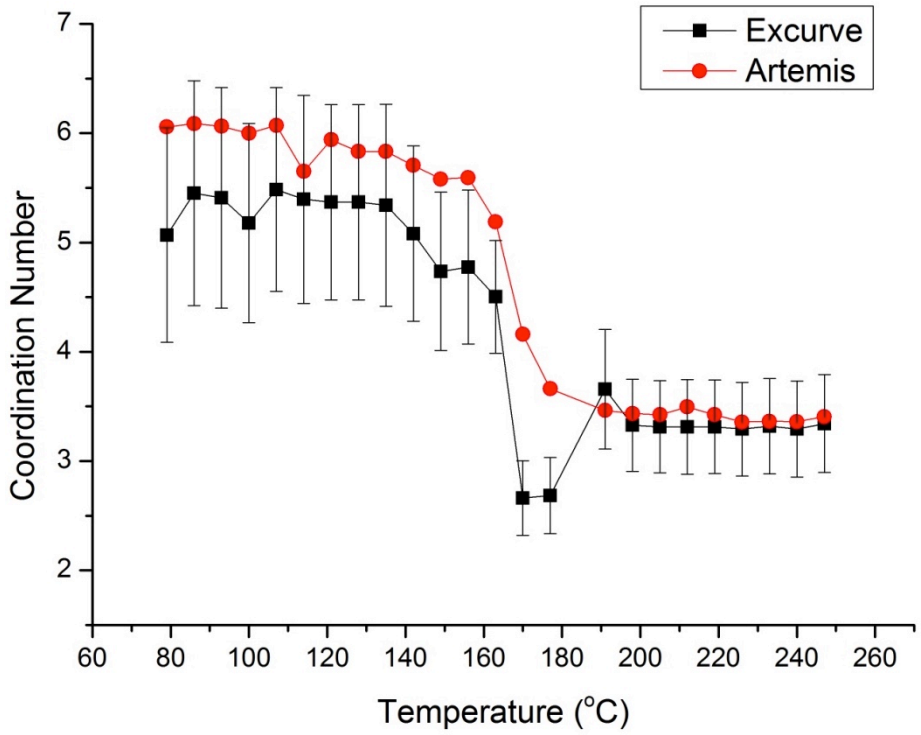

Figure 6-25 - Change in the coordination number of the first shell of zinc peroxide against temperature for both Excurve and Artemis fitted software.

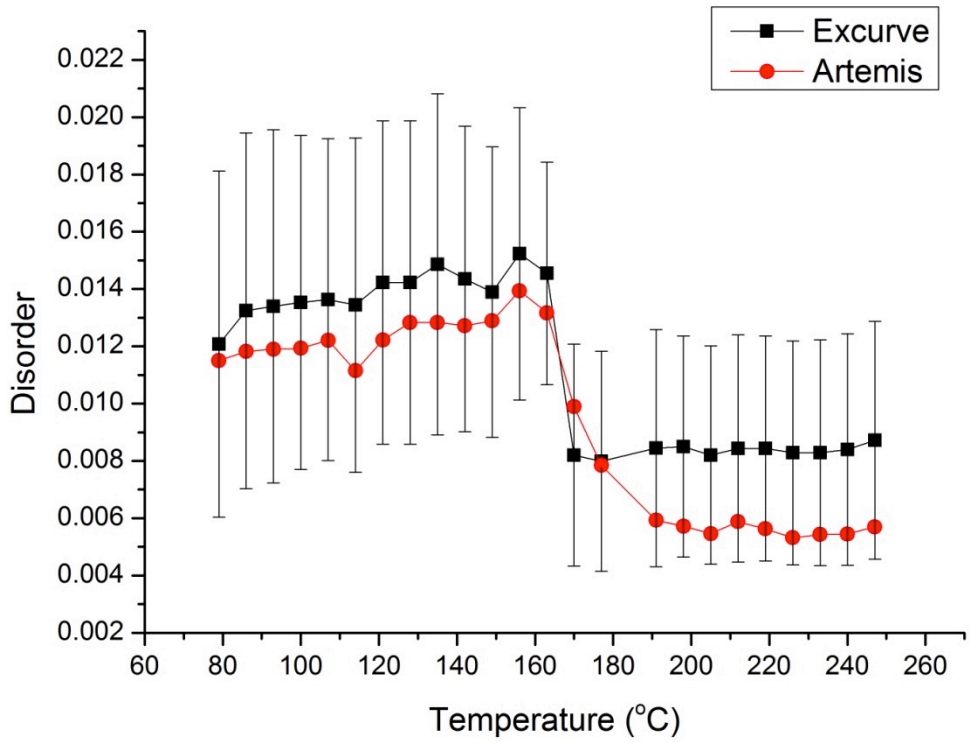

Figure 6-26 - Change in the disorder against temperature of the first shell of zinc peroxide against temperature for both Excurve and Artemis fitted software.

The change in the disorder for both fitting models matches well with in error. The errors for the Excurve fits below 160°C have a larger error; the error decreases with higher temperature and decreases further once the coordination number changes to 4. Essentially both fitting methods show that there is a decrease in the disorder of the system upon transforming from 6-coordinate to 4-coordinate.

6.8.3 First Shell mixing model

Using a two-phase model, consisting of the zinc peroxide and zinc oxide phases, an investigation of the conversion can be undertaken using EXAFS. Fitting was done in Artemis software with the parameters fitted to peroxide standard at room temperature.

The initial coordination number of the zinc peroxide first shell is 5.85, very close to the expected value of 6 for the Zn-O first shell. This value remains quite consistent till about 160 °C where it decreases slightly, before dramatically dropping to a value of 1.95 at 212 °C. This decrease is accompanied by a sharp rise in the coordination number for the zinc oxide first shell, from 0.46 to 3.1. The value for the oxide first shell stabilises at ca 3.8 with increasing temperature matching the expected value of 4 for the first shell.

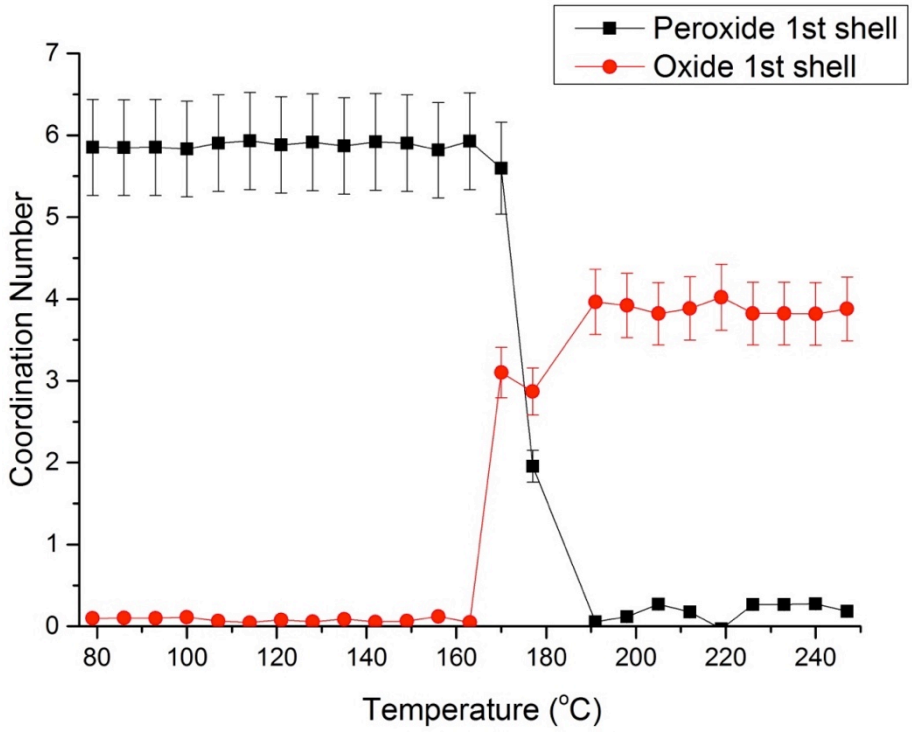

Figure 6-27 - Change in the coordination number of the first shells of zinc peroxide and zinc oxide with temperature.

There is a slight discrepancy between these values and those obtained earlier for the peroxide fitting model. Comparison with the LCF results also indicate that the transition should be slightly more gradual beginning at around 120°C and reaching 50% conversion by 160°C (Figure 6-28). This can be explained due to higher sensitivity of EXAFS fitting to changes in the local structure than LCF which utilises only the XANES and is highly dependent on the quality of the standards. At 190°C both models indicate the material has completely transitioned to the oxide phase.

As previously explained the fitting of coordination numbers is slightly less accurate in Artemis, however with in errors it is close to the expected values for the system. Additionally because this fitting model utilised only the first shell it could potentially introduce a bias towards one phase or another. The discrepancies with regards to the TGA phase change region are believed to be due to the slower temperature ramp, 2 °C per minute for the TGA compared with 5 °C per minute for the XAS measurements. The rate was lowered for the TGA in order to make sure that the phase change was not missed.

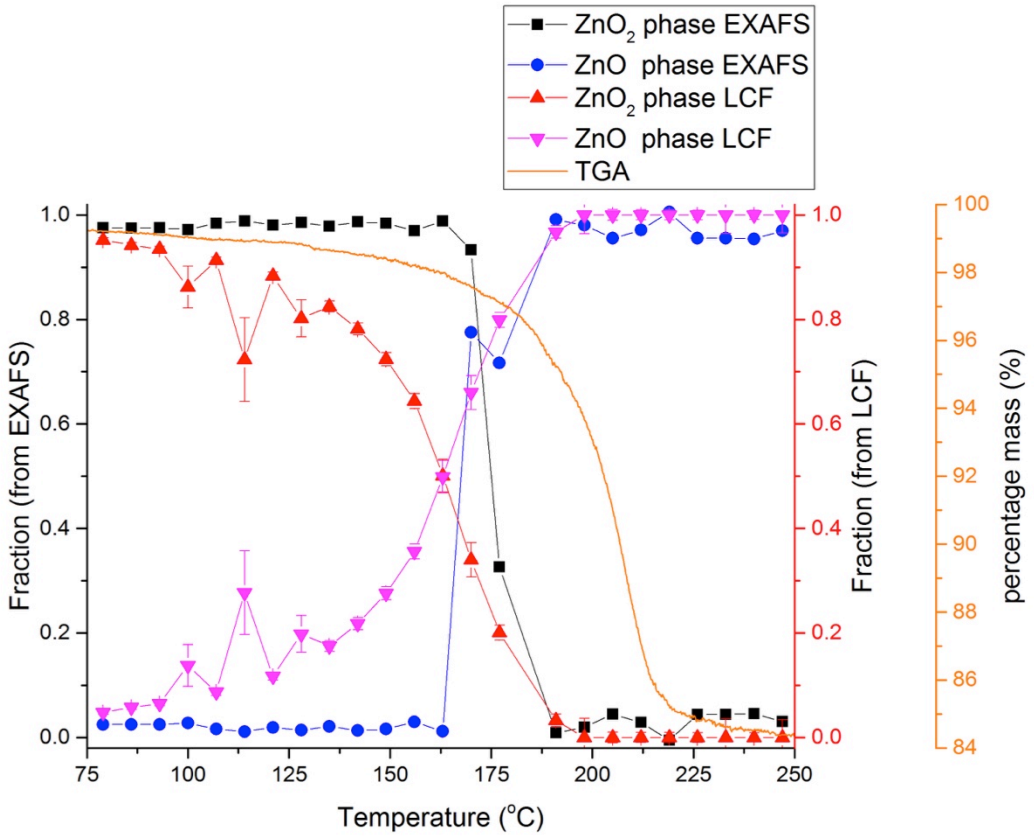

Figure 6-28 - Comparison of first shell mixing model phase fractions with the results from LCF and the change in mass from TGA.

The bond distance of the first shell for zinc peroxide appears to increase at 180°C before decreasing to near zero at 220°C (Figure 6-29). The errors in the bond distance also increase dramatically in the phase change region between 180°C and 220°C. The bond distance for the oxide first shell remains around 1.95 Å, whilst before the phase change region it fluctuates between 1.92 Å and 1.97 Å; it should be noted that in this region the amount of oxide present is 0.3 introducing errors in fitting the low percentage to the model.

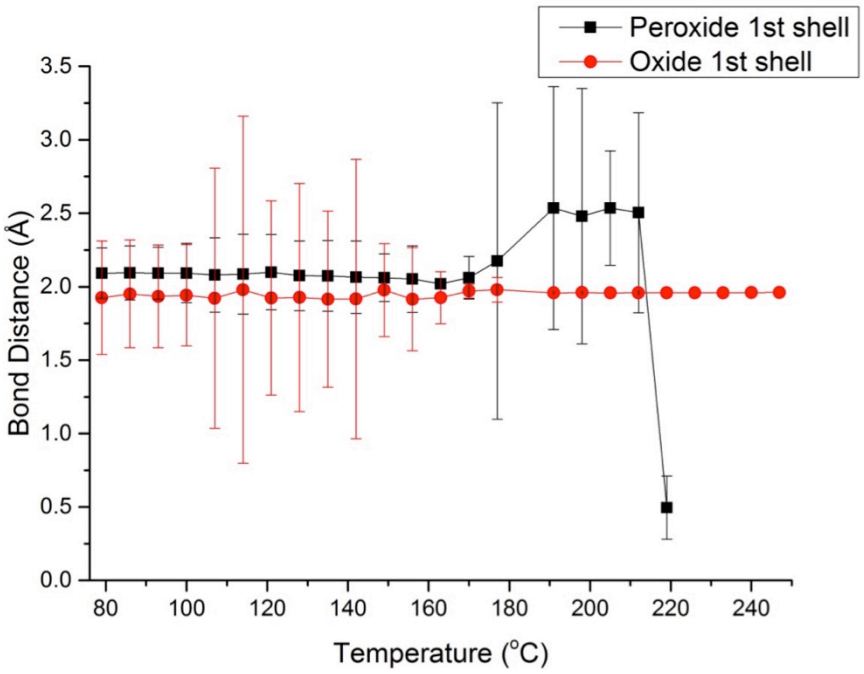

Figure 6-29 - Change in the bond distance of the first shells of zinc peroxide and zinc oxide with temperature.

The disorder for the peroxide shell increases sharply around 160°C when the transition to the oxide phase begins to occur. By comparison the disorder in the oxide first shell is negative below 170 °C indicating that the oxide is not present at this stage of the reaction. Both the coordination number and bond distance results support this, indicating that although the peroxide structure begins to distort by 165°C the oxide is not formed for another 5°C.

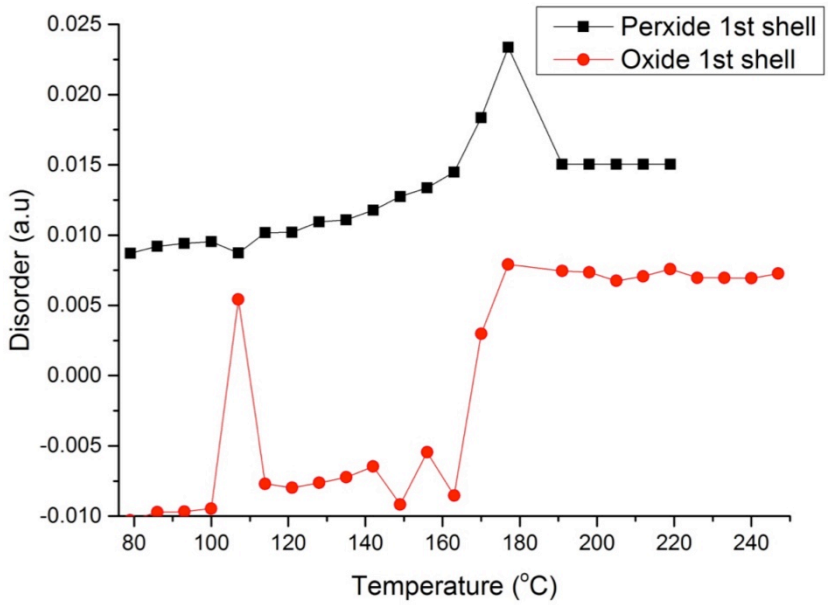

Figure 6-30 - Change in the disorder of the first shells of zinc peroxide and zinc oxide with temperature.

6.8.4 Oxide Growth Model

After 200 °C the material can be fitted as the pure oxide without using the peroxide shells. This fitting model explores the growth occurring as the material is heated to 500 °C and cooled back to room temperature. Examples of the fits are shown in Figure 6-31, the material has clearly converted to the zinc oxide as evidenced by the second shell peak at 3.24 Å. This peak increases in magnitude during the decomposition, which corresponds to an increase in the coordination number for the shell (Figure 6-32).

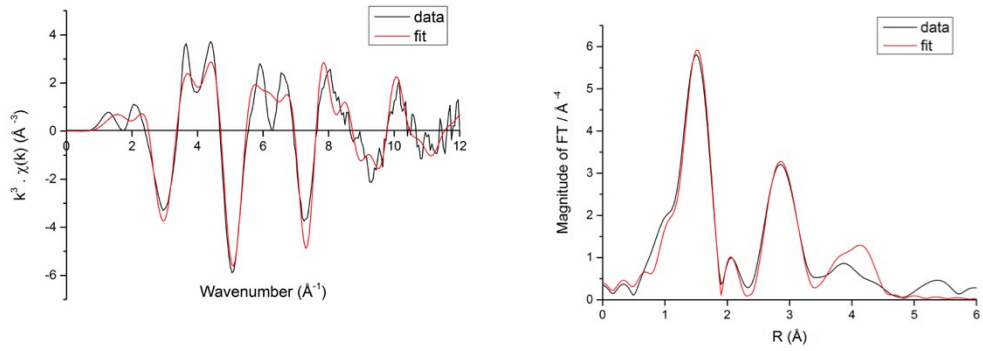

Figure 6-31 - Plots showing the k^3-weighted data (left) and the Fourier transform (right) for the ZnO oxide growth model at 350 °C.

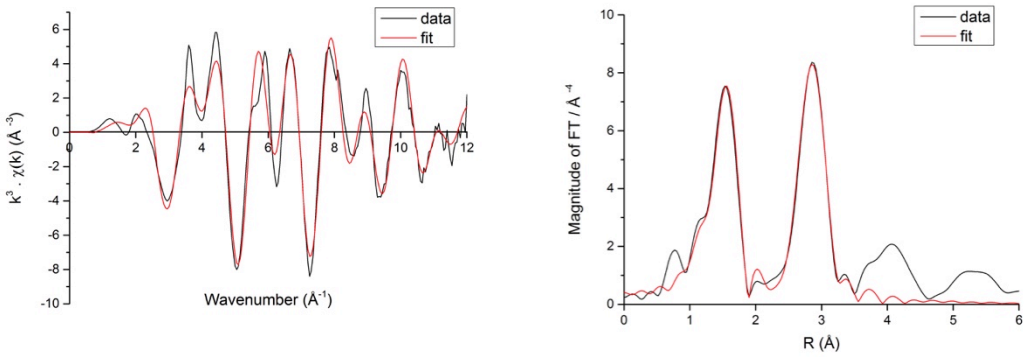

Figure 6-32 - Plots showing the k^3-weighted data (left) and the Fourier transform (right) for the ZnO oxide growth model at the end of the decomposition.

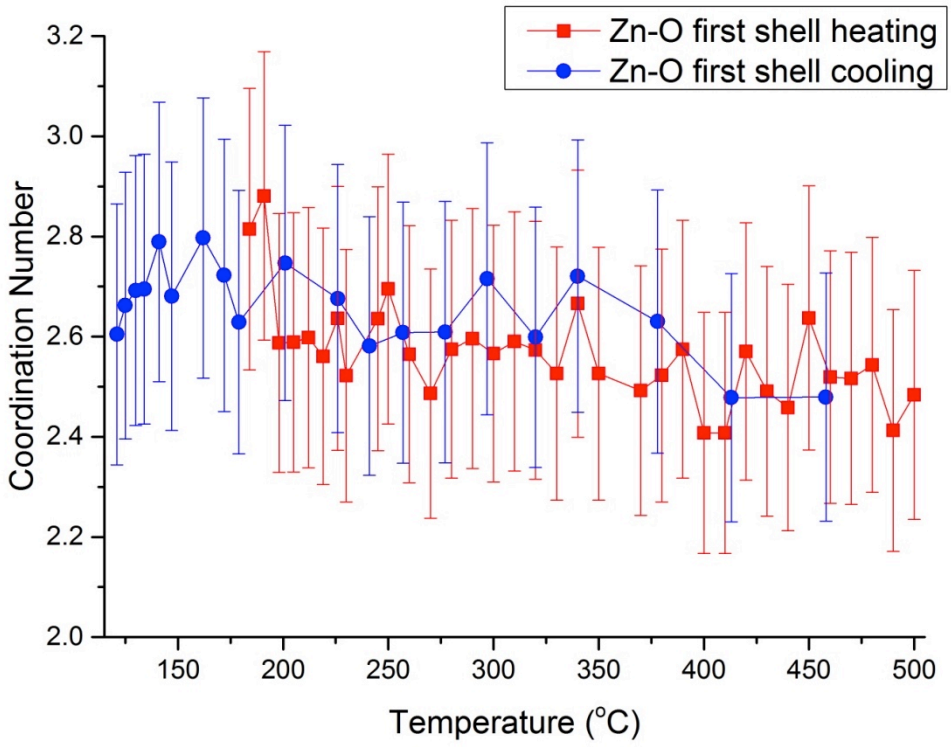

Figure 6-33 - Change in the coordination number of the first Zn-O shell upon heating and cooling.

The coordination number for the first shell varies upon heating, ranging from 2.85 to 1.98 at 500 °C. This is in contrast to the previous results, partly due to the increased accuracy of using higher shells in the fitting model and due to the temperature effects. When taken between errors the values for the coordination number are more consistent. Upon cooling there is moderate increase in the value of the first shell coordination number stabilising around 2.6. This indicates that although a zinc oxide structure is formed from the peroxide decomposition it is by no means a perfect structure. There appear to be vacancies or gaps in

the structure potential formed by the removal of oxygen during the decomposition. Upon cooling some of these vacancies seem to be filled resulting in the increase in the coordination number of the first shell.

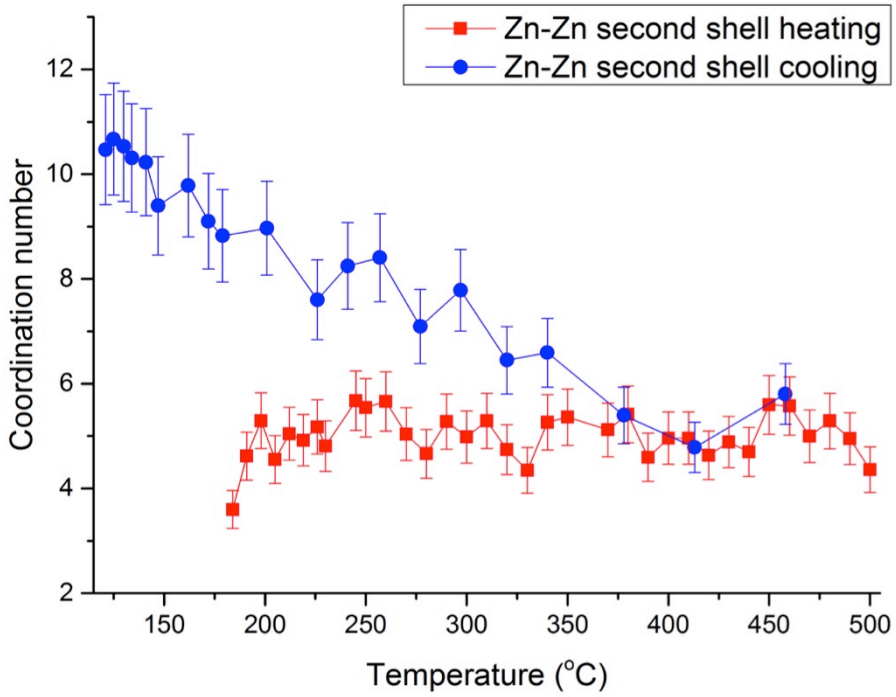

Figure 6-34 - Change in the coordination number of the second shell Zn-Zn upon heating and cooling.

The value for the second shell rises slowly with increasing temperature from 3.5 to ca 5.1 and remains at near this value upon heating to 500 ^{o}C (Figure 6-34). On cooling there is a dramatic rise in the coordination number from 5 to 8 by 240 ^{o}C finishing at a 10.5, which is close to the expected value of 12 for the oxide second shell. These results indicate that a slow growth of the clusters occurs upon heating backed up by the comparison in the change of XRD intensities for the oxide shell.

The bond distance for the first shell deviates very little for from the literature value of 1.98 Å. The exception to this occurs on cooling, with the calculated value increasing to 2.00 Å. With in error it is still close to the literature value, and this discrepancy is put down to the lowered coordination number resulting in a distortion of the bond distance.

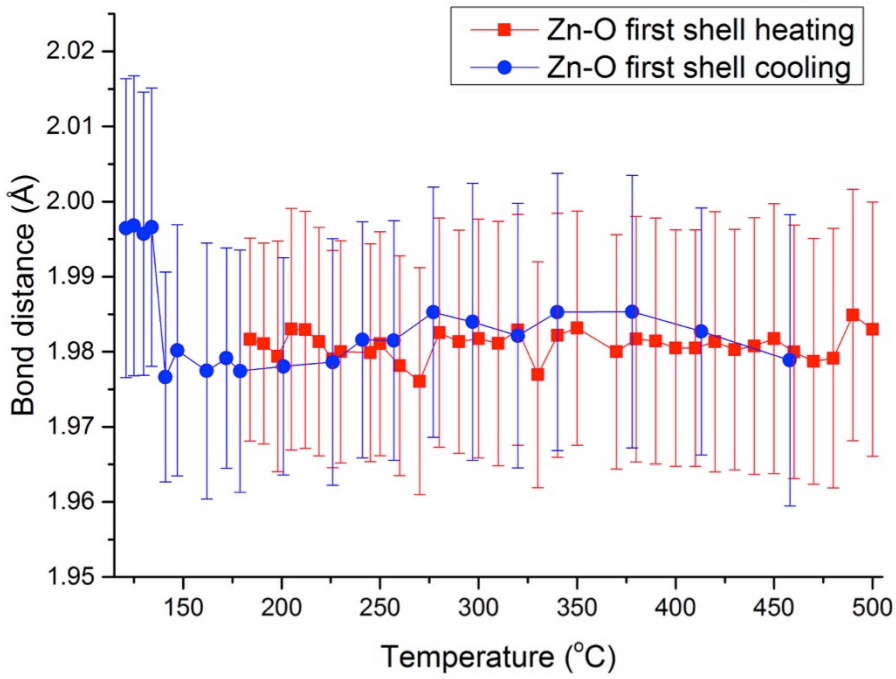

Figure 6-35 - Change in the bond distance of the first shell Zn-O bond upon heating and cooling.

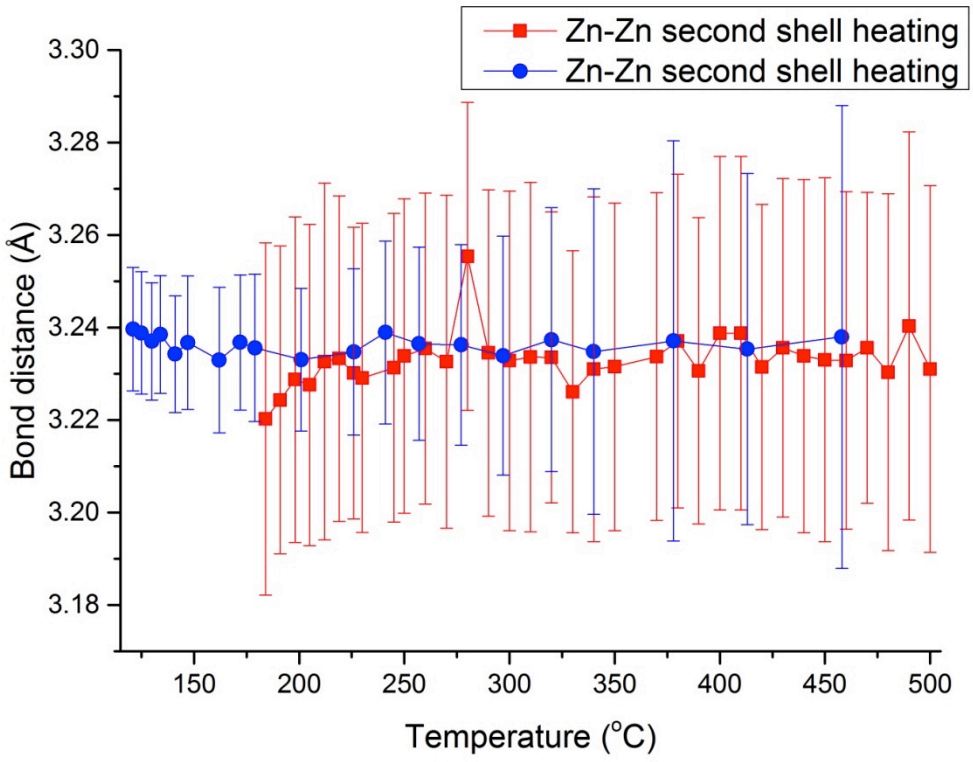

Figure 6-36 - Change in the bond distance of the second shell Zn-Zn bond upon heating and cooling.

The bond distance for the second shell grows slowly from 3.22 to 3.23 after an increase in temperature of 20^{o}C and remains around this value for the duration of the temperature ramp. The error in the bond distance increases with increasing temperature as the system becomes slightly distorted. Upon cooling, the value for the bond distance increases in value from 3.23 to 3.24, with the error reducing dramatically below 250^{o}C. This change is most likely related to the effects of increased temperature on the bonds. These variations in the bond distance are all valid within the calculated errors.

6.9 Raman Spectroscopy

Raman spectroscopy was also used in order to confirm the findings from the XAS analysis, as it is also a local structural tool. An *in situ* Raman set up was used with a stepwise ramping process with a 50 ^{o}C step size, this was lowered in the main area of interest between 180 and 250 ^{o}C to 10 ^{o}C steps (Figure 6-37). It was found that the initial peroxide O-O stretching bond of O^{2+} increased steadily before reducing sharply at 150 ^{o}C and disappearing by 180 ^{o}C. This confirms that the transformation from 6-coordinate to 4-coordinate on the local scale is completed in the region from 180-200 ^{o}C as demonstrated by the XAS results. Following this there is a steady increase in the intensity of the oxide spectra accompanied by a reduction in the remaining peroxide peaks. By monitoring the peaks which do not overlap such as the O-O stretching band in the peroxide and the Zn^{2} -O^{2-} band it is much easier to follow the transformation for comparison.[27]

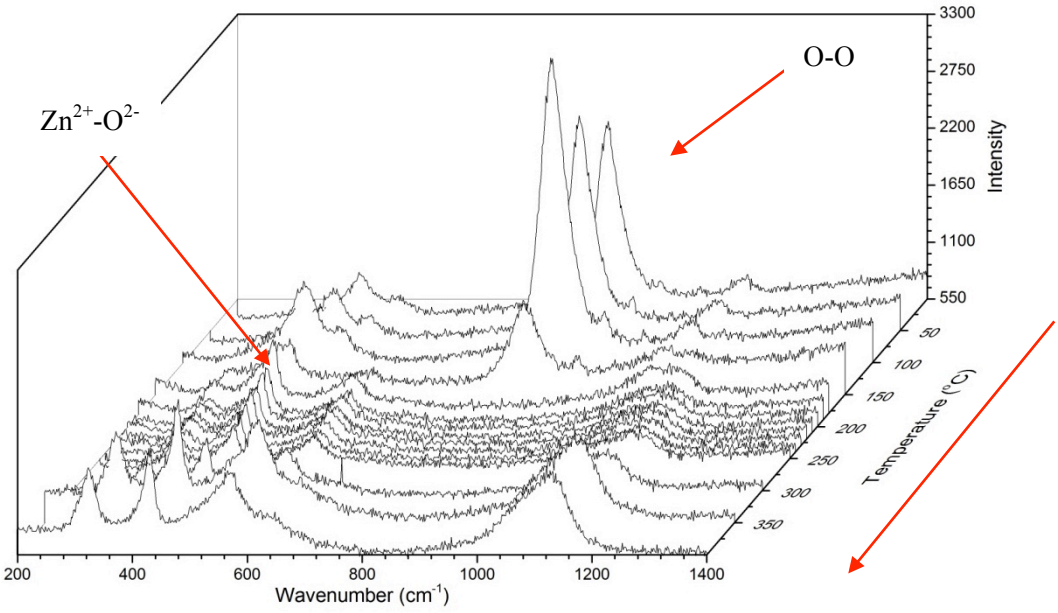

Figure 6-37 - Raman spectra obtained in situ with increasing temperature in a step ramp process, with the peroxide O-O and oxide Zn^{2+}-O^{2-} bands highlighted.

6.10 Conclusion

We have successfully monitored to thermal decomposition of Zinc peroxide into Zinc oxide. Through the combined XAS/XRD measurements we can see that there is an initial structural deformation across the long-range structure, accompanied by a local change from 6-coordinated to 4-coordinated. This is followed by a gradual growth of the zinc oxide clusters. Comparison with other techniques such as TGA and Raman spectroscopy has helped to confirm these results.

Initially there is gradual reduction in the size of the zinc peroxide clusters; this can be observed through the reduction in the intensity of the reflections in XRD. Following this there is rapid rearrangement of the local structure from 6-coordinate to 4-coordinate, followed by a slow growth of the oxide clusters.

The combination of *in-situ* XRD and EXAFS reveals more information than using techniques individually. The insights gained into the decomposition of the zinc peroxide and the growth of zinc oxide can be used to tailor the synthesis and improve particle-size control in future synthesis.

6.11 References

(1) Hussain, B.; Akhtar Raja, M. Y.; Lu, N.; Ferguson, I. *2013 High Capacit. Opt. Networks Emerging/Enabling Technol.* **2013**, 88–93.

(2) Frederickson, C. J.; Koh, J.-Y.; Bush, A. I. *Nat. Rev. Neurosci.* **2005**, *6*, 449–462.

(3) Heideman, G.; Datta, R. N.; Noordermeer, J. W. M.; Baarle, B. Van. *J. Appl. Polym. Sci.* **2005**, *95*, 1388–1404.

(4) Lehr, D.; Luka, M.; Wagner, M. R.; Bu, M.; Ho, A.; Polarz, S. *Chem. Mater.* **2012**, *24*, 1771–1778.

(5) Deyá, C.; Romagnoli, R.; del Amo, B. *J. Coatings Technol. Res.* **2007**, *4*, 167–175.

(6) Viswanathan, R.; Gupta, R. B. *J. Supercrit. Fluids* **2003**, *27*, 187–193.

(7) Erten-Ela, S.; Cogal, S.; Turkmen, G.; Icli, S. *Curr. Appl. Phys.* **2010**, *10*, 187–192.

(8) Sharma, G.; Mishra, M. C.; Dhaka, M. S.; Kothari, R. K.; Joshi, K. B.; Sharma, B. K. *J. Electron. Mater.* **2013**, *42*, 3429–3437.

(9) Chem, A.; Moiler, J.; Weil, S. *Fresenius J. Anal. Chem.* **1994**, *349*, 380–384.

(10) Choina, J.; Bagabas, a.; Fischer, C.; Flechsig, G.-U.; Kosslick, H.; Alshammari, a.; Schulz, a. *Catal. Today* **2015**, *241*, 47–54.

(11) Espitia, P. J. P.; Soares, N. D. F. F.; Coimbra, J. S. D. R.; de Andrade, N. J.; Cruz, R. S.; Medeiros, E. A. A. *Food Bioprocess Technol.* **2012**, *5*, 1447–1464.

(12) Rasmussen, J. W.; Martinez, E.; Louka, P.; Wingett, D. G. *Expert Opin. Drug Deliv.* **2010**, *7*, 1063–1077.

(13) Perl, A. S. *Am. Ceram. Soc. Bull.* **1993**, *72*, 122–123.

(14) Mahmud, S.; Johar Abdullah, M.; Putrus, G.; Chong, J.; Karim Mohamad, a. *Synth. React. Inorganic, Met. Nano-Metal Chem. (formerly Synth. React. Inorg. Met. Chem.* **2006**, *36*, 155–159.

(15) Oliveira, A. P. A. *Chem. Mater.* **2003**, *15*, 3202–3207.

(16) Uekawa, N.; Mochizuki, N.; Kajiwara, J.; Mori, F.; Wu, Y. J.; Kakegawa, K. *Phys. Chem. Chem. Phys.* **2003**, *5*, 929–934.

(17) Guo, L.; Yang, S.; Bay, C. W.; Kong, H.; Yang, C.; Yu, P.; Wang, J.; Ge, W.; Wong, G. K. L. *Chem. Mater.* **2000**, *12*, 2268–2274.

(18) Meulenkamp, E. A. *J. Phys. Chem. B* **1998**, *5647*, 5566–5572.

(19) Hoyer, P.; Weller, H. *Chem. Phys. Lett.* **1994**, *2614*, 379–384.

(20) Redmond, G.; Keeffe, A. O.; Burgess, C.; Machale, C.; Fitzmaurice, D. *J. Phys. Chem.* **1993**, *97*, 11081–11086.

(21) Yusoff, A. R. B. M.; Kim, H. P.; Jang, J. *Nanoscale* **2014**, *6*, 1537–1544.

(22) Unalan, H. E.; Hiralal, P.; Kuo, D.; Parekh, B.; Amaratunga, G.; Chhowalla, M. *J. Mater. Chem.* **2008**, *18*, 5909.

(23) Kim, K.; Jung, B.; Kim, J.; Kim, W. *Sol. Energy Mater. Sol. Cells* **2010**, *94*, 1835–1839.

(24) Jitianu, M.; Goia, D. V. *J. Colloid Interface Sci.* **2007**, *309*, 78–85.

(25) LAPORTE, O.; MEGGERS, W. F. *J. Opt. Soc. Am.* **1925**, *11*, 459–460.

(26) Bunker, G. *Introduction to XAFS A Practical Guide to X-ray Absorption Fine Structure Spectroscopy*; Illinois, 2010.

(27) Damen, T. C. Porto, S. P. S. Tell, B. *Phys. Rev.* **1966**, *142*, 571–574.

Chapter 7 - Conclusions

In this thesis work a number of methodologies were developed for investigating catalytic materials *in situ* using synchrotron radiation techniques. Materials investigated have ranged from metal oxides to supported nanoparticles and bimetallic clusters. Various different *in situ* cells have been utilised and the potential for exploring different catalytic systems explored. Presented here is a summary of the findings from this body of work.

The investigation of supported Pd nanoparticles on various inorganic supports was successful carried out on the Pd K- and L_{III}-edges. The formation of Pd hydride was confirmed by use of the Pd L_{III}-edge, through the extra peak present after the edge caused by additional electronic interactions between Pd and H; an effect not seen in the Pd K-edge due to the nature of the excitations not involving bonding orbitals. K-edge measurements however provide detailed EXAFS measurements of the materials showing the expansion of the bond distance, which occurs in the same temperature regions as Pd hydride formation is observed in the L_{III}-edge.

Further XAS metal support experiments have been used to determine the difference in reducibility between supported platinum group metals. Both supported Pd and Rh catalysts showed signs of reduction, with the level of reduction for Rh being much lower than for Pd. Pd material showed an interesting expansion of the bond distance at low temperature in the presence of H_2 attributed to Pd hydride formation. The lower level of Rh reduction can be linked to the reduction capabilities of Rh_2O_3. Although the materials were reduced, the reduction did not go to completion in either case, with a maximum conversion of ca 65% reported in both Pd and Rh. Whilst this could be mere coincidence due to incomplete reduction, it could also be evidence to another effect of the support materials. It could be possible that the reduction of the material is impeded by the ceria support. It is well documented that ceria possesses a remarkable oxygen storage capacity; this stored oxygen could be transferred to the metal NPs during the reduction. This effect would be limited to metal clusters within a specific distance to the ceria, or impeded in defect sites in the ceria structure. Further data is required to confirm this theory.

QuEXAFS measurements on both the Au and Cu edges were utilised to study $AuCu/SiO_2$ catalysts for the oxidation of propene. The activation process was followed *in situ* using EXAFS to provide insights into the changes occurring on the local structure. Reduction of the Au and Cu precursors is required in order to form AuCu alloys. Whilst the catalyst was successfully reduced, no interaction in the local structure between the metals could be determined. Calcination of the catalyst leads to the growth of Au metal and CuO species with little to no interaction between the metals.

The thermal decomposition of zinc peroxide into zinc oxide was successful followed in a combine XAS/XRD experiment. Through the combined study it can be see that there is an initial structural deformation across the long range structure, accompanied by a local change from 6-coordinate to 4-coordinate. This is followed by a gradual growth of the zinc oxide clusters. Comparison with other techniques such as TGA and Raman spectroscopy has helped to confirm these results. Initially there is gradual reduction in the size of the zinc peroxide clusters; this can be observed through the reduction in the intensity of the reflections in XRD. Following this there is rapid rearrangement of the local structure from 6 coordinate to 4-coordinate, followed by a slow growth of the oxide clusters. The combination of *in-situ* XRD and EXAFS reveals more information than using techniques individually. The insights gained into the decomposition of the zinc peroxide and the growth of zinc oxide can be used to tailor the synthesis and improve particle-size control in future synthesis.

Throughout the work it has been shown that synchrotron radiation techniques, specifically XAS, are a powerful characterisation techniques with direct applications to catalysis. The combination of XAS with other techniques both *in situ* at the beamline for combined measurements and *ex situ* characterisation provides a comprehensive analysis of the structure of the materials. The main advantages of utilised XAS, such as element specific and time-resolution allows for the collection of *in-situ* data of catalysts under real operating conditions. This is essential in order to understand and fine-tune the synthesis and reactions of future catalytic systems.

Chapter 8 - Future work

Whilst conducting the experiments and investigations of the thesis work, there were a number of areas for potential expansion. A lot of these areas fell outside the scope of this project, however the potential for new discoveries will be explored here.

For chapter 4 there is potential for expansion by investigating the effect of calcination environment using XAS. The *in situ* studies would focus on the calcination of the catalysts in dry and wet atmosphere and reduction in hydrogen (5% H_2/N_2) to determine the structure of metal particles and the effect of water on the metal support interaction (MSI). The proposed experiments would provide details on both the local and electronic structures, allowing information relating to the nanoparticle binding sites to be determined. Additionally the effects of moisture on the catalyst would be explored using *in situ* XAS measurements.

In this study the focus would be on observing the metal support interaction (MSI) of Rh and Pd nanoparticles deposited on a variety of inorganic supports, to determine the effect if any on the catalysis. Moisture has a large effect on the perfermance of catalytic materials in industry. The effects of moisture in catalyst pre-treatment will be investigated by reducing materials prepared in the prescence and absence of moisture. Additionally the effects of moisture on the material will be investigated by performing *in situ* calcinations in both wet and dry conditions and comparing the structures of the materials formed with their catalytic performance. additionally the effect of the support with regards to moisture, such as the ceria oxygen storage capability, will be taken ito consideration in this study.

The aim of this investigation is to conduct *in situ* studies at the Pd and Rh K- edge and on the support edges for Ceria and Titania supports to study; (a) Metal support interaction and (b) The effect of moisture with regards to catalyst pre-treatment and nanoparticle binding. These measurements should lead to an improved understanding of the metal support interaction between Pd- and Rh- nanoparticles and various inorganic supports. Additionally the effects of moisture on the materials will be investigated the results of which could potentially be of benefit to industry. The methodology developed in this investigation can be applied to a variety of different catalytic systems, such as other second row transition metals and bimetallic clusters.

The AuCu catalysts investigated in chapter 5, were successful used for the oxidation of propene. Combining these investigations with MSI effects developed in chapters 3 and 4 would have some interesting areas of development. SiO_2 has been repeatedly shown to be a poor support for metal nanoparticles due to the weak interactions between the support and the metals.[1] Using reactive supports such as titania could have interesting potential with regards to

improving the catalysis, as titania and gold have a number of synergistic effects.[2] In the same area ceria has a strong interaction with metal nanoparticles. Additionally the oxygen storage capacity (OSC) of ceria is could have an impact on the catalysis of the material, whether it improves or hinders the process is a subject for investigation. [3]

The preparation method for the AuCu clusters was focused on a two-stage deposition method.[4] Alternatively there are a number of reported methods by nano-scientists for producing AuCu NPs with various different structures and architectures.[5,6] Investigating these materials in terms of the catalytic activation in comparison to deposited results could lead to some excited new developments. Furthermore the use of these structures could be used to obtain a range of standards for Au-Cu bonds in various ratios of Au:Cu. This information could then be used to provide a more realistic Au-Cu path for the fitting models, allowing for a more accurate interpretation of the interaction. Finally combination with XPS measurements, lab based and synchrotron based for *in situ* measurements, would allow for determination of charge transfer effects that should be present if mixed AuCu particles are being formed.

Decomposition of zinc peroxide has been shown to produce zinc oxide particles. Through the combined XAS/XRD measurements, it was shown that calcination temperature can have an impact on the size of the particles formed. Further work in this area would involve controlling the temperature to tailor the size of the particles formed. As the properties of zinc oxide particles are linked to the size this is an important step in creating nanoparticles for specific purposes. Another area of expansion would be to investigate the potential for developing this method for use as a deposition method for ZnO particles.

Finally as a general comment for the future work in the development of *in situ* characterisation of catalytic materials, the determination of the active site and the way they are activated and changed during the reaction is another vastly important area for catalytic development. This can be done through EXAFS although there is some difficulty; this is due to EXAFS being a bulk technique. Combination with surface techniques such as electron yield XAFS would provide an interesting comparative analysis. Furthermore investigating the catalysts using total scattering (PDF) would provide information on every atom location in the system. This would not only help for the development of testing for active sites, but would also allow for determination of defect sites. Defects are important in catalysis as they can provide ideal places for nanoparticles to deposit and grow.[7]

The work conducted in chapter 3 demonstrated the potential to use the L_{III}-edge of first row transition metals to provide information about the changes in the electronic state. This can be

combined with any of the above investigations to expand understanding of the processes and changes occurring during catalyst preparation and use. Expansion in this area would require the use of computational modelling in order to better interpret the results, and to help with the tailoring of experimental set-ups.

8.1 References

(1) Li, W.; Wang, A.; Liu, X.; Zhang, T. *Appl. Catal. A Gen.* **2012**, *433-434*, 146–151.

(2) Tauster, S. J. *Acc. Chem. Res.* **1987**, *20*, 389–394.

(3) Rodriguez, J. a.; Si, R.; Evans, J.; Xu, W.; Hanson, J. C.; Tao, J.; Zhu, Y. *Catal. Today* **2015**, *240*, 229–235.

(4) Bracey, C. L.; Ellis, P. R.; Hutchings, G. J. *Chem. Soc. Rev.* **2009**, *38*, 2231–2243.

(5) Sra, A. K.; Ewers, T. D.; Schaak, R. E. *ChemInform* **2005**, *36*, 758–766.

(6) Rodríguez-López, J. L.; Montejano-Carrizales, J. M.; José-Yacamán, M. *Appl. Surf. Sci.* **2003**, *219*, 56–63.

(7) Zro, C. À.; Institut, P.; Fakultät, T. *ACS Nano* **2013**, 2999–3013.

Chapter 9 - Appendix

9.1 Appendix A – Chapter 2

Acquired XAS data can be processed by a number of different software programs developed by individuals and the EAXFS community.[1] The main programs which will be used during the course of this EngD are Viper, Excurv98,[2] and the Athena/Artemis package[3] which runs using IFFEFIT.[4] The basic outline for analysing data is the same regardless of the software used.

An outline of the initial data processing method is given here, using Athena software.[3] The first step in the analysis involves converting the recorded data into a plot of energy vs. absorption coefficient (Figure 9-1). This is done using the relations given in Equation 2-6 and Equation 2-7 for transmission and fluorescence respectively.

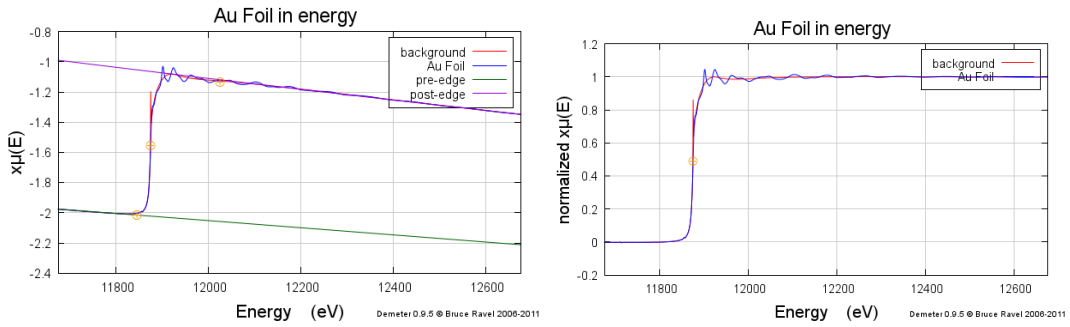

Figure 9-1 - Example of data analysis process using Athena to analyse Au foil data on the Au L_3 edge; (Left) imported energy vs. absorption coefficient showing pre and post-edge lines for normalisation and spline function for background subtraction; (Right) normalised data

Once data has been successfully imported the value for the edge transition and E_0 can be applied. Following this, the background which is the data obtained from single atom behaviour, is removed; this leaves the data caused by scattering from nearest neighbours. The background subtraction utilises a spline function that can be adjusted to fit the data.[3] The data is then normalised, which removes any variances due to, for example, sample mass (Figure 9-1). This normalised data, containing the neighbouring oscillations, can also be known as $\chi(E)$ which can be defined as;

$$\chi(E) = \frac{\mu(E) - \mu_0(E)}{\Delta\mu_0}$$

Equation 9-1

Where Definition of the EXAFS function where $\mu(E)$ is the x-ray absorption coefficient and $\mu_0(E)$ is the atomic background. χ(E) is then converted to χ(k) as this allows for the oscillations to be interpreted as a function of the photoelectron wave number (see Equation 2-3 for wave vector equation). The data is usually multiplied by a power of *k*, usually k^3; this is to emphasise the oscillations and compensate for attenuations at high *k*-values as well as large oscillations at low *k* values; in essence this minimises the noise and maximises the data. EXAFS data can then be obtained by taking the derivative of the normalised and background subtracted data and applying a Fourier transformation (Equation 9-2); where, R is the interatomic distance between the absorber and scatterer.[5]

$$fR = \int_{kmin}^{kmax} \chi(k) e^{ikr}\, dk$$

Equation 9-2

The Fourier transform separates neighbouring atoms from the central atom according to the distance to the central atom (Figure 9-2). The amplitude of the oscillations is dependent upon the number of atoms present at each distance.

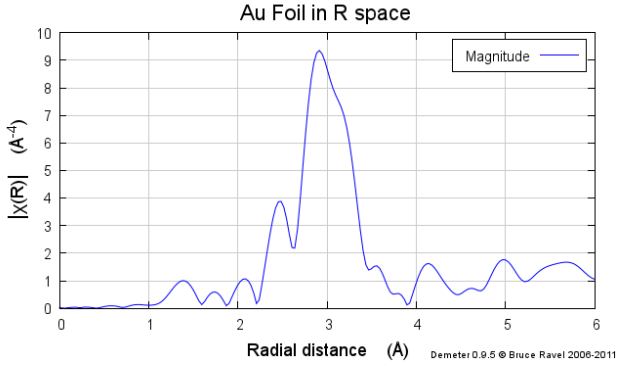

Figure 9-2 - Fourier transform of Au l_3 edge gold foil

Once Data has been processed to this stage the EXAFS data can be analysed using either Artemis or Excurve.[3,4] These programs are designed to fit theoretical structural models to the EXAFS data allowing for determination of information such as coordination number and structure through comparison. The basic outline of analysis is the same for both programs. The first step is to define the atom types present in the material. The next is to set up a model structure; this can either be done by importing a crystallographic information file (CIF file) or

by creating a structure using the software. Once a structure has been created or imported the phase and amplitude factors for the material are calculated. Finally the various parameters of interest such as bond distances, coordination numbers, can be refined until a best match between the calculated and experimental values is obtained.

9.1.1.1 EXAFS Analysis: Artemis Software

The Artemis software package is part of the same group of programs developed by Bruce Ravel for the analysis of XAS data.[3] Analysis of the EXAFS region first requires the processing of the data in a dedicated software package such as Viper or Athena.[3] The processed data can then be loaded into Artemis and the EXAFS data analysed in depth.

The first part of the analytical process is to determine the Amplitude term using a chemical standard, usually a metal foil for transition metals. The Amplitude term takes into account all the subtle variations that can occur on the beamline, and as such must be recalculated each time the absorption edge is changed and between different beamtimes. Once the amplitude term has been determined for a given element it can be transferred to other datasets within the same experiment, and for comparisons between different experiments.

The next step in the analytical process is to fit the data to known structural models. This can be easily accomplished by utilising a crystallographic information file, or CIF, from a structure data base such as the International Crystal Structure Database (ICSD).[6]

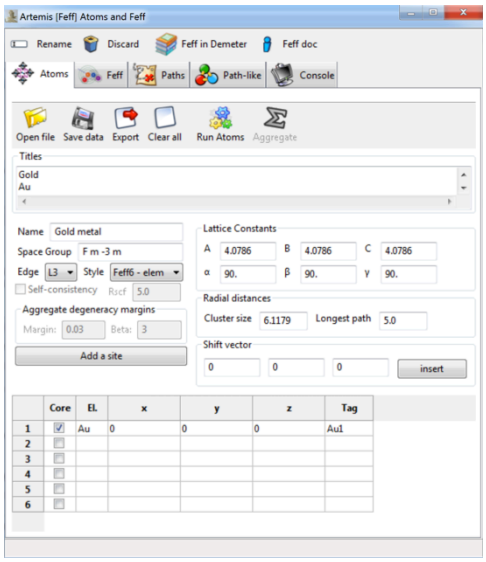

Figure 9-3 - Feff calculation for Au metal using Artemis software, showing element and position selection.

For example with Au foil the cif file selected would be one for bulk gold metal. Once the crystallographic file has been selected, the scattering element needs to be selected (Figure 9-3). For this example only Au atoms are present but for metal oxides and other multi-element systems it becomes necessary to specify the required element.

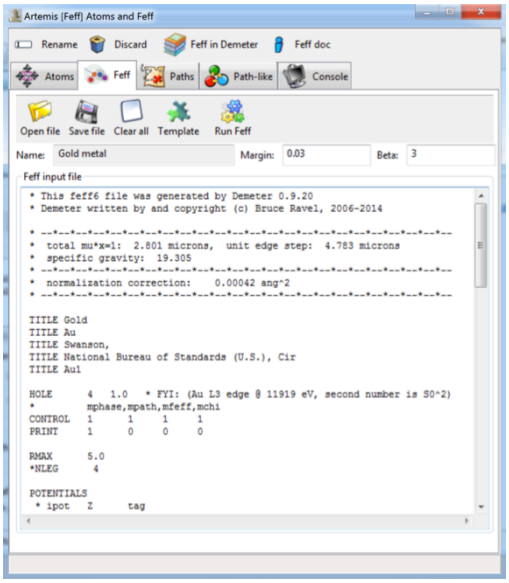

Figure 9-4 - Screen capture from Artemis after running the Atoms calculation to determine atom positions based upon symmetry and space group information.

The next step is to determine the local geometry and symmetry using the information contained in the .cif file by performing an Atoms calculation (Figure 9-4). This generates the unit cell that will be used to calculate the scattering paths.

Finally it is possible to perform a FEFF calculation to determine the scattering paths in the material (Figure 9-5). Once the scattering paths have been generated, the software provides information about the type of scattering whether it is single scattering from a neighbouring atom or multiple scattering dependent upon backscattering from more than one neighbouring atom position. The contribution is also provided in terms of a percentage and the paths and positions can be plotted for easy visual determination (Figure 9-6). Prior knowledge of the material in addition to some experience with fitting EXAFS data is then required in order to select the key contributing paths and add them to the data analysis window as part of the fitting model.

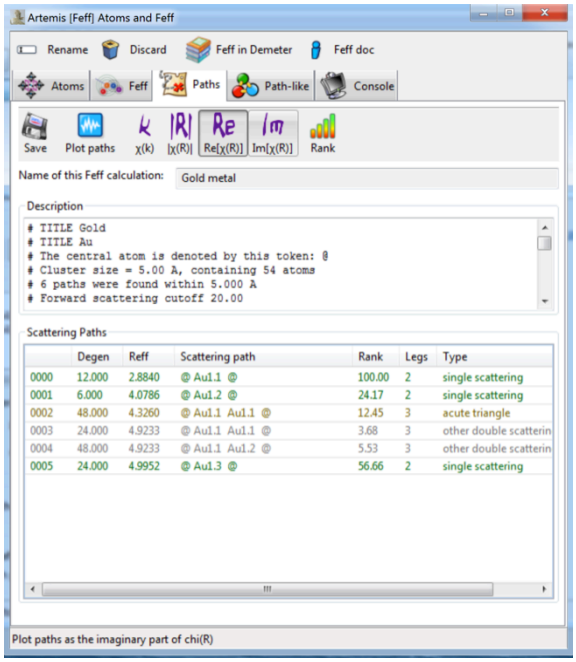

Figure 9-5 - Screen capture from Artemis after the Feff calculation showing the scattering paths arising from gold metal. Also indicated is the contribution of each path, the degeneracy and the nature of scattering, for example single scattering.

The next stage requires parameterising the selected paths with independent variables. The number of variables available is related to the Nyquist equation and is dependant on the size of the k and R-ranges selected. This provides a maximum number of variables that can be used in the fitting model, fewer parameters can mean a better fit and requires an understanding of the chemical system being studied. For example with Au metal the first path is at, 2.88Å with the second path at 4.08Å. As the contributions from these to paths are, 100 and 24 respectively an initial fitting model, in R-range 1-4 Å can be made by just considering these two paths.

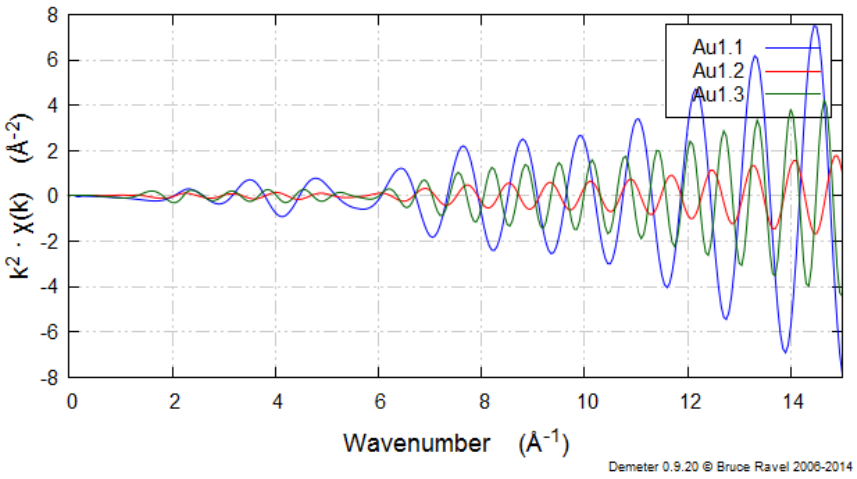

Figure 9-6 - Graph from Artemis showing the individual contributions in k-space for the first 3 shells of Gold metal

For parameterisation, the same amplitude must be fitted to both paths (as this is a standard we assume ideal coordination numbers). The delr or Δr term is the related to the change in the bond distance compared to the literature value. This can vary between shells so should be kept independent. The σ^2 (sigma-squared or ss) terms are related to the disorder of the respective path. These terms should be kept separate depending on the elements, for example in a metal oxide (MO) system the σ^2 term for the M-M paths should always be spate from the σ^2 terms for the M-O paths.

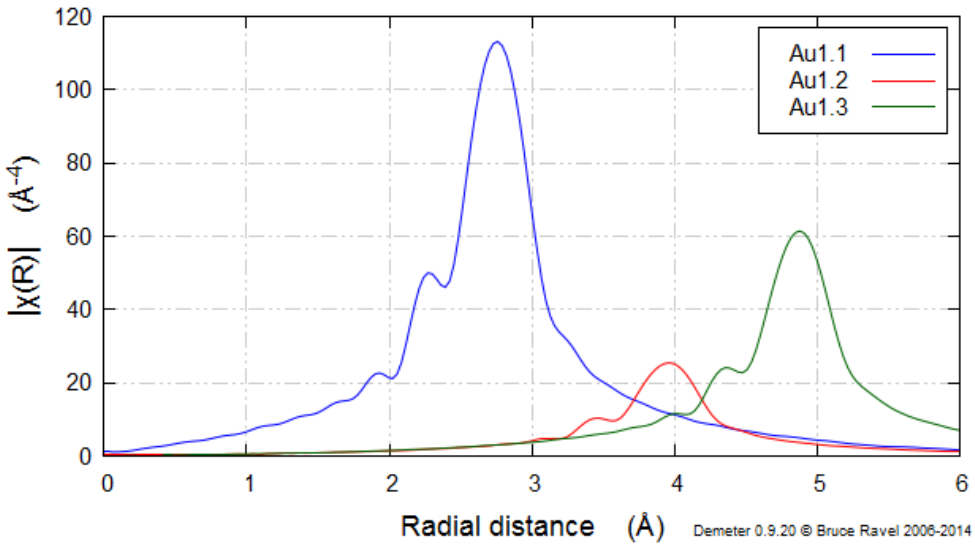

Figure 9-7 - Plot from Artemis for the individual contributions from the first 3 shells of in real space

Paths can be parameterised with any name, but for functionality it is useful to follow a system so that the terms are easily identifiable when reading the output file from the calculation.

Once the paths have been parameterised the terms used must be entered into the GDS or Guess, Set, Define, window. Spelling is crucial; all terms must be entered the exact same way as they were when parameterising the paths. Following on from this the fit can be performed.

Artemis provides an output file containing all the relevant information from the fit. The key factors to look out for are the R-factor, which is a statistical measure for the wellness of fit and the fitting parameters to make sure the results make sense (Figure 9-8). A comparative plot of the data with the fitting model is also provided to allow for a visual comparison of the theoretical and experimental data (Figure 9-9). A word of caution, do not judge a fit by looks alone, sometimes a perfect visual fit, makes no chemical sense.

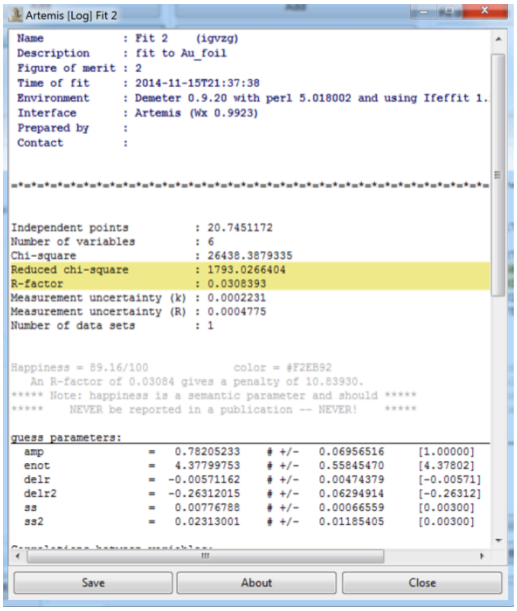

Figure 9-8 - Fit report from Artemis for fitting of Au foil data.

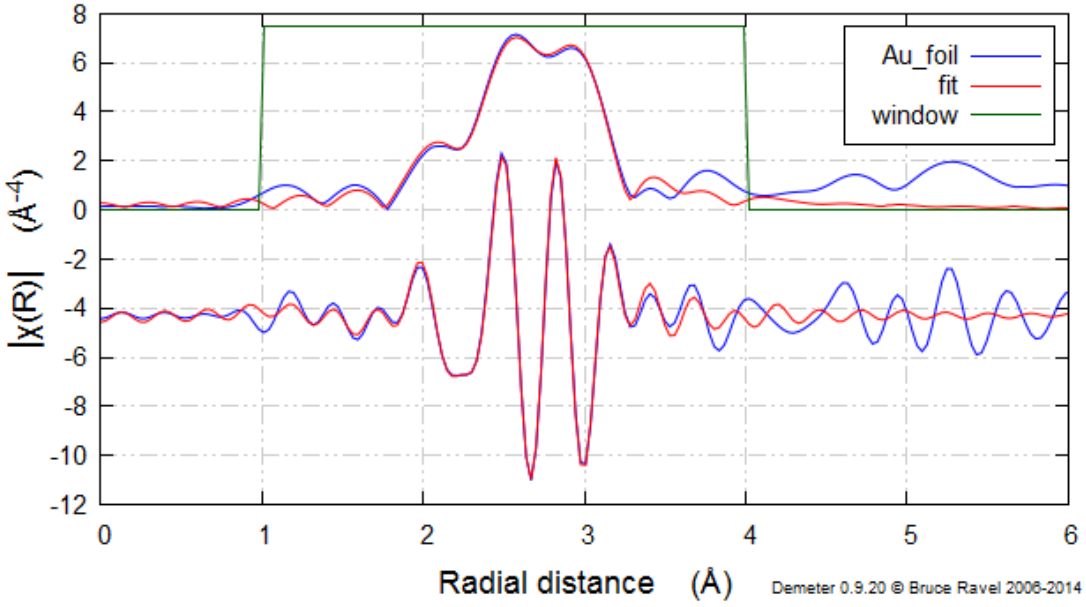

Figure 9-9 - plot from Artemis of the experimental and theoretical data for visual comparison.

The fitting process is repeated until the user is satisfied with the quality and interpretation of the data. More paths and parameters can be added or removed as required, allowing for the fitting of more interesting and complex systems.

For fitting some systems such as distorted crystal structures or amorphous materials with no ong range order there may be no cif file available. In these cases it is necessary to either take paths from similar chemical systems or to edit the crystal file using software such as Mercury. Artemis does provide a quick first shell theory function that calculates the first shell scattering path from a system for any two elements, with user control over the bond distance and the coordination number. For *in-situ* data this can be used as an alternative to creating an input file for a structure.

It is also possible to fit coordination numbers in Artemis, though not directly. This is achieved by adding an extra term to the S_0^2 path once the amplitude has been set, and by taking the approximation that the most significant contribution to the amplitude, once the value has been set, is the variation of coordination number. For example adding an extra parameter, xau, to the Au-Au first shell would provide the coordination number by multiplying the value of xau with the degeneracy of the shell, which in this case is 12. This can be done for multiple paths with experience and practice.

9.2 References

(1) Ankudinov, A. L.; Ravel, B.; Rehr, J. J.; Conradson, S. D. **1998**, *58*, 7565–7576.

(2) Newville, M. *J. Synchrotron Radiat.* **2001**, *8*, 96–100.

(3) Ravel, B.; Newville, M. *J. Synchrotron Radiat.* **2005**, *12*, 537–541.

(4) Newville, M. *J. Synchrotron Radiat.* **2001**, *8*, 322–324.

(5) Sayers, D. E.; Stern; Lytle, F. *Phys. Rev. Lett.* **1971**, *2*, 1204.

(6) Inorganic Crystal Structure Database

http://cds.dl.ac.uk/cds/datasets/crys/icsd/llicsd.html.